The expression of climate in pedogenic carbonates: using modern analogues to better understand ancient records

by

RACHEL ELIZABETH HAVRANEK

M.S., University of Colorado Boulder, 2017

B.A., Pomona College, 2014

A thesis submitted to the

Faculty of the Graduate School of the

University of Colorado in partial fulfillment

of the requirement for the degree of

Doctor of Philosophy

Department of Geological Sciences

2023

Committee Members:

Kathryn Snell

Suzanne Anderson

Gabe Bowen

Sebastian Kopf

Eve-Lyn Hinckley

Abstract

Rachel E. Havranek (Ph.D., Department of Geological Sciences)

The expression of climate in pedogenic carbonates: using modern analogues to better understand ancient records

Thesis directed by Assistant Professor Kathryn Snell.

The Paleocene-Eocene Thermal Maximum (PETM) is an ancient example of relatively rapid climate change that has been widely studied as a potential analogue for modern climate change. To understand how terrestrial environments respond to rapid warming, researchers have turned to a thick stack of paleosols that record the PETM that are preserved in the Bighorn Basin, WY. The fine-grained, clay-rich paleosols of the Bighorn Basin preserve an extensive floral and faunal fossil record and provide other environmental information from a variety of geochemical proxy records that allows researchers to reconstruct the whole ecosystem response to the PETM. Despite the abundance of work that has been done, the community still lacks an understanding of how temperature evolved through the PETM in the basin. A pedogenic carbonate clumped isotope thermometry record would provide critical context for the other biological and sedimentological data. However, it is not clear how the temperature recorded by pedogenic carbonate that forms in fine-grained and clay-rich soils relates to mean annual air temperatures of the environment.

Investigating modern analogues for ancient environments allows geoscientists to probe the assumptions and constraints of the proxy tools we use.

Recent modern calibration work indicates that soil grain size may control how carbonate clumped isotope temperatures relate to mean annual air temperature. To date though, few studies of pedogenic carbonate have included fine-grained soils. To address this knowledge gap, I studied three modern carbonate-bearing, clay-rich, fine-medium grained soils. I monitored both environmental parameters, like air and soil temperature, as well as geochemical parameters, like soil water stable isotope composition, to better understand the timing and drivers of carbonate nodule formation so that I could better interpret a new record of temperature change that I produced for the PETM.

Because clumped isotope thermometry of paleosol carbonates provides both a mineral formation temperature and an estimate of the oxygen isotope composition of soil water, one primary objective of my dissertation was to create a time series of modern soil water isotopes. In chapters 2 and 3 of my dissertation, I present the full development of the Soil Water Isotope Storage System (SWISS), an automated field deployable system that enables the collection of serial soil water isotope datasets that are necessary for understanding ancient estimates of soil water oxygen isotopes. This system is capable of automatically collecting soil water vapor and then storing that vapor for up to 40 days before it is returned to the lab to be measured, enabling the collection of soil water datasets from relatively remote areas. In chapter 4, I use the datasets derived from the SWISS deployments, alongside climatological data, to better understand how pedogenic carbonates from three fine-medium grained soils record information about climate. I found that in

two of the three soils, clumped isotope temperatures were consistent with mean annual temperature. In the third soil, however, clumped isotope temperatures were most consistent with summer temperatures, though it is unclear whether those temperatures reflect isotopic equilibrium, or are an artifact resulting from isotopic disequilibrium. Finally, in chapter 5, I use my understanding of pedogenic carbonate in fine grained soils to inform my interpretation of a clumped isotope record through the PETM. I find that mean annual temperatures increased ~20°C during the PETM to peak temperatures of 36.2 ± 3.8°C. These hot temperatures indicate significant terrestrial amplification of warming and have implications for floral and faunal changes during this event. Altogether, my findings demonstrate that adding independent measurements of soil water isotopes provides an additional constraint on pedogenic carbonate formation, which improves our understanding of ancient climate records.

Acknowledgements

This thesis is the culmination of so much love and support from my community. I always say that science is a team sport, and I am eternally grateful to my large and wonderful team that have supported both the science in this thesis and my ability to do that science.

Thank you to my committee – Suzanne Anderson, Gabe Bowen, Sebastian Kopf, and Eve-Lyn Hinckley – for their support and guidance throughout this process. Eve, I learned so much from your class and I am so appreciative that you always encouraged me to think about the broader context of my research. Seb, thank you so much for your unending patience as I learned to build the automation system and for always helping me fail forward. I am so excited to take what I have learned about microcontrollers and coding and using it not only in my science but also in my personal life.

Thank you to everyone in the INSTAAR Stable Isotope Lab for making me feel so at welcome and immediately at home. I really could not have asked for a better lab to spend so many days and weeks in. Thank you especially to Bruce Vaughn and Valerie Morris. Bruce, I am so appreciative of your encouragement and guidance while building and testing the SWISS. You were so generous with your expertise, and I learned so much from brainstorming with you. Valerie, I am so grateful for your technical expertise and all of our chats. You were so generous with your time, and I will always be in awe of your ability to tighten Swagelok fittings just right.

Thank you to everyone in the TerraPaleo lab, including Brett Davidheiser-Kroll, Anne Fetrow, Lina Pérez-Ángel, Juliana Olsen-Valdez, Vikki Crystal, Dave Colwyn, and Haley Brumberger. I am so appreciative for such a wonderfully kind group of humans who always let me be my fully weird self and supported my love of snacks. Thank you all for reading my terrible first drafts, for helping me stay productive even when I made my best attempts to distract you all, and for the help over many, many field days. I want to especially thank Brett, who taught me tinker and to just take the first step even if it's not perfect. Brett, your approach to science and failure has been a powerful life lesson for me, and for that I will always be so grateful.

Graduate school can take a toll on many students, and I am no exception. But, that toll was greatly buffered by the love and support of my family and friends. To my parents, thank you for making me so many dinners, for creating space for me to decompress at home, and for providing endless support and love. To my sister Katie, thank you for all the memes and the terrible reality TV recommendations, only you know how much those things have helped me keep going. Lina, you give the best pep talks and always helped me keep moving forward when things felt tough. Ciara, you were the best role model for building a balanced life that included creating space to decompress and pursue other things that bring me joy. Bella, thank you so much for helping me not take this whole PhD thing too seriously, and for always bringing me tasty vegetables when I couldn't make them for myself. You have been such a wonderfully consistent friend over the years. Tina, your kindness

and empathy always amaze me. Your ability to help me see evenly see the challenges and joys of being a grad student helped me weather the storm. I will also be eternally grateful that on my 30th birthday you drove to the field with me, and still managed to make that day feel special. Anne, your incredibly consistent support truly made this PhD possible. I am so grateful that I had someone to always take me for runs, to read all of the emails that made me anxious, and to lean on when I didn't know how to take the next step forward.

To my husband, Spencer, your endless love, support, cheerleading and hole-digging skills truly made this PhD possible. I will never be able to thank you enough for the support you've given me over the last 5 years. From being my #1 field assistant, to making sure I was always fed, to helping me physically build so much of my equipment, you were critical to the success of these projects.

Lastly, thank you to my advisor Katie Snell. Words can't really describe what you've done for me as a scientist. From my first day as your student you expressed so much confidence in me, and your support helped me to take so many risks over the last five and half years. You have this uncanny ability to coach me through the projects and tasks that I either don't want to do or think I can't do, and have helped me become a much stronger scientist and overall human. I will always remember blasting Sjowgren late at night driving back from the field, eating way too much popcorn during group meetings, and the epic Halloween parties at your house. I am so grateful that I found an advisor who let me bring my entire self to the PhD.

Table of Contents

List of Tables

List of Figures

Chapter I: Introduction

One of the fundamental questions of geology is how Earth's climate has evolved over time and how that has influenced (or been influenced by) both tectonic processes and biotic change through time. In the last 50 years, the need to understand how climate is modulated over geologic timescales has become even more urgent as we face a warming planet from anthropogenic CO_2 emissions. By looking into the geologic past, we can learn about fundamental controls on Earth's climate system, and therefore make better predictions about, and therefore choices for, the future. In particular, we can use climate scenarios from the geologic past to test the validity of the climate models we depend on to make policy choices for the future (e.g. Tierney et al., 2020; Steinthorsdottir et al., 2020; Inglis et al., 2020; Rae et al., 2021).

One of the most widely studied and best characterized climate event in Earth's history is the Paleocene – Eocene Thermal Maximum (PETM) because it is a relatively rapid warming event that was driven by an increase in atmospheric greenhouse gases over 8-23 Kyr (Kennett and Stott, 1991; Koch et al., 1992; Zachos et al., 2001; McInerney and Wing, 2011; Westerhold et al., 2020). It is one of the few moments in Earth's history where the geoscience community can determine how the climate system responds to a sudden input of greenhouse gases and explore the environmental impacts both in the ocean and on land.

The Bighorn Basin (BHB) in Wyoming, USA preserves one of the best, and most widely studied terrestrial records of the PETM (e.g. Koch et al., 1992; Bowen

et al., 2001; Gingerich, 2001; Wing et al., 2005; Kraus et al., 2015). The paleosols of the BHB host records of floral and faunal change in the basin from the Upper Cretaceous through the Eocene, and so have been ideal for studying how climate change influences biotic change on land during rapid warming. Additionally, these paleosols have been ideal for giving insight into how sedimentary systems respond to and record climate change. Though temperature change during the PETM has been estimated a few different ways (Fricke and Wing, 2004; Wing et al., 2005; Secord et al., 2012; Snell et al., 2013), those records offer either low temporal resolution estimates of absolute temperature change during the PETM (e.g. Fricke and Wing, 2004; Wing et al., 2005), or they provide estimates of the magnitude of temperature change but not absolute temperature estimates (e.g. Secord et al., 2010). To better contextualize abiotic and biotic responses in the basin, ideally, we need a higher resolution record of absolute temperatures through time. One way to create that record is by applying carbonate clumped isotope thermometry (Δ_{47}) to the abundant pedogenic carbonate nodules of the basin.

Carbonate clumped isotope thermometry exploits the dependency of bond ordering of the heavier, rare ^{13}C and ^{18}O isotopes in carbonate minerals on temperature to estimate mineral formation temperature (Wang et al., 2004; Eiler 2007). In addition, an independent estimate of temperature from Δ_{47} can be used with the simultaneously measured $\delta^{18}O$ of carbonate to estimate the $\delta^{18}O$ composition of the water from which the carbonate formed, using the temperature-dependent fractionation of oxygen isotopes between carbonate minerals and water

(e.g. Kim and O'Neil, 1997). The development of this tool represents a large step forward for the paleoclimate community in estimating environmental temperatures in the geologic past. However, this tool provides only an estimate of mineral formation temperature, and does not give direct estimates of key climate parameters like mean annual air temperature. So, one question that has persisted in the clumped isotope community over the last 10-15 years is how to interpret pedogenic carbonate clumped isotope temperatures in terms of climate parameters (Peters et al., 2013; Hough et al., 2014; Burgener et al., 2016; Oerter and Amundson, 2016; Kelson et al., 2020). If the goal is to produce data that is useful for creating a holistic view of climate in the past, or data that is ultimately useful for climate models, we need to clearly understand the relationship between landscape conditions and the isotopic composition of carbonate.

Modern calibration studies of paleoclimate proxies, in which geoscientists study how a proxy material (e.g. pedogenic carbonate) forming in the modern environment relates to an environmental parameter that we want to reconstruct in the geologic past, allow researchers to explicitly probe the assumptions and limitations of the proxy tool. Since the 1980's, researchers have been exploring how aspects of vegetation and key components of climate, like precipitation and temperature, are encoded into pedogenic carbonate stable isotopes (Cerling, 1984; Cerling and Quade, 1993; Breecker et al., 2009; Oerter and Amundson, 2016). Carbonate clumped isotope thermometry provides an additional control on the timing of pedogenic carbonate and has reinvigorated modern calibration studies of

soil carbonates (Passey et al., 2012; Peters et al., 2013; Hough et al., 2014; Burgener et al., 2016; Gallagher and Sheldon, 2016; Burgener et al., 2018; Huth et al., 2019; Kelson et al., 2020). Broadly, studies thus far indicate that pedogenic carbonate records a warm-season bias and likely forms during soil dry-down events, with some exceptions. One caveat to the body of work highlighted above is that the studies were primarily completed in coarse-grained and relatively immature soils. Those soils were targeted because of abundant pedogenic carbonate and were often selected as part of specific regional climate or elevation gradients. That means that our understanding of carbonate formation dynamics in fine grained, clay-rich paleosols, like those of the Bighorn Basin, is limited. Furthermore, given that soil dry-down has been called upon as the primary mechanism driving carbonate formation (e.g. Hough et al., 2014; Huth et al., 2019), and that soil texture plays a dominant role in controlling soil dewatering rates, soil texture should exert a control on the timing of pedogenic carbonate formation, which in turn affects how these carbonates record climate information. Indeed, a recent meta-analysis of pedogenic carbonate formation found that there are significant differences in the seasonal bias of clumped isotope temperatures between different soil textures (Kelson et al., 2020).

Modern calibration studies are most useful when key parameters of modern environments, like soil grain size, are similar to the paleoenvironment being reconstructed. The primary goal of this dissertation is to better understand carbonate formation in fine-grained soils so that I can interpret a record of climate

change in the Bighorn Basin during the PETM. To understand carbonate formation dynamics at a more process-based level in fine-grained soils, I wanted to be able to understand how soil water evolves on a seasonal timescale and at the timescale of precipitation events, so that I could relate the stable isotope composition of soil water to the calculated $\delta^{18}O$ of water from the clumped isotope measurement. Adding the constraint of soil water isotopes gives me additional insight into hypothesized carbonate formation mechanisms like evaporation and soil dry-down, and the timing of carbonate formation. However, one technical barrier to that has been the arduous nature of collecting soil water samples for stable isotope analysis.

Historically, obtaining soil water samples has required manual intervention at the time of sampling, either through lysimeter sample collection or by digging a pit, and collecting a mass of soil to bring back to the lab for subsequent water extraction. The latter method disrupts the soil profile each time a sample is collected, and therefore inhibits the creation of soil-water isotope time series datasets (e.g. Orlowski et al., 2016). To limit the amount of manual intervention needed to create time-series datasets, the ecohydrology community developed a variety of in situ water sampling methods over the last 10 years (e.g. Rothfuss et al., 2013; Volkmann and Weiler, 2014; Gaj et al., 2015; Oerter et al., 2016; Beyer et al., 2020), but those methods still require laser spectroscopy systems to be deployed in the field, which limits their utility in remote sites. For this study, it was important to be able to create soil water isotope records at field sites where pedogenic carbonate was forming. So, I set out to create a way to collect serial soil water

isotope datasets that capitalized on technical advances in soil water vapor collection but did not require field deployment of laser spectroscopy systems. In Chapter II, I present the prototype testing of a novel system, the Soil Water Isotope Storage System (SWISS), demonstrating that the system stores water vapor for up to 30 days prior to stable isotope analysis without alteration of the original stable isotope values. Chapter III presents the further testing, optimization, and automation of the SWISS, and demonstrates that the SWISS units can automatically collect water vapor from a soil profile at a regular time interval and store that water vapor until it can be measured back in a laboratory setting. The combination of the autonomous sampler and the CRDS instrument offers a flexible and reliable solution to obtain data that is otherwise difficult to collect from soil profiles, and will make it possible for the soil hydrology community to produce an even broader range of datasets in more remote locations than at present.

To complement existing literature on carbonate formation in modern soils, I present a modern calibration study of pedogenic carbonate clumped isotope thermometry and $\delta^{18}O$ of soil water in three fine-medium grained soils in Colorado and Nebraska, USA in Chapter IV. In this study I compare the clumped isotope thermometry of pedogenic carbonate to climatological records, soil temperature and moisture records, and soil water isotope records to better understand the timing and drivers of carbonate formation in fine grained soils. This work provides the foundation for the interpretation of a paleoclimate records from the Bighorn Basin, but is also useful to the broader paleoclimate community, because fine-grained,

clay-rich paleosols are relatively abundant in the geologic record. Lastly, in Chapter V, I apply my understanding of pedogenic carbonate formation in fine grained soils to a record of ancient temperature and water oxygen isotope change in the Bighorn Basin, WY derived from paleosol carbonates. This record provides critical context for other floral and faunal data in the basin, and provides a terrestrial constraint on the magnitude of warming through the PETM.

Works Cited:

Beyer, M., Kühnhammer, K., & Dubbert, M. (2020). In situ measurements of soil and plant water isotopes : a review of approaches , practical considerations and a vision for the future. *Hydrology and Earth System Sciences*, *24*, 4413–4440. https://doi.org/https://doi.org/10.5194/hess-24-4413-2020

Bowen, G. J., Koch, P. L., Gingerich, P. D., Norris, D., Bains, S., & Corfield, R. M. (2001). Refined isotope stratigraphy across the continental Paleocene-Eocene boundary on Polecat Bench in the northern Bighorn Basin. In *Paleocene-Eocene Stratigraphy and Biotic Change in the Bighorn and Clarks Fork Basins, Wyoming,* University of Michigan Papers on Paleontology, p. 73–88.

Breecker, D. O., Sharp, Z. D., & McFadden, L. D. (2009). Seasonal bias in the formation and stable isotopic composition of pedogenic carbonate in modern soils from central New Mexico, USA. *Bulletin of the Geological Society of America*, *121*(3–4), 630–640. https://doi.org/10.1130/B26413.1

Burgener, L. K., Huntington, K. W., Hoke, G. D., Schauer, A., Ringham, M. C., Latorre, C., & Díaz, F. P. (2016). Variations in soil carbonate formation and seasonal bias over >4 km of relief in the western Andes (30°S) revealed by clumped isotope thermometry. *Earth and Planetary Science Letters*, *441*, 188–199. https://doi.org/10.1016/j.epsl.2016.02.033

Burgener, L. K., Huntington, K. W., Sletten, R., Watkins, J. M., Quade, J., & Hallet, B. (2018). Clumped isotope constraints on equilibrium carbonate formation and kinetic isotope effects in freezing soils. *Geochimica et Cosmochimica Acta*, *235*, 402–430. https://doi.org/10.1016/j.gca.2018.06.006

Cerling, T. E. (1984). The stable isotopic composition of modern soil carbonate and its relationship to climate. *Earth and Planetary Science Letters*, *71*, 229–240.

Cerling, T. E., & Quade, J. (1993). Stable Carbon and Oxygen Isotopes in Soil Carbonates. *Geophysical Monograph Series*, *78*, 217–231.

Eiler, J. M. (2007). "Clumped-isotope" geochemistry - The study of naturally-occurring, multiply-substituted isotopologues. *Earth and Planetary Science Letters*, *262*(3–4), 309–327. https://doi.org/10.1016/j.epsl.2007.08.020

Fricke, H. C., & Wing, S. L. (2004). Oxygen isotope and paleobotanical estimates of temperature and δ18O-latitude gradients over North America during the Early Eocene. *American Journal of Science*, *304*(7), 612–635. https://doi.org/10.2475/ajs.304.7.612

Gaj, M., Beyer, M., Koeniger, P., Wanke, H., Hamutoko, J., & Himmelsbach, T. (2015). In-situ unsaturated zone stable water isotope (^{2}H and ^{18}O) measurements in semi-arid environments using tunable off-axis integrated cavity output spectroscopy. *Hydrology and Earth System Sciences Discussions*, *12*(6), 6115–6149. https://doi.org/10.5194/hessd-12-6115-2015

Gallagher, T. M., & Sheldon, N. D. (2016). Combining soil water balance and clumped isotopes to understand the nature and timing of pedogenic carbonate formation. *Chemical Geology*. https://doi.org/10.1016/j.chemgeo.2016.04.023

Gingerich, P. D. (2001). Paleocene-Eocene Stratigraphy and Biotic Change in the Bighorn and Clarks Fork Basins, Wyoming. In *Paleocene-Eocene Stratigraphy*

and Biotic Change in the Bighorn and Clarks Fork Basins, Wyoming, University of Michigan Papers on Paleontology, p. 89–96.

Hough, B. G., Fan, M., & Passey, B. H. (2014). Calibration of the clumped isotope geothermometer in soil carbonate in Wyoming and Nebraska, USA : Implications for paleoelevation and paleoclimate reconstruction. *Earth and Planetary Science Letters*, *391*, 110–120. https://doi.org/10.1016/j.epsl.2014.01.008

Huth, T. E., Cerling, T. E., Marchetti, D. W., Bowling, D. R., Ellwein, A. L., & Passey, B. H. (2019). Seasonal bias in soil carbonate formation and its implications for interpreting high-resolution paleoarchives: evidence from southern Utah. *Journal of Geophysical Research: Biogeosciences*. https://doi.org/10.1029/2018JG004496

Inglis, G. N., Bragg, F., Burls, N. J., Cramwinckel, M. J., Evans, D., Foster, G. L., Huber, M., Lunt, D. J., Siler, N., Steinig, S., Tierney, J. E., Wilkinson, R., Anagnostou, E., de Boer, A. M., Dunkley Jones, T., Edgar, K. M., Hollis, C. J., Hutchinson, D. K., and Pancost, R. D.: Global mean surface temperature and climate sensitivity of the early Eocene Climatic Optimum (EECO), Paleocene–Eocene Thermal Maximum (PETM), and latest Paleocene, Clim. Past, 16, 1953–1968, https://doi.org/10.5194/cp-16-1953-2020, 2020.

Kelson, J. R., Huntington, K. W., Breecker, D. O., Burgener, L. K., Gallagher, T. M., Hoke, G. D., & Petersen, S. v. (2020). A proxy for all seasons? A synthesis of clumped isotope data from Holocene soil carbonates. *Quaternary Science Reviews*, *234*, 106259. https://doi.org/10.1016/j.quascirev.2020.106259

Kennett, J. P., & Stottt, L. D. (1991). Abrupt deep-sea warming, palaeoceanographic changes and benthic extinctions at the end of the Palaeocene. *Nature*, *353*, 225–229. https://doi.org/10.1038/353225a0

Koch, P. L., Zachos, J. C., & Gingerich, P. D. (1992). Correlation between isotope records in marine and continental carbon reservoirs near the Palaeocene/Eocene boundary. *Nature*, *358*. https://doi.org/https://doi.org/10.1038/358319a0

Kraus, M. J., Woody, D. T., Smith, J. J., & Dukic, V. (2015). Alluvial response to the Paleocene-Eocene Thermal Maximum climatic event, Polecat Bench, Wyoming (U.S.A.). *Palaeogeography, Palaeoclimatology, Palaeoecology*, *435*, 177–192. https://doi.org/10.1016/j.palaeo.2015.06.021

McInerney, F. A., & Wing, S. L. (2011). The Paleocene-Eocene Thermal Maximum: A Perturbation of Carbon Cycle, Climate, and Biosphere with Implications for the Future. *Annual Review of Earth and Planetary Sciences*, *39*(1), 489–516. https://doi.org/10.1146/annurev-earth-040610-133431

Oerter, E. J., Perelet, A., Pardyjak, E., & Bowen, G. J. (2016). Membrane inlet laser spectroscopy to measure H and O stable isotope compositions of soil and sediment pore water with high sample throughput. *Rapid Communications in Mass Spectrometry*, *31*(1), 75–84. https://doi.org/10.1002/rcm.7768

Oerter, E. J., & Amundson, R. (2016). Climate controls on spatial temporal variations in the formation of pedogenic carbonate in the western Great Basin of North Americ. *Bulletin of the Geological Society of America*, *128*(7), 1095–1104. https://doi.org/10.1130/B31367.1

Orlowski, N., Pratt, D. L., & McDonnell, J. J. (2016). Intercomparison of soil pore water extraction methods for stable isotope analysis. *Hydrological Processes*, *30*(19), 3434–3449. https://doi.org/10.1002/hyp.10870

Passey, B. H. (2012). Reconstructing terrestrial environments using stable isotopes in fossil teeth and paleosol carbonates. *Reconstructing Earth's Deep-Time Climate*, *18*, 167–193. https://doi.org/10.1017/S1089332600002606

Peters, N. A., Huntington, K. W., & Hoke, G. D. (2013). Hot or not? Impact of seasonally variable soil carbonate formation on paleotemperature and O-isotope records from clumped isotope thermometry. *Earth and Planetary Science Letters*, *361*, 208–218. https://doi.org/10.1016/j.epsl.2012.10.024

Rae, J.W., Zhang, Y.G., Liu, X., Foster, G.L., Stoll, H.M. and Whiteford, R.D., 2021. Atmospheric CO2 over the past 66 million years from marine archives. *Annual Review of Earth and Planetary Sciences*, *49. https://doi.org/10.1146/annurev-earth-082420-063026*

Rothfuss, Y., Vereecken, H., & Brüggemann, N. (2013). Monitoring water stable isotopic composition in soils using gas-permeable tubing and infrared laser absorption spectroscopy. *Water Resources Research*. https://doi.org/10.1002/wrcr.20311

Secord, R., Gingerich, P. D., Lohmann, K. C., & MacLeod, K. G. (2010). Continental warming preceding the Palaeocene-Eocene thermal maximum. *Nature*, *467*(7318), 955–958. https://doi.org/10.1038/nature09441

Snell, K.E., Thrasher, B.L., Eiler, J.M., Koch, P.L., Sloan, L.C. and Tabor, N.J., 2013. Hot summers in the Bighorn Basin during the early Paleogene. *Geology*, *41*(1), pp.55-58.

Steinthorsdottir, M., Coxall, H. K., de Boer, A. M., Huber, M., Barbolini, N., Bradshaw, C. D., Burls, N. J., Feakins, S. J., Gasson, E., Henderiks, J., Holbourn, A., Kiel, S., Kohn, M. J., Knorr, G., Kürschner, W. M., Lear, C. H., Liebrand, D., Lunt, D. J., Mörs, T., Pearson, P. N., Pound, M. J., Stoll, H., and Strömberg, C. A. E., 2020: The Miocene: the Future of the Past: Paleoceanography and Paleoclimatology, 36(4), e2020PA004037. https://doi.org/10.1029/2020PA004037

Tierney, J. E., Zhu, J., Li, M., Ridgewell, A., Hakim, G. J., Poulsen, C. J., Whiteford, R. D. M., Rae, J. W. B., & Kump, L. R. (2022). Spatial patterns of climate change across the Paleocene-Eocene Thermal Maximum. *Proceedings of the National Academy of Science*, *119*(42). https://doi.org/https://doi.org/10.1073/pnas.2205326119

Volkmann, T. H. M., & Weiler, M. (2014). Continual in situ monitoring of pore water stable isotopes in the subsurface. *Hydrology and Earth System Sciences*, *18*(5), 1819–1833. https://doi.org/10.5194/hess-18-1819-2014

Wang, Z., Schauble, E. A., & Eiler, J. M. (2004). Equilibrium thermodynamics of multiply substituted isotopologues of molecular gases. *Geochimica et Cosmochimica Acta*, *68*(23), 4779–4797. https://doi.org/10.1016/j.gca.2004.05.039

Westerhold, T., Marwan, N., Drury, A. J., Liebrand, D., Agnini, C., Anagnostou, E., Barnet, J. S. K., Bohaty, S. M., de Vleeschouwer, D., Florindo, F., Frederichs, T., Hodell, D. A., Holbourn, A. E., Kroon, D., Lauretano, V., Littler, K., Lourens, L. J., Lyle, M., Pälike, H., … Zachos, J. C. (2020). An astronomically dated record of Earth's climate and its predictability over the last 66 million years. *Science*, *369*(6509), 1383–1387. https://doi.org/10.1126/science.aba6853

Wing, S. L., Harrington, G. J., Smith, F. a, Bloch, J. I., Boyer, D. M., & Freeman, K. H. (2005). Transient Floral Change and Rapid Global Warming at the Paleocene - Eocene Boundary. *Science*, *310*(November), 993–996. https://doi.org/10.1126/science.1116913

Zachos, J., Pagani, M., Sloan, L., Thomas, E., & Billups, K. (2001). Trends, Global Rhythms, Aberrations in Global Climate 65Ma to Present. *Science*, *292*(5517), 686–693. https://doi.org/10.1126/science.1059412

Chapter II: The Soil Water Isotope Storage System (SWISS): An integrated soil water vapor sampling and multiport storage system for stable isotope geochemistry

Rachel E. Havranek, Kathryn E. Snell, Brett Davidheiser-Kroll, Gabriel J. Bowen, Bruce Vaughn

Published in Rapid Communications in Mass Spectrometry, 13 March 2020

Abstract

Rationale: Soil water stable isotopes are a powerful tool for tracking interactions between the hydrosphere, geosphere, atmosphere, and biosphere. The challenges associated with creating high temporal resolution soil water stable isotope data sets from a diversity of sites have limited the utility of stable isotope geochemistry in addressing a range of complex problems. A device that can enable further development of higher temporal resolution soil water isotope datasets that are created with minimal soil profile disruption from remote sites would greatly expand the utility of soil water stable isotope analyses.

Methods: We designed a method for sampling and storing soil water vapor for stable isotope analysis that leverages recent advances in soil water sampling strategies. Here, we test the reliability of the storage system by introducing water vapor of known oxygen and hydrogen isotopic composition into the storage system, storing the water vapor for a pre-determined amount of time, and then measuring the stable isotope composition of the vapor after the storage period.

Results: We demonstrate that water vapor stored in our flasks reliably maintains its isotope composition within overall system uncertainty (± 0.5‰ for $\delta^{18}O$ values and ± 2.4‰ for $\delta^{2}H$ values) for up to 30 days.

Conclusion: This method has the potential to enable the collection of high temporal resolution soil water isotope data sets from remote sites that are not accessed daily in a time- and cost-effective manner. All of the components used in the system can be easily controlled by open-source microcontrollers, which will be used in the future to automate sampling routines for remote field deployment. The system is designed to be an open-source tool for use by other researchers.

2.1 Introduction

Water stable isotopes are fractionated by a variety of biologic and physical processes (e.g. microbial respiration, condensation, evaporation, etc.). As a result of these fractionations, geochemists have long used the oxygen and hydrogen stable isotope composition of water ($\delta^{18}O$ and $\delta^{2}H$) to study interactions between the hydrosphere, geosphere, atmosphere, and biosphere[1–10]. Specifically, the study of soil water isotopes has deepened our understanding of water infiltration timescales, water bioavailability, evaporation, and improved our application of stable isotope paleoclimate proxies[2,6,9–12]. Most commonly, these previous studies have used destructive soil sampling techniques. Destructive methods limit the feasibility of long-term monitoring studies because the soil profile is inevitably disrupted after the first sampling effort. More recently, in situ techniques have been used to sample soil water, but remain technically challenging and expensive, in part because they require field measurement of the water isotope ratios.

2.1.1 Background

Bulk soil water isotope values have typically been analyzed from bulk soil samples that are manually collected from the soil profile (e.g. Orlowski[13], Sprenger[14]). Manual sampling requires that a researcher dig a soil pit and remove a soil sample that is taken back to the lab for subsequent soil water extraction and analysis. Sampling in this way is labor intensive, and makes repeated, high temporal resolution sampling difficult because it inevitably disrupts the drainage behavior and temperature gradients of the soil profile after the initial sampling effort. Studies that utilize manual sampling must also take care to control for isotopic fractionation during collection and transport prior to isotopic analysis[15].

After collection, soil water must then be extracted from a sample. The methods currently used for extraction have recently been the subject of much debate within the community[13–15]. Specifically, current research focuses on understanding both the portion of soil water extracted (i.e. bulk vs. mobile vs. immobile) as well as the reproducibility of the different extraction techniques. Broadly, soil water can be divided into the mobile and the immobile fraction. The mobile soil water fraction consists of water that is held at suctions less than field capacity, whereas the immobile water fraction is tightly bound to the colloidal fraction of the soil and is held at suctions greater than field capacity. The mobility of the water influences how available that water is for biologic and inorganic (e.g. evaporation) processes. Bulk soil water represents both the mobile and immobile portions of soil water and soil water isotopes. The most common method for soil water extraction, cryogenic vacuum

extraction, requires complete extraction of soil water from a sample to minimize uncertainty associated with fractionation and is thought to represent bulk soil water[13–15]. In contrast, lysimeter extraction is thought to represent just the mobile portions of soil water[13]. Finally, mechanical separation techniques like mechanical squeezing and centrifugation may differentially separate portions of the soil water based on gravimetric water content and soil composition. Each of these methods comes with its own advantages and challenges, and while all of these extraction methods ultimately give us a complex and nuanced view of soil water, they are all limited in their ability to provide high temporal resolution data sets from remote locations because they often require in-person sample collection.

Laser-based stable isotope analyzers, such as cavity ring down spectroscopy (CRDS) instruments, have made it possible to measure soil water isotope ratios in the field. This led to an effort in the last decade to develop new sampling systems that can make use of the new approach to isotopic analysis and enable higher temporal resolution sampling with less disruption of the soil profile[16–19]. Both polypropylene hydrophobic membrane tubing (e.g. 3M capillary membrane MF-PP, St. Paul, MN, USA), and hydrophobic microporous polyethylene tubing (e.g. Porex Technologies, Fairburn, Ga, USA) fractionate water isotopes reliably, such that using common standard correction techniques, both methods can be used to reliably sample pore water[16–19]. Rothfuss and others[17] demonstrated fidelity of the polypropylene membrane tubing using water of known isotopic composition in tightly controlled experimental soil columns. Further experimental work using a controlled soil column

demonstrated that over a 290-day period, daily use of the membrane tubing (> 30 min of vapor extraction time for each use) did not create a vapor gradient in the soil, and therefore, faithfully recorded the isotopic composition of the soil water over a long time period[20]. Early field applications of membrane inlet probes have demonstrated the utility of the method in arid environments[21–23], as well as in temperate environments[18,19,22,24]. While this represents a step forward, these early field experiments used CRDS instruments in the field, which limits the feasibility of developing high-temporal resolution data sets from regions that cannot be easily accessed frequently. This limits researchers' ability to interrogate questions that require specific soil types, or climatic regimes that are not proximal to a research center. These high temporal resolution datasets are critical in order to address many outstanding questions in ecohydrology, vadose zone hydrology and interpretation of soil-based paleoclimate proxies.

2.1.2 Study Aims

Our long-term goal is to be able to create high-temporal resolution datasets of soil water isotopes from potentially remote field settings. As a first step towards this broader goal, our primary objective for this study was to test, in a controlled laboratory setting, the basic viability of glass flasks as a water vapor storage reservoir, prior to any more formal field tests that will inherently introduce more uncontrolled variables. Here, our results demonstrate that the storage system is able

to faithfully store pure water vapor for isotopic analysis for up to 30 days in a laboratory setting.

To be able to meet our long term goal, we kept three specific design goals for the storage system in mind. First, we wanted to eliminate the need to bring a CRDS instrument into a field setting. Second, we wanted to create a sampling system that is easy to automate so as to limit the need for frequent intervention, and lastly, we wanted to use comparatively inexpensive and open source components so that these systems may be reproduced and widely applied. With the goal of making the system widely applicable, we also made the system amenable to common standard correction techniques used by stable isotope geochemists. We have named the system we created to achieve these goals the Soil Water Isotope Storage System (SWISS).

2.2 Experimental

2.2.1 SWISS system design

The storage system we designed for the lab tests uses many of the same components as the 'IsoWagon' presented by Oerter and Bowen[22]. The schematic of the system is shown in Figure 1. Briefly, dry N_2 (approx. 1 ppm H_2O, Airgas, Denver, CO, USA) is directed towards the vapor source, where it passes through vapor permeable tubing immersed in water. The mixture of dry N_2 and water vapor are carried into a 16-port manifold that selects 750 mL glass flasks. After the dry N_2 and water vapor mixture passes through the flask, it is directed to the CRDS instrument. Prior to entering the CRDS instrument, there is a diluting flow of dry N_2 that is used to control the water vapor mixing ratio.

Bev-A-Line IV tubing (Cole-Parmer, Vernon Hills, IL, USA) is used for all gas lines. Both the carrier stream and dilution stream of N_2 were regulated using thermal-type mass flow controllers (SmartTrak 100, Sierra Instruments, Monterey, CA, USA). The thermal-type mass flow controller was chosen because it is less sensitive to the variable temperatures typical of field conditions.

To sample the water vapor, we use polypropylene vapor permeable tubing that has been previously tested for this application[17,20]. This section of tubing will be referred to as a probe hereafter. The probes were cut to 10 cm lengths, and were constructed as described by Oerter and others[19] (Figure 1). In this study, we used two probes (hereafter, probe 1 and probe 2) for the analyses.

Water vapor is stored in custom 750 mL glass flasks with both inlet and outlet tubes (Figure 1). The large flask volume allows for the long (10-minute average) sampling time required for a precise CRDS instrument measurement. Flasks are coupled to a 16-port manifold (1/8" ST trapping flow path selector Valco valve, Valco Instruments Co. Inc., Houston, TX, USA) using Swagelok union fittings (Swagelok, Solon, OH, USA) with PTFE ferrules on all glass connections (Ohio Valley Specialty Company, Marietta, OH, USA) and metal 1/8" OD tubing (McMaster-Carr, Elmhurst, IL, USA). The multiport Valco valve was chosen so that flasks could be individually isolated during sample collection, and were effectively sealed when not selected[25].

One port on the Valco valve was used to create a 'jumper loop' as a way to introduce references through the SWISS in a way as similar as possible to the sample introduction, but would allow for faster measurement than passing references

through flasks. We used reference water measurements made through the 'jumper loop' to perform routine CRDS standardization and monitoring. The jumper loop is a 10 cm length of 1/8" metal tubing, with no glass flask (Figure 2-1). The volume of this tubing is much smaller than a flask, and so it can be dried, and memory effects can be mitigated much faster than would occur through a flask. For future field-based studies, we envision that researchers would take a subsample of the soil from which soil water vapor samples are coming, dry that soil, and re-wet it with water of known composition[24]. This would allow researchers to correct for site specific mineral-water interactions[22]. The jumper loop will also allow for 'pre-flushing' of the gas lines with dry N_2 in a field setting prior to sampling.

Water vapor was analyzed using a Picarro L2130-*i* Isotope and Gas Concentration Analyzer (Picarro, Santa Clara, CA, USA). Finally, we used an open split so as to not over-pressurize the CRDS instrument (Figure 2-1).

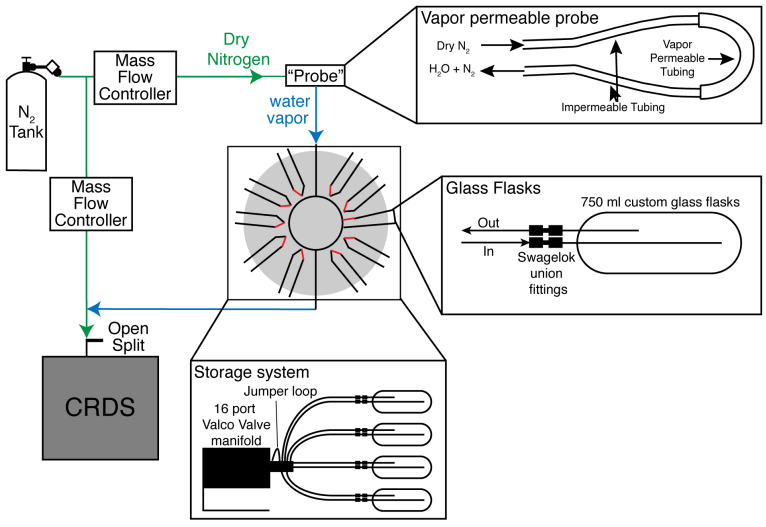

Figure 2-1: Storage system schematic. The storage system uses Bev-A-Line tubing to carry dry N_2 gas into the vapor permeable probes. Water vapor is then carried into a Valco valve, which is coupled with 750 ml glass flasks using 1/8" stainless steel tubing. A flask can be effectively closed off simply by changing the port on the Valco valve. The valve is connected to the CRDS instrument using Bev-A-Line tubing.

2.2.2 Experimental procedure for storage tests

Broadly, the goal of the storage tests was to assess the ability of the SWISS to faithfully store water vapor for extended periods of time under controlled laboratory conditions. To demonstrate the efficacy of the flask approach, we completed five storage experiments. During the first experiment, we simply filled flasks with dry N_2 to test that the flasks were sufficiently resistant to atmospheric intrusion. In this experiment, we flushed the flasks with dry N_2 until water vapor mixing ratio was approximately 300 ppm H_2O. Flasks were then closed off for five days and then measured at the end of the storage period. For the second and third experiments, we filled the flasks with water vapor of known composition and then closed the flasks off overnight. For the fourth storage experiment, the flasks were closed off for 24 days (2019-02-25 – 2019-03-21), and for the fifth storage experiment, flasks were closed off for 30 days (2019-05-20 – 2019-06-19) (Table 2-1). Below, we detail the experimental procedure used for all 5 storage experiments, and the procedure is summarized in Figure 2-2.

2.2.3 Water Vapor Collection and storage

Prior to starting any experiment, the flasks were dried by flushing dry N_2 until the water vapor mixing ratio of the flask was ≤ 300 ppm. To monitor instrument stability, and to be able to appropriately correct data, reference waters were analyzed both at the start of the analytical day and throughout the analytical day (Figure 2-2). Reference water vapor sampled using the vapor permeable probes was introduced to the CRDS via the 'jumper loop' (Figure 2-2A).

After drying the flasks and checking instrument stability, deionized water (hereafter, "DI") vapor in a dry N_2 carrier gas was flushed at 60 mL/min through the flask for

approximately 40 minutes (Figure 2-2B). The second mass flow controller provided a 'dilution' flow of dry N_2 at 20 mL/min so that the water vapor mixing ratio did not exceed the limits of the instrument. The flask was flushed until both the oxygen and hydrogen isotope values were stable within the uncertainty of the Picarro instrument measurement (approx. ± 0.2‰ for $\delta^{18}O$ values, ± 0.6‰ for $\delta^{2}H$ values) for 10 minutes (Figure 2-2C). This 'initial' isotope value in the flask was recorded as an average of the last 600 seconds of flushing the flask (Table 1). Following water vapor collection, the Valco valve port was rotated to seal off the flasks for the duration of each storage experiment (Figure 2-2D).

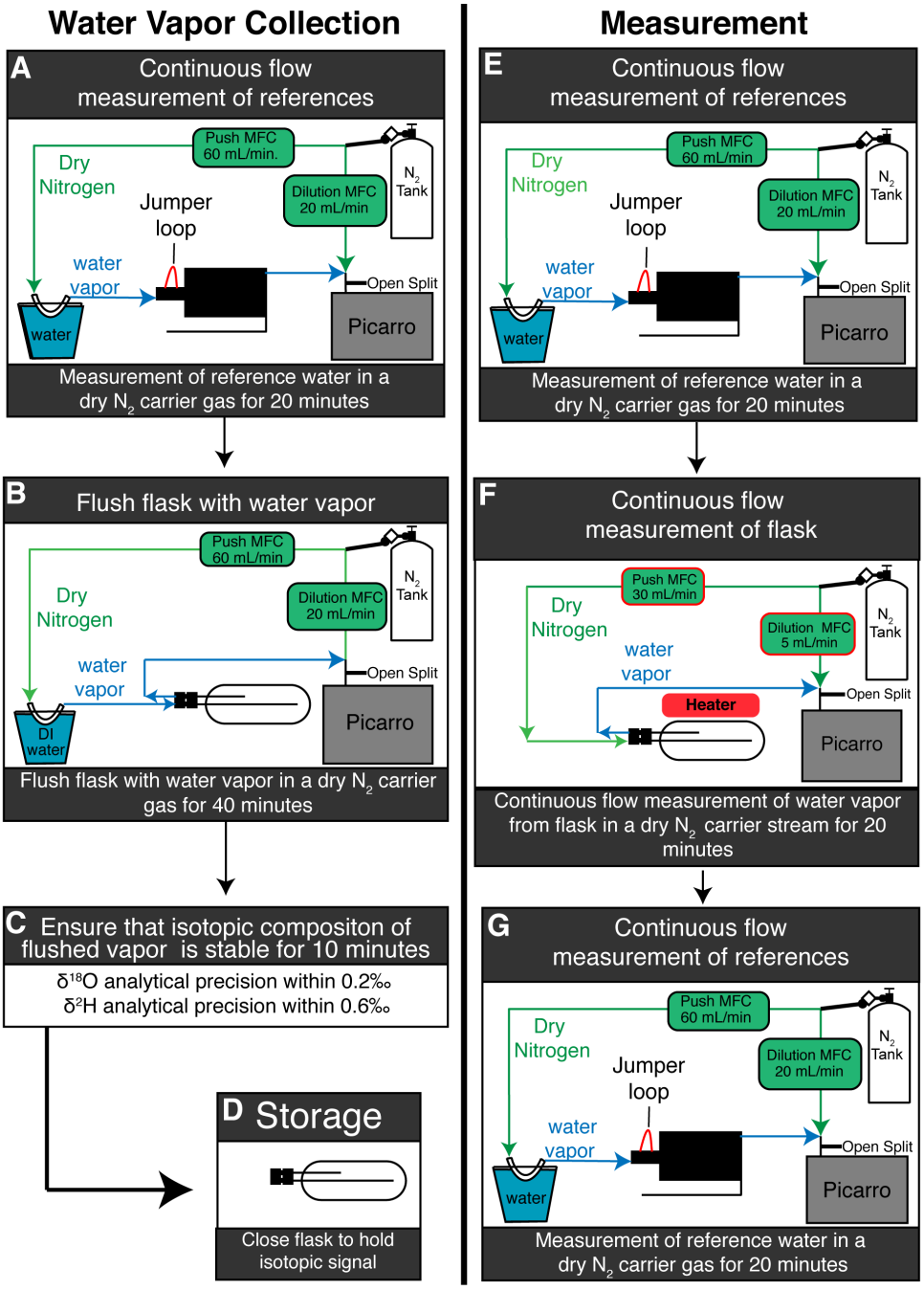

Figure 2-2: Experimental process. During the water vapor collection phase, A) two standard waters are sampled and measured. B) After standard measurement, the flasks are filled with DI water vapor. C) Flasks were flushed with water vapor until the water isotope values (δ^2H and $\delta^{18}O$) were stable within the precision of the Picarro instrument. D) After the water vapor collection phase, water vapor is stored in the flask for a pre-determined amount of time. E) Two standard waters are sampled and measured prior to measuring the flask water vapor. F) Measurement of flask water vapor. G) Two standard waters are sampled and measured to standard bracket at the end of the analytical day.

TABLE 2-1.

Flask	Date	$\delta^{18}O$ average value (‰)	$\delta^{2}H$ average value (‰)	Flask	Date	$\delta^{18}O$ average value (‰)	$\delta^{2}H$ average value (‰)	$\delta^{18}O$ (‰)	$\delta^{2}H$ (‰)
			Overnight Experiment #1					**Difference**	
1	2019-02-07	-16.2	-123.7	1	2019-02-08	-15.5	-120.6	0.8	3.1
2	2019-02-07	-16.2	-123.7	2	2019-02-08	-16.1	-122.1	0.1	1.7
3	2019-02-07	-15.9	-121.5	3	2019-02-08	-15.9	-121.2	0.0	0.3
			Overnight experiment #2					**Difference**	
1	2019-02-23	-16.6	-121.1	1	2019-02-24	-15.7	-117.1	1.0	4.0
2	2019-02-23	-16.3	-118.3	2	2019-02-24	-16.1	-117.6	0.2	0.7
3	2019-02-23	-16.2	-118.2	3	2019-02-24	-16.2	-116.9	0.1	1.3
			24 Day Experiment					**Difference**	
1	2019-02-25	-16.4	-120.9	1	2019-03-21	-15.6	-116.6	0.9	4.3
2	2019-02-25	-16.5	-121.4	2	2019-03-21	-16.2	-120.8	0.3	0.6
3	2019-02-25	-16.5	-121.8	3	2019-03-21	-16.2	-120.7	0.4	1.1
			30 Day Experiment					**Difference**	
1	2019-05-20	-16.8	-122.3	1	2019-06-19	-15.4	-114.9	1.4	7.4
2	2019-05-20	-16.5	-120.9	2	2019-06-19	-16.3	-119.3	0.2	1.6
3	2019-05-20	-16.6	-120.7	3	2019-06-19	-16.0	-118.1	0.6	2.6

TABLE 2-1: RESULTS FROM WATER VAPOR STORAGE EXPERIMENTS OVER SHORT TERM (OVERNIGHT) AND LONGER TERM (24 OR 30 DAY) PERIODS. THE SAME FLASKS WERE USED FOR ALL EXPERIMENTS.

2.2.4 Measurement

Like during the water vapor collection phase, reference waters were measured throughout the analytical day to monitor instrument stability (Figures 2-2E, 2-2G). Ten minutes prior to analysis we applied a blanket heater to the flask and heated it to 40 ± 3 °C (Figure 2-2F). This helped to stabilize the measured isotope value quickly, and is therefore a best practice, but is not necessary. The 'push' mass flow controller was set to 30 mL/min to push dry N_2 into the flask at the rate at which the Picarro analyzer takes in air. The second, 'dilution' mass flow controller was set to 5 mL/min, to provide minimal dilution to the water vapor while also ensuring that the water vapor mixing ratio did not exceed the limits of the instrument (Figure 2-2F). Vapor from the flask was measured for at least 10 minutes (@1 Hz, yielding ~600 measurements). During this phase, the measured water vapor mixing ratio continuously decreased because we used a dry N_2 carrier gas for the continuous flow measurement and there is no additional source of water vapor (Figure 2-SI 1A).

2.2.5 Calculation of isotope values

To remove the effects of the initial pulse of water vapor into the Picarro during the start of the measurement phase, which can bias the isotopic average, we used the rate of change of the water concentration slope to determine the point in time when the flask water concentration declined steadily (i.e. $\frac{d^2[H_2O]}{dt^2} = 0$) (Figure 2-SI 2-1B, 1C). Functionally, this included calculating the second derivative of a 25-second moving average of water concentration (Figure 2-SI 1C). We used the isotopic composition of

the first 300 seconds after the second derivative reached a value of 0±0.75 ppm/s^2 to calculate an average isotopic value.

2.2.6 Data Correction

For all water vapor introduced using the vapor permeable probes, water vapor isotope values were corrected to liquid water isotopic values according to Rothfuss and others[17], assuming a constant temperature of 22°C, which is our estimate of the temperature in the lab. Room temperature was not measured during the experiments. We then applied a mass discrimination correction calculated from three waters with 'known' values (Table SI1). To make the mass discrimination correction, we regressed a line between the three waters (isotopically light, intermediate, and heavy), and then used that line to correct all data which fell along the line. We did not correct for water vapor mixing ratio, because typically it was >25,000 ppm, and the uncertainty created by changes in water vapor mixing ratio are much smaller than the overall uncertainty of the system.

2.2.7 Evaluation of Uncertainty

The uncertainty associated with using the vapor permeably probes was previously evaluated by Oerter and Bowen[22] during the creation of the 'IsoWagon' on which we closely modeled our setup. In that study, the authors compared soil water vapor that was extracted with probes to soil water that was cryogenically vacuum extracted from the same bulk samples. Assuming the bulk soil water isotope value from vacuum extraction is the 'correct' value, then the authors calculated uncertainty

of the membrane tubing to be ± 2.4‰ and ± 0.5‰ for δ^2H and $\delta^{18}O$, respectively[22]. While this magnitude of uncertainty may not be appropriate for all questions in soil hydrology, it is sufficient for a variety of problems in soil hydrology, such as understanding both temporal and spatial heterogeneity of soil water isotopes in temperate envrionments[22,23].

The magnitude of one standard deviation for all of our reference waters except for one (heavy-1, which is detailed below), is smaller than the uncertainty calculated by Oerter and others. Because any further determination of the uncertainty associated with using the probes is beyond the scope of this study, we conservatively adopt the uncertainty of ± 2.4‰ and ± 0.5‰ for δ^2H and $\delta^{18}O$ values, respectivey[22].

2.2.8 Measured Waters

To be able to use standard correction techniques commonly used by isotope geochemists, we created six different waters for daily instrument monitoring. Three of the waters were isotopically light, one was intermediate, and two of the waters were isotopically heavy. The isotopically light and heavy waters were used to monitor instrument stability and for the mass discrimination correction. The isotopically intermediate water was used to 'fill' the flasks with water vapor for all storage experiments.

The light reference waters were created from freshly fallen snow collected from Boulder, CO, adjacent to Boulder Creek along Hwy 119. The fresh snow was divided into two portions and allowed to melt in the lab in unsealed containers. Both portions

were initially filtered using a 20 μm filter to remove any particulates. We initially measured the first portion (hereafter, "light-1"), and found that the variability of the isotopic composition of the water was higher than acceptable (greater than ± 0.5‰ for $\delta^{18}O$ values and ± 2.4‰ for $\delta^{2}H$ values). We therefore filtered both portions of the light water with an activated carbon and ion exchange resin; these two waters are referred to as "light-1f" and "light-2f". This is discussed in greater detail in section 3.2.1. The isotopically intermediate water was DI water from the University of Colorado Boulder campus. The isotopically heavy reference waters were created by simmering two separate beakers (hereafter, "heavy-1" and "heavy-2") of DI water until the water was approximately 20% of its original volume.

To be able to move our data into a known reference frame (i.e. VSMOW), we established known values of the three waters: light-2f, DI, and heavy-2, by measuring each water twice using a Picarro vaporizer module (V1102-i). These three waters were calibrated using in-house standards established by the IsoLab at the Institute of Arctic and Alpine Research at the University of Colorado Boulder (Boulder, CO, USA). The isotope value of the light-2f water is $\delta^{18}O$ = -21.25 ± 0.12‰, $\delta^{2}H$= -161.65 ± 0.89‰. The isotope value of DI water is $\delta^{18}O$ = -16.13‰ ± 0.12‰, $\delta^{2}H$ = -120.7 ± 0.89‰. The isotope value of the heavy-2 water is $\delta^{18}O$ = 1.85‰ ± 0.12‰, $\delta^{2}H$ = -66.75 ± 0.89‰.

We present the corrected average composition of all waters measured via the vapor permeable probes through the 'jumper loop' in Table 2-2 and Figure 2-3.

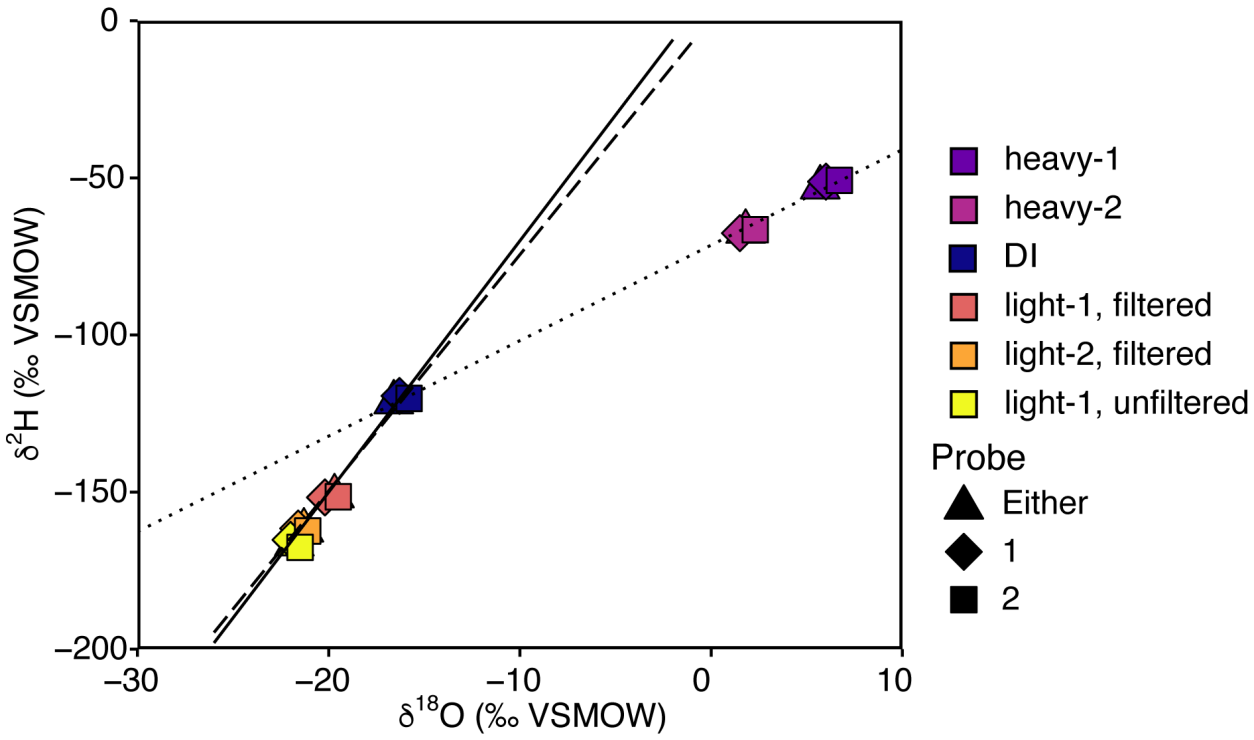

Figure 2-3: Plot showing the average isotopic value (δ^2H and $\delta^{18}O$) of all measured waters. The solid line is the global meteoric water line, the dashed line is the local meteoric water line of Boulder, CO, and the dotted line is a linear regression through both evaporated waters, projected through the intersection with the GMWL. Symbols are colored by water, symbol shape is used to denote which probe was used to collect the water vapor (i.e. measurements made with probe 1 vs. measurements made with probe 2, or all measurements combined). The DI water average only includes water vapor run through the 'jumper' loop, and not through flasks to eliminate dispersion associated with storage experiments. Uncertainty is smaller than the symbol size.

Table 2-2.

Water	n	Source	$\delta^{18}O$ average value (‰)	$\delta^{18}O$ standard deviation (‰)	$\delta^{2}H$ average value (‰)	$\delta^{2}H$ standard deviation (‰)
Light-1	17	melted snow	-21.7	0.7	-166.2	4.5
Light-1f	9	Melted snow, filtered using an activated carbon resin	-19.7	0.4	-151.3	1.1
Light-2f	24	Melted snow, filtered using an activated carbon resin	-21.3	0.3	-162.0	1.5
DI	8	CU-Boulder deionized water	-16.0	0.4	-119.9	1.1
Heavy-1	25	Simmered DI	6.0	0.4	-52.5	2.5
Heavy-2	17	Simmered DI	1.8	0.4	-67.1	0.8

Table 2-2. Average composition of all references waters where the water vapor was collected using the vapor permeable probes and introduced to the CRDS via the 'jumper loop'.

2.3 Results and Discussion

2.3.1 Storage Tests

2.3.1.1 Suitability of the 'jumper' loop for standardization process

To evaluate the suitability of the 'jumper loop' as a way to quickly introduce references through the SWISS, we compared DI water introduced both through the 'jumper loop' and flasks (Figure 2-SI 2). There is no bias in the composition of DI water measured through the 'jumper loop' as compared to DI water measured through a flask (Figure 2-SI 2). This allows for the possibility of measuring a range of water compositions in rapid succession, which enables researchers to assess common issues that require correction, such as drift in values throughout an analytical period. We therefore used the 'jumper loop' to quickly measure both a light (light-1f or light-2f) and heavy reference water (heavy-1 or heavy-2) before, during and after every storage experiment for common standardization techniques used in stable isotope geochemistry.

2.3.1.2 Dry N_2 storage experiment

After being closed off for 5 days, the flasks maintained a water vapor mixing ratio much lower than the surrounding atmosphere (i.e. maintained < 300 ppm H_2O, when room is typically ca. 8000 ppm H_2O) (Figure 2-SI 3). A positive result of this short experiment demonstrated it was reasonable to expect that the SWISS may be appropriate for longer storage of water vapor, and that our configuration was appropriate for further testing.

2.3.1.3 Overnight water vapor storage experiments

For all six of the replicates, the difference between the starting and final $\delta^{18}O$ value ranged between 0‰ and 1.0‰. The difference between the initial and final flask

δ^2H values ranged between 0.3‰ and 4.0‰. For all of the replicates, the isotope value of DI water vapor measured after the holding period was within estimated error of the initial water vapor isotope value (1 SD) (Figure 2-4, Table 2-1).

2.3.1.4 Long-term water vapor storage experiments

During both the 24-day test and the 30-day test, the isotope value of water vapor measured at the end of the holding period was within error of the measured value at the start of the holding period for two of the three flasks. During the 24-day experiment, the difference between the starting and final $\delta^{18}O$ value was 0.3‰ and 0.4‰ for flasks 2 and 3, respectively. The difference between the starting and final δ^2H value was 0.6‰ and 1.1‰ for flasks 2 and 3, respectively (Figure 2-5A, Table 1). Flask 1, had a difference in $\delta^{18}O$ values of 0.9‰, and a difference in δ^2H values of 4.3‰ (Figure 2-5A, Table 1). These values overlap within uncertainty of the vapor probes, but are at the edge of acceptability, and we therefore conclude that the flask did not faithfully hold its isotope value during the experiment.

During the 30-day experiment the difference between the starting and final $\delta^{18}O$ value was 0.2‰ and 0.6‰ for flasks 2 and 3, respectively (Figure 2-5B, Table 1). The difference between the starting and final δ^2H value was 1.6‰ and 2.5‰ for flasks 2 and 3, respectively. The consistent success of these flasks during both long-term storage experiments provides confidence that this system is able to provide adequate storage within the uncertainty of the vapor permeable probe system. The flask that

did not faithfully hold its isotope value for the 30-day test, flask 1, had a difference in $\delta^{18}O$ values of 1.4‰ and a difference in $\delta^{2}H$ values of 7.1‰ (Figure 2-5B, Table 1).

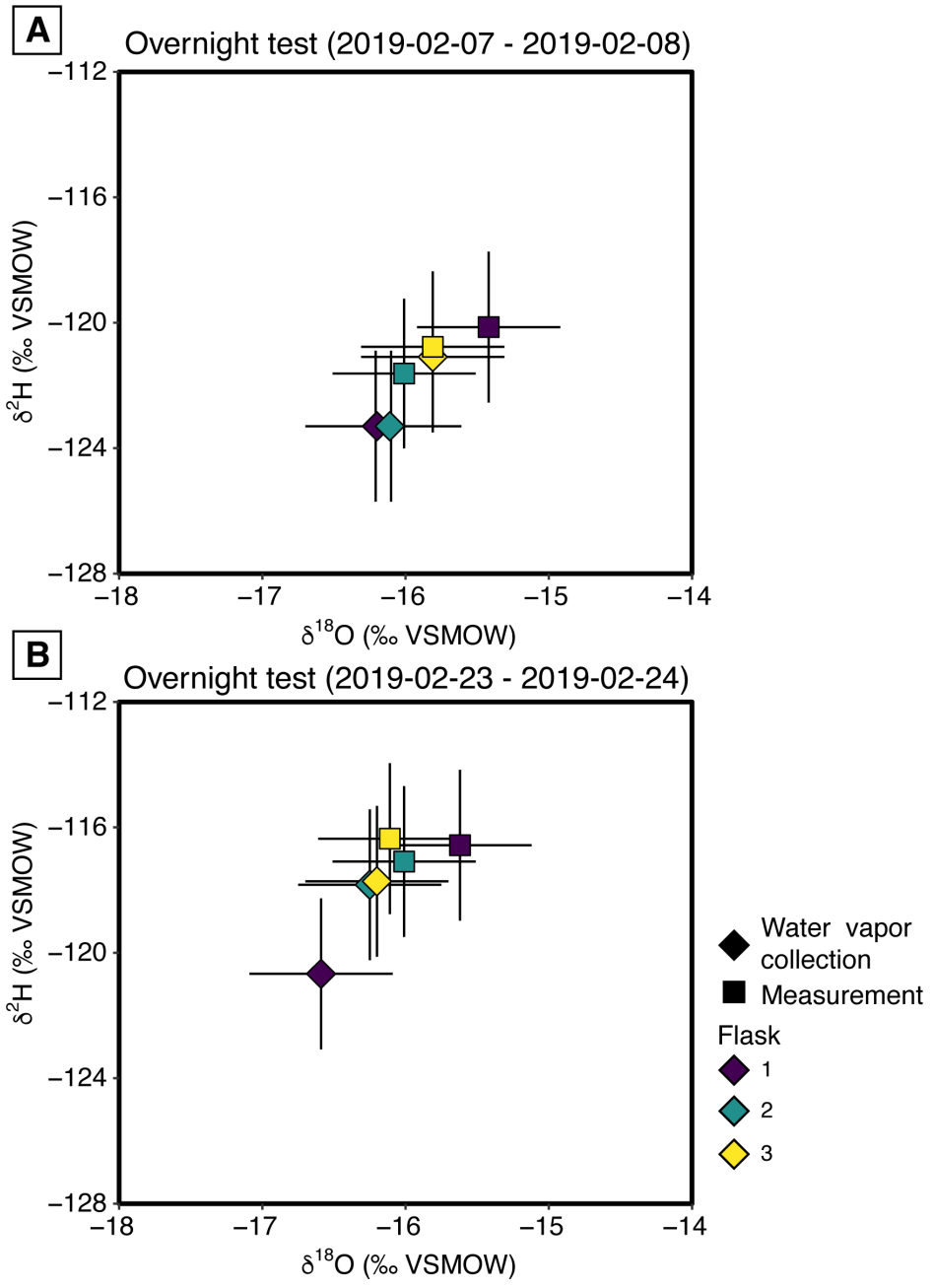

Figure 2-4: Results from both overnight storage experiments. Water isotope values ($\delta^{2}H$ and $\delta^{18}O$) measured during the water collection phase are shown in diamonds, and water isotope values ($\delta^{2}H$ and $\delta^{18}O$) measured after the storage period are shown in squares. The symbols are colored by flask. A) The results from the 2019-02-07 – 2019-02-08 experiment. B) The results from the 2019-02-23 – 2019-02-24 experiment.

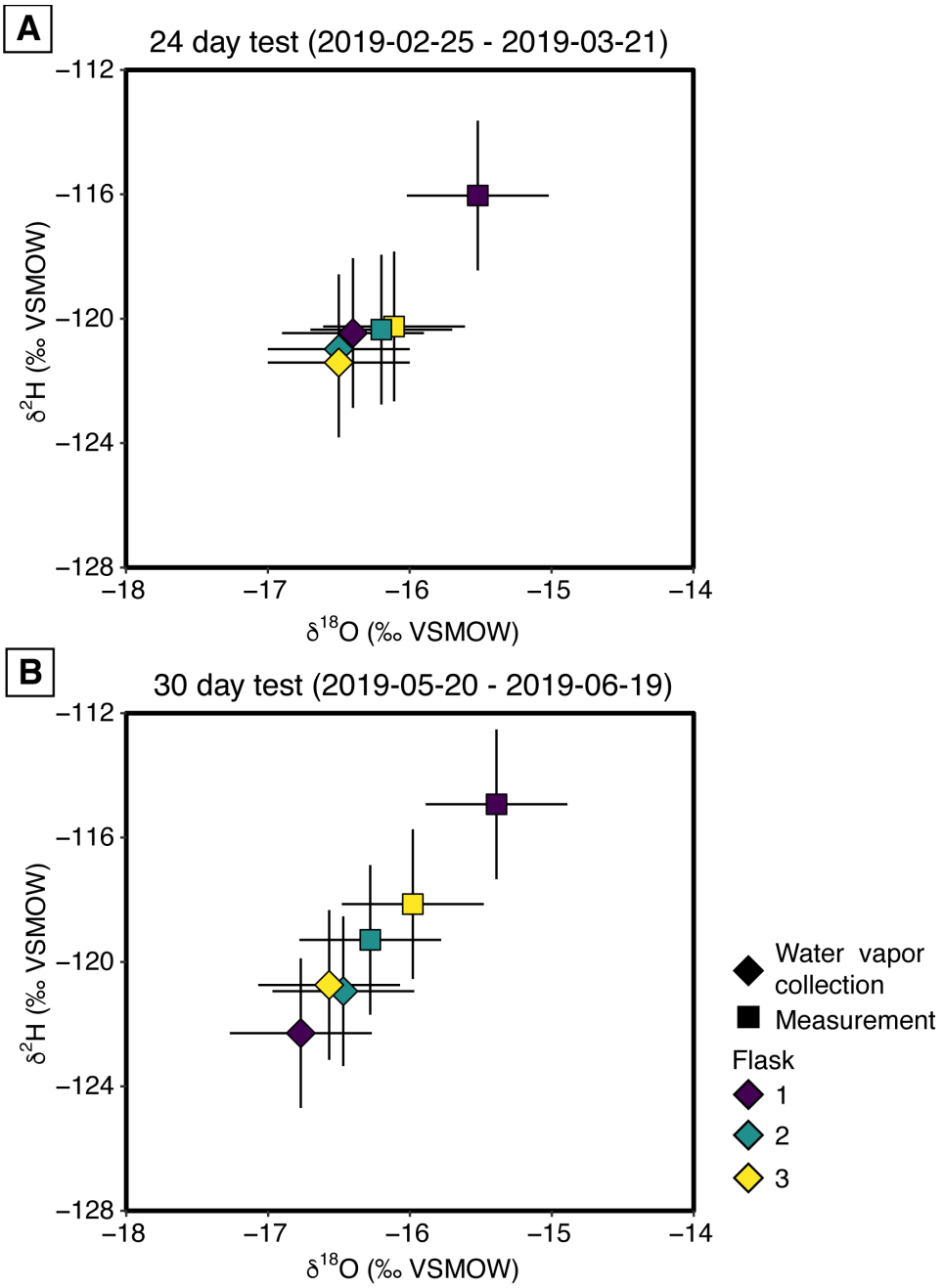

Figure 2-5: Results from the long storage tests. Water isotope values (δ^2H and $\delta^{18}O$) measured during the water collection phase are shown in diamonds, and water isotope values (δ^2H and $\delta^{18}O$) measured after the storage period are shown in squares. The symbols are colored by flask. A) The results from the 24-day (2019-02-25 – 2019-03-21) experiment. B) The results from the 30-day (2019-05-20 – 2019-06-19) experiment.

2.3.1.5 Implications from the storage experiments

During the long-term experiments, flask 1 did not reliably hold its isotopic composition. Following the 30-day experiment, we discovered that the PTFE ferrule on flask 1 had been overtightened and was therefore very slowly leaking. This explains the consistency of results (i.e. that flask 1 had the poorest results for all four water vapor storage tests). The cause of the leak in these experiments can be mitigated in the future with careful installation of the flasks. Based on the results of the water vapor storage tests, we suggest that quality control tests prior to field deployment of a SWISS should include at least an intermediate length storage test (e.g. 7 days).

Generally, the two overnight storage experiments and the two longer-term storage experiments demonstrate that we can reliably store water vapor using the SWISS, and that this tool may be useful for field deployment. For field deployment, however, the SWISS should be closely monitored for standard 'wear and tear'. For example, it is known that Valco valves can wear out and become less air tight over time due to grime and grit intrusion and erosion of the rotor. These problems may be mitigated by occasional re-testing of each SWISS system under laboratory conditions.

2.3.2 Implications from the reference water dataset

Broadly, there are two additional observations from our reference water dataset that further support our conclusion that this system will be useful for making environmental observations. First, we are able to detect variability in two aliquots of similar water. Namely, we are able to detect variability in two portions of a snow-pack sample (i.e. light-1f vs. light-2f). The second

observation is that after using standards to move our data into a 'known' framework, snow melt water and DI water fall near the local meteoric water line for Boulder, CO as expected[26]. Likewise, the two heavy-water references (heavy-1 and heavy-2), which were created by evaporating DI water, form an evaporative enrichment line that connects through the DI reference. Together, these observations are encouraging because they demonstrate that the sampling system we have built and tested here is able to measure and reproduce water references in a predictable way. Below we detail two complexities associated with this dataset.

2.3.2.1 Error associated with unfiltered snow-melt (light-1)

The reference water light-1 was created by melting snow and was filtered with a 20 μm filter. The composition of this water the composition of light-1, measured using the vapor permeable probes was $\delta^{18}O$ = -21.7‰ ± 0.7‰, $\delta^{2}H$ = -166.6‰ ± 4.6‰ (n=17) (Figure 2-2, Figure 2-6A, Table 2-1). There was significant scatter about the mean in both $\delta^{2}H$ and $\delta^{18}O$ values and this variability occurred both across and within analytical days (Figure 2-SI 4A). We considered such a large standard deviation of measurements unacceptable, so we filtered the aliquot of water using an activated carbon and ion exchange resin. The filtered light-1 aliquot is referred to as 'light-1f', and the average isotopic composition is $\delta^{18}O$ = -19.7‰ ± 0.4‰, $\delta^{2}H$ = -151.3‰ ± 1.1‰ (n = 16) (Figure 2-2, Figure 2-6A, Figure 2-6B). It is unclear why filtering the snow melt water caused a reduction in scatter about the mean. It is largely beyond the scope of this study to determine the exact cause. Given that this large scatter was not present in either the heavy reference water or in DI water run on the same analytical days (Figure 2-6C, Figure 2-SI4), we can rule out variable analytical conditions as the cause of scatter. Previous work has demonstrated that alcohols and water impurities present in stem and leaf water creates spectroscopic interferences in the

Picarro (e.g. Brand[27]). However, this explanation is unlikely in this scenario given the low organics to water ratio. Furthermore, a spectral interference would be likely to affect only one isotope ratio (i.e. either oxygen or hydrogen), while these data are normally distribution about the mean in both oxygen and hydrogen isotopes (Figure 2-6A). The second potential explanation could be a change in transfer efficiency stemming from physical interactions between particles and the membrane tubing. This explanation is unlikely given the successful use of the membrane tubing to measure water isotopes across a variety of soil textures[17,20,28]. The third potential explanation could be unconstrained minor changes in the measurement conditions, like temperature swings, membrane efficiency, or volatile degassing from the membrane material. Further exploration of this phenomena will be important for understanding the constraints of field deploying this system.

2.3.2.2 Inter-probe variability

During the experiments, we observed that there was consistent offset in $\delta^{18}O$ values between the different vapor permeable probes used to introduce water vapor into the system (Figure 2-6B, Figure 2-6D). There was no apparent offset between the probes in $\delta^{2}H$ values. There was a similar amount of offset between the probes for both the filtered light and heavy reference waters (Figure 2-6B, Figure 2-6D). Other work has suggested that small lengths of the membrane probe may cause incomplete liquid-vapor equilibration[28]. The variability between the probes is within the uncertainty of the overall system, and so does not affect our conclusions here. However, it is worth noting that variability may be reduced in field deployments of the SWISS and other applications of the membrane probes by properly standardizing membrane tube length and Bev-A-Line tube length. Therefore, we

recommend that each probe is used to measure reference material before it is deployed in a field setting so that probe-specific offsets can be identified and minimized.

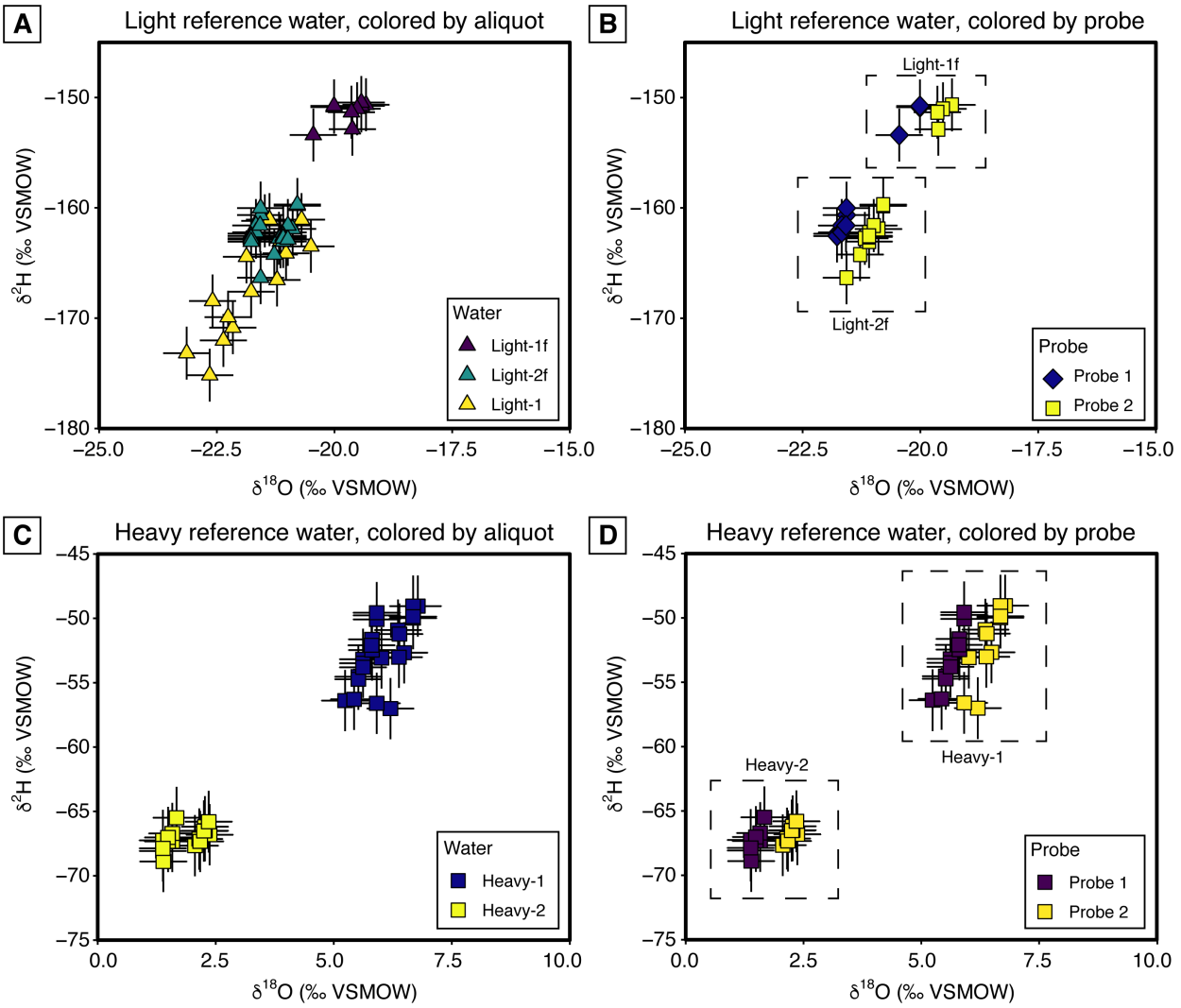

Figure 2-6: A) The isotopic value (δ^2H and $\delta^{18}O$) of all measurements of the light reference waters made using the vapor permeable probes, colored by aliquot. The two aliquots (i.e. light-1 and light-2) are two portions of a melted snow column. Filtering the light reference water with an activated carbon and ion exchange resin reduced the dispersion of isotope data (i.e. light-1 vs. light-1f). B) The light-1f and light-2f reference waters are colored by probe. Note, this plot excludes the unfiltered light-1 data. C) The isotopic value (δ^2H and $\delta^{18}O$) of all measurements of the heavy reference water, colored by aliquot. The two heavy water aliquots were created by evaporating two separate beakers of DI water. D) The heavy reference waters colored by probe.

2.4 Conclusions:

We have described the development and testing of a flask system that is designed to autonomously sample and store water vapor for up to at least one month. This system is designed to leverage the use of vapor permeable probes that can be used to make repeat measurements from a soil column with minimal soil disruption, and enables the creation of high-temporal resolution datasets from remote locations. In this contribution, we demonstrate that the SWISS can accurately preserve the stable oxygen and hydrogen isotope composition of water vapor for up to one month in a laboratory setting. Reliability of the storage system was demonstrated with 5 storage experiments. In the first experiment, flasks were filled with dry N_2 and they maintained a water vapor mixing ratio much lower than ambient atmosphere. In the second and third experiments, water vapor of known stable isotope composition was stored overnight. In the fourth and fifth experiments water vapor of known isotopic composition was stored for 24 days and 30 days, respectively. These experiments identified that careful quality control is required to detect leaks before deployment of the SWISS into a field setting. In addition, the effect of membrane length and other impurities that may alter the measured isotopic composition should be considered before field deployment of the SWISS. These are effects that can be controlled with intentional design of the final device, and should be considered whenever researchers deploy membrane probes, regardless of whether they measure the water vapor in the field or store it for later analysis via a system like the SWISS. Finally, the components used here can be easily automated using common open source and inexpensive

microcontroller technologies, and controlled via open-source custom software. This contribution expands the feasibility of isotopic datasets from remote field sites.

Acknowledgements

We thank Will Skorski for insightful conversations about other potential storage reservoirs. We also thank two anonymous reviewers for helpful comments that greatly improved the quality of this manuscript. This work was funded by a Geologic Society of America Graduate Student Research grant, as well as, the Dudley and Marion Boylard Scholarship from the Rocky Mountain Association of Geologists to R. Havranek, and by funds from the University of Colorado to K. Snell.

Works Cited

1. Dansgaard W. Stable isotopes in precipitation. *Tellus*. 1964:436-468. doi:10.3402/tellusa.v16i4.8993
2. Zimmermann U, Munnich KO, Roether W. Tracers Determine Movement of Soil Moisture and Evapotranspiration. *Science (80-).* 1966;152(3720):346-347. doi:10.1126/science.152.3720.346
3. Peterson BJ, Fry B. Stable Isotopes in Ecosystem Studies. *Annu Rev Ecol Syst*. 1987;18:293-320. http://www.jstor.org/stable/2097134 REFERENC.
4. Gat JR. Oxygen and Hydrogen Isotopes in the Hydrologic Cycle. *Annu Rev Earth Planet Sci*. 1996:1-38. doi:10.1146/annurev.earth.24.1.225
5. Boutton TW, Archer SR, Midwood AJ. Stable isotopes in ecosystem science: Structure, function and dynamics of a subtropical savanna. *Rapid Commun Mass Spectrom*. 1999;13(13):1263-1277.
6. Brooks JR, Barnard HR, Coulombe R, McDonnell JJ. Ecohydrologic separation of water between trees and streams in a Mediterranean climate. *Nat Geosci*. 2010;3(2):100-104. doi:10.1038/ngeo722
7. Rothfuss Y, Braud I, Le Moine N, et al. Factors controlling the isotopic partitioning between soil evaporation and plant transpiration: Assessment using a multi-objective calibration of SiSPAT-Isotope under controlled conditions. *J Hydrol*. 2012;442-443:75-88. doi:10.1016/j.jhydrol.2012.03.041
8. Bowen GJ, Good SP. Incorporating water isoscapes in hydrological and water resource investigations. *Wiley Interdiscip Rev Water*. 2015;2(2):107-119. doi:10.1002/wat2.1069

9. Evaristo J, Jasechko S, McDonnell JJ. Global separation of plant transpiration from groundwater and streamflow. *Nature*. 2015;525(7567):91-94. doi:10.1038/nature14983

10. Sprenger M, Leistert H, Gimbei G, Weiler M. Illuminating hydrological processes at the soil-vegetation-atmosphere interface with water stable isotopes. *Rev Geophys*. 2016;54:674-704. doi:10.1002/ 2015RG000515

11. Quade M, Brüggemann N, Graf A, Vanderborght J, Vereecken H, Rothfuss Y. Investigation of Kinetic Isotopic Fractionation of Water during Bare Soil Evaporation. *Water Resour Res*. 2018;54(9):6909-6928. doi:10.1029/2018WR023159

12. Huth TE, Cerling TE, Marchetti DW, Bowling DR, Ellwein AL, Passey BH. Seasonal bias in soil carbonate formation and its implications for interpreting high-resolution paleoarchives: evidence from southern Utah. *J Geophys Res Biogeosciences*. 2019. doi:10.1029/2018JG004496

13. Orlowski N, Pratt DL, McDonnell JJ. Intercomparison of soil pore water extraction methods for stable isotope analysis. *Hydrol Process*. 2016;30(19):3434-3449. doi:10.1002/hyp.10870

14. Sprenger M, Herbstritt B, Weiler M. Established methods and new opportunities for pore water stable isotope analysis. *Hydrol Process*. 2015;29(25):5174-5192. doi:10.1002/hyp.10643

15. Orlowski N, Breuer L, Mcdonnell JJ. Critical issues with cryogenic extraction of soil water for stable isotope analysis. *Ecohydrology*. 2016;9(1):3-10.

doi:10.1002/eco.1722

16. Herbstritt B, Gralher B, Weiler MF. Continuous in situ measurements of stable isotopes in liquid water. *Water Resour Res*. 2012;48(3):1-6. doi:10.1029/2011WR011369

17. Rothfuss Y, Vereecken H, Brüggemann N. Monitoring water stable isotopic composition in soils using gas-permeable tubing and infrared laser absorption spectroscopy. *Water Resour Res*. 2013. doi:10.1002/wrcr.20311

18. Volkmann THM, Weiler M. Continual in situ monitoring of pore water stable isotopes in the subsurface. *Hydrol Earth Syst Sci*. 2014;18(5):1819-1833. doi:10.5194/hess-18-1819-2014

19. Oerter EJ, Perelet A, Pardyjak E, Bowen GJ. Membrane inlet laser spectroscopy to measure H and O stable isotope compositions of soil and sediment pore water with high sample throughput. *Rapid Commun Mass Spectrom*. 2016;31(1):75-84. doi:10.1002/rcm.7768

20. Rothfuss Y, Merz S, Vanderborght J, et al. Long-term and high-frequency non-destructive monitoring of water stable isotope profiles in an evaporating soil column. *Hydrol Earth Syst Sci*. 2015;19(10):4067-4080. doi:10.5194/hess-19-4067-2015

21. Gaj M, Beyer M, Koeniger P, Wanke H, Hamutoko J, Himmelsbach T. In-situ unsaturated zone stable water isotope (2H and 18O) measurements in semi-arid environments using tunable off-axis integrated cavity output spectroscopy. *Hydrol Earth Syst Sci Discuss*. 2015;12(6):6115-6149.

doi:10.5194/hessd-12-6115-2015

22. Oerter EJ, Bowen GJ. In situ monitoring of H and O stable isotopes in soil water reveals ecohydrologic dynamics in managed soil systems. *Ecohydrology*. 2017;10(4):1-13. doi:10.1002/eco.1841

23. Oerter EJ, Bowen GJ. Spatio-temporal heterogeneity in soil water stable isotopic composition and its ecohydrologic implications in semiarid ecosystems. *Hydrol Process*. 2019;(March):1-15. doi:10.1002/hyp.13434

24. Quade M, Klosterhalfen A, Graf A, et al. In-situ monitoring of soil water isotopic composition for partitioning of evapotranspiration during one growing season of sugar beet (Beta vulgaris). *Agric For Meteorol*. 2019;266-267(December 2018):53-64. doi:10.1016/j.agrformet.2018.12.002

25. Theis DE, Saurer M, Blum H, Frossard E, Siegwolf RTW. A portable automated system for trace gas sampling in the field and stable isotope analysis in the laboratory. *Rapid Commun Mass Spectrom*. 2004;18(18):2106-2112. doi:10.1002/rcm.1596

26. IAEA/WMO. *Global Network of Isotopes in Precipitation. The GNIP Database. Accessible at: Http://Www.Iaea.Org/Water*.; 2019.

27. Brand WA, Geilmann H, Crosson ER, Rella CW. Cavity ring-down spectroscopy versus high-temperature conversion isotope ratio mass spectrometry; a case study on d2H and d18O of pure water samples and alcohol/water mixtures. *Rapid Commun Mass Spectrom*. 2009;23(12):119-130. doi:10.1002/rcm

28. Oerter EJ, Singleton M, Thaw M, Davisson ML. Water vapor exposure chamber for constant humidity and hydrogen and oxygen stable isotope composition. *Rapid Commun Mass Spectrom*. 2019;33(October 2018):89-96. doi:10.1002/rcm.8311

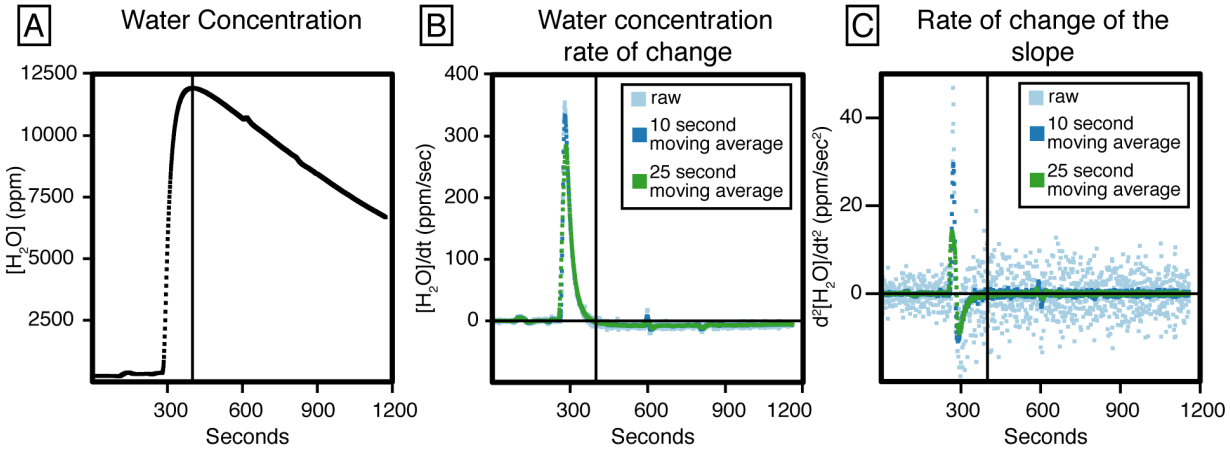

Figure 2-SI1: A) Water vapor mixing ratio vs. time, in seconds, during the 'measurement' phase of a storage experiment. B) The first derivative of water vapor mixing ratio with respect to time. C) The second derivative of water concentration with respect to time. Data were averaged for the 'final' isotope value after the slope of the rate of change of water concentration was 0 ± 0.75 ppm/s^2, shown in all three plots with a vertical solid black line.

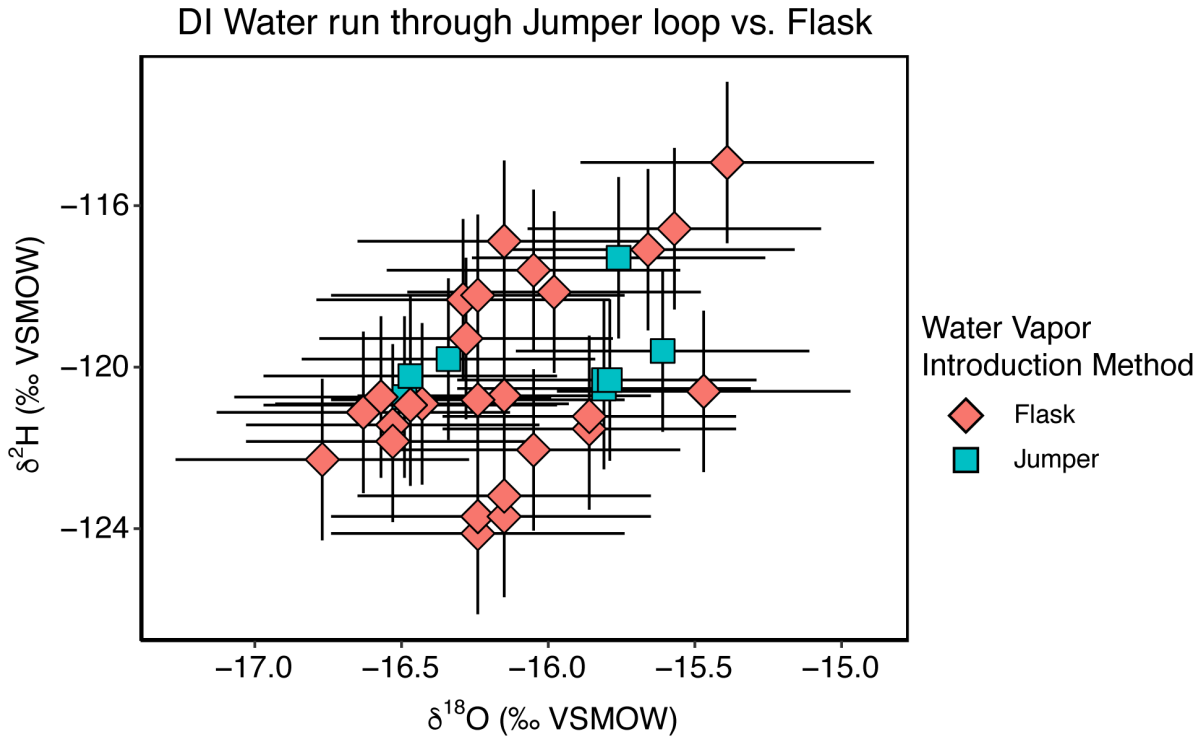

Figure 2-SI2: DI water measured through the 'jumper loop' was within uncertainty of DI water vapor measured via a flask flow path. Blue squares represent measurements made via the 'jumper loop' and red diamonds represent measurements of DI water vapor made via a flask.

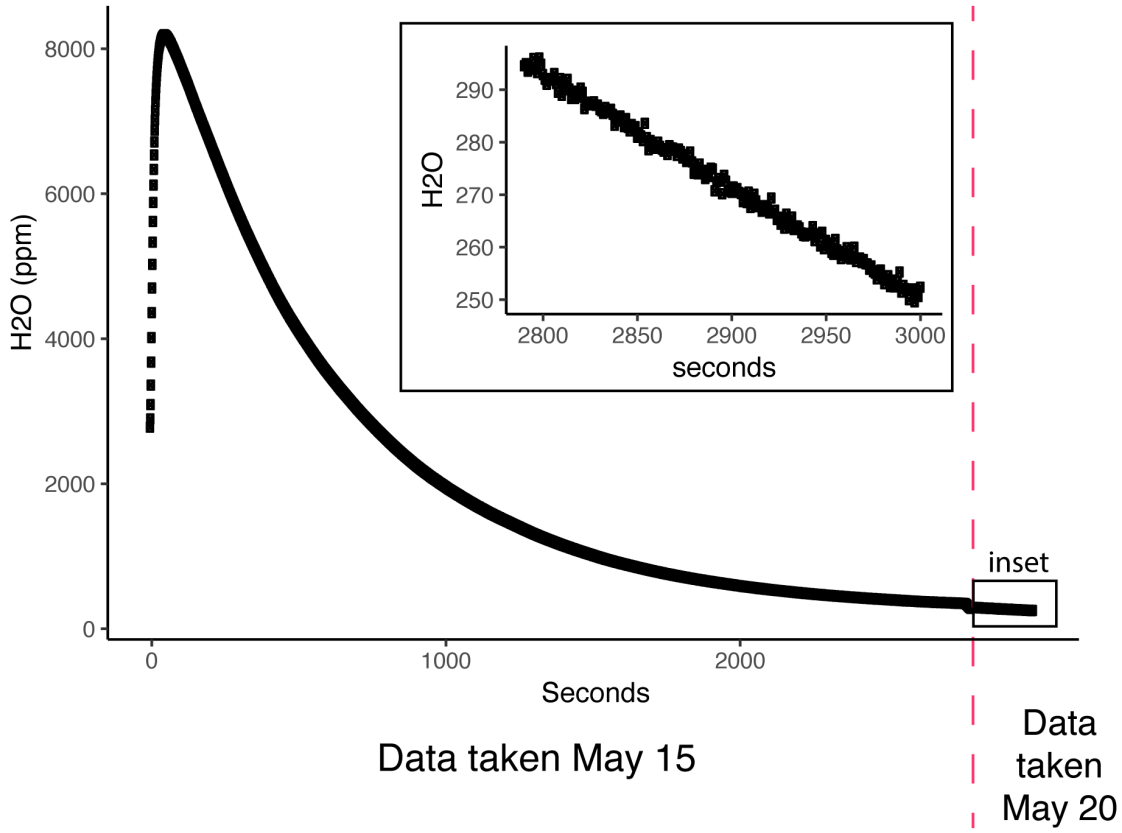

Figure 2-SI3: An example of a dry air test. Water vapor mixing ratio versus time in seconds is shown as the flask is dried from atmosphere conditions. The vertical dashed red line represents a gap in time of 5 days. This example shows the flask maintaining a low water concentration for five days. The inset shows the water vapor mixing ratio measured in the flask after 5 days.

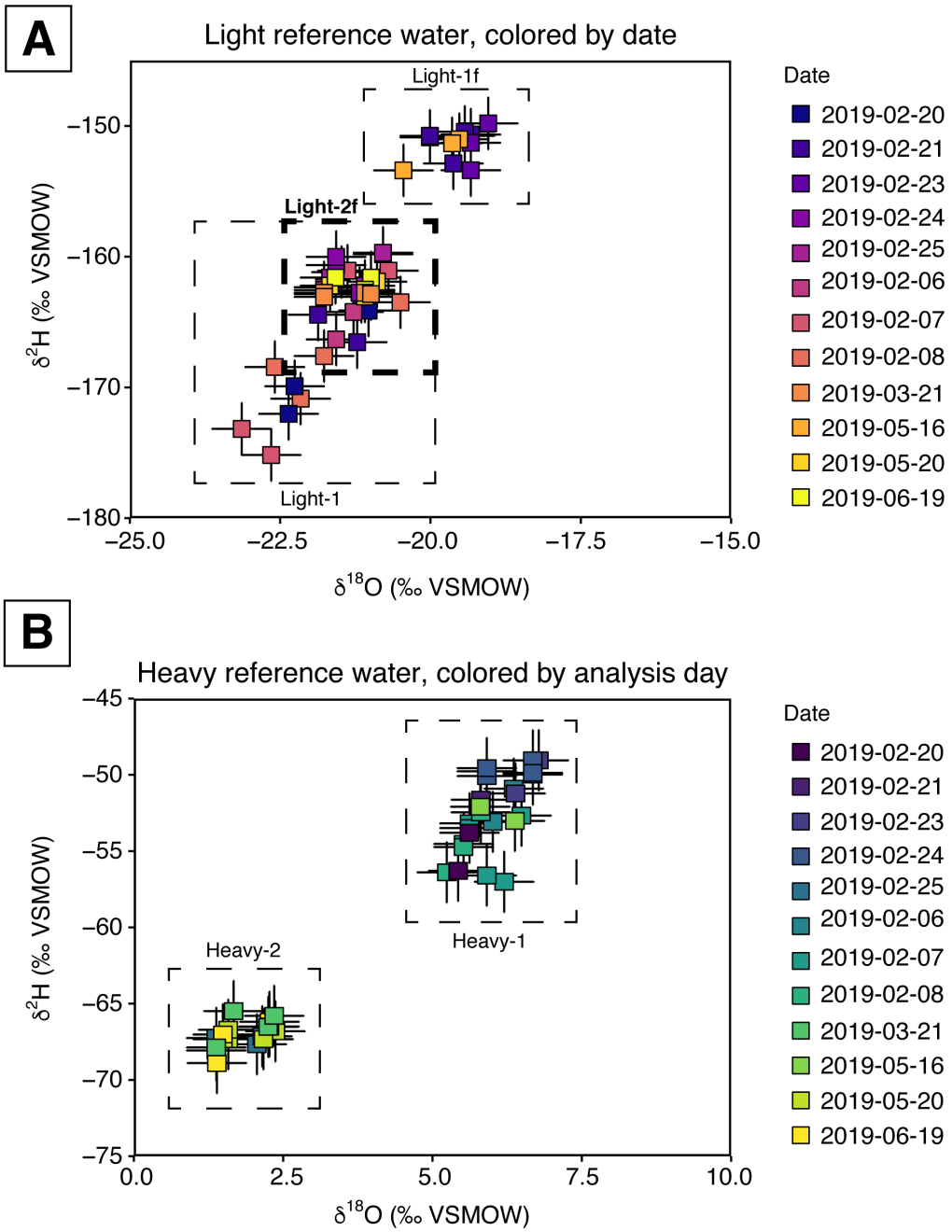

Figure 2-SI4: The isotope value (δ^2H and $\delta^{18}O$) of all measurements of the A) Light and B) Heavy reference waters, colored by day. There was no significant drift, nor was any single day contributing unduly to uncertainty

Table 2-SI 1: All data collected during the experiments

Probe #	Water name	Port on Valco valve	Date	Start time	End. time	Ave. Time (min.)	d18O (‰)	d18O_sd (‰)	dD (‰)	dD_sd (‰)	H2O (ppm)	H2O _sd (ppm)	Picarro	Donotuse	where	d18O_liq	d2H_liq	d18O_iso_disc_corr	d2H_iso_disc_ corr	d18O_guac_disc_ corr	d2H_guac_disc_ corr	d18O_disc_corr	dD_disc_corr	d-excess (‰)
1	Heavy-1	1	2/6/19	3:20	3:30	10	-5.5	0.2	-138.1	0.6	NA	NA	IsoLab	TRUE	Jumper	4.2	-65.9	6.6	-53.1	2.5	-65.3	6.6	-53.1	-105.7
2	Heavy-1	1	2/6/19	3:34	3:43	9	-5.1	0.2	-136.4	0.6	NA	NA	IsoLab	TRUE	Jumper	4.6	-64.1	7	-51.3	2.9	-63.5	7	-51.3	-107.1
1	Heavy-1	1	2/6/19	3:45	4:20	10	-5	0.2	-134.9	0.5	NA	NA	IsoLab	TRUE	Jumper	4.7	-62.5	7.1	-49.8	3	-61.9	7.1	-49.8	-106.3
2	Heavy-1	1	2/6/19	4:30	4:45	10	-5.73	0.2	-136	0.5	NA	NA	IsoLab	FALSE	Jumper	4	-63.6	6.4	-50.9	2.2	-63.1	6.4	-50.9	-101.8
1	Heavy-1	1	2/6/19	4:45	5:05	10	-5	0.2	-135.1	0.5	NA	NA	IsoLab	TRUE	Jumper	4.7	-62.7	7.1	-50	3	-62.2	7.1	-50	-106.5
2	Heavy-1	1	2/6/19	5:08	5:18	10	-6.1	0.2	-138.1	0.7	NA	NA	IsoLab	FALSE	Jumper	3.6	-65.9	6	-53.1	1.9	-65.3	6	-53.1	-101.2
1	Heavy-1	1	2/6/19	5:24	5:36	10	-5	0.2	-135.5	0.5	NA	NA	IsoLab	TRUE	Jumper	4.7	-63.1	7.1	-50.4	3	-62.6	7.1	-50.4	-107
2	tap	1	2/7/19	7:52	8:04	10	-28.2	0.2	-203.7	0.6	27300	95	IsoLab	TRUE	Jumper Jumper	-18.5	-136.2	-15.3	-120.9	-19.8	-133.3	-15.3	-120.9	1.3
1	tap	1	###	###	###	10	-28.9	0.2	-203.4	0.6	###	143	IsoLab	###	Jumper Jumper	-19.2	-135.9	-16	-120.6	-20.5	-133	-16	-120.6	7
2	Light-1	1	2/7/19	8:24	8:40	12	-35.8	0.2	-255.7	0.5	27000	71	IsoLab	FALSE	Jumper	-26.1	-192	-22.6	-174.7	-27.3	-187.2	-22.6	-174.7	6.1
1	Light-1	1	2/7/19	8:44	9:02	12	-36.3	0.2	-253.8	0.8	26580	128	IsoLab	FALSE	Jumper	-26.6	-190	-23.1	-172.7	-27.8	-185.2	-23.1	-172.7	11.9
2	Heavy-1	1	2/7/19	9:08	9:31	15	-6.7	0.3	-149.9	1.6	15700	159	IsoLab	TRUE	Jumper	3	-78.5	5.4	-65.3	1.3	-77.5	5.4	-65.3	-108.7
2	Heavy-1	1	2/7/19	9:33	9:47	9	-5.9	0.2	-141.9	0.5	28560	91	IsoLab	FALSE	Jumper	3.8	-70	6.2	-57	2.1	-69.2	6.2	-57	-106.6
1	Heavy-1	1	2/7/19	9:50	10:05	10	-6.6	0.2	-139.5	0.5	28990	38	IsoLab	FALSE	Jumper	3.1	-67.4	5.5	-54.5	1.4	-66.7	5.5	-54.5	-98.7
2	DI	2	2/7/19	10:10	10:54	10	-29.2	0.2	-206.8	0.5	28700	70	IsoLab	FALSE	Flask	-19.5	-139.6	-16.2	-124.1	-20.8	-136.5	-16.2	-124.1	5.8
2	DI	14	2/7/19	10:55	11:40	10	-29.1	0.2	-205.5	0.8	28700	260	IsoLab	TRUE	Flask	-19.4	-138.2	-16.2	-122.8	-20.7	-135.2	-16.2	-122.8	6.4

1		Light-1	1		2/7/19	11:43	11:57	10	-34.6	0.2	-242.4	0.4	30550	87	IsoLab	FALSE	Jumper	-24.9	-177.7	-21.4	-160.9	-26.1	-173.4	-21.4	-160.9	10.6
2		Light-1	1		2/7/19	12:00	12:13	10	-33.8	0.2	-242.3	0.5	30460	200	IsoLab	FALSE	Jumper	-24.1	-177.6	-20.7	-160.8	-25.3	-173.3	-20.7	-160.8	4.5
1		Heavy-1	1		2/7/19	12:15	12:36	10	-6.5	0.2	-138.2	0.6	29670	14	IsoLab	FALSE	Jumper	3.2	-66	5.6	-53.2	1.5	-65.4	5.6	-53.2	-98.1
2		DI	15		2/7/19	12:40	1:25	10	-29.2	0.2	-206.4	0.5	27750	140	IsoLab	FALSE	Flask	-19.5	-139.1	-16.2	-123.7	-20.8	-136.1	-16.2	-123.7	6.2
2		DI	16		2/7/19	1:30	2:17	10	-29.1	0.2	-206.4	0.5	27880	72	IsoLab	FALSE	Flask	-19.4	-139.1	-16.2	-123.7	-20.7	-136.1	-16.2	-123.7	5.5
1		Light-1	1		2/7/19	2:20	2:47	10	-34.9	0.2	-244	0.5	29610	34	IsoLab	FALSE	Jumper	-25.2	-179.5	-21.7	-162.6	-26.4	-175.1	-21.7	-162.6	11.3
2		Heavy-1	1		2/7/19	2:50	3:20	10	-6.2	0.2	-141.5	0.5	28000	40	IsoLab	FALSE	Jumper	3.5	-69.5	5.9	-56.6	1.8	-68.8	5.9	-56.6	-103.9
0		DI	2		2/7/19	3:50	4:10	5	-29.1	0.2	-205.9	0.6	NA	NA	IsoLab	FALSE	Flask	-19.4	-138.6	-16.2	-123.2	-20.7	-135.6	-16.2	-123.2	6
1		Light-1	1		2/7/19	4:48	5:05	10	-34.5	0.2	-242.3	0.6	31300	355	IsoLab	FALSE	Jumper	-24.8	-177.6	-21.4	-160.8	-26	-173.3	-21.4	-160.8	10
2		Heavy-1	1		2/7/19	5:08	5:22	10	-5.6	0.2	-137.7	0.6	30800	62	IsoLab	FALSE	Jumper	4.1	-65.5	6.5	-52.7	2.4	-64.8	6.5	-52.7	-104.6
1		Heavy-1	1		2/7/19	5:25	5:40	10	-6.5	0.2	-138.5	0.5	30230	90	IsoLab	FALSE	Jumper	3.2	-66.3	5.6	-53.5	1.5	-65.7	5.6	-53.5	-98.5
2		DI	2		2/7/19	5:45	6:30	10	-28.8	0.2	-204.3	0.5	29770	102	IsoLab	FALSE	Flask	-19.1	-136.9	-15.9	-121.5	-20.4	-133.9	-15.9	-121.5	5.3
1		Light-1	1		2/8/19	6:52	7:06	10	-35.74	0.2	-249.3	0.7	33000	215	IsoLab	FALSE	Jumper	-26.1	-185.1	-22.5	-168.1	-27.2	-180.6	-22.5	-168.1	12.3
2		Light-1	1		2/8/19	7:09	7:37	10	-35.3	0.2	-251.6	1	30420	91	IsoLab	FALSE	Jumper	-25.6	-187.6	-22.1	-170.4	-26.8	-183	-22.1	-170.4	6.5
2		Heavy-1	1		2/8/19	7:57	8:15	10	-6.5	0.2	-144.2	0.6	29720	70	IsoLab	TRUE	Jumper	3.2	-72.4	5.6	-59.4	1.5	-71.6	5.6	-59.4	-104.4
1		Heavy-1	1		2/8/19	8:18	8:35	10	-6.9	0.2	-141.3	0.8	29600	180	IsoLab	FALSE	Jumper	2.8	-69.3	5.2	-56.4	1.1	-68.6	5.2	-56.4	-98.3
0		Di	16		2/8/19	8:42	8:52	5	-29	0.2	-204.8	0.7	NA	NA	IsoLab	FALSE	Flask	-19.3	-137.4	-16.1	-122.1	-20.6	-134.4	-16.1	-122.1	6.4
0		DI	15		2/8/19	9:00	9:08	5	-28.4	0.2	-203.4	0.5	NA	NA	IsoLab	FALSE	Flask	-18.7	-135.9	-15.5	-120.6	-20	-133	-15.5	-120.6	3.2

2	Light-1	1	2/8/19	9:12	9:35	10	-34.9	0.2	-248.5	0.5	30300	10	IsoLab	FALSE	Jumper	-25.2	-184.3	-21.7	-167.2	-26.4	-179.7	-21.7	-167.2	6.6
1	Heavy-1	1	2/8/19	9:40	10:00	10	-6.6	0.2	-139.7	0.6	30000	180	IsoLab	FALSE	Jumper	3.1	-67.6	5.5	-54.7	1.4	-66.9	5.5	-54.7	-98.9
0	DI	14	2/8/19	10:00	10:21	5	-27.63	0.2	-196.2	0.6	NA	NA	IsoLab	TRUE	Flask	-18	-128.2	-14.7	-113.2	-19.3	-125.5	-14.7	-113.2	4.7
0	DI	2	2/8/19	10:31	10:36	5	-28.8	0.2	-204	0.6	NA	NA	IsoLab	FALSE	Flask	-19.1	-136.6	-15.9	-121.2	-20.4	-133.6	-15.9	-121.2	5.7
2	Light-1	1	2/8/19		11:02	10	-33.6	0.2	-244.6	0.4	33170	75	IsoLab	FALSE	Jumper	-23.9	-180.1	-20.5	-163.2	-25.1	-175.7	-20.5	-163.2	0.6
1	Heavy-1	1	2/8/19		0:00	10	-6.3	0.2	-137.5	0.6	NA	NA	IsoLab	FALSE	Jumper	3.4	-65.2	5.8	-52.5	1.7	-64.6	5.8	-52.5	-98.9
1	tap	1	2/20/19	7:40	8:00	NA	NA	NA	NA	NA	NA	NA	IsoLab	TRUE	Jumper	NA	NA	NA	NA	NA	NA	NA	NA	NA
2	Light-1	1	2/20/19	8:00	8:20	15	-34.14	0.25	-245.2	1	NA	296.9	IsoLab	FALSE	Jumper	-24.5	-180.7	-21	-163.8	-25.6	-176.3	-21	-163.8	4.2
1	Heavy-1	1	2/20/19	8:20	8:40	10	-6.5	0.2	-138.8	0.5	286300	72	IsoLab	FALSE	Jumper	3.2	-66.6	5.6	-53.8	1.5	-66	5.6	-53.8	-98.8
2	Light-1	1	2/20/19	8:47		15	-35.5	0.3	-252.7	1.4	25600	474	IsoLab	FALSE	Jumper	-25.8	-188.8	-22.3	-171.6	-27	-184.1	-22.3	-171.6	6.9
1	Heavy-1	1	2/20/19	9:15	9:35	10	-6.7	0.2	-141.2	0.6	28160	161	IsoLab	FALSE	Jumper	3	-69.2	5.4	-56.3	1.3	-68.5	5.4	-56.3	-99.7
3	Light-1	1	2/20/19	9:50	10:10	10	-35.4	0.22	-250.7	0.61	28880	117	IsoLab	FALSE	Jumper	-25.7	-186.6	-22.2	-169.5	-26.9	-182	-22.2	-169.5	8.2
1	Light-1	1	2/20/19	10:22		NA	NA	NA	NA	NA	NA	NA	IsoLab	FALSE	Jumper	NA	NA	NA	NA	NA	NA	NA	NA	NA
1	Light-1	2	2/20/19	10:25	11:15	NA	NA	NA	NA	NA	NA	NA	IsoLab	FALSE	Flask	NA	NA	NA	NA	NA	NA	NA	NA	NA
1	Light-1	1	2/21/19	8:00	8:24	10	-35	0.2	-245.5	0.5	23570	81	IsoLab	FALSE	Jumper	-25.3	-181.1	-21.8	-164.1	-26.5	-176.6	-21.8	-164.1	10.5
2	Light-1	1	2/21/19	8:28	8:48	10	-34.34	0.2	-247.5	0.5	27990	100	IsoLab	FALSE	Jumper	-24.7	-183.2	-21.2	-166.2	-25.8	-178.7	-21.2	-166.2	3.3
3	Light-1	1	2/21/19			10	-34.27	0.2	-244.2	0.5	28690	144	IsoLab	FALSE	Jumper	-24.6	-179.7	-21.1	-162.8	-25.8	-175.3	-21.1	-162.8	6.3

2	Light-1f	1	2/21/19	9:25	9:45	15	-32.4	0.2	-232.4	0.5	29880	121	IsoLab	FALSE	Jumper	-22.7	-167	-19.3	-150.6	-23.9	-163.1	-19.3	-150.6	4
1	Light-1f	1	2/21/19	9:50	10:15	10	-33.1	0.2	-232.6	0.5	29720	82	IsoLab	FALSE	Jumper	-23.4	-167.2	-20	-150.8	-24.6	-163.3	-20	-150.8	9.2
3	Light-1f	1	2/21/19	10:20	10:40	15	-32.5	0.2	-232.5	0.5	29140	52	IsoLab	FALSE	Jumper	-22.8	-167.1	-19.4	-150.7	-24	-163.2	-19.4	-150.7	4.7
2	Light-1f	1	2/21/19	10:45	11:15	10	-32.7	0.2	-234.5	0.5	28890	71	IsoLab	FALSE	Jumper	-23	-169.3	-19.6	-152.8	-24.2	-165.2	-19.6	-152.8	4.1
1	Light-1f	1	2/21/19	11:20	11:40	10	-33.1	0.2	-232.5	0.5	29830	101	IsoLab	FALSE	Jumper	-23.4	-167.1	-20	-150.7	-24.6	-163.2	-20	-150.7	9.3
3	Light-1f	1	2/21/19	11:45	12:00	10	-32.5	0.2	-232.2	0.5	29760	76	IsoLab	FALSE	Jumper	-22.8	-166.8	-19.4	-150.4	-24	-162.8	-19.4	-150.4	5
1	Heavy-1	1	2/21/19	12:05	12:25	10	-6.3	0.2	-136.7	0.5	30790	61	IsoLab	FALSE	Jumper	3.4	-64.4	5.8	-51.6	1.7	-63.8	5.8	-51.6	-98.1
1	DI	1	2/21/19	12:40	1:10	10	-28.7	0.2	-200.2	0.6	30840	56	IsoLab	FALSE	Jumper	-19	-132.5	-15.8	-117.3	-20.3	-129.7	-15.8	-117.3	8.8
4	Light-1f	1	2/22/19	9:30	9:50	10	-32.1	0.2	-231.6	0.5	30500	243	IsoLab	TRUE	Jumper	-22.4	-166.2	-19	-149.8	-23.6	-162.2	-19	-149.8	2.6
4	Light-1f	1	2/22/19	10:15	10:30	10	-32.4	0.2	-233	0.5	30290	51	IsoLab	TRUE	Jumper	-22.7	-167.7	-19.3	-151.2	-23.9	-163.7	-19.3	-151.2	3.3
4	Light-1f	1	2/22/19	10:53	11:10	10	-32.4	0.2	-235	0.5	29530	53	IsoLab	TRUE	Jumper	-22.7	-169.8	-19.3	-153.3	-23.9	-165.7	-19.3	-153.3	1.3
3	tap	1	2/23/19	11:15	11:30	10	-26	0.2	-194.5	0.5	29200	56	IsoLab	TRUE	Jumper	-16.3	-126.4	-13.2	-111.4	-17.7	-123.7	-13.2	-111.4	-6.1
2	Heavy-1	1	2/23/19	11:34	11:54	10	-5.4	0.2	-135.1	0.5	32110	144	IsoLab	FALSE	Jumper	4.3	-62.7	6.7	-50	2.6	-62.2	6.7	-50	-103.4
1	Heavy-1	1	2/23/19	11:58	12:18	10	-6.2	0.2	-134.9	0.5	32540	111	IsoLab	FALSE	Jumper	3.5	-62.5	5.9	-49.8	1.8	-61.9	5.9	-49.8	-97.1
2	Heavy-1	1	2/23/19	12:22	12:36	10	-5.3	0.2	-134.2	0.5	33340	117	IsoLab	FALSE	Jumper	4.4	-61.7	6.8	-49.1	2.7	-61.2	6.8	-49.1	-103.3
1	Light-2f	1	2/23/19	12:44	1:04	10	-34.7	0.2	-241.9	0.4	33760	57	IsoLab	FALSE	Jumper	-25	-177.2	-21.5	-160.4	-26.2	-172.9	-21.5	-160.4	11.9

2		Light-2f	1		2/23/19			1 0	-34.3	0.2	-243.9	0.4	33250	33		IsoLab	FALSE	Jumper	-24.6	-179.4	-21.2	-162.5	-25.8	-175	-21.2	-162.5	6.7
1		DI	14		2/23/19	2/23/19	1:30	2:15	1 0	-29.7	0.2	-204	0.4	32000	200	IsoLab	IsoLab	TRUE	Flask	-20	-136.6	-16.7	-121.2	-21.3	-133.6	-16.7	-121.2	12.5
1		DI	15		2/23/19	2/23/19	2:15	3:00	1 0	-29.6	0.2	-203.9	0.4	32400	136	IsoLab	IsoLab	FALSE	Flask	-19.9	-136.5	-16.6	-121.1	-21.2	-133.5	-16.6	-121.1	11.9
2		Light-2f	1		2/23/19		3:04	3:20	1 0	-33.9	0.2	-241	0.4	35420	40	IsoLab	IsoLab	FALSE	Jumper	-24.2	-176.2	-20.8	-159.5	-25.4	-172	-20.8	-159.5	6.7
1		Light-2f	1		2/23/19		3:22	3:40	1 0	-34.7	0.2	-241.3	0.4	34890	45	IsoLab	IsoLab	FALSE	Jumper	-25	-176.6	-21.5	-159.8	-26.2	-172.3	-21.5	-159.8	12.5
2		Heavy-1	1		2/23/19		3:43	4:00	1 0	-5.7	0.2	-136.3	0.5	34500	150	IsoLab	IsoLab	FALSE	Jumper	4	-64	6.4	-151.2	2.3	-163.4	6.4	-151.2	-102.3
1		DI	16		2/23/19	2/23/19	4:02	4:50	1 0	-29.25	0.2	-201.2	0.4	34540	60	IsoLab	IsoLab	FALSE	Flask	-19.6	-133.6	-16.3	-111.8	-20.8	-133.7	-16.3	-111.8	12
1		DI	2		2/23/19	2/23/19	4:50	5:35	1 0	-29.2	0.2	-201.1	0.4	34300	62	IsoLab	IsoLab	FALSE	Flask	-19.5	-133.5	-16.2	-111.8	-20.8	-130.6	-16.2	-111.8	11.7
2		Light-2f	1		2/23/19		5:38	5:56	1 0	-33.9	0.2	-241.1	0.5	35100	140	IsoLab	IsoLab	FALSE	Jumper	-24.2	-176.3	-20.8	-159.6	-25.4	-172.1	-20.8	-159.6	6.6
1		DI	1		2/23/19	2/23/19	6:02	6:20	1 0	-6.2	0.2	-134.9	0.6	35000	70	IsoLab	IsoLab	FALSE	Jumper	3.5	-62.5	5.9	-49.8	1.8	-61.9	5.9	-49.8	-97.1
3		tap	1		2/24/19	2/24/19	11:20	11:35	1 0	-25	0.3	-191.5	0.5	29700	285.9	IsoLab	IsoLab	TRUE	Jumper	-15.3	-123.2	-12.2	-108.3	-16.7	-120.6	-12.2	-108.3	-10.7
1		Light-2f	1		2/24/19		11:43	12:08	1 0	-34.9	0.2	-243.5	0.5	32280	65	IsoLab	IsoLab	FALSE	Jumper	-25.2	-178.9	-21.7	-162.1	-26.4	-174.6	-21.7	-162.1	11.8
2		Light-2f	1		2/24/19		12:11	12:31	1 0	-34.2	0.2	-243.4	0.4	32930	49	IsoLab	IsoLab	FALSE	Jumper	-24.5	-178.8	-21.1	-162	-25.7	-174.5	-21.1	-162	6.5
1		Heavy-1	1		2/24/19	2/24/19	12:35	12:56	1 0	-6.2	0.2	-135.2	0.6	34540	129	IsoLab	IsoLab	FALSE	Jumper	3.5	-62.8	5.9	-50.1	1.8	-62.3	5.9	-50.1	-97.4
2		Heavy-1	1		2/24/19	2/24/19	1:01	1:21	1 0	-5.4	0.2	-134.2	0.4	35040	77	IsoLab	IsoLab	FALSE	Jumper	4.3	-61.7	6.7	-49.1	2.6	-61.2	6.7	-49.1	-102.5
0		DI	2		2/24/19	2/24/19	1:28	1:48	5	-29.1	0.2	-199.8	0.6	31420	2383	IsoLab	IsoLab	FALSE	Flask	-19.4	-132.1	-16.2	-116.9	-20.7	-129.2	-16.2	-116.9	12.3
0		DI	16		2/24/19	2/24/19	2:12	2:32	5	-29	0.2	-200.5	0.4	29900	2361	IsoLab	IsoLab	FALSE	Flask	-19.3	-132.8	-16.1	-117.6	-20.6	-130	-16.1	-117.6	10.8
1		Light-2f	2		2/24/19		2:35	2:56	5	-34.8	0.2	-242.8	0.4	35530	57	IsoLab	IsoLab	FALSE	Flask	-25.1	-178.2	-21.6	-161.3	-26.3	-173.8	-21.6	-161.3	11.8

2		Heavy-1	2	2/24/19	2:59	3:22	8	-5.4	0.2	-135	0.5	35910	33	IsoLab	FALSE	Flask	4.3	-62.6	6.7	-49.9	2.6	-62	6.7	-49.9	-103.3	
0		DI	15	2/24/19	3:30	3:55	5	-28.6	0.2	-200	0.6	24900	1996	IsoLab	FALSE	Flask	-18.9	-132.3	-15.7	-117.1	-20.2	-129.5	-15.7	-117.1	8.2	
0		DI	14	2/24/19	3:56	4:16	5	-29.3	0.2	-201.2	0.5	29400	2291	IsoLab	TRUE	Flask	-19.6	-133.6	-16.3	-118.3	-20.9	-130.7	-16.3	-118.3	12.4	
2		Light-2f	1	2/24/19	4:17	4:38	10	-33.9	0.2	-241	0.5	36960	41	IsoLab	FALSE	Jumper	-24.2	-176.2	-20.8	-159.5	-25.4	-172	-20.8	-159.5	6.7	
1		Heavy-1	1	2/24/19	4:40	5:00	10	-6.2	0.2	-134.7	0.5	36870	29	IsoLab	FALSE	Jumper	3.5	-62.2	5.9	-49.6	1.8	-61.7	5.9	-49.6	-96.8	
1		Heavy-2	1	2/25/19	10:56	11:20	10	-10.9	0.2	-152.6	0.5	29290	58	IsoLab	FALSE	Jumper	-1.2	-81.4	1.4	-68.1	-2.8	-80.3	1.4	-68.1	-79.1	
2		Heavy-2	1	2/25/19	11:23	11:45	10	-10.2	0.2	-152.2	0.5	29430	40	IsoLab	FALSE	Jumper	-0.5	-81	2.1	-67.7	-2.1	-79.9	2.1	-67.7	-84.1	
1		Light-2f	1	2/25/19	11:51	12:15	10	-34.9	0.2	-243.7	0.5	30220	62	IsoLab	FALSE	Jumper	-25.2	-179.1	-21.7	-162.3	-26.4	-174.8	-21.7	-162.3	11.6	
2		Light-2f	1	2/25/19	12:18	12:45	10	-34.4	0.2	-245.3	0.5	29910	73	IsoLab	FALSE	Jumper	-24.7	-180.9	-21.3	-163.9	-25.9	-176.4	-21.3	-163.9	6.1	
1		DI	14	2/25/19	12:52	1:45	10	-29.6	0.2	-204.5	0.6	30460	145	IsoLab	TRUE	Flask	-19.9	-137.1	-16.6	-121.7	-21.2	-134.1	-16.6	-121.7	11.3	
1		DI	15	2/25/19	1:55	2:40	10	-29.4	0.2	-203.7	0.5	30100	129	IsoLab	FALSE	Flask	-19.7	-136.2	-16.4	-120.9	-21	-133.3	-16.4	-120.9	10.5	
2		Light-2f	1	2/25/19	2:42	3:00	10	-34.4	0.2	-245.3	0.5	30520	80	IsoLab	FALSE	Jumper	-24.7	-180.9	-21.3	-163.9	-25.9	-176.4	-21.3	-163.9	6.1	
1		Heavy-2	1	2/25/19	3:08	3:30	10	-10.9	0.2	-151.8	0.5	31110	42	IsoLab	FALSE	Jumper	-1.2	-80.6	1.4	-67.3	-2.8	-79.5	1.4	-67.3	-78.3	
2		Heavy-2	1	2/25/19	3:40	4:00	10	-10.1	0.2	-151.7	0.5	30900	53	IsoLab	FALSE	Jumper	-0.4	-80.5	2.2	-67.1	-2.1	-79.4	2.2	-67.1	-84.3	
1		DI	16	2/25/19	4:05	4:50	10	-29.5	0.2	-204.2	0.4	30080	127.9	IsoLab	FALSE	Flask	-19.8	-136.8	-16.5	-121.4	-21.1	-133.8	-16.5	-121.4	10.8	
1		DI	2	2/25/19	5:00	5:45	10	-29.5	0.2	-204.6	0.5	29080	111	IsoLab	FALSE	Flask	-19.8	-137.2	-16.5	-121.8	-21.1	-134.2	-16.5	-121.8	10.4	
2		Light-2f	1	2/25/19	5:50	6:10	10	-34.7	0.2	-247.3	0.5	29240	74	IsoLab	FALSE	Jumper	-.25	-183	-21.5	-166	-26.2	-178.5	-21.5	-166	6.3	
1		Heavy-2	1	2/25/19	6:15	6:35	10	-11.6	0.2	-157	0.6	28650	88	IsoLab	TRUE	Jumper	-1.9	-86.2	0.7	-72.6	-3.5	-84.9	0.7	-72.6	-78.3	

2	DI	1	5/15/19	11:35	12:05	25	-24.12	0.17	-191.4	0.47	29900	170	Guac	FALSE	Jumper	-14.4	-123	-11.4	-108.2	-15.8	-120.5	-15.8	-120.5	6
1	DI	1	5/15/19	12:15	12:45	25	-24.82	0.17	-191.6	0.47	30010	178	Guac	FALSE	Jumper	-15.1	-123.3	-12	-108.4	-16.5	-120.7	-16.5	-120.7	11.2
2	DI	1	5/15/19	1:30	2:10	25	-23.92	0.17	-190.5	0.4	30010	126.3	Guac	FALSE	Jumper	-14.2	-122.1	-11.2	-107.3	-15.6	-119.6	-15.6	-119.6	5.3
1	DI	1	5/15/19	2:10	2:40	25	-24.66	0.17	-190.7	0.4	30000	200	Guac	FALSE	Jumper	-15	-122.3	-11.9	-107.5	-16.3	-119.8	-16.3	-119.8	10.9
2	DI	1	5/15/19	2:50	3:10	10	-24.12	0.17	-191.2	0.38	30150	28	Guac	FALSE	Jumper	-14.4	-122.8	-11.4	-108	-15.8	-120.3	-15.8	-120.3	6.2
2	Light-1f	1	5/16/19	10:21	10:33	5	-27.9	0.17	-220.8	0.5	28920	13	Guac	FALSE	Jumper	-18.2	-154.6	-15	-138.6	-19.5	-151	-19.5	-151	5.1
1	Heavy-1	1	5/16/19	10:36	10:47	5	NA	NA	NA	NA	NA	NA	Guac	FALSE	Jumper	NA	NA	NA	NA	NA	NA	NA	NA	NA
2	Heavy-1	1	5/16/19		11:10	10	-1.51	0.17	-126.3	0.5	29630	71	Guac	FALSE	Jumper	8.2	-53.2	10.4	-40.9	6.4	-53	6.4	-53	-104.1
1	Heavy-1	1	5/16/19	11:20	11:35	10	-2.1	0.17	-125.4	0.45	30080	73	Guac	FALSE	Jumper	7.6	-52.3	9.9	-40	5.8	-52.1	5.8	-52.1	-98.5
2	Light-1f	1	5/16/19	11:40	11:49	5	-28.03	0.17	-221.1	0.5	30180	26	Guac	FALSE	Jumper	-18.4	-154.9	-15.1	-138.9	-19.6	-151.3	-19.6	-151.3	5.8
1	Light-1f	1	5/16/19	11:55	12:10	10	-28.85	0.19	-223.1	0.59	29250	267	Guac	FALSE	Jumper	-19.2	-157	-15.9	-141	-20.5	-153.4	-20.5	-153.4	10.2
1	Heavy-2	1	5/20/19	11:35	11:55	10	-6.4	0.18	-140.1	0.41	29480	92	Guac	FALSE	Jumper	3.3	-68	5.7	-55.2	1.6	-67.3	1.6	-67.3	-80
2	Heavy-2	1	5/20/19	12:00	12:20	10	-5.6	0.17	-139.6	0.4	30060	38	Guac	FALSE	Jumper	4.1	-67.5	6.5	-54.6	2.4	-66.8	2.4	-66.8	-85.8
1	Light-2f	1	5/20/19	12:25	12:45	10	-30.1	0.17	-231.6	0.4	29870	120	Guac	FALSE	Jumper	-20.4	-166.2	-17.1	-149.8	-21.7	-162.2	-21.7	-162.2	11.1
2	Light-2f	1	5/20/19	12:50	1:10	10	-29.5	0.17	-232.4	0.4	30160	85	Guac	FALSE	Jumper	-19.8	-167	-16.5	-150.6	-21.1	-163.1	-21.1	-163.1	5.7
1	DI	14	5/20/19	1:15	2:00	10	-25.1	0.17	-192.9	0.39	29220	221	Guac	TRUE	Flask	-15.4	-124.7	-12.3	-109.8	-16.8	-122.1	-16.8	-122.1	12.1
1	DI	15	5/20/19	2:00	2:45	10	-25.1	0.17	-193.1	0.42	29800	154	Guac	FALSE	Flask	-15.4	-124.9	-12.3	-110	-16.8	-122.3	-16.8	-122.3	11.9
2	Light-2f	1	5/20/19	2:50	3:10	10	-29.5	0.17	-232	0.43	30280	84	Guac	FALSE	Jumper	-19.8	-166.6	-16.5	-150.2	-21.1	-162.6	-21.1	-162.6	6.1

1		Heavy-2	1	5/20/19	3:15	3:35	10	-6.5	0.17	-140.1	0.44	30250	107	Guac	Guac	FALSE	Jumper	3.2	-68	5.6	-55.2	1.5	-67.3	1.5	-67.3	-79.3
2		Heavy-2	1	5/20/19	3:40	4:00	10	-5.8	0.17	-140.1	0.4	30350	62	Guac	Guac	FALSE	Jumper	3.9	-68	6.3	-55.2	2.2	-67.3	2.2	-67.3	-84.7
1		DI	16	5/20/19	4:15	5:00	10	-24.8	0.17	-191.8	0.4	29730	156.5	Guac	Guac	FALSE	Flask	-15.1	-123.5	-12	-108.6	-16.5	-120.9	-16.5	-120.9	10.8
1		DI	2	5/20/19	5:00	5:45	10	-24.9	0.17	-191.6	0.4	30020	129	Guac	Guac	FALSE	Flask	-15.2	-123.3	-12.1	-108.4	-16.6	-120.7	-16.6	-120.7	11.8
2		Light-2f	1	5/20/19	5:50	6:10	10	-29.3	0.18	-231.3	0.43	30470	32	Guac	Guac	FALSE	Jumper	-19.6	-165.8	-16.3	-149.5	-20.9	-161.9	-20.9	-161.9	5.2
1		Heavy-2	1	5/20/19	6:15	6:35	10	-6.4	0.17	-139.5	0.5	30190	76	Guac	Guac	FALSE	Jumper	3.3	-67.4	5.7	-54.5	1.6	-66.7	1.6	-66.7	-79.4
2		tap	1	6/19/19	10:15	10:30	0	0	0	0	0	0	0	Guac	Guac	FALSE	Jumper	9.7	82.2	11.9	89.7	7.9	78	7.9	78	15
1		Light-2f	1	6/19/19	10:35	10:55	10	-30	0.17	-231	0.4	29940	103	Guac	Guac	FALSE	Jumper	-20.3	-165.5	-17	-149.1	-21.6	-161.6	-21.6	-161.6	11
2		Light-2f	1	6/19/19	11:00	11:20	0	-29.4	0.16	-231	0.4	20800	35	Guac	Guac	FALSE	Jumper	-19.7	-165.5	-16.4	-149.1	-21	-161.6	-21	-161.6	6.3
1		Heavy-2	1	6/19/19	11:25	11:45	10	-6.5	0.17	-139.8	0.46	29850	110	Guac	Guac	FALSE	Jumper	3.2	-67.7	5.6	-54.8	1.5	-67	1.5	-67	-78.9
2		Heavy-2	1	6/19/19	11:50	12:10	10	-5.7	0.18	-139	0.4	30770	62	Guac	Guac	FALSE	Jumper	4	-66.9	6.4	-54	2.3	-66.2	2.3	-66.2	-84.4
0		DI	2	6/19/19	12:20	12:45	5	-24.3	0.2	-189.1	0.7	NA	NA	Guac	Guac	FALSE	Flask	-14.6	-120.6	-11.5	-105.8	-16	-118.1	-16	-118.1	9.7
0		DI	16	6/19/19	12:55	1:20	5	-24.6	0.17	-190.2	0.5	NA	NA	Guac	Guac	FALSE	Flask	-14.9	-121.8	-11.8	-107	-16.3	-119.3	-16.3	-119.3	11
1		Light-2f	1	6/19/19	1:25	1:45	10	-30	0.17	-231	0.5	30490	188	Guac	Guac	FALSE	Jumper	-20.3	-165.5	-17	-149.1	-21.6	-161.6	-21.6	-161.6	11
2		Heavy-2	1	6/19/19	1:50	2:10	10	-5.7	0.18	-139.3	0.4	30570	56	Guac	Guac	FALSE	Jumper	4	-67.2	6.4	-54.3	2.3	-66.5	2.3	-66.5	-84.7
0		DI	15	6/19/19	2:28	2:38	10	-23.7	0.18	-186	0.5	NA	NA	Guac	Guac	FALSE	Flask	-14	-117.3	-11	-102.6	-15.4	-114.9	-15.4	-114.9	8.2
0		DI	14	6/19/19	2:50	2:55	5	-22.4	0.21	-185.9	0.5	NA	NA	Guac	Guac	TRUE	Flask	-12.7	-117.2	-9.7	-102.5	-14.1	-114.8	-14.1	-114.8	-1.9
2		Light-2f	1	6/19/19	3:55	4:15	10	-29.5	0.18	-231.9	0.54	29900	80	Guac	Guac	FALSE	Jumper	-19.8	-166.5	-16.5	-150.1	-21.1	-162.5	-21.1	-162.5	6.2

1		Heavy-2	1	6/19/19	4:20	4:40	10	-6.6	0.18	-14 1.6	0.6	30100	160	Guac	FALSE	Jumper	3.1	-69.6	5.5	-56.7	1.4	-68.9	1.4	-68.9	-80
2		DI	1	6/19/19	4:50	5:05	10	-24.1	0.17	-19 1.2	0.4	29520	171	Guac	FALSE	Jumper	-14.4	-12 2.8	-11.3	-10 8	-15.8	-12 0.3	-15.8	-12 0.3	6
1		DI	1	6/19/19	5:17	5:40	10	-24.8	0.17	-19 1.1	0.5	30000	140	Guac	FALSE	Jumper	-15.1	-12 2.7	-12	-10 7.9	-16.5	-12 0.2	-16.5	-12 0.2	11.5
1		Light-2f	1	3/21/19	8:02	8:25	10	-34.9	0.2	-24 3.9	0.5	28730	67	IsoLab	FALSE	Jumper	-25.2	-17 9.4	-21.7	-16 2.5	-26.4	-17 5	-21.7	-16 2.5	11.4
2		Light-2f	1	3/21/19	8:28	8:48	10	-34.2	-0.2	-24 3.9	0.4	29000	60	IsoLab	FALSE	Jumper	-24.5	-17 9.4	-21.1	-16 2.5	-25.7	-17 5	-21.1	-16 2.5	6
1		Heavy-2	1	3/21/19	8:52	9:20	10	-10.9	0.2	-15 2.4	0.5	28740	120	IsoLab	FALSE	Jumper	-1.2	-81.2	1.4	-67.9	-2.8	-80.1	1.4	-67.9	-78.9
2		Heavy-2	1	3/21/19	9:27	9:50	10	-10	0.2	-15 1.1	0.5	29270	60	IsoLab	FALSE	Jumper	-0.3	-79.8	2.3	-66.5	-2	-78.7	2.3	-66.5	-84.5
0		DI	2	3/21/19	10:06	10:30	5	-29.1	0.2	-20 3.5	0.6	23930	1991	IsoLab	FALSE	Flask	-19.4	-13 6	-16.2	-12 0.7	-20.7	-13 3.1	-16.2	-12 0.7	8.5
0		DI	16	3/21/19	10:40	11:00	15	-29.2	0.2	-20 3.6	0.74	NA	NA	IsoLab	FALSE	Flask	-19.5	-13 6.1	-16.2	-12 0.8	-20.8	-13 3.2	-16.2	-12 0.8	9.1
1		Light-2f	1	3/21/19	11:12	11:30	10	-34.9	0.2	-24 4.2	0.5	30000	60	IsoLab	FALSE	Jumper	-25.2	-17 9.7	-21.7	-16 2.8	-26.4	-17 5.3	-21.7	-16 2.8	11.1
2		Heavy-2	1	3/21/19	11:35	12:00	10	-9.9	0.2	-15 0.4	0.5	30500	80	IsoLab	FALSE	Jumper	-0.2	-79.1	2.4	-65.8	-1.9	-78	2.4	-65.8	-84.6
0		DI	15	3/21/19	12:09	12:41	5	-28.5	0.2	-19 9.5	0.6	22720	1815	IsoLab	FALSE	Flask	-18.8	-13 1.7	-15.6	-11 6.6	-20.1	-12 8.9	-15.6	-11 6.6	8
0		DI	14	3/21/19	12:45	1:05	5	-27.9	0.2	-19 8	0.65	18960	4320	IsoLab	FALSE	Flask	-18.2	-13 0.1	-15	-11 5	-19.5	-12 7.4	-15	-11 5	4.9
2		Light-2f	1	3/21/19	1:15	1:35	10	-34.1	0.2	-24 4	0.5	304430	69	IsoLab	FALSE	Jumper	-24.4	-17 9.5	-21	-16 2.6	-25.6	-17 5.1	-21	-16 2.6	5.1
1		Heavy-2	1	3/21/19	1:40	2:00	10	-10.6	0.2	-15 0.1	0.5	31190	44	IsoLab	FALSE	Jumper	-0.9	-78.8	1.7	-65.5	-2.5	-77.7	1.7	-65.5	-78.9
1		DI	1	3/21/19	3:30	4:20	10	-29.6	0.2	-20 4.5	0.5	NA	NA	ISoLab	TRUE	Jumper	-19.9	-13 7.1	-16.6	-12 1.7	-21.2	-13 4.1	-21.2	-13 4.1	35.3

Chapter III: Lessons from and best practices for the deployment of the Soil Water Isotope Storage System

Rachel E. Havranek [1], Kathryn Snell[1], Sebastian Kopf[1], Brett Davidheiser-Kroll[2], Valerie Morris[3], Bruce Vaughn[3]

Rachel Havranek, Kathryn Snell, Sebastian Kopf, Brett Davidheiser-Kroll, Valerie Morris, Bruce Vaughn

[1]Geological Sciences, University of Colorado Boulder, Boulder, 80303, USA

[2]Thermo Fisher Scientific (Bremen) GmbH, Bremen, Germany

[3]Institute of Arctic and Alpine Research, University of Colorado Boulder, Boulder, 80303, USA

In review, Hydrologic Earth System Sciences

Abstract

Soil water isotope datasets are useful for understanding connections between the hydrosphere, atmosphere, biosphere, and geosphere. However, they have been underproduced compared to other reservoirs (i.e. meteoric water and groundwater) because of technical challenges associated with collecting those datasets. Here, we present the testing and automation of the Soil Water Isotope Storage System (SWISS). The unique innovation of the SWISS is that we are able to automatically collect water vapor from the critical zone at a regular time interval and then store that water vapor until it can be measured back in a laboratory setting. Through a series of quality assurance and quality control tests, we rigorously tested that the SWISS is resistant to both atmospheric intrusion and leaking in both laboratory and field settings. We assessed the accuracy and precision of the SWISS through a series of experiments where water vapor of known composition was introduced into the flasks, stored for 14 days, and then measured. From these experiments, after applying an offset correction, we assess the precision of the SWISS at 0.9‰ and

3.7‰ for $\delta^{18}O$ and $\delta^{2}H$, respectively. We deployed three SWISS units to three different field sites to test whether the SWISS stores water vapor reliably enough that we are able to differentiate dynamics both among the sites as well within a single soil column. Overall, we demonstrate that the SWISS is able to retain the stable isotope composition of soil water vapor for long enough to allow researchers to address a wide range of ecohydrologic questions.

3.1 Introduction

Understanding soil water dynamics across a range of environments and soil properties is critical to food and water security (e.g. Mahindawansha et al., 2018; Quade et al., 2019; Rothfuss et al., 2021); understanding biogeochemical cycles, such as the nitrogen and phosphorus cycles (e.g. Hinckley et al., 2014; Harms and Ludwig, 2016); and understanding connections between the hydrosphere, biosphere, geosphere and atmosphere (e.g. Vereeken et al., 2022). One approach that can be used to understand water use and movement in the critical zone is the stable isotope geochemistry of soil water (e.g. Sprenger et al., 2016; Bowen et al., 2019). Variations in the stable isotope ratios of oxygen and hydrogen of soil water ($\delta^{18}O$, $\delta^{2}H$) track physical processes like infiltration, root water uptake and evaporation. In particular, stable water isotopes are useful for disentangling complex mixtures of water from multiple sources (e.g. Dawson and Ehleringer, 1991; Brooks et al., 2010; Soderberg et al., 2012; Good et al., 2015; Bowen et al., 2018; Gomez-Navarro et al., 2019; Sprenger and Allen 2020). Despite the long-recognized utility of measuring soil water isotopes for understanding a range of processes (e.g. Zimmerman et al.,

1966; Peterson & Fry, 1987), soil water isotope datasets have been under-produced as compared to groundwater and meteoric water isotope datasets (Bowen et al., 2019).

The primary barrier to producing soil water isotope datasets has been the arduous nature of collecting samples. Historically, there are two primary methods for collecting soil water samples, either by digging a pit and collecting a mass of soil to bring back to the lab for subsequent water extraction or via lysimeter. The former method disrupts the soil profile each time a sample is collected, inhibiting the creation of long-term records of soil water isotopes. Lysimeters on the other hand provide the means to collect multi-year soil water isotope datasets (e.g. Green et al., 2015; Groh et al., 2018; Hinkley et al., 2014; Stumpp et al., 2012, Zhao et al., 2013), but the choice of lysimeter can affect the portion of soil water (i.e. mobile vs. bound) that is sampled (Hinkley et al., 2014; Sprenger et al., 2015) and the soil conditions that are sampleable (i.e. saturation state). Soil water samples collected from lysimeters often require manual intervention at the time of sampling. To limit soil column disruption and the need for manual intervention, the ecohydrology community has developed a variety of in situ water sampling methods over the last 10 years (e.g. Wassenaar et al., 2008; Rothfuss et al., 2013; Volkmann and Weiler, 2014; Gaj et al., 2015; Oerter et al., 2016; Beyer et al., 2020). These methods have helped to shed light on a range of ecohydrologic questions from evaporation and water use dynamics in managed soils (e.g. Oerter et al., 2017; Quade et al., 2019) to

better understanding where plants and trees source their water (e.g. Beyer et al., 2020).

The expansion of in situ sampling methods allows for a greater understanding of ecohydrologic dynamics temporally, but with current methods these studies are often done in close proximity to the institutions performing the studies because of logistical constraints. The spatial constraints limit what we can learn about soil hydrology in remote and traditionally understudied landscapes. Beyond the ecohydrology community, the creation of high temporal resolution soil water isotope data sets is useful to a broad set of stakeholders. For example, long-term temporal records of soil water can be used to better understand geologic proxy development (e.g. stable isotope records from pedogenic carbonate, br-GDGTs, etc.). These projects, however, commonly have environmental constraints like soil type or local climate state that may not be located near institutions performing those studies, creating the need for a system that is capable of collecting water vapor from remote settings in an automated way.

In this contribution, we report on the further development and testing of a field deployable system first introduced in Havranek et al., (2020). This system is now capable of independently sampling soil water vapor in situ, storing that water vapor for a period of time until the samples can be brought back to a laboratory to be measured. In our case, we used a Picarro L-2130*i* water isotope analyzer (Picarro, Inc. Santa Clara, CA) to measure both water concentration and the oxygen and hydrogen isotope ratios of the soil water vapor. The combination of the

autonomous sampler and the CRDS instrument offers a flexible and reliable solution to obtain data that is otherwise difficult to collect from soil profiles. Here, we present the testing and optimization of the Soil Water Isotope Storage System (SWISS). First, we present a quality assurance and quality control (QA/QC) procedure that we strongly recommend any future user to complete prior to deploying this kind of system for either a field or lab experiment. Second, we demonstrate the viability of this system under field-conditions through two field suitability experiments. Lastly, we sampled three different field sites to show that the automation schema works on a monthly timescale and that the system preserves soil water vapor isotopes signals with sufficient precision to distinguish between three different field settings and vertical profile differences.

3.2 Background

In recent years, a number of technical innovations have made it easier to sample and measure soil water for stable isotope analysis. Advances in laser-based instrumentation (e.g. cavity ring-down spectroscopy, CRDS) have made high throughput, high precision measurements of both water concentration and water stable isotopes possible. Field deployments with laser-based instruments are technically possible and have been conducted successfully (e.g. Oerter et al., 2017; Quade et al., 2019; Künhammer et al.,2021), but require uninterrupted AC power, adequate shelter as well as safe and stable operating environments for best results. These prerequisites are not often available at most field sites, especially in more remote locations and for longer sampling time frames.

Second, the testing and adoption of vapor permeable tubing provides a way to sample soil water vapor with minimal disturbance to the soil profile (e.g. Rothfuss et al., 2013; Quade et al., 2018; Oerter and Bowen, 2019; Beyer et al., 2020; Kubert et al., 2020). This method works by flushing dry nitrogen (or dry air) through the vapor permeable membrane (Accurrell PP V8/2HF, 3M, Germany), creating a water vapor gradient from inside the probe to the soil, thus inducing water vapor movement across the membrane. Water vapor is then entrained in the dry nitrogen and flushed to either a CRDS system or into a storage container. The adoption of vapor permeable tubing has been a large step forward for the ecohydrology community, and opened the possibility of creating long-term soil water stable isotope records, particularly when paired with measurement in the field by spectroscopic instruments. While this application is a major advancement, it has many practical limitations for remote field sites, therefore, we aimed to develop a system, termed the SWISS, that is capable of independently collecting samples and can then store those samples for a period of time before being returned to the lab for analysis.

3.2.1 Soil Water Isotope Storage System details and previous work

The Soil Water Isotope Storage System (SWISS) uses three basic components for water vapor storage of multiple samples: glass flasks, stainless steel tubing and a flask selector valve (Fig. 3-1, Supplementary Table 1). The ability of the SWISS to reliably store water vapor for up to 30 days was demonstrated previously using a

series of lab experiments (Havranek et al., 2020). This proof of concept demonstrated that the flasks retain original water isotope values, but the laboratory system was not field deployable or have customizable automation. Here, we present a fully autonomous, field-ready system that has been thoroughly tested under both laboratory conditions and field conditions, including development and testing of a solar-powered, battery backed automation system that enables pre-scheduled water vapor sampling without manual intervention in remote field locations.

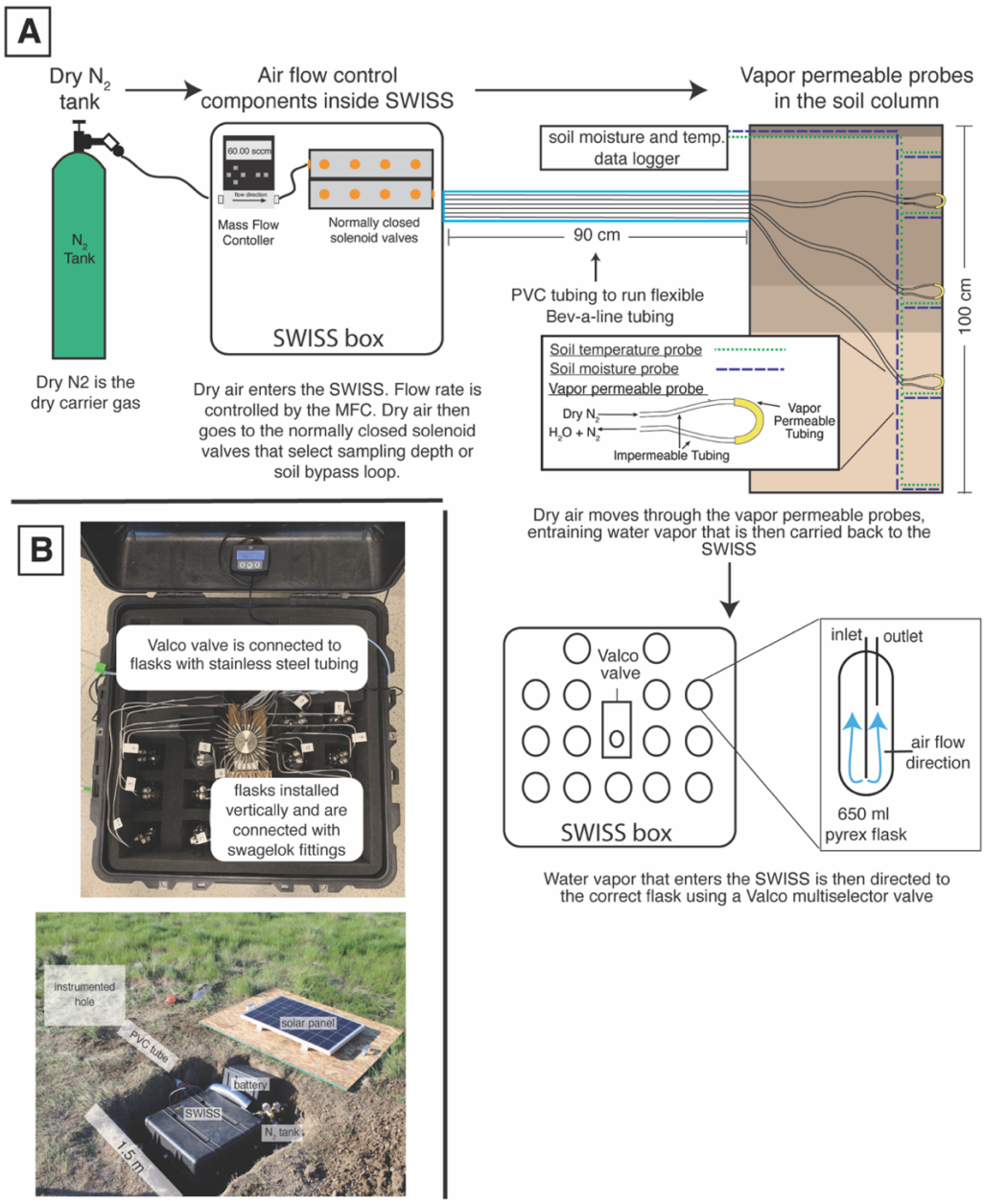

Figure 3-1. A) The sampling flow path. To sample soil water, dry nitrogen is regulated at a specific rate using a mass flow controller, and then directed to one of the three sampling depths, or the soil bypass loop using a set of solenoid valves. Both the mass flow controller and solenoid valves are housed inside the SWISS. Once directed to the correct sampling depth, dry nitrogen is carried to the vapor permeable probes via gas impermeable tubing that is buried approximately 15 cm depth. After passing through the vapor permeable probe, the entrained soil water vapor is carried back to the SWISS where it is directed to the correct flask using a Valco multiselector valve. B) Photos of a built-out SWISS and the layout of a field site. Each of the system components (I.e. solar panel, battery, N2 tank, SWISS, PVC tube) are labeled, in addition to the location of the instrumented hole in which all of the probes are buried. The hole which houses the SWISS, power, and N2 tank is approximately 1.5 m wide.

3.2.2 Field Sites:

3.2.2.1 Site Set-Up

In figure 3-1 we show the field-setup employed at all of our field sites. At each site we dug two holes. One hole is instrumented with soil moisture and temperature data loggers at 25 cm, 50 cm, 75 cm, and 100 cm depths, as well as the water vapor permeable probes at 25 cm, 50 cm and 75 cm depths (Fig 3-1A). All probes were deployed >9 months before the first samples were collected to allow the soil to settle and return to natural conditions as much as possible. During probe deployment we took care to retain the original soil horizon sequence and horizon depths as much as possible. The second hole is where the SWISS unit, dry nitrogen tank, and associated components to power the SWISS are stored (Fig 3-1B). The water vapor probes, which connect to the SWISS with Bev-A-Line impermeable tubing, are run through a PVC pipe buried at approximately 15 cm depth. We chose to run the impermeable tubing to the SWISS underground to limit the effect of diurnal temperature variability on the impermeable tubing, so as to limit condensation as water travels from the relatively warm soil to the SWISS.

3.2.2.2 Site description

We deployed the SWISS at three field locations: Oglala National Grassland, Nebraska, USA; Briggsdale, Colorado,USA; and Seibert, Colorado, USA. The Briggsdale, CO and Seibert, CO sites are co-located with Colorado Agricultural Meteorological Network sites run by the Colorado Climate Center

The Oglala National Grassland site (Lat: 42.9600/Long:, -103.5979/elev: 1117 m) is located in northwestern Nebraska, USA in a cold semi-arid climate. The soil at this site is described as an aridisol with a silt-loam texture. It is part of the Olney series (Natural Resources Conservation Service, 2022).

The Briggsdale site (Lat: 40.5947/Long: -104.3190/elev: 1480 m) is located in northeastern Colorado, USA in a cold semi-arid climate. The soil at this site is described as an alfisol with a loamy sand - sandy loam texture. It is part of the Olnest series (Natural Resources Conservation Service, 2022).

The Seibert site (Lat: 39.1187/Long: -102.9250/Elev: 1479 m) is located in eastern Colorado, USA in a cold semi-arid climate. The soil at this site has been described as an alfisol, that has a sand loam texture in the top 50 cm of the profile, and a silt loam texture between 50 - 100 cm. It is part of the Stoneham series (Natural Resources Conservation Service, 2022).

3.3 Materials

3.3.1 SWISS Hardware components

In each SWISS there are 15 custom made ~650 ml flasks. These flasks are designed similarly to those used for other water vapor applications. For example, a similar flask is currently used in an unmanned aerial vehicle to collect atmospheric water vapor samples for stable isotope analysis (Rozmiarek et al., 2021). The flasks have one long inlet tube that extends into the flask almost to the base, and one shorter outlet tube so that vapor exiting the flask is well mixed and representative of the whole flask (Fig. 3-1A). The large flask volume is advantageous because there

is a low glass surface area to volume ratio, and therefore we are able to reliably measure vapor from the flasks on a CRDS instrument without interacting with vapor bound to the flask walls. The 15 glass flasks are connected to a 16-port, multi-selector Valco valve. We chose to use a Valco valve because these have previously been shown to sufficiently seal off sample volumes for subsequent stable isotope analysis (Theis et al., 2004). The valve and flasks are connected by 1/8 inch stainless steel tubing and stainless steel 1/4 inch to 1/8 inch union Swagelok fittings; we use PTFE ferrules on the glass flasks with the Swagelok fittings. The first port of the Valco valve is 1/8 inch stainless steel tubing that serves as a flask bypass loop, which enables flushing of either dry air or water vapor through the system without interacting with a flask. All components are contained in a 61 cm x 61 cm x 61 cm Pelican case with foam. This case is insulated, and provides enough protection to allow reliable transport of the SWISS by vehicle to field sites.

3.3.2 Soil Probes

There are three components for the collection and interpretation of soil water vapor: vapor permeable probes, soil temperature loggers, and soil moisture sensors (Fig 3-1B, Supp. Table 3-1). Here, we use a vapor permeable membrane (ACCURELL PP V8/2HF, 3M, Germany) that was first tested by Rothfuss et al., (2013). We opted to use this tubing because it has been shown to deliver reliable data over time (i.e. Rothfuss et al., 2015), and is easy to use and customize to individual needs. We previously observed that variability in the length of the vapor

permeable tubing can lead to systematic offsets in the stable isotope composition of measured waters (Havranek et al., 2020). Therefore, we were careful to construct all probes such that the length of the Accurrell vapor permeable tubing was 10 cm long, and the impermeable Bev-A-Line IV connected on each side of the vapor permeable tubing was 2 m long. We also constructed the vapor permeable probes to be used in the lab setting for standards in an identical fashion. Soil temperature loggers (Onset HOBO MX2201), used for applying a temperature correction to all soil water vapor data, were buried at the same depths as the vapor permeable probes. Soil moisture sensors (Onset S-SMD-M005) were also buried at the same depths as the vapor permeable probes.

3.3.3 Automation components, code style, and remote setting power

The philosophy behind the automation of the SWISS was to make it as easy to reproduce as possible, and as flexible as possible to meet different users' sampling needs. We therefore use widely available hardware components and electronics parts; for each product there are numerous alternatives which should be equally viable and could be swapped to better meet each user's needs. In an effort to make our system as accessible and customizable as possible for the scientific community, all automation code is completely open source and will continue to be refined for future applications and hardware improvements. We note that all code is provided as is and should be tested carefully for use in other experiments.

The overall sampling scheme used in this paper is described in figure 3-2 and table 3-1. Our experimental goal was to create a time series of soil water vapor data from three discrete sampling depths (25 cm, 50 cm, 75 cm). Prior to sampling any soil water vapor, we flushed away any water vapor present in the lines within the SWISS prior to flushing the sample loops. Then, at the start of sampling for each depth, we also flushed the water vapor probe to remove condensation or 'old' water vapor. The gas from both of those steps was expelled via the flask bypass loop. Each soil depth was then sampled for 45 minutes by flushing through the next flask designated in the sequence.

Supplement Figure 3-SI 1 shows the components of the automation system. To automate and program the sampling scheme, we used: (1) a microcontroller to run the automation script; (2) a coin-cell battery powered real time clock so that the microcontroller was always capable of keeping track of time through power losses, and therefore maintain the sampling schedule; (3) an RS-232 to TTL converter for serial communication with the Valco valve; (4) solenoid valves that were used to control which depth was being sampled and the associated VDC power relay; (5) a mass flow controller used to control the rate at which dry nitrogen (1 ppm H_2O) is flushed through the probes; and (6) a power relay used to power the Valco valve and mass flow controller. All parts are described in detail in Supplemental Table 3-2.

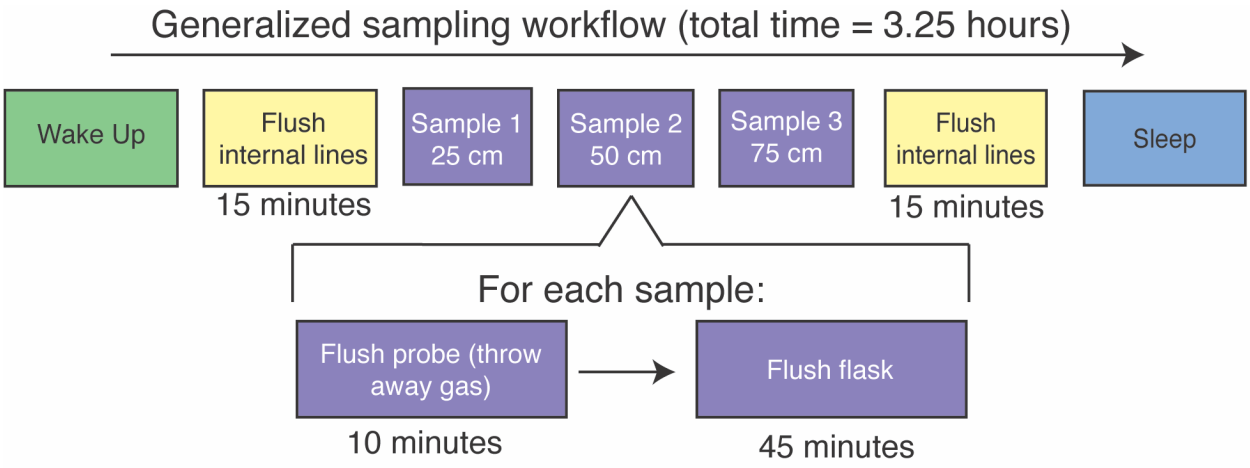

Figure 3-2. Flow chart of the instrument schedule used for sampling during all field experiments.

Table 3-1. Description of soil water sampling steps

Code Step	Wake-up	Flush internal lines	Flush depth 1	Sample depth 1	Flush depth 2	Sample depth 2	Flush depth 3	Sample depth 3	Flush internal lines	sleep
time (min.)	1	15	10	45	10	45	10	45	15	1
Valco valve position	flask bypass	flask bypass	flask bypass	2, 5, 8,11, or 14	flask bypass	3, 6, 9, 12, or 15	flask bypass	4, 7, 10, 13, or 16	flask bypass	flask bypass
solenoid valve position	none	soil bypass	25 cm	25 cm	50 cm	50 cm	75 cm	75 cm	soil bypass	none

In a remote setting, the SWISS units are powered using the combination of a 12V deep-cycle battery and a 12VDC, 100W solar panel that is used to charge the battery. The solar panel is mounted to a piece of plywood that covers the hole where the SWISS is deployed (note, the hole is uncovered in figure 3-1B for illustrative purposes). We opted for this setup because the underground storage of all parts of the system creates a discreet field site that attracts minimal attention from other land users. In the field, we used a 12VDC-120VAC power inverter to provide simple plug and play power for the Valco valve and mass flow controller. This simple combination was suitable for summertime in the Western U.S. where there are a

great number of sunny hours, and the solar panel was able to easily charge the 12V battery. This setup may need to be adjusted based on location and desired sampling time. Like the automation system, there are many commercial options available for products, and they can be easily adjusted for users' needs; example parts are described in detail in supplemental table 3-2. We also note that in areas where it is possible to plug into a power grid, the deep cycle battery, solar panel and power inverter can be removed.

3.4 Methods

3.4.1 QA/QC: Testing the SWISS under lab conditions

The highest order concern for the SWISS is that it remains leak-free because any leaks introduce potential for fractionation or mixing of atmosphere that would alter the stable isotope ratio of the water vapor in the flask. So, we developed a three-part quality assurance and quality control (QA/QC) procedure that must be completed for each new SWISS prior to the first deployment. The first step detects any significant leaks using helium detection methods; the second step is to perform a dry air test to detect medium scale leaks; and the third step is to perform a water vapor test to detect slow leaks. Below, we quickly summarize each of these QA/QC steps. Full procedural descriptions are available in supplementary material and the data processing code is available via GitHub.

3.4.1.1 Step 1: using helium to detect large scale leaks

After initial assembly of the SWISS plumbing, we filled the flasks with helium and used a helium leak detector to find large leaks. Typically, the kinds of

leaks we were able to detect with this method were due to cracking of the inlet or outlet on the glass flask that occurred while tightening the Swagelok fittings. Another easy alternative is to complete a short dry air test (described below) that requires on the order of 12-24 hours.

3.4.1.2 Step 2: dry air tests detect medium scale leaks

Once we felt sure that there were no major leaks in our systems, we completed a dry air test. The goal of this test was to catch any second order, medium-scale leaks. Typically, this test found Swagelok fittings that had been under tightened. The advantage of this kind of test is that it is easy and quick to complete. This test started with a dry air fill. A *dry air fill* consists of flushing flasks with air that is filtered through Drierite (which has a water vapor mole fraction of less than 500 ppm), at 2 L/min for five minutes. With a flask volume of 650 ml, this means the volume of the flask is turned over 15 times. Flasks were then sealed and left to sit for seven days.

At the end of the seven-day period we measured each flask using the *dead-end pull sample introduction* (note, italicized terms are specific methods, and are explained in greater detail in supplementary material) method on a Picarro L2130-*i* Isotope and Gas Concentration Analyzer. For this sample introduction method, the inlet to the Valco valve was sealed with a ¼ inch Swagelok cap and there was no introduction of a carrier gas. As a result, air was removed from the flask based on the flow rate of the Picarro CRDS (typically 27 - 31 ml/min).

We found that in a low-humidity environment, we needed a week to really see leaks, but this timescale would likely be shorter in more humid locations. Additionally, this test could be modified based on available equipment (for example, if an instrument is available to measure trace atmospheric gases, that could be used instead). To ensure that SWISS units continue to operate as expected, this test should be done between field deployments on every SWISS unit.

We repeated dry air tests until the majority (typically at least 13/15) flasks had a water vapor mole fraction value of less than 500 ppm at the end of the seven day experiment. Water vapor values from the CRDS have not been independently calibrated, but relative variations are believed to be reliable.

3.4.1.3 Step 3: Water vapor tests detect small scale leaks

The purpose of this experiment was to mimic storage of water vapor at concentrations similar to what we might expect in a soil, and for durations similar to those of our field experiments. Additionally, these tests were used to demonstrate that flasks that were filled early in the sampling sequence did not lead by the time the samples were returned to the lab for measurement. For this experiment, flasks were filled with water vapor of known isotopic composition and known concentration, sealed for 14 days, and then we measured the water vapor concentration and isotope values.

Prior to putting any water vapor into the flasks (either in the field or in the lab), we completed a dry air fill (as defined above) that served to purge the flasks of any prior water vapor that might exchange with the new sample.

To supply water vapor to the flasks, we used the vapor permeable tubing immersed in water. Across three different measurement sessions, we used three different waters that are used as tertiary standards in the INSTAAR SIL lab to complete these experiments: a light water made from melting and filtering Rocky Mountain snow (-25.5‰ and -187.5‰ VSMOW, for $\delta^{18}O$ and $\delta^{2}H$, respectively), an intermediate water that is deionized (DI) water from the University of Colorado Boulder Campus (~-16.2‰ and -120.7‰ VSMOW for $\delta^{18}O$ and $\delta^{2}H$, respectively) and a heavy water that is filtered water sourced from Florida, USA (~ -0.8‰ and -2.8‰ VSMOW for $\delta^{18}O$ and $\delta^{2}H$, respectively). All secondary lab standards are characterized relative to international primary standards obtained from the International Atomic Energy Agency and are reported relative to the V-SMOW/SLAP standard isotope scale. We flushed the flasks at a rate of 150 ml/min for 30 minutes, and measured the $\delta^{18}O$ and $\delta^{2}H$ values and mole fraction of water vapor as each flask was filled. To calculate the input value, we averaged $\delta^{18}O$ and $\delta^{2}H$ over the last three minutes of the filling period.

At the end of the 14-day storage period, we measured each flask to evaluate if the isotope composition had significantly changed over the storage period. To mitigate memory effects between flasks, we ran dry air via the flask bypass loop (port one of every Valco valve) for five minutes between each flask measurement. During this five minute window, we used a heat gun to manually warm each flask. The purpose of the heating was to help create a longer, more stable window of

measurement time. While the temperature of the flask was not strictly controlled or regulated, they were all warm to the touch.

Once the flask was warmed and the impermeable tubing dried, water vapor was introduced to the CRDS using one of two methods: 1) the dead-end pull method described above, or 2) a *dry air carrier gas sample introduction* method. The dead-end pull method is preferable when the water vapor mole fraction inside the flask is low (<17,000 ppm). But, the major downside of the dead-end pull method is that condensation forms in the stainless steel tubing that connects the flasks to the Valco valve, as well as the Valco valve itself, far more commonly as compared to the *dry air carrier gas method*. During the dry air carrier gas method, dry air is continuously flowing through the flask at a rate of 27-31 ml/min for the entire 12 minute measurement period. Additionally, to reach a water vapor mole fraction of approximately 25,000 ppm (the optimal humidity range for the CRDS), we diluted the water vapor with dry air at a rate of 10 ml/min. Without dilution, the concentration out of the flasks is as high as 35,000 - 40,000 ppm, which leads to saturation issues on a Picarro L2130-*i*. Providing a carrier gas prevents condensation from forming in the Valco valve and tubing, and prevents fractionation that may occur because of changing pressure within the flask. The dry air carrier gas method is our preferred method for sample introduction in most cases.

For each flask we looked at signal stability individually, and for approximately 90% of the flasks we found that after excluding the first three

minutes of measurement of each flask, the subsequent three minutes were the most stable and consistent. For some flasks, using either a later portion of the measurement period, or slightly earlier offered a more stable signal.

During these experiments, instrument drift and stability were monitored using a suite of four waters of known composition that were introduced to the CRDS using a flash evaporator system, described in detail by Rozmiarek and others (2021). Additionally, instrument stability was assessed by measuring water vapor of known composition that was produced using the vapor probes, in a fashion that is identical to how the flasks were flushed.

3.4.2 Field suitability and Field application experiments:

3.4.2.1 Field suitability experiment #1: Long term field leak test

As a complement to the QA/QC we did under lab conditions, we also completed long term dry air tests at our field sites. The purpose of these experiments was to demonstrate that even under field conditions the flasks are still resistant to atmospheric intrusion. Furthermore, this leak test was used to demonstrate that the flasks filled last during the sampling sequence had not taken on an atmospheric isotope composition prior to sampling.

Like all field deployments, we started with a dry air fill, and then one SWISS was deployed to each of our three field sites. No soil water was collected during these deployments. The duration between filling the flasks with dry air to measuring the flasks was anywhere between 34 - 52 days.

3.4.2.2. Field suitability experiment #2: Mock field tests

To demonstrate that the automation code and sampling scheme we propose worked as expected on short, observable timescales, we set up an experiment to simulate field deployment of one SWISS unit (Meringue) near the University of Colorado Boulder. This test used the automation components and remote power setup described in the materials section. During this field-simulation experiment, our goal was to collect three discrete samples each sampling period, to simulate collection of samples from three depths at each field site. Importantly, we wanted to demonstrate that the sampling scheme does not introduce significant memory effects between samples.

Over the course of 25 hours, all 15 flasks were filled with three different vapors. Two were water vapors, created from the light water and intermediate water as described above in the water vapor test section. The third was water vapor from the ambient atmosphere. For this experiment we filled three flasks per cycle with each one of the waters (e.g. Flask 2 = light, Flask 3 = intermediate, Flask 4 = Atmosphere).

For seven days, the SWISS unit was stored in a simulated field setting, while the water vapor remained in the flasks. At the end of the seven days, flasks with a higher water vapor mole fraction (light and intermediate water vapor samples) were measured using the carrier gas sample introduction method, whereas those with a low water vapor mole fraction (atmosphere) were measured using the dead end pull sample introduction method. We used equations 2A and 2B from Rothfuss et al.,

(2013) to convert from water vapor to liquid values. Then, using tertiary standards, data were corrected into the VSMOW data frame. Finally, the SWISS unit offset correction (detailed below) was applied.

3.4.2.3 Full field deployment experiment: One month period

We deployed one SWISS unit each to the three field sites described. We sampled at three depths (25 cm, 50 cm, and 75cm) on each sampling day, following the protocol in figure 2. We sampled at each depth every five days (protocol length = 25 days total). At the end of a 28-day period, the SWISS units were returned to the lab, and measured. The measurement protocol and data reduction protocol follows the procedures described in the water vapor QA/QC test section above. The data correction scheme follows as in the section above.

3.5 Results

3.5.1 QA/QC Results

3.5.1.1 Dry air test

Figure 3-3 shows the results of a seven-day dry air test for three SWISS units (marked by the box name) (SI Table 3-3). For all three SWISS units, at least 13/15 of the flasks maintained a water vapor mole fraction value of less than 500 ppm over the seven day period. In two of the three SWISS units (Lindt and Raclette), the water vapor mole fraction for flasks was randomly distributed around approximately 350 ppm. In Toblerone there was a systematic decrease in water

vapor mole fraction from flask 2 through flask 16, matching the order in which the flasks were filled with dry air initially. In both Lindt and Toblerone, flask 2 had the highest water vapor mole fraction of all the flasks.

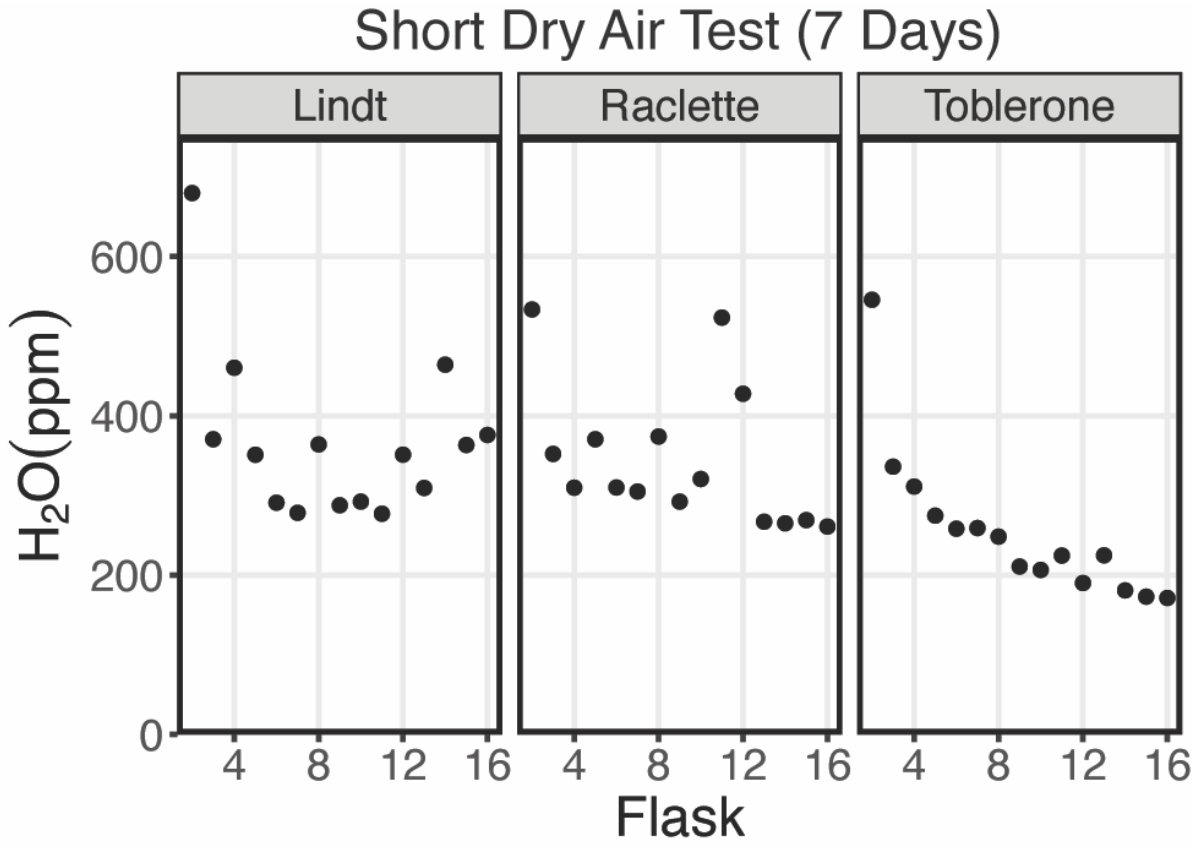

Figure 3-3. Results of a dry air test from three different SWISS units named: Lindt, Raclette and Toblerone. The majority of the flasks maintain a water vapor mixing ratio of less than 500 ppm.

3.5.1.2. Water vapor test

In panels a and b of figures 3-4 and 3-5, we show the results of 11 different water vapor tests performed across three analytical sessions using 6 different SWISS units. This dataset includes water vapor tests using three different water vapors (light, intermediate and heavy) and uses both the dead-end pull and dry-air carrier gas methods to introduce water vapor to the CRDS. Across these three sessions, we measured 164 flasks while filling them with water vapor and at the

end of the two week hold period. After correcting for instrument drift, we calculated the difference between the starting and end values to assess drift in water vapor isotope values due to leaking or other measurement bias.

Ideally, we expect a normal distribution centered about 0 within the uncertainty limits of the water vapor probes (Oerter et al., 2016). For $\delta^{18}O$, the mean difference between the start and end values for the flasks is 1.1‰ with a standard deviation of 0.72‰ (outliers removed). There is a consistent positive offset, with a few clear outliers (Fig. 3-4A). We do not observe a consistent difference between water vapor sample introduction methods (Supp. Fig. 3-2). After removing outliers (< Q1 - 1.5*IQR or > Q3 + 1.5*IQR, n = 15) from the dataset, we compared the kernel density estimate shape to a normal distribution calculated from the mean and standard deviation of the dataset to assess dataset normality (Fig. 3-4B). A normal distribution slightly overestimates the center of the data, but captures the overall shape fairly well. Therefore, we used the median offset (1.0‰) to correct our water vapor isotope values, and used the interquartile range of the dataset (outliers removed) to estimate uncertainty of the SWISS as ± 0.9‰. In figure 3-5C, for simplicity, we just present the results from 45 flasks (three SWISS units), with the 1.0‰ offset correction applied. After correction, data are randomly distributed about 0, and are within the uncertainty range of ± 0.9‰ (Supp. Table 3-4).

For $\delta^{2}H$, the mean difference between the start and end values is 2.6‰ with a standard deviation of 2.9‰ (outliers removed). Similarly to $\delta^{18}O$, we ideally expected a normal distribution of differences centered around 0. As with $\delta^{18}O$, there

was a consistent positive offset with some outliers (i.e. < Q1 - 1.5*IQR or > Q3 + 1.5*IQR) (Fig. 3-5A). After removing outliers (n = 26) from the dataset, we compared the kernel density estimate to a normal distribution calculated from the mean and standard deviation of the dataset to assess dataset normality (Fig. 3-5B). As for $\delta^{18}O$, the center of the dataset is overestimated by the mean, but the overall peak shape is roughly captured. We therefore use the median value of 2.3‰ as an offset correction, and estimate uncertainty at ±3.7‰ for $\delta^{2}H$ from the interquartile range. In figure 3-5C, we present the results from 45 flasks (three SWISS units), with the 2.3‰ offset correction applied. Data are randomly distributed about 0, and are within the uncertainty range of ± 3.7‰ (Supp. Table 3-4).

3.5.2 Field suitability and field deployment experiment results

3.5.2.1. Dry air test

Figure 3-6A shows the result of placing SWISS units that were flushed with dry air out into field conditions over the course of 34 - 52 days (SI Table 3-3). We chose these time intervals because they bracket the typical length of a deployment, which helped us determine how quickly flasks should be measured after bringing a SWISS back to the lab. At the timescale of 34 - 43 days, 13 of the 15 flasks typically maintained a water vapor mole fraction of less than 1000 ppm. At the timescale of 52 days, eight of the 15 flasks had a water vapor mole fraction between 1000 - 2500 ppm, and the remaining seven flasks had a water vapor mole fraction of less than

1000 ppm. Given that these tests were completed with different SWISS units, these data also include some of the inter-unit variability.

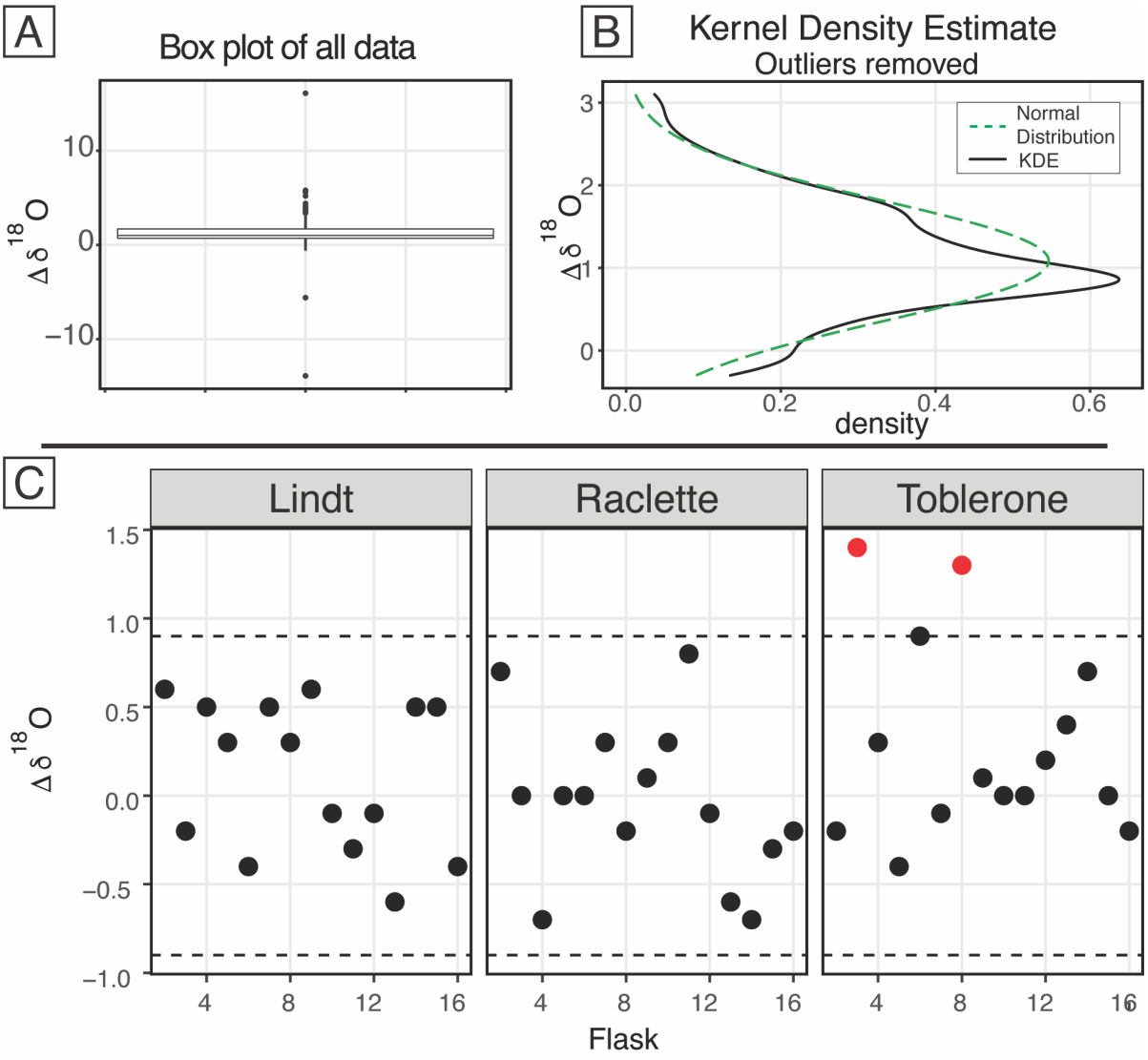

Figure 3-4. Results of the water vapor tests. A) Boxplot of the difference between the starting $\delta^{18}O$ value and the final $\delta^{18}O$ value of all 164 flasks. B) After removing the outliers from the dataset, the kernel density estimate (black line) and the normal distribution calculated from the dataset (dashed green) are shown. C) After applying the offset correction of 1.0‰, the difference between the starting $\delta^{18}O$ value and the final $\delta^{18}O$ value for three boxes from the August 2022 session are shown. An uncertainty of ± 0.9‰ is marked with a dashed line, and data points that fall outside that uncertainty are colored red.

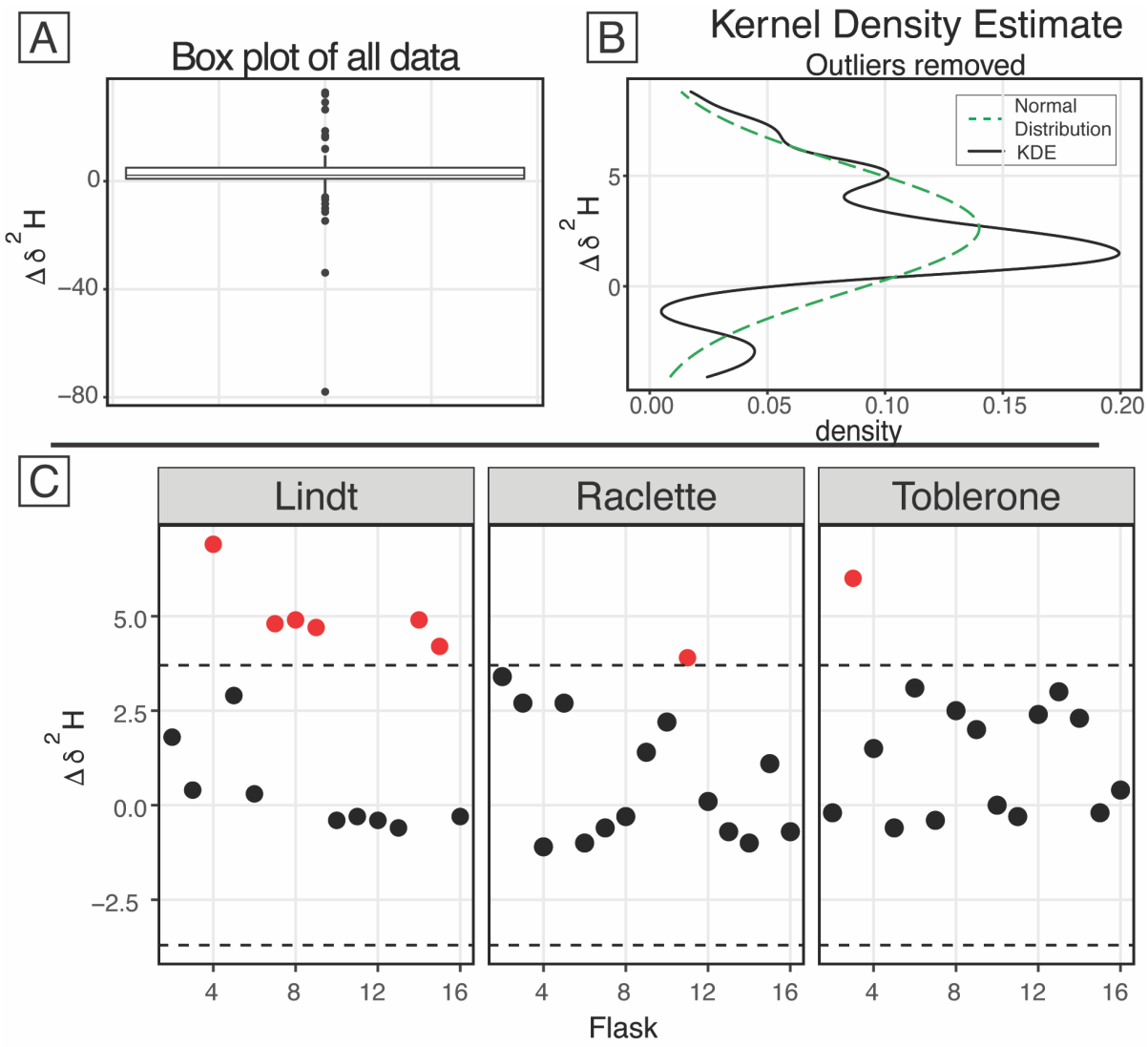

Figure 3-5. Results of the water vapor tests A) Boxplot of the difference between the starting δ^2H value and the final δ^2H value of all 164 flasks. B) After removing the outliers from the dataset, the kernel density estimate (black line) and the normal distribution calculated from the dataset (dashed green) are shown. C) The difference between the starting δ^2H value and the final δ^2H value for three boxes from the August 2022 session are shown after applying the offset correction of 2.3‰. An uncertainty of ± 3.7‰ is marked with a dashed line, and data points that fall outside that uncertainty are colored red.

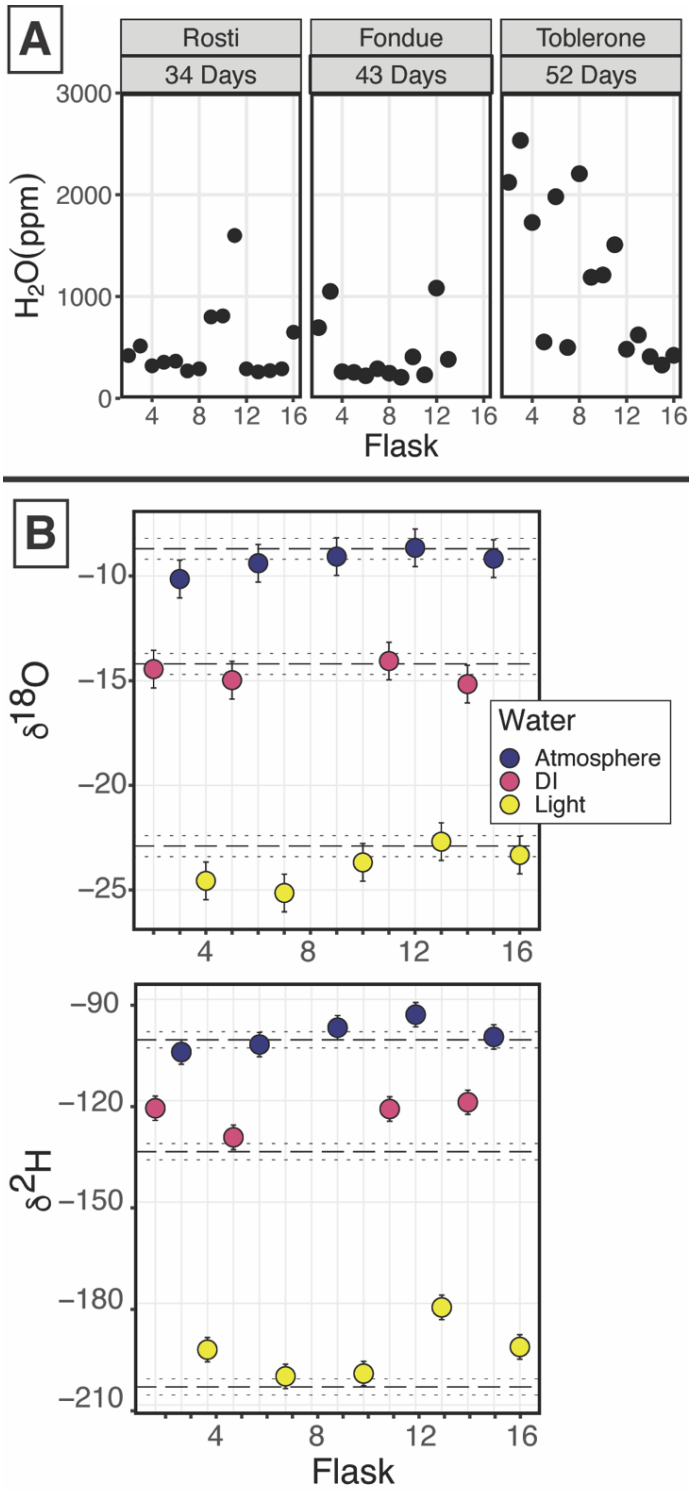

Figure 3-6. A) Results from three different field-based long dry air tests. B) Results from the automation field suitability tests using the SWISS unit named Meringue. Flasks that sampled atmosphere are shown in blue, flasks that sampled deionized water (DI) are shown in pink, and flasks that sampled the light water are shown in yellow. The top plot shows the $\delta^{18}O$ results, and the bottom plot shows the $\delta^{2}H$ results.

3.5.2.2. Automation test

Figure 3-6B shows the result of using the automation code to collect and store water vapor of known composition for seven days (Table 3-2). In both plots, the known values of the water are shown as a long-dash line. Uncertainty on those measurements is estimated at 0.5‰ and 2.4‰ for $\delta^{18}O$ and $\delta^{2}H$ respectively (Oerter et al., 2016), shown as the dotted lines. We estimated the isotope value of the atmosphere at the time of sampling with data from the CRDS in the lab. The corrected isotope value of each flask is shown, with uncertainty associated with the SWISS units estimated at 0.9‰ and 3.7‰ for $\delta^{18}O$ and $\delta^{2}H$, respectively.

Seven of the nine flasks filled with water vapor overlap within uncertainty of the known $\delta^{18}O$ value for those standards (top plot, Fig. 3-6B), and four of the five flasks filled with atmospheric vapor overlap within uncertainty of our estimated $\delta^{18}O$ value. Flasks that fall outside of the bounds of uncertainty tend to have lower $\delta^{18}O$ values than the expected value. For $\delta^{2}H$, (bottom plot, Fig. 3-6B) only three of the nine flasks filled with water vapor overlap within uncertainty of the known value of those standards, while four of the five flasks filled with atmospheric vapor overlap within uncertainty of the estimated $\delta^{2}H$ value. Flasks that fall outside of the bounds of uncertainty typically have higher $\delta^{2}H$ values than the expected value.

Table 3-2. Results of the Automation test

SWISS	Flask	water	δ¹⁸O (‰)	δ²H (‰)
Meringue	2	DI	-14.4	-122.2
Meringue	3	Atmosphere	-10.1	-105.6
Meringue	4	Light	-24.6	-193.7
Meringue	5	DI	-15.0	-130.8
Meringue	6	Atmosphere	-9.4	-103.4
Meringue	7	Light	-25.1	-201.5
Meringue	8	DI	-17.3	-140.5
Meringue	9	Atmosphere	-9.1	-98.4
Meringue	10	Light	-23.7	-200.7
Meringue	11	DI	-14.1	-122.5
Meringue	12	Atmosphere	-8.7	-94.5
Meringue	13	Light	-22.7	-181.2
Meringue	14	DI	-15.2	-120.5
Meringue	15	Atmosphere	-9.2	-101.1
Meringue	16	Light	-23.3	-192.9

3.5.2.3 Field deployment

Figure 3-7 shows the results from three field deployments in Oglala National Grassland, Nebraska; Briggsdale, Colorado; and Seibert, Colorado (table 3-3).

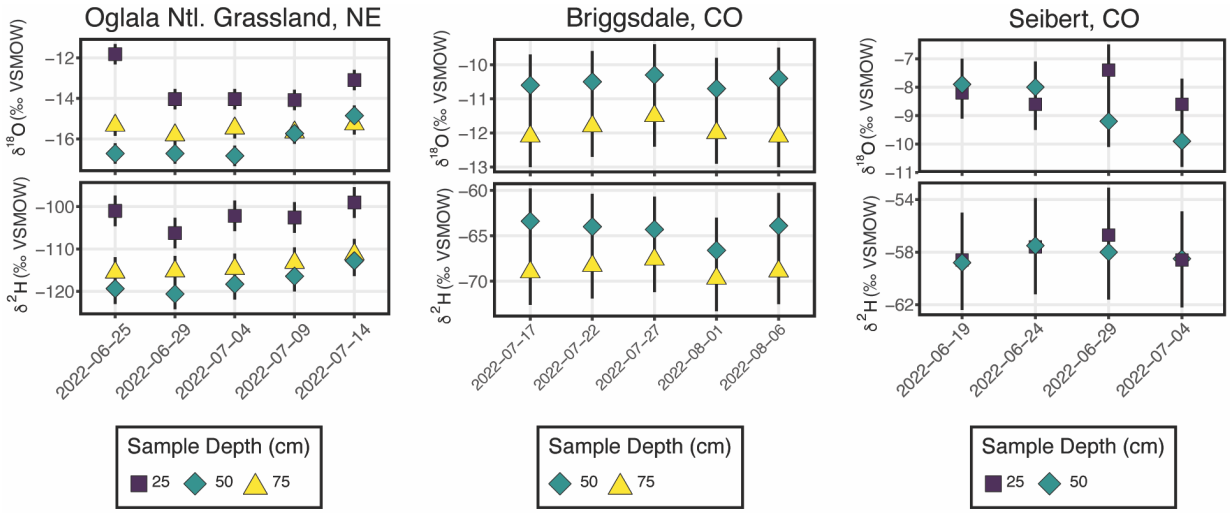

Figure 3-7. Results from all three field deployments to Oglala National Grassland, NE, Briggsdale, CO and Seibert, CO. Note, the y-axis scale for all three plots is different.

Table 3-3. Results from the three field deployments of SWISS.

Site	Date	Sample Depth (cm)	Flask	T (°C)	$\delta^{18}O$ (‰)	$\delta^{18}O$ (‰) Analytical Precision	$\delta^{2}H$ (‰)	$\delta^{2}H$ (‰) Analytical Precision
Briggsdale	7/17/22	50	3	23	-10.6	0.2	-63.4	0.6
Briggsdale	7/17/22	75	4	23	-12.1	0.2	-69	0.7
Briggsdale	7/22/22	50	6	23	-10.5	0.3	-64	0.7
Briggsdale	7/22/22	75	7	23	-11.8	0.2	-68.3	0.6
Briggsdale	7/27/22	50	9	23	-10.3	0.3	-64.3	0.6
Briggsdale	7/27/22	75	10	23	-11.5	0.2	-67.6	0.7
Briggsdale	8/1/22	50	12	23	-10.7	0.2	-66.6	0.7
Briggsdale	8/1/22	75	13	23	-12	0.2	-69.7	0.7
Briggsdale	8/6/22	50	15	23	-10.4	0.2	-63.9	0.6
Briggsdale	8/6/22	75	16	23	-12.1	0.2	-68.9	0.7
Seibert	6/19/22	25	2	23	-8.2	0.2	-58.6	0.6
Seibert	6/19/22	50	3	23	-7.9	0.2	-58.8	0.6
Seibert	6/24/22	25	5	23	-8.6	0.2	-57.6	0.7
Seibert	6/24/22	50	6	23	-8	0.2	-57.5	0.7
Seibert	6/29/22	25	8	23	-7.4	0.2	-56.7	0.6
Seibert	6/29/22	50	9	23	-9.2	0.2	-58	0.7
Seibert	7/4/22	25	11	23	-8.6	0.2	-58.6	0.7
Seibert	7/4/22	50	12	23	-9.9	0.2	-58.5	0.6
Oglala Ntl. Grassland	6/25/22	25	2	23	-11.8	0.2	-101.0	0.7
Oglala Ntl. Grassland	6/25/22	50	3	22.8	-16.7	0.2	-119.3	0.7
Oglala Ntl. Grassland	6/25/22	75	4	21.5	-15.3	0.2	-115.5	0.8
Oglala Ntl. Grassland	6/29/22	25	5	25	-14.0	0.2	-106.2	0.7
Oglala Ntl. Grassland	6/29/22	50	6	22.8	-16.7	0.2	-120.6	0.7
Oglala Ntl. Grassland	6/29/22	75	7	21.3	-15.8	0.2	-115.2	0.7
Oglala Ntl. Grassland	7/4/22	25	8	25	-14.0	0.2	-102.2	0.7
Oglala Ntl. Grassland	7/4/22	50	9	23	-16.8	0.2	-118.3	0.6
Oglala Ntl. Grassland	7/4/22	75	10	22	-15.5	0.2	-114.7	0.6
Oglala Ntl. Grassland	7/9/22	25	11	23	-14.1	0.2	-102.6	0.6
Oglala Ntl. Grassland	7/9/22	50	12	22.8	-15.7	0.2	-116.4	0.7
Oglala Ntl. Grassland	7/9/22	75	13	22	-15.7	0.2	-113.2	0.6
Oglala Ntl. Grassland	7/14/22	25	14	23	-13.1	0.2	-99.0	0.6
Oglala Ntl. Grassland	7/14/22	50	15	22.8	-14.9	0.3	-112.8	0.7
Oglala Ntl. Grassland	7/14/22	75	16	22	-15.3	0.2	-111.2	0.7

There are 15 samples from Oglala National Grassland (Fig. 3-7); five from 25 cm depth, five from 50 cm depth and five from 75 cm depth. Samples were taken approximately every five days from 2022-06-25 to 2022-07-14. Four of the five samples from 25 cm overlap within uncertainty in $\delta^{18}O$ value, and all five samples overlap with uncertainty in $\delta^{2}H$ value. There is a significant decrease in the $\delta^{18}O$ value at 25 cm between 2022-06-25 and 2022-06-29. There is no similar shift in $\delta^{2}H$ value over the same time period. The first three samples from 50 cm overlap in both $\delta^{18}O$ and $\delta^{2}H$ values, then the final two samples drift to higher isotope values. All five samples from 75 cm overlap in $\delta^{18}O$ and $\delta^{2}H$ values. Similar to the samples from 50 cm, there is a trend towards higher $\delta^{2}H$ values for the last three samples. Overall, $\delta^{18}O$ and $\delta^{2}H$ values from 25 cm are significantly higher than the values from 50 and 75 cm depth. Generally, samples from 50 cm depth have lower $\delta^{18}O$ and $\delta^{2}H$ values than samples from 75 cm depth.

There are 10 samples from Briggsdale, CO (Fig. 3-7); five samples are from a vapor probe buried at 50 cm depth and five samples are from a vapor probe buried at 75 cm depth. Data from 25 cm at Briggsdale, CO were excluded because the water vapor mole fraction from all of the flasks with samples at this depth had extremely low water vapor mole fractions (<13,000 ppm), and so those data may either represent atmosphere or soil gas from an extremely dry soil. Samples were taken every five days between 2022-07-17 and 2022-08-06. All samples overlap within uncertainty in both $\delta^{18}O$ and $\delta^{2}H$ values, however samples from 50 cm are

clearly offset to higher values for both $\delta^{18}O$ and $\delta^{2}H$ as compared to samples from 75 cm.

There are 8 samples from Seibert, CO (Fig. 3-7); four samples are from a vapor probe buried at 25 cm depth and four samples are from a vapor probe buried at 50 cm depth. Samples collected from 75 cm depth at Seibert, CO were discarded because there were significant problems with condensation while measuring these flasks, and so all data were considered spurious. Samples were collected every five days between 2022-06-19 and 2022-07-04. At 25 cm depth, $\delta^{18}O$ values of three of the four samples overlap within uncertainty; the 25 cm sample from 2022-06-29 that does not overlap has a higher $\delta^{18}O$ value than the other three samples. At 25 cm depth, $\delta^{2}H$ values overlap within uncertainty for all four samples. At 50 cm depth, there is a steady decrease in $\delta^{18}O$ value over the sampling period, while $\delta^{2}H$ values for all four samples remain steady.

3.6 Discussion

3.6.1 QA/QC and field suitability tests

3.6.1.1 Dry Air tests

For the seven day dry air tests, the flasks were able to maintain a water vapor mole fraction typically less than 400 ppm, and all flasks maintain a water vapor mole fraction of less than 700 ppm (Fig. 4). In Colorado, the ambient atmosphere during the summertime typically sits at a water vapor mole fraction between 10,000 - 20,000 ppm, and in winter the water vapor mole fraction can drop

as low as 4000 ppm. If the flasks allowed in a significant amount of atmosphere, the flasks would have had much higher water vapor molar fractions. This suggests that the system is resistant to atmospheric intrusion.

There seems to be a systemic bias towards a high water vapor mole fraction for the first flask that is measured (flask two). There are two potential analytical sources of this. First, its possible that during the filling phase, not all of the atmospheric vapor has been flushed out of the system before starting the fill process. Similarly, it is possible that not all of the atmospheric water vapor was flushed from the line that connects to the CRDS prior to the start of the measurements.

3.6.1.2 Water vapor tests

The in-lab water vapor tests served three functions: 1) they allowed us to test the best method for measuring soil water vapor at fairly high water vapor mole fractions that might be representative of field conditions (i.e. > 25,000 ppm), 2) to test if there is any systemic bias introduced through the building materials or measurement schema, and, 3) test whether soil water vapor samples can yield reliable stable isotope values.

We completed 11 water vapor tests using 6 SWISS units and three analytical sessions, resulting in 164 measurements of water vapor. Across the three analytical sessions, three waters with different isotopic compositions were used to produce water vapor (1 heavy, 1 intermediate, and 1 light). If there was alteration of original values due to leaky flasks, we might expect the $\delta^{18}O$ and $\delta^{2}H$ values to converge on

the $\delta^{18}O$ and $\delta^{2}H$ value of the atmosphere. For example, we might expect water vapor from the light water test to have the most significant change in isotope value, towards that of the ambient atmosphere.

Figures 3-4 and 3-5 demonstrate that there is a consistent offset in both $\delta^{18}O$ and $\delta^{2}H$ of the water vapor from the start of storage to the end for all three analytical sessions. After removing outliers from the dataset, there remains a consistent bias across all SWISS boxes and analytical sessions (Figs 3-5B, 3-6B). The consistency across >135 flasks, different starting water vapor isotope values, sample introduction methods, and multiple analytical sessions suggests that this difference is a function of the storage and measurement. Additionally, the normality of the distribution suggests that there is a systematic bias that we can reliably correct for. We chose to use the median value as an offset correction over the mean of the normal distribution, because the median is not biased by higher isotope difference values that are a complex combination of systematic bias and slow leaking. The calculated average offset is 1.0‰ and 2.6‰ for $\delta^{18}O$ and $\delta^{2}H$, respectively.

Based on the results of the water vapor tests, we estimate the uncertainty of the SWISS at 0.9‰ and 3.7‰ for $\delta^{18}O$ and $\delta^{2}H$, respectively using the interquartile range (IQR) of the water vapor test results after removing outliers from the dataset. We prefer the IQR over the calculated standard deviation of the normal distribution, because IQR is not biased by outlier values. In figures 3-5C and 3-6C, we show the results of 3 water vapor tests from the August 2022 analytical session,

with an offset correction applied. 43 of the 45 measured flasks faithfully retained the starting $\delta^{18}O$ value of the water vapor, and 37 of the 45 measured flasks faithfully retained the starting $\delta^{2}H$ value of the water vapor. Additionally, after the offset correction was applied, most flasks also fall within the uncertainty of the water vapor permeable probes ($\delta^{18}O$ = 0.5‰ and $\delta^{2}H$ = 2.4‰).

Supplemental figure 3 shows a kernel density estimate plot of the results from two water vapor test sessions, with the offset correction applied. During the March 2022 session, flasks were measured using the dead-end pull sample introduction method and during the August 2022 session, flasks were measured using the dry air carrier gas sample introduction method. There is no significant difference in the measured difference between the two sample introduction methods. We prefer the dry air carrier gas method, because it is far simpler to control the water vapor mixing ratio, and optimize the concentration to be around 25,000 ppm, which is the concentration at which the Picarro L2130-i is most reliable. The dry air carrier gas method also makes it far easier to control for and monitor for condensation in the stainless steel tubing and vapor impermeable tubing, which can bias a measurement.

3.6.1.3 Field suitability tests

In Figure 3-7A, we observe that the flasks typically maintained a low water vapor mole fraction (< 1000 ppm) under field conditions, and at timescales relevant to 4-6 week field deployments (34 - 43 days). The 34-day test was done during June 2022, and therefore tests the SWISS under warm summertime conditions. The 43-

day test was done in October 2021, which included nights where temperatures fell below 0°C, and therefore tests the suitability of the SWISS to maintain integrity under freezing conditions. We observe that the SWISS did considerably worse at maintaining a low water vapor mole fraction over a 52-day time period during similar summertime conditions as compared to the 34 – 43 day time period. Over the 52 days, seven flasks maintained a water vapor mole fraction less than 1000 ppm and the remaining 8 had a water vapor mole fraction between 1000 - 2500 ppm. Though the SWISS performed considerably worse after 52 days than it did from 34 - 43 days, it is important to note that the atmospheric water vapor mole fraction during the storage time period was likely 15,000 - 20,000 ppm, and so the measured values demonstrate that the SWISS are still quite resistant to atmospheric intrusion at that timescale.

In figure 7B, the data show that the flasks faithfully preserved the $\delta^{18}O$ value of both water vapor produced using the vapor permeable probe and the atmosphere over a seven day period. One flask was removed from the dataset (flask eight), because there was noticeable condensation in the impermeable tubing during the measurement phase, with an increase of > 5‰ for $\delta^{18}O$ during the measurement period. Notably, the two flasks whose $\delta^{18}O$ oxygen isotope values do not overlap within uncertainty are more negative than expected, rather than drifting towards atmospheric values or values expected with kinetic fractionation. It is possible that those samples were also affected by condensation at the start of the experiment; during condensation, we expect that ^{18}O will preferentially go into the liquid phase,

and that the water vapor that enters the flask will have a lower than expected $\delta^{18}O$ value.

Surprisingly, only 3 flasks filled with either DI or light water vapor overlap within uncertainty of the known $\delta^{2}H$ values, while four of the five flasks overlap within uncertainty of the estimated atmosphere isotope value. The flasks tend to drift towards the value of the atmosphere, but retain the overall data pattern from the oxygen isotope values.

3.6.1.4 Lessons learned and recommendations from the QA/QC and field suitability tests:

The dry air test is a time-efficient method for identifying flasks that are leaky and will not preserve the sampled water vapor value, therefore we recommend these tests as a required step prior to field deployment of future SWISS units. For example, supplemental figure 4 shows that it is possible to drastically reduce the water vapor mole fraction in a flask filled with dry air between tests by tightening and/or replacing problematic fittings (both those attached to the glass flasks and those on the Valco valve) and in some cases the glass flask itself. This shows we can reduce the leakiness of the flasks. The dry air test is also an easy baseline test that also allowed us to test building materials. For example, in supplemental figure 5, we tested using PTFE Swagelok fittings with ⅛" PTFE tubing rather than stainless steel. These materials would be advantageous because they are much easier to install and are significantly lighter. We found that these fittings and tubing *may be* sufficient to store water for up to a single week, but on longer timescales (e.g. 27

days) we observed greater exchange and leaking than the stainless steel. We encourage any future user using this modification to rigorously test these fittings on a timescale appropriate for their application.

From the water vapor tests, we get a sense of the accuracy and precision of the SWISS. The calculated uncertainty of the flasks (0.9‰ and 3.7‰ for $\delta^{18}O$ and $\delta^{2}H$, respectively) is somewhat larger than the uncertainty associated just with the use of the water vapor probes (0.5‰ and 2.4 ‰ for $\delta^{18}O$ and $\delta^{2}H$, respectively, Oerter et al., 2016), but is sufficient for many critical zone applications, given the magnitude of seasonal variability that can be observed in natural systems (e.g. Oerter et al., 2017; Quade et al., 2019).

We opted to use a large flask volume because it allows us to measure a sample for long enough on a CRDS that we get reliable data, without interacting with vapor bound to the flask walls. The drawback of this, however, is that we must sample soil water vapor for a relatively long period of time (45 minutes). In supplemental figure 6, we show that the sampling regime, and particularly the length of time we pump dry air through the tubing, does not significantly alter the soil moisture content of the soil. Additionally, we demonstrate that the sampling regime we use does not introduce significant memory effects.

Based on the results of the long, field dry air test, we recommend that the water vapor storage time doesn't exceed 40 days for reliable results, or that the user undertake multiple dry air tests with lower concentration benchmarks if deployments may exceed 40 days.

Overall, the quality control and quality assurance as well as the field suitability tests demonstrate that the SWISS are able to faithfully retain the isotope value of water vapor collected using water vapor permeable probes. Like many other systems that measure dual isotopes, each system (i.e. $\delta^{18}O$ and $\delta^{2}H$) must be evaluated separately. In general, we interpret oxygen isotope data with a higher degree of confidence than the hydrogen isotope data. As the automation test revealed however, even when the absolute $\delta^{2}H$ value is not correct, the general pattern can reveal information about soil water dynamics. One particular challenge with the vapor permeable probes, that others have noted, is condensation in any portion of the system (e.g. Quade et al., 2019; Kühnhammer et al., 2019). As much as possible, it is helpful to have the impermeable tubing at warmer temperatures than the soil or water it is sampling. In many situations it may be worthwhile to warm the transfer tubing, but this should be done in a way that does not alter the thermal structure of the soil, and in remote settings, can operate safely independently. Additionally, taking care to ensure that the SWISS is evenly and lightly warmed in the lab setting helps to prevent condensation from forming in the stainless steel tubing and Valco valve.

3.6.2 Field Deployments

In Figure 7 we show the results of three field deployments completed during summer 2022 (Table 3). At the Oglala National Grassland site, we used the SWISS named Lindt to collect samples. During the August 2022 water vapor test on Lindt,

all of the oxygen isotope values fall within uncertainty of the system, and nine of the fifteen flasks fall within uncertainty of the system. Therefore, we interpret the $\delta^{18}O$ values with a higher amount of confidence and the $\delta^{2}H$ values with a lower amount of confidence (Figs. 3-4C and 3-5C). We note that most of the $\delta^{18}O$ and $\delta^{2}H$ values follow the same trends, and fall on the global meteoric water line (Figs. 3-7 and 3-8A). In general, soil water from 25 cm had higher $\delta^{18}O$ and $\delta^{2}H$ values than soil water from both 50 and 75 cm (Fig. 3-8A). Given that 4 of the 5 samples from 25 cm overlap with the GMWL and have a d-excess that overlaps within error of 10‰, the soil water from that depth may reflect summer precipitation with higher $\delta^{18}O$ and $\delta^{2}H$ values. Soil water from 75 cm had intermediate $\delta^{18}O$ and $\delta^{2}H$ values for most of the study period, and soil water from 50 cm depth had the lowest $\delta^{18}O$ and $\delta^{2}H$ values for most of the study period, which may reflect a more mean-annual or winter precipitation biased value. The d-excess value of soil water collected from 75 cm is centered around a global meteoric water line value of 10‰ (Fig. 3-8B). Based on data available from the National Weather Service (Chadron, NE), there were likely significant precipitation events on 2022-06-25 and 2022-07-08 at the field site. There is a significant shift to lower $\delta^{18}O$ values at a sampling depth of 25 cm between 2022-06-25 and 2022-06-29, as well as a marked increase in the d-excess value (Fig. 3-8A). We interpret this shift as infiltration of precipitation with lower $\delta^{18}O$ values, and is supported by a return of d-excess values to ~10‰ (Fig. 8A). The National Weather Service reported 0.84 inches of rain at Chadron Municipal Airport, approximately 50 km from the study site on 2022-07-08, which likely was

associated with at least some precipitation at our field site. Following the significant rain event on 2022-07-08, we observe a marked increase in the stable isotope value of water vapor from a sampling depth of 50 cm, towards values that are much closer to those at 25 cm depth. This indicates that after a large precipitation event, there is mixing and the creation of a far more uniform soil water isotope profile to a depth of 50 cm, but at the depth of 75 cm, the oxygen isotope data remain fairly uniform across the sampling period.

At Briggsdale, CO we used the SWISS named Raclette to collect soil water vapor samples. Data from 25 cm depth at Briggsdale, CO were discarded because the water vapor mole fraction was much lower than would be expected given the soil temperature (i.e. < 15,000 ppm). The gravimetric water concentration at that soil depth at the time of sampling was approximately 4% through the sampling period. Given the low water concentration, it is possible that there was simply not enough water vapor to sufficiently sample. Based on the results of the August 2022 water vapor test done on Raclette where all flasks fell within uncertainty of the SWISS system for both $\delta^{18}O$ and $\delta^{2}H$, except for flask 11 (Figs. 3-4C and 3-5C), which corresponds to the 25 cm depth sample from 2022-07-27, we interpret all of the data with a higher level of confidence. This sample was already removed from the dataset because of low water vapor mole fraction associated with the very dry soil. The soil water $\delta^{18}O$ and $\delta^{2}H$ values from a sampling depth of 50 cm and 75 cm overlap within uncertainty, but the soil water $\delta^{18}O$ and $\delta^{2}H$ values from 50 cm have a higher isotopic value than the samples from 75 cm. All of the data from within

each sampling depth group (i.e. 50 cm and 75 cm) overlap within uncertainty, conforming to the expectation that soil water from these sampling depths should be fairly invariant (e.g. Oerter et al., 2017). There were precipitation events at the study site on 2022-07-24, 2022-07-28 and 2022-07-31. It is possible that the slight negative shift in both $\delta^{18}O$ and $\delta^{2}H$ on 2022-08-01 reflects infiltration of precipitation to those depths, but this is not certain given that all of the measurements from within a sampling depth overlap within uncertainty.

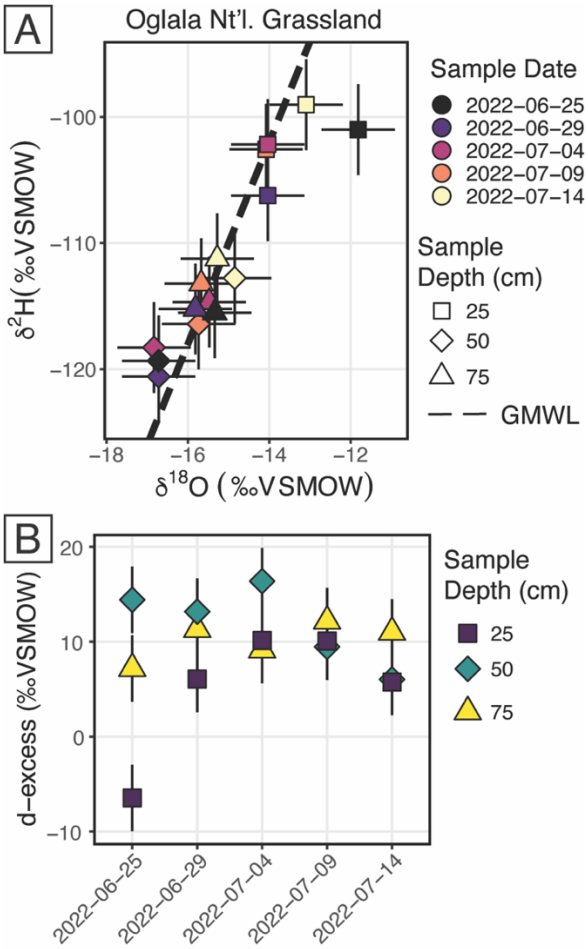

Figure 3-8. Results from the Oglala National Grassland, NE field site. A) $\delta^{2}H$ vs. $\delta^{18}O$, where the dashed line is the global meteoric water line. The shape of the depth sampled matches figure 7, and the color of the points is the date on which the soil water was sampled B) A plot of d-excess. Note, both the color and shape match figure 3-7.

At Seibert, CO we used the SWISS named Toblerone to collect soil water vapor samples. Data from 75 cm depth at Seibert, CO were discarded because of evidence of condensation during the measurement of the flasks associated with that sampling depth. Based on the results of the August 2022 water vapor test done on Toblerone, we interpret all of the data with a high degree of confidence, except for Flask 3, which is the 50 cm sample from 2022-06-19 (Figs. 3-4C and 3-5C). Unlike data from the other two field sites, soil water from 25 cm and 50 cm overlap within uncertainty. There were two precipitation events at the field site during the sampling period on 2022-06-25 and 2022-07-01, but both events were quite small (<0.02 inches, CoAgMet). There is no significant influence of the precipitation events on the $\delta^{18}O$ and $\delta^{2}H$ values. The >1.0‰ increase in $\delta^{18}O$ values on 2022-06-29 is surprising given that there is not a comparable magnitude increase in $\delta^{2}H$ value, and that the values measured from 2022-07-04 more closely match the $\delta^{18}O$ and $\delta^{2}H$ values from the two earlier sampling days. There are two potential explanations for this data. First, that is a real signal from an evaporation driven increase in the $\delta^{18}O$ value, and the reset to a lighter $\delta^{18}O$ value on 2022-07-04 is due to the infiltration of precipitation. This explanation is corroborated by a low d-excess value associated with this measurement (Supplemental Fig. 3-9). The second possible explanation is that the 25 cm sample from 2022-06-29 is influenced by condensation at the time of sampling. Dew point at the field site on 2022-06-29 significantly decreased as compared to the other sampling days to a monthly minimum of 20.6°C. It is possible that environmental conditions encouraged the formation of condensation in the

impermeable tubing at the time of sampling. There were no obvious signs of condensation during the time of measurement in the lab. These results highlight the utility of having broad contextual environmental data to aid in the interpretation of soil water isotope data.

All together, these three soil water isotope datasets demonstrate two main findings. First, data from these samples show that the differences between field sites is easily resolvable using the SWISS. For example, at 50 cm depth the oxygen isotopes range between -14.4 to -16.3‰, -9.9 to -10.3‰, and -7.4 to -9.3‰ for the Oglala, Briggsdale and Seibert sites, respectively. These differences likely reflect differences in the stable isotope composition of precipitation and evaporation dynamics. Second, the sample data retrieved from a SWISS are sufficiently precise to be able to meaningfully resolve vertical profile soil water isotope data. For example, at the Oglala National Grassland field site, soil water from 25 cm clearly has higher $\delta^{18}O$ and $\delta^{2}H$ values as compared to soil water from a depth of 50 and 75 cm.

3.6.3 Future improvements

One significant SWISS unit hardware improvement that could be made would be to install a heating implement to the flasks. One source of uncertainty on the current system is the potential effect of uneven heating of the flasks prior to measurement. This could be improved in subsequent iterations of the SWISS with the addition of heat tape or blankets that can deliver controlled and consistent

amounts of heat. This improvement could also help limit the amount of manual intervention needed during measurement, and could improve automation of flask measurement.

In addition, we have made a few improvements to the automation system that were not implemented for the data presented in this contribution, but will be part of future deployments. First, we will track conditions inside the SWISS with a temperature and relative humidity sensor inside the case. Second, we plan to eliminate the power inverter by powering both the Valco valve and mass flow controller with VDC using a power step up controller. Lastly, we will add an IoT cellular router to be able to remotely monitor and control the SWISS units.

Finally, there are two future considerations for field deployments. The first is finding a way to safely and automatically heat the impermeable tubing that connects the water vapor probes and the SWISS in a way that doesn't change the inherent thermal structure of the soil, and is safe for unmonitored use. Additionally, we plan to test SWISS unit resilience during air travel so that these units can be used at field sites that are not within driving distance of a research facility.

3.7 Conclusions

We presented the evolution of the soil water isotope storage system (SWISS) from a prototype to a fully built out and tested system. We also presented a quality control and quality assurance procedure that can be used to ensure the reliable storage of soil water vapor over long time periods (up to 40 days). In addition, these

quality control and quality assurance tests shed light on the accuracy and precision of the SWISS. After applying an offset correction, we determine the overall precision of the SWISS to be 0.9‰ and 3.7‰ for $\delta^{18}O$ and $\delta^{2}H$, respectively. In a field setting, flasks reliably resist atmospheric intrusion. Additionally, the proposed sampling schema does not introduce significant memory effects. Lastly, we demonstrate that the precision of the SWISS still allows us to distinguish between field sites and between soil water dynamics within a single soil column. Taken as a whole, these data show that the SWISS can be used as a tool to answer many emerging ecohydrological questions, and will enhance researchers' ability to collect soil water isotope datasets from more remote and traditionally understudied field sites.

Acknowledgements

We thank the numerous field assistants who helped to make the field work presented in this paper possible, including Spencer Burns, Anne Fetrow, Sarah Brookins, Juliana Olsen-Valdez, and Haley Brumberger. We acknowledge that both field work and laboratory work for this study was done on the traditional territories and ancestral homelands of the Arapahoe, Ute and Cheyenne peoples. This work was supported by startup funding from CU Boulder and NSF funding from grant EAR-2023385 awarded to K. Snell. Additionally, this work was supported by the University of Colorado Boulder Beverly Sears Research Grant and the Clay Minerals Society Graduate Student Research Grant both awarded to R. Havranek. CUBES–SIL is a CU Boulder Core Facility associated with RRID: SCR_019300.

Works Cited

Beyer, M., Kühnhammer, K., & Dubbert, M. (2020). In situ measurements of soil and plant water isotopes : a review of approaches , practical considerations and a vision for the future. *Hydrology and Earth System Sciences*, *24*, 4413–4440. https://doi.org/https://doi.org/10.5194/hess-24-4413-2020

Bowen, G. J., Cai, Z., Fiorella, R. P., & Putman, A. L. (2019). Isotopes in the Water Cycle: Regional- to Global-Scale Patterns and Applications. *Annual Review of Earth and Planetary Sciences*, *47*(1), 453–479. https://doi.org/10.1146/annurev-earth-053018-060220

Bowen, G. J., Putman, A., Brooks, J. R., Bowling, D. R., Oerter, E. J., & Good, S. P. (2018). Inferring the source of evaporated waters using stable H and O isotopes. *Oecologia*, *187*(4), 1025–1039. https://doi.org/10.1007/s00442-018-4192-5

Brooks, J. R., Barnard, H. R., Coulombe, R., & McDonnell, J. J. (2010). Ecohydrologic separation of water between trees and streams in a Mediterranean climate. *Nature Geoscience*, *3*(2), 100–104. https://doi.org/10.1038/ngeo722

CoAgMet, Colorado Climate Center, 2023, Colorado State Univerisity, Fort Collins, Colorado. https://climate.colostate.edu/. Accessed 03/31/2023.

Dawson, T. E., & Ehleringer, J. R. (1991). Streamside trees that do not use stream-water: evidence from hydrogen isotopes ratios. *Nature*, *350*(March), 335–337.

Gaj, M., Beyer, M., Koeniger, P., Wanke, H., Hamutoko, J., & Himmelsbach, T. (2015). In-situ unsaturated zone stable water isotope (2H and 18O)

measurements in semi-arid environments using tunable off-axis integrated cavity output spectroscopy. *Hydrology and Earth System Sciences Discussions*, *12*(6), 6115–6149. https://doi.org/10.5194/hessd-12-6115-2015

Gómez-Navarro, C., Pataki, D. E., Bowen, G. J., & Oerter, E. J. (2019). Spatiotemporal variability in water sources of urban soils and trees in the semiarid, irrigated Salt Lake Valley. *Ecohydrology*, *12*(8). https://doi.org/10.1002/eco.2154

Good, S. P., Noone, D., & Bowen, G. J. (2015). Hydrologic connectivity constrains partitioning of global terrestrial water fluxes. *Science*, *349*(6244), 175–177. https://doi.org/10.1126/science.aaa5931

Green, M. B., Laursen, B. K., Campbell, J. L., Mcguire, K. J., & Kelsey, E. P. (2015). Stable water isotopes suggest sub-canopy water recycling in a northern forested catchment. *Hydrological Processes*, *29*(25), 5193–5202. https://doi.org/10.1002/hyp.10706

Groh, J., Stumpp, C., Lücke, A., Pütz, T., Vanderborght, J. and Vereecken, H., (2018), Inverse estimation of soil hydraulic and transport parameters of layered soils from water stable isotope and lysimeter data. *Vadose Zone Journal*, *17*(1), pp.1-19.

Harms Sarah M, & Ludwig, T. K. (2016). Retention and removal of nitrogen and phosphorus in saturated soils of arctic hillslopes. *Biogeochemistry*, *127*, 291–304. https://doi.org/10.1007/s10533-016-0181-0

Havranek, R. E., Snell, K. E., Davidheiser-Kroll, B., Bowen, G. J., & Vaughn, B. (2020). The Soil Water Isotope Storage System (SWISS): An integrated soil water vapor sampling and multiport storage system for stable isotope geochemistry. *Rapid Communications in Mass Spectrometry*, *34*(12), 1–11. https://doi.org/10.1002/rcm.8783

Hinckley, E.-L. S., Barnes, R. T., Anderson, S. P., Williams, M. W., & Bernasconi, S. M. (2014). Nitrogen retention and transport differ by hillslope aspect at the rain-snow transition of the Colorado Front Range. *Journal of Geophysical Research: Biogeosciences*, *119*, 12811896. https://doi.org/10.1002/2013JG002588

Kübert, A., Paulus, S., Dahlmann, A., Werner, C., Rothfuss, Y., Orlkowski, N., & Dubbertm Maren. (2020). Water Stable Isotopes in Ecohydrological Field Research : Comparison Between In Situ and Destructive Monitoring Methods to Determine Soil Water Isotopic Signatures. *Frontiers in Plant Science*, *11*(April), 1–13. https://doi.org/10.3389/fpls.2020.00387

Kühnhammer, K., Dahlmann, A., Iraheta, A., Gerchow, M., Birkel, C., Marshall, J. D., & Beyer, M. (2022). Continuous in situ measurements of water stable isotopes in soils, tree trunk and root xylem: Field approval. *Rapid Communications in Mass Spectrometry*, *36*(5). https://doi.org/10.1002/rcm.9232

Mahindawansha, A., Orlowski, N., Kraft, P., Rothfuss, Y., Racela, H., & Breuer, L. (2018). Quantification of plant water uptake by water stable isotopes in rice paddy systems. *Plant and Soil*, *429*(1–2), 281–302. https://doi.org/10.1007/s11104-018-3693-7

Oerter, E. J., Perelet, A., Pardyjak, E., & Bowen, G. J. (2016). Membrane inlet laser spectroscopy to measure H and O stable isotope compositions of soil and sediment pore water with high sample throughput. *Rapid Communications in Mass Spectrometry*, *31*(1), 75–84. https://doi.org/10.1002/rcm.7768

Oerter, E. J., & Bowen, G. J. (2017). In situ monitoring of H and O stable isotopes in soil water reveals ecohydrologic dynamics in managed soil systems. *Ecohydrology*, *10*(4), 1–13. https://doi.org/10.1002/eco.1841

Oerter, E. J., & Bowen, G. J. (2019). Spatio-temporal heterogeneity in soil water stable isotopic composition and its ecohydrologic implications in semiarid ecosystems. *Hydrological Processes*, *March*, 1–15. https://doi.org/10.1002/hyp.13434

Peterson, B. J., & Fry, B. (1987). Stable Isotopes in Ecosystem Studies. *Annual Reviews of Ecology and Systematics*, *18*, 293–320. http://www.jstor.org/stable/2097134 REFERENC

Quade, M., Klosterhalfen, A., Graf, A., Brüggemann, N., Hermes, N., Vereecken, H., & Rothfuss, Y. (2019). In-situ monitoring of soil water isotopic composition for partitioning of evapotranspiration during one growing season of sugar beet (Beta vulgaris). *Agricultural and Forest Meteorology*, *266–267*(December 2018), 53–64. https://doi.org/10.1016/j.agrformet.2018.12.002

Quade, M., Brüggemann, N., Graf, A., Vanderborght, J., Vereecken, H., & Rothfuss, Y. (2018). Investigation of Kinetic Isotopic Fractionation of Water during Bare

Soil Evaporation. *Water Resources Research*, *54*(9), 6909–6928. https://doi.org/10.1029/2018WR023159

Rothfuss, Y., Vereecken, H., & Brüggemann, N. (2013). Monitoring water stable isotopic composition in soils using gas-permeable tubing and infrared laser absorption spectroscopy. *Water Resources Research*. https://doi.org/10.1002/wrcr.20311

Rothfuss, Y., Merz, S., Vanderborght, J., Hermes, N., Weuthen, A., Pohlmeier, A., Vereecken, H., & Brüggemann, N. (2015). Long-term and high-frequency non-destructive monitoring of water stable isotope profiles in an evaporating soil column. *Hydrology and Earth System Sciences*, *19*(10), 4067–4080. https://doi.org/10.5194/hess-19-4067-2015

Rothfuss, Y., Quade, M., Brüggemann, N., Graf, A., Vereecken, H., & Dubbert, M. (2021). Reviews and syntheses: Gaining insights into evapotranspiration partitioning with novel isotopic monitoring methods. In *Biogeosciences* (Vol. 18, Issue 12, pp. 3701–3732). Copernicus GmbH. https://doi.org/10.5194/bg-18-3701-2021

Rozmiarek, K. S., Vaughn, B. H., Jones, T. R., Morris, V., Skorski, W. B., Hughes, A. G., Elston, J., Wahl, S., Faber, A. K., & Steen-Larsen, H. C. (2021). An unmanned aerial vehicle sampling platform for atmospheric water vapor isotopes in polar environments. *Atmospheric Measurement Techniques*, *14*(11), 7045–7067. https://doi.org/10.5194/amt-14-7045-2021

Soderberg, K., Good, S. P., Wang, L., & Caylor, K. (2012). Stable Isotopes of Water Vapor in the Vadose Zone: A Review of Measurement and Modeling Techniques. *Vadose Zone Journal*, *11*(3), 0. https://doi.org/10.2136/vzj2011.0165

Soil Survey Staff, Natural Resources Conservation Service, United States Department of Agriculture. Soil Series Classification Database. Available online. Accessed 09/10/2022.

Sprenger, M., Herbstritt, B. and Weiler, M., (2015(. Established methods and new opportunities for pore water stable isotope analysis. *Hydrological Processes*, *29*(25), pp.5174-5192.

Sprenger, M., Leistert, H., Gimbei, G., & Weiler, M. (2016). Illuminating hydrological processes at the soil-vegetation-atmosphere interface with water stable isotopes. *Reviews in Geophysics*, *54*, 674–704. https://doi.org/10.1002/2015RG000515

Sprenger, M., & Allen, S. T. (2020). What Ecohydrologic Separation Is and Where We Can Go With It (2020). In *Water Resources Research* (Vol. 56, Issue 7). Blackwell Publishing Ltd. https://doi.org/10.1029/2020WR027238

Stumpp, C., Stichler, W., Kandolf, M. and Šimůnek, J., (2012). Effects of land cover and fertilization method on water flow and solute transport in five lysimeters: A long-term study using stable water isotopes. *Vadose Zone Journal*, *11*(1).

Theis, D. E., Saurer, M., Blum, H., Frossard, E., & Siegwolf, R. T. W. (2004). A portable automated system for trace gas sampling in the field and stable isotope

analysis in the laboratory. *Rapid Communications in Mass Spectrometry*, *18*(18), 2106–2112. https://doi.org/10.1002/rcm.1596

Vereecken, H., Amelung, W., Bauke, S. L., Bogena, H., Brüggemann, N., Montzka, C., Vanderborght, J., Bechtold, M., Blöschl, G., Carminati, A., Javaux, M., Konings, A. G., Kusche, J., Neuweiler, I., Or, D., Steele-Dunne, S., Verhoef, A., Young, M., & Zhang, Y. (2022). Soil hydrology in the Earth system. *Nature Reviews Earth & Environment*. https://doi.org/10.1038/s43017-022-00324-6

Volkmann, T. H. M., & Weiler, M. (2014). Continual in situ monitoring of pore water stable isotopes in the subsurface. *Hydrology and Earth System Sciences*, *18*(5), 1819–1833. https://doi.org/10.5194/hess-18-1819-2014

Wassenaar, L. I., Hendry, M. J., Chostner, V. L., & Lis, G. P. (2008). High resolution pore water δ2H and δ18O measurements by H2O(liquid)-H2O (vapor) equilibration laser spectroscopy. *Environmental Science and Technology*, *42*(24), 9262–9267. https://doi.org/10.1021/es802065s

Zhao, P., Tang, X., Zhao, P., Wang, C. and Tang, J., 2013. Identifying the water source for subsurface flow with deuterium and oxygen-18 isotopes of soil water collected from tension lysimeters and cores. *Journal of Hydrology*, *503*, pp.1-10

Zimmermann, U., Munnich, K. O., & Roether, W. (1966). Tracers Determine Movement of Soil Moisture and Evapotranspiration. *Science*, *152*(3720), 346–347. https://doi.org/10.1126/science.152.3720.346

Supplemental Information

Automation components and wiring

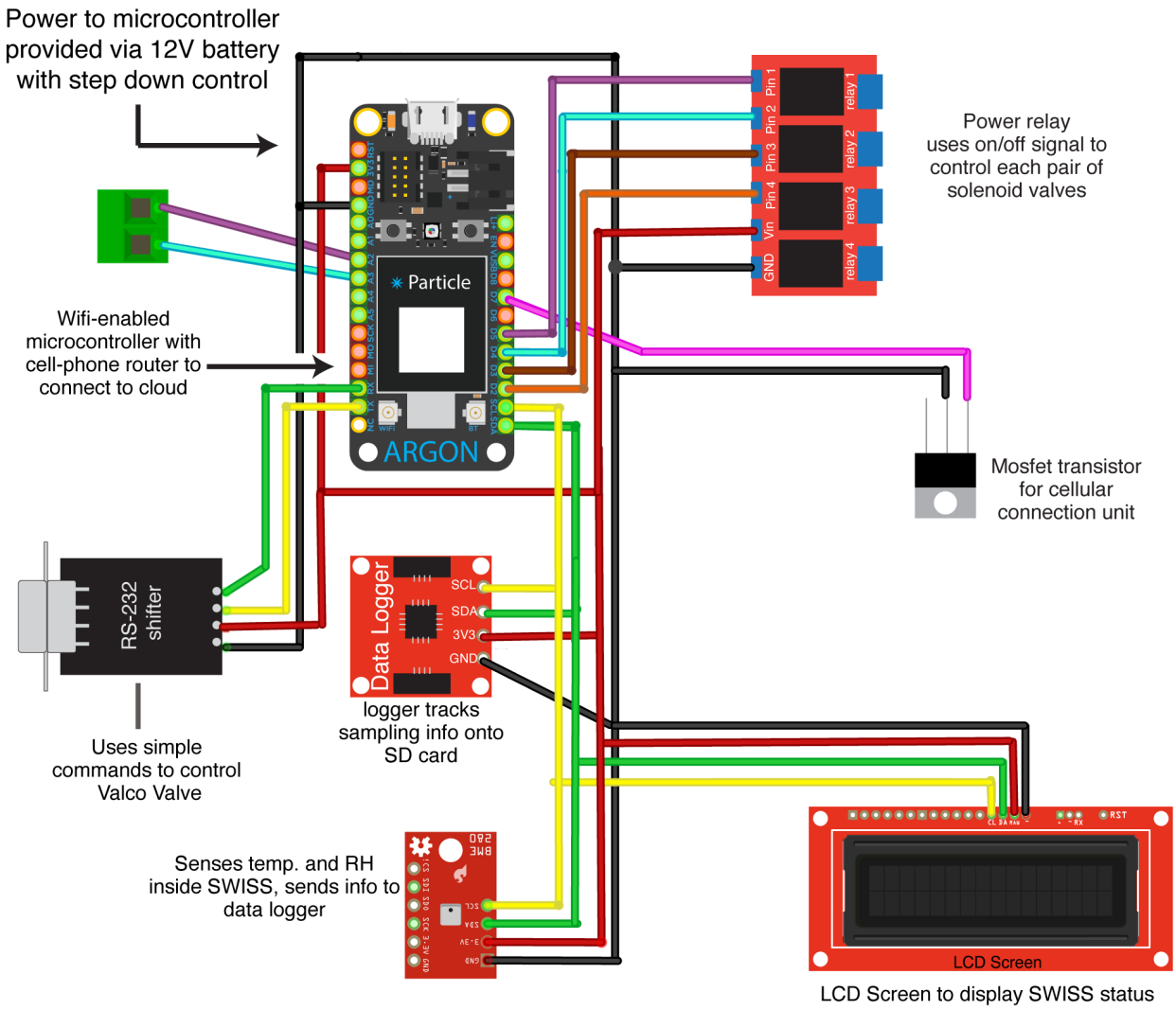

Supplemental Figure 3-1. Wiring diagram for the components used to automate the SWISS. All of the components can be optimized for each user's needs.

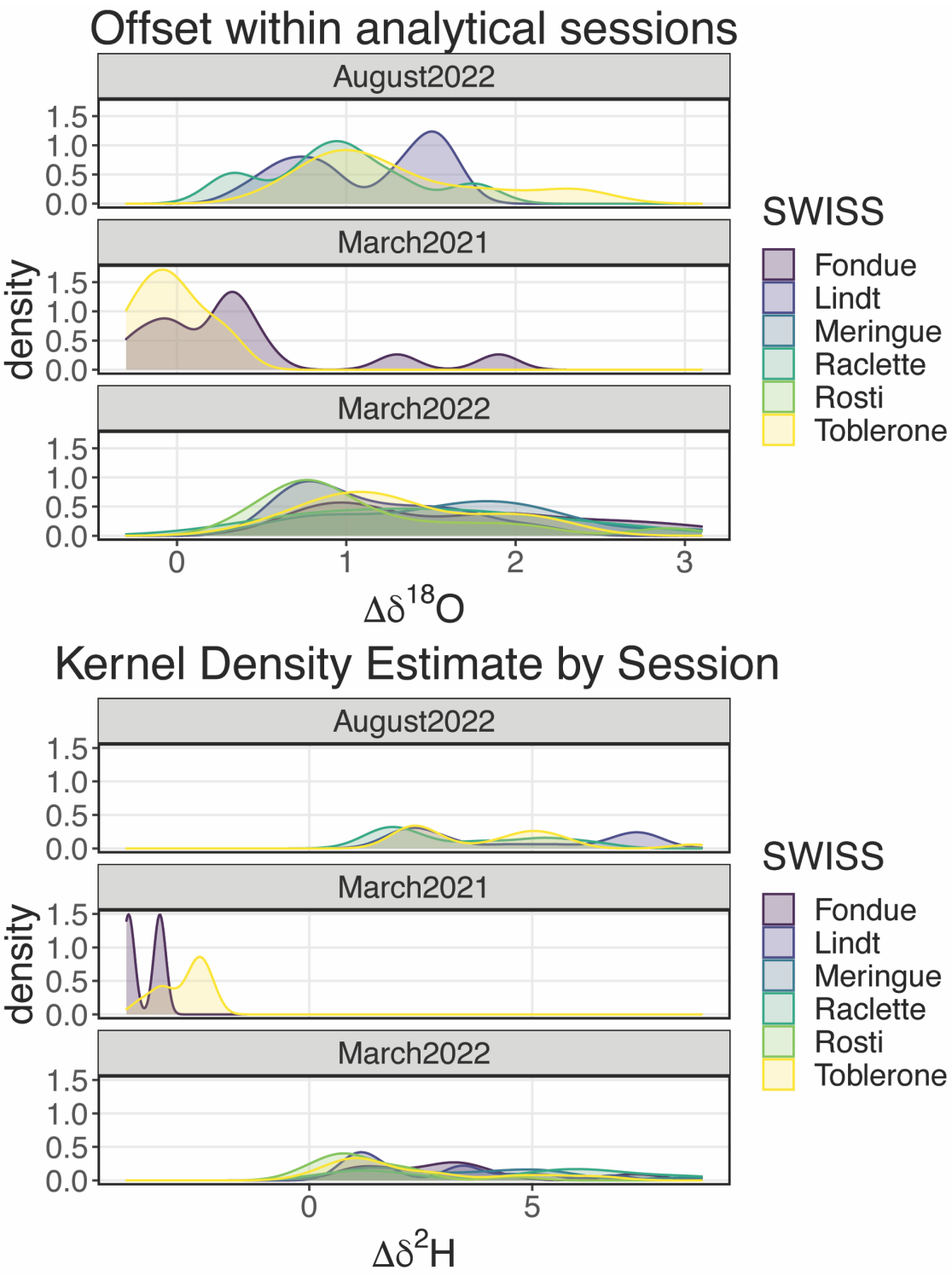

Supplemental Figure 3-2. Kernel density estimate of the difference between the starting and final δ18O and δ2H values, separated by analytical session.

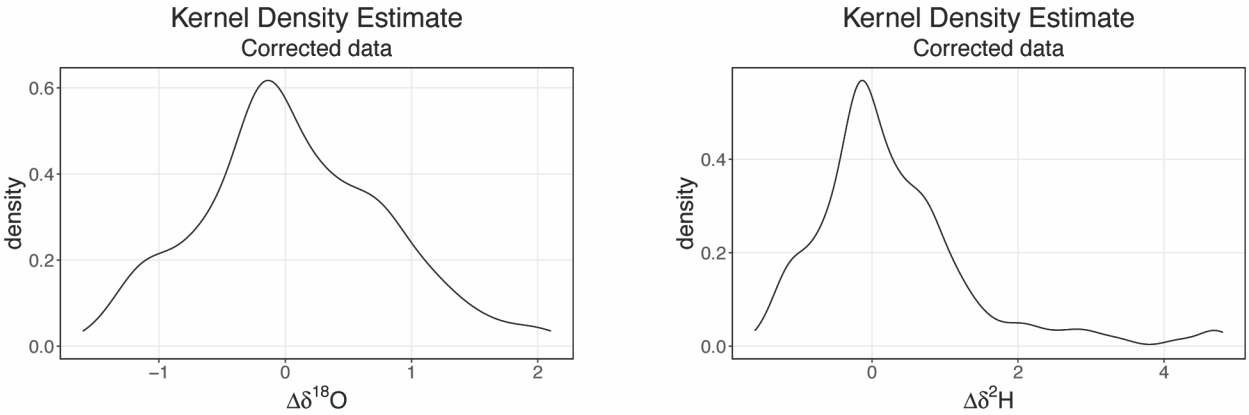

Supplemental Figure 3-3. Kernel density estimate of the difference between the starting and final δ18O and δ2H values after the offset correction is applied to each dataset.

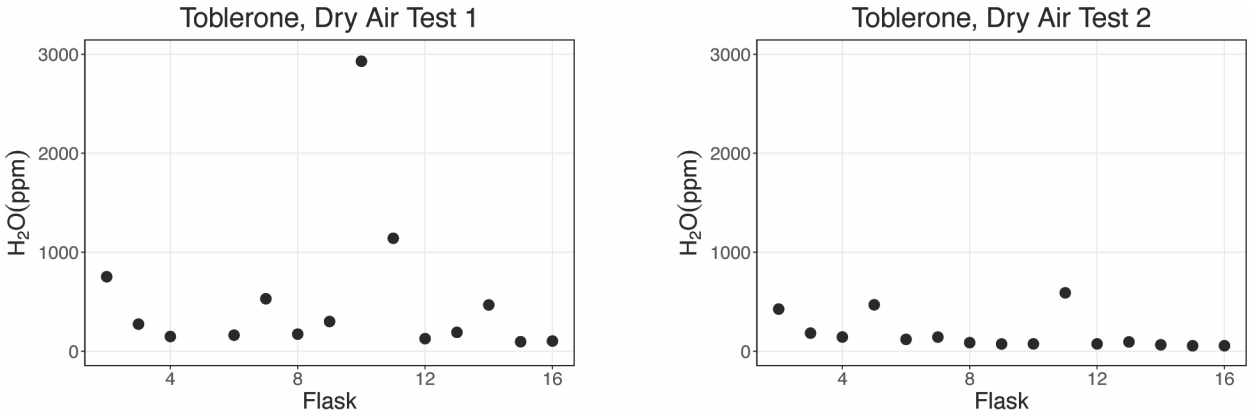

Supplemental figure 3-4. The results of two successive dry air tests where we show that tightening of the fittings can significantly improve a flask's resistance to leaking. The dry air test is a time efficient test to find and fix problematic flasks.

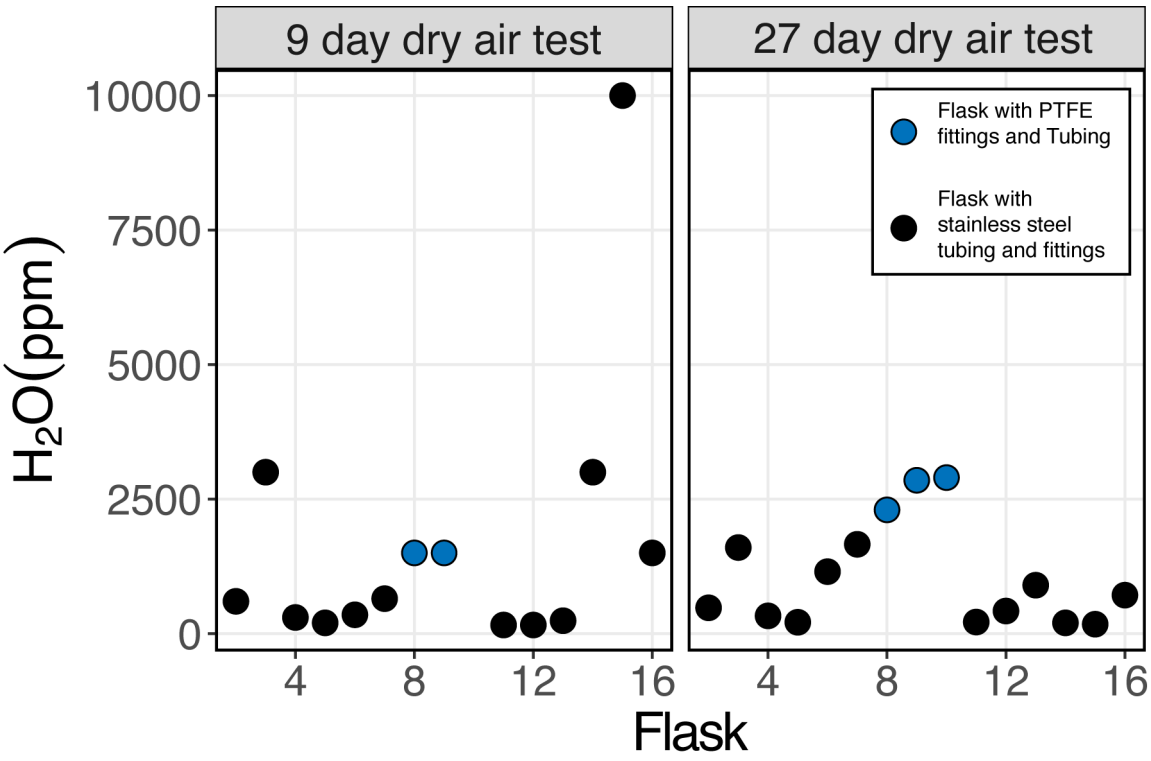

Supplemental Figure 5
Havranek et al.,

Supplemental Figure 3-5. The results of a seven day and 27 day dry air test. Flasks 8, 9, and 10 were all fitted with Swagelok PTFE unions and ⅛" PTFE tubing. On a seven-day timescale, the PTFE fittings performed similarly to the stainless steel tubing, but over 27 days, the PTFE fittings performed worse than the other fittings.

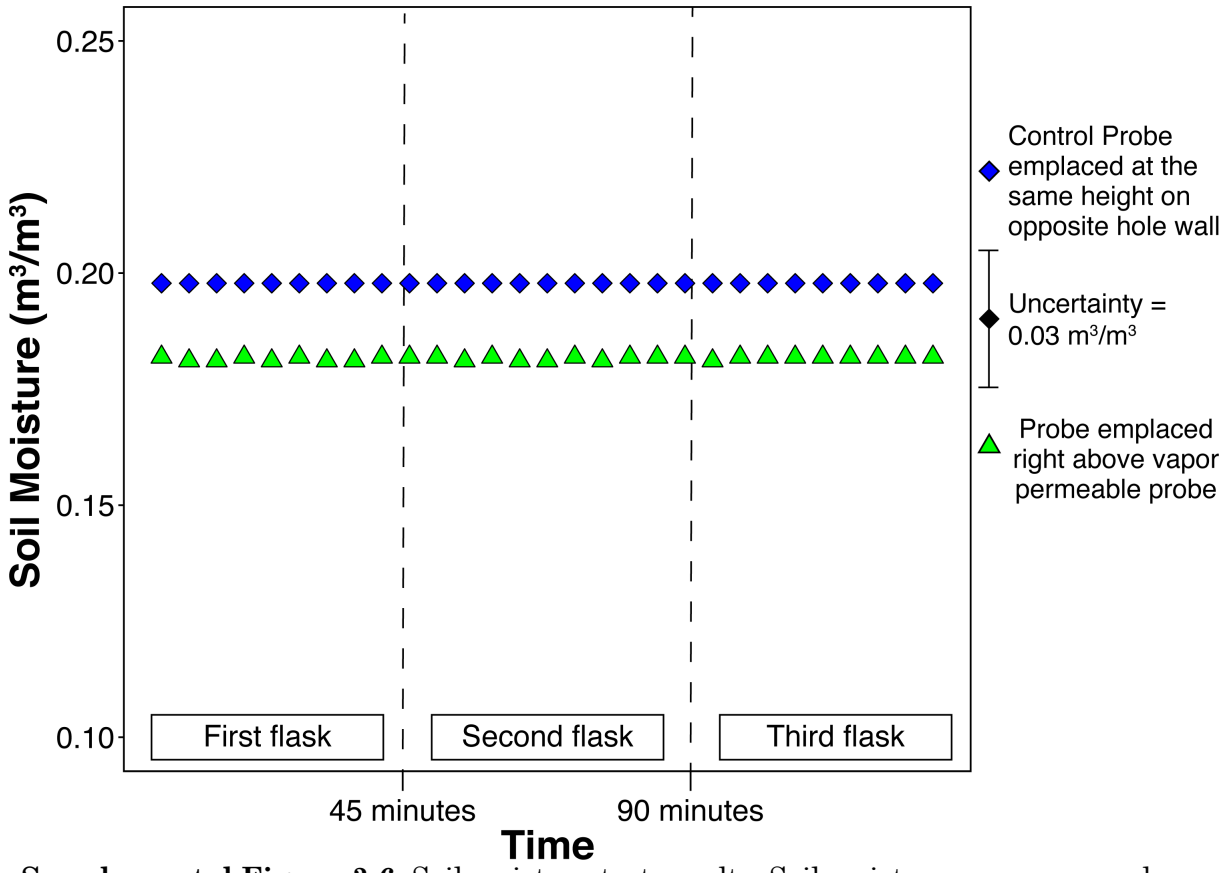

Supplemental Figure 3-6. Soil moisture test results. Soil moisture was measured every 5 minutes during three consecutive sample collection phases to fill flasks with water vapor. Green triangles indicate the soil moisture measured directly above (< 2 cm away) the vapor permeable membrane probe, blue diamonds represent soil moisture measured at the same height on the opposite wall of the hole. Uncertainty, based on manufacturer specifications, on all measurements is 0.03 m3/m3.

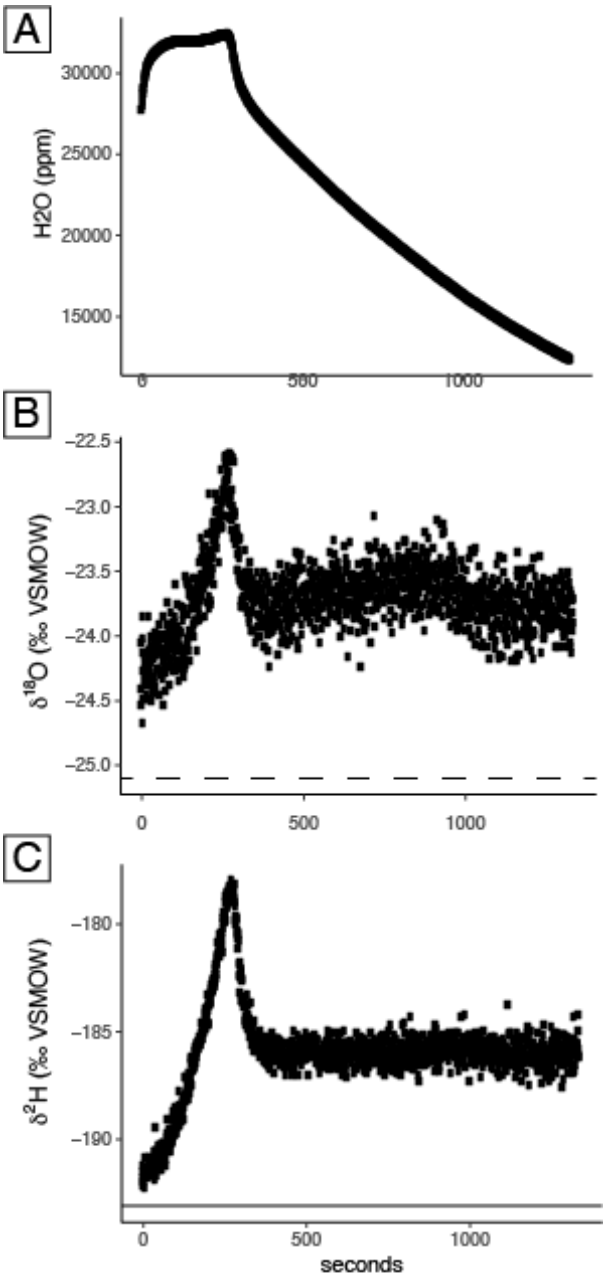

Supplemental Figure 3-7. A) Plot of water concentration vs. time during the measurement of a flask where there is condensation in the stainless steel tubing between the flask and valco valve. B) and C) are plots δ18O and δ2H, respectively through the same measurement period.

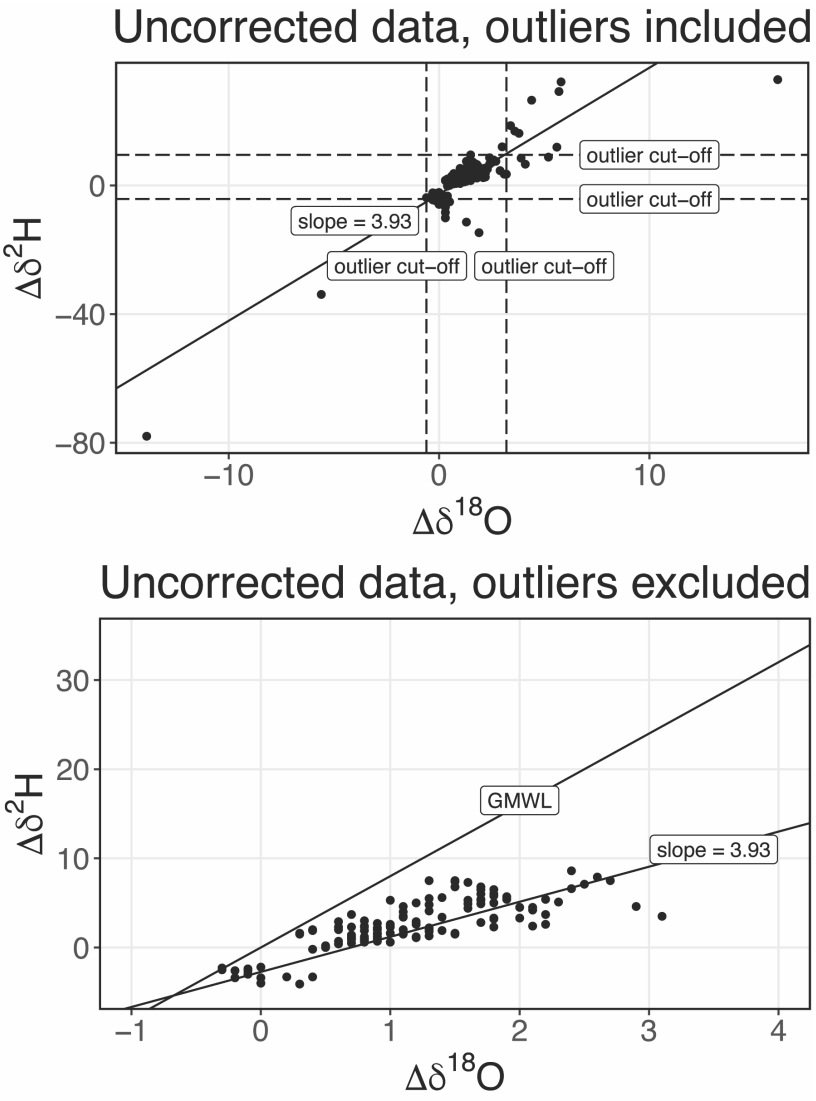

Supplemental Figure 3-8. The difference between the start and end of the water vapor isotopes during the water vapor tests. The top plot includes all data, and the outlier cutoffs are marked with dashed lines. The line is a calculated linear regression across all of the data. The bottom plot excludes outliers, and also includes the global meteoric water line as a reference slope.

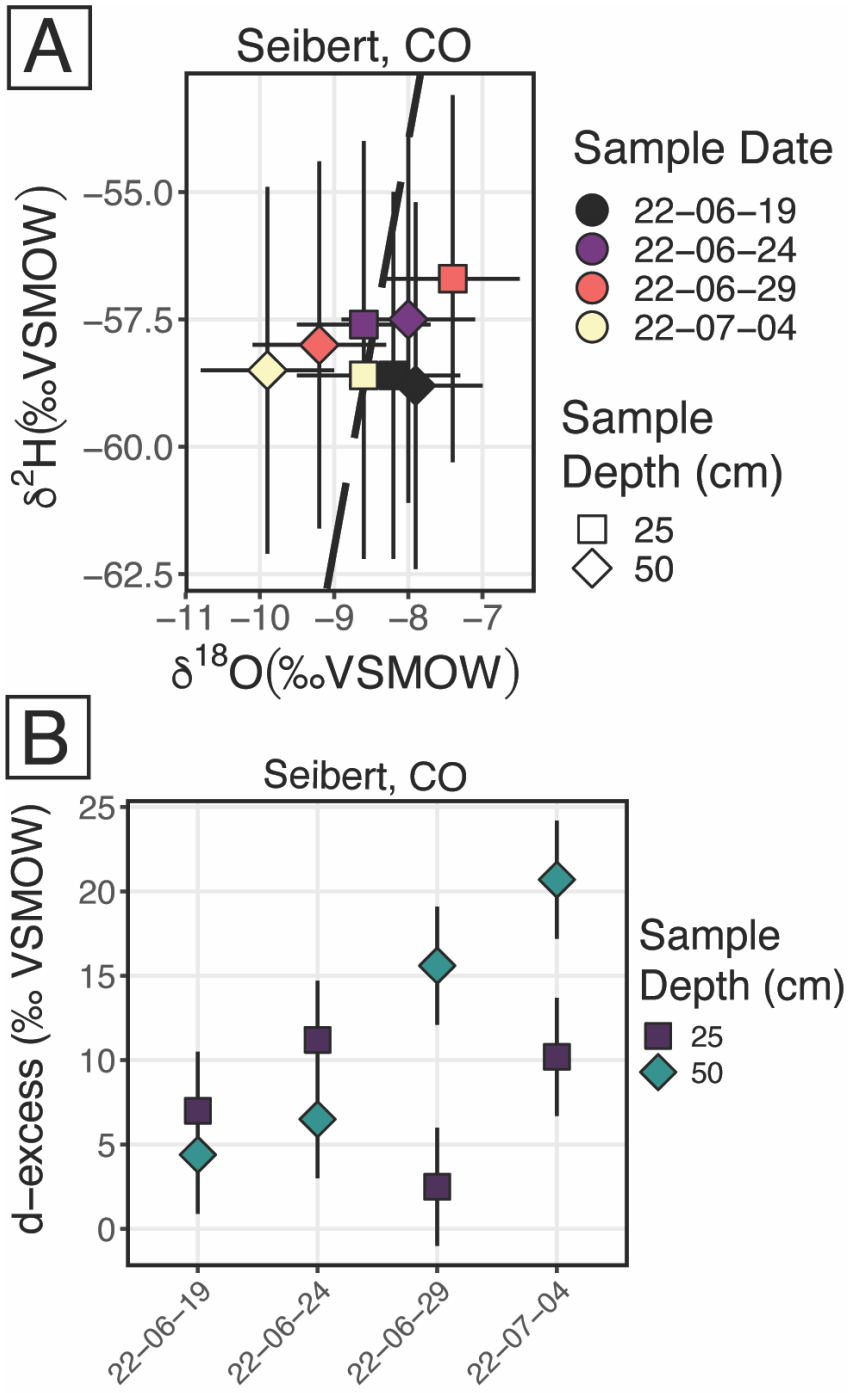

Supplemental Figure 3-9. A) δ^2H vs. $\delta^{18}O$ for data from Seibert, CO. B) D-excess through time from Seibert, CO.

Supplemental Table 1: A list of parts required to build a SWISS and sample a soil.

SWISS Hardware				
Item	**Source and/or Distributor**	**Approximate Cost (USD) *prices as of 2020, and may vary***	**Location**	**Potential Adaptions**
650 ml Flasks	Precision Glass Blowing Inc.,	$110/Flask, total = $1870	Englewood, Colorado, USA	Cost is for 17 flasks, assuming 1 is broken during building + 1 backup during deployments. Flask size and dimensions can be adapted (especially if there are weight concerns)
Valco Multiselector Valve with RS-232 communication	Valco Instruments Co. Inc.,	$2100/valve	Houston, Texas, USA	Number of selectable ports ranges from 2 - 16; communication style (e.g. RS-232) can be done in multiple ways
1/8th inch stainless steel tubing	Swagelok	$180, ~100 feet	Ohio, USA	
1/4" - 1/8" union fittings	Swagelok	$17/fitting, total = $544	Ohio, USA	32 fittings / SWISS
1/4" - 1/4" union fittings	Swagelok	$13/fitting, total = $26	Ohio, USA	
1/4" PTFE Fittings	Ohio Valley Specialty Co.	17/10 ferrules, total = $85	Marietta, Ohio, USA	50 ferrules
Waterproof, insulated case (61 cm x 61 cm x 61 cm with Pick n' Pluck foam)	Pelican Products Inc.	$550	Torrance, CA, USA	Case size and internal configuration
1/4" push to fit bulkhead fittings	McMaster Carr	$5/fitting, $30 total		
Mass Flow Controller	200 SCCM Flow Controller	$1400/controller, $2800 total	Alicat Scientific	Tuscon, Arizona, USA

Vapor Probes				
Item	Part Number		Soure and/or Distributor	Loacation
Vapor Permeable Tubing	ACCURELL PP V8/2HF		3M	Germany
Vapor impermeable tubing	Bev-A-Line® IV Transfer Pump Tubing	$35	Cole-Parmer	Vernon Hills, Illinois, USA
Soil temperature logger	HOBO MX2201	$69/logger	Onset Computer Corporation	Bourne, Massachusets, USA

Soil moisture Logger	S-SMD-M005	$190/probe	Onset Computer Corporation	Bourne, Massachusets, USA
Logging microstation for soil moisture	H21-USB	$260	Onset Computer Corporation	Bourne, Massachusets, USA

	Remote Power			
12V Deep Cycle Battery	ECO-WORTHY 12V Lithium Battery, 30Ah Rechargeable LiFePO4 Lithium Ion Phosphate Deep Cycle Battery	$179		
12 V, 100 Watt Solar Panel	Renogy 100W 12V Monocrystalline Solar Starter Kit w/Wanderer 30A Charge Controller	$87		
DC to AC Power Inverter	Renogy 1000 W 12V Pure Sine Wave Inverter	$210		

Table SI 2: A list of example parts that can be used to replicate our automation system

Item	Part (where applicable)	Source and/or Distributor	Approximate Cost (USD)	Location	Notes and Potential Adaptions
Microcontroller	Photon Wifi Development Board	Particle Industries Inc.	$28	San Francisco, California, USA	Many microcontrollers are commercially available, and all have their strengths and weaknesses
Normally Closed 2 port Solenoid Valves with 1/4" push to fit fittings	VVX214BO4B, VX2A0AZ1EH, KQ2H07-36NS, KQ2H07-35NS	SMC Corporation of America	$800		Voltage, push to fit fitting size, number of ports available (aka # of sampling depths)
VDC Power relay			$11		Should be able to step either 3.3 V or 5V up to 12 V, widely available product
VAC Power Relay	IoT Power Relay II	Digital Loggers	$30	Santa Clara, California, USA	This can be bypassed if the mass flow controller and Valco valve can be directly powered by direct current
RS-232 Shifter			$11		Widely available product made by multiple manufacturers
Coin Cell Battery holder	Lilypad Coincell Battery holder	Sparkfun	$2	Boulder, Colorado, USA	
Data Logger	Sparkfun QWICC OpenLog	Sparkfun	$19	Boulder, Colorado, USA	

Table SI 3: Results of the dry air tests

SWISS	Days	H2O (ppm)	H2O Standard Dev. (ppm)	SWISS	Days	H2O (ppm)	H2O Standard Dev. (ppm)
Lindt	7	680	43	Fondue	43 Days	695	61
Lindt	7	371	9	Fondue	43 Days	1051	7
Lindt	7	351	7	Fondue	43 Days	262	22
Lindt	7	291	7	Fondue	43 Days	255	15
Lindt	7	278	9	Fondue	43 Days	222	12
Lindt	7	364	13	Fondue	43 Days	291	6
Lindt	7	288	7	Fondue	43 Days	248	9
Lindt	7	292	9	Fondue	43 Days	207	2
Lindt	7	277	8	Fondue	43 Days	408	25
Lindt	7	309	5	Fondue	43 Days	231	10
Lindt	7	464	20	Fondue	43 Days	383	18
Lindt	7	363	6	Fondue	43 Days	1084	14
Lindt	7	376	10	Rosti	34 Days	650	
Lindt	7	460	10	Rosti	34 Days	290	
Lindt	7	351	11	Rosti	34 Days	272	
Raclette	7	534		Rosti	34 Days	260	
Raclette	7	352		Rosti	34 Days	290	
Raclette	7	310		Rosti	34 Days	1600	
Raclette	7	371		Rosti	34 Days	810	
Raclette	7	310		Rosti	34 Days	800	
Raclette	7	305		Rosti	34 Days	290	
Raclette	7	374		Rosti	34 Days	270	
Raclette	7	292		Rosti	34 Days	365	
Raclette	7	321		Rosti	34 Days	355	
Raclette	7	523		Rosti	34 Days	320	
Raclette	7	428		Rosti	34 Days	515	
Raclette	7	267		Rosti	34 Days	420	
Raclette	7	265		Toblerone	52 Days	2123	57
Raclette	7	269		Toblerone	52 Days	2535	422
Raclette	7	261		Toblerone	52 Days	1728	452
Toblerone	7	546	10	Toblerone	52 Days	554	13
Toblerone	7	336	2	Toblerone	52 Days	1981	438
Toblerone	7	311	7	Toblerone	52 Days	500	75
Toblerone	7	275	6	Toblerone	52 Days	2207	460
Toblerone	7	258	9	Toblerone	52 Days	1189	401
Toblerone	7	259	6	Toblerone	52 Days	1212	413
Toblerone	7	248	9	Toblerone	52 Days	1509	458
Toblerone	7	211	5	Toblerone	52 Days	483	17
Toblerone	7	207	6	Toblerone	52 Days	623	11
Toblerone	7	225	7	Toblerone	52 Days	410	8
Toblerone	7	190	7	Toblerone	52 Days	328	7
Toblerone	7	225	7	Toblerone	52 Days	423	9
Toblerone	7	181	5				
Toblerone	7	173	6				
Toblerone	7	171	7				

Table SI4: Results of the water vapor tests

SWISS	Days	Session	Δ $\delta^{18}O$ (‰)	Δ $\delta^{2}H$ (‰)
Lindt	14	Aug-22	0.6	1.8
Lindt	14	Aug-22	0.5	6.9
Lindt	14	Aug-22	-0.4	0.3
Lindt	14	Aug-22	0.5	4.8
Lindt	14	Aug-22	0.6	4.7
Lindt	14	Aug-22	-0.1	-0.4
Lindt	14	Aug-22	-0.3	-0.3
Lindt	14	Aug-22	-0.1	-0.4
Lindt	14	Aug-22	-0.6	-0.6
Lindt	14	Aug-22	0.5	4.9
Lindt	14	Aug-22	0.5	4.2
Lindt	14	Aug-22	-0.4	-0.3
Lindt	14	Aug-22	-0.2	0.4
Lindt	14	Aug-22	0.3	2.9
Lindt	14	Aug-22	0.3	4.9
Raclette	14	Aug-22	0.7	3.4
Raclette	14	Aug-22	0.0	2.7
Raclette	14	Aug-22	0.0	2.7
Raclette	14	Aug-22	0.0	-1.0
Raclette	14	Aug-22	0.3	-0.6
Raclette	14	Aug-22	-0.2	-0.3
Raclette	14	Aug-22	0.1	1.4
Raclette	14	Aug-22	0.3	2.2
Raclette	14	Aug-22	0.8	3.9
Raclette	14	Aug-22	-0.6	-0.7
Raclette	14	Aug-22	-0.7	-1.0
Raclette	14	Aug-22	-0.3	1.1
Raclette	14	Aug-22	-0.2	-0.7
Raclette	14	Aug-22	-0.7	-1.1
Raclette	14	Aug-22	-0.1	0.1
Toblerone	14	Aug-22	-0.2	-0.2
Toblerone	14	Aug-22	1.4	6.0
Toblerone	14	Aug-22	0.3	1.5
Toblerone	14	Aug-22	-0.4	-0.6
Toblerone	14	Aug-22	0.9	3.1
Toblerone	14	Aug-22	-0.1	-0.4
Toblerone	14	Aug-22	1.3	2.5
Toblerone	14	Aug-22	0.1	2.0
Toblerone	14	Aug-22	0.0	0.0
Toblerone	14	Aug-22	0.0	-0.3
Toblerone	14	Aug-22	0.2	2.4
Toblerone	14	Aug-22	0.4	3.0
Toblerone	14	Aug-22	0.7	2.3
Toblerone	14	Aug-22	0.0	-0.2
Toblerone	14	Aug-22	-0.2	0.4

Supplement Section 1: Detailed Build-Out Description

This supplement describes how to build a SWISS as we have built ours. There are many places where the system could be modified or adjusted based on a user's needs.

Step 1: Prepare the storage case

To prep the case for the build out the two main tasks are:

Pluck the foam so you can place the Valco stands & flasks

Drill the holes that you'll put the air and power cords through. I like to put the holes in the back (the one side without latches) so its easiest to route cords without having to go over the flasks later on.

Materials and tools needed for step 1:

Pelican 0370 Protector Cube Case with Pluck n' Peel foam

¼" Push-to-fit Bulkhead Fittings (e.g. **5779K677**) (2 per sampling depth + 1 for the dry air inlet)

Cordless drill

Plucking foam:

Inside your pelican case there are 7 pieces of foam: one base piece, 4 layers of Pluck N' Peel (we'll work with the top three) & two lid pieces. Each pluckable piece is 1" x 1" x 4" (l x w x h). For each flask we need to pull out a zone that is 3" x 3" X 12".

Working from the top piece of pluckable foam, pull out 15 3x3 holes for the flasks and one section that is 4" wide and 11" long. My preferred layout is to have the Valco valve hole in the center of the box, a row of 5 flask holes along the front, and 5 flasks arranged on either side of the valco valve.

Pull out the same pattern from the second and third pieces of foam. Note: the pieces are not all the exact same size and so they won't align perfectly.

Holes:

While there aren't breakable glass flasks in the box it can be nice to drill the holes you'll eventually feed power and sample air through. Drill one hole for each push to fit bulkhead fitting you will need, making the hole as small as allowable. I prefer to drill these holes on the back of the box so that my tubing can efficiently run out the box, and won't interfere with the valco at all. You will also want to eventually drill one hole for the power cords, but that one can be done later once power is all worked out. I tend to drill this hole on the side of the box to make cord management easier.

Step 2: Mount Valco valve vertically

Materials and tools:

Wood

Wood screws

6 X 1/8" diameter, 2" long machine with nuts and washers

Valco valve and associated cords

Hand drill

We used scrap 2x4's to build stands to mount the valco valve so that the head of the valco valve is positioned up. We used a 12" vertical piece, attached to an 11" horizontal piece of wood with screws. The Valco valve was then mounted onto the wood with 1/8" diameter, 2" long machine screws so that there was a 4" gap below the back of the valco valve so that cords can be plugged in/unplugged as needed.

** Note: it is very advantageous to attach all of the necessary cords (RS-232, power, display) at this step - it is very tricky once it is placed inside the box.

Step 3: Prep stainless steel tubing

Materials and tools:

316 Stainless Steel 1/8" OD tubing, Tube cutter, De-burring tool , Optional: aluminum ⅛" OD tubing for mocking up tubes and string, Valco valve fittings, ⅜" wrench, Valco valve

With a flask placed in each spot in the case, and the valco valve mounted and placed in the correct location, use aluminum tubing to create a mock-up tube that goes from the correct Valco valve port to the desired flask location. As you mock the tubing up make sure to have the tubing that attaches to the valco valve be completely vertical for 1 - 1.5" so that as you tighten the swagelok fittings there is no angular force. Don't forget to make a jumper loop on port 1 of the valco valve, as well as an inlet and outlet tube!

Then use string to measure the length of each mock-up. Cut the ⅛" stainless steel tubing to the correct length. Be sure to thoroughly de-bur and clean the tubing after cutting. Any small pieces of stainless steel tubing that make its way into the Valco valve can scratch and wear down the valco valve, making it leaky.

Then, once all of the tubing has been cut and de-burred, use the mounted Valco valve to attach the fittings to one side. Make sure that the ferrule is clamped down and can no longer slide around.

Step 4: Prep glass flasks

I find it easiest to put the Swagelok fittings onto the glass flasks prior to putting them into the box.

Materials and tools:

Glass flasks, ¼" to ⅛" reducing union fittings from Swagelok, PTFE ferrules, ½" and 9/16" wrenches

I like to take a piece from the lid and the topmost plucked foam piece and to put all the flasks out into their spots. I then take all of the ¼"-1/8" (32) reducing unions from the box, and remove the stainless steel ferrule from the ¼" side. I take a spare piece of bev-a-line or other flexible ¼" tubing, and put the stainless steel ferrules onto the flexible tubing to save for other uses. They're good to save because each ferrule set is about $2.50. I then put the ¼" caps on all the flasks, followed by a ¼" teflon ferrule from ohio valley. I typically buy about 20 extra teflon ferrules per

SWISS box because you will inevitably break a few flasks as you go through the building process, and they're nice to just have on hand. Then tighten the rest of the union fitting onto the glass flask.

Step 5: Bend the stainless steel tubing

Materials and tools:

Tube bender, Mounted valco valve, Prepped stainless steel tubing, prepped flasks placed in case

Bend the stainless steel tubes attached to the valco valve so that they easily slide in and out of the swagelok fittings.

Pro-tips:

I position all of the flasks to start so that the center tube (the long one that goes to the bottom) is on the left side – and I attach the bottom Valco fitting to the center tube. I've done this so that is my inlet side and so air gets pushed down to the bottom and then you flush out the top.

While I'm tube bending, sometimes I flip the position of the flask – but still make sure the bottom goes to the center tube. Particularly for the flasks on the far right side of the box, it can be helpful to twist them around so you have a lot more room to fit wrenches in.

You should aim to have the portion of the tube that attaches to the flask to be completely vertical for 1 - 1.5" because the Swagelok fitting has to perfectly line up, otherwise you'll snap the tube in the tightening process. As much as possible don't have tubes crossed – it makes your life a pain later if you need to replace something.

Step 6: Tighten Swagelok fittings

Materials and tools:

Wrenches, Infinite patience.

Use an extra union fitting to tighten the swagelok ferrules onto the stainless steel tubing. Then, attach and tight the stainless steel tubing to the union fittings. This is the most common step where flasks break. Go slowly and patiently through this step.

Supplement Section 2: Detailed Protocols for QA/QC

Terminology:

Dry air fill: Flush flasks with dry air for a period of time such that the air in the flask is fully turned over 10 times.

Water vapor fill: Flash flasks with water vapor of either known or unknown composition such that the gas in the flask is fully turned over at least 5 times.

Dry air test: A short (e.g. 7 day) test where dry air is put into the flasks, allowed to sit for a period of time, and then the water vapor molar fraction is measured at the end of the test. The goal is for flasks to maintain a low water vapor mole fraction.

Dead end pull measurement: There is no input of dry-air into the flasks during a measurement period. A cap is placed over the inlet tube on the Valco valve. During the dead-end pull method, there is no supply of a carrier gas and the picarro intakes gas at a rate of approximately 29 - 31 ml/min.

Carrier gas measurement: Dry-air or dry-N_2 is supplied to the inlet of the Valco valve at a rate of 30 ml/min during the measurement phase. It is expected that fractionation would occur as pressure decreases, and so using a carrier gas prevents large pressure changes that might induce fractionation.

Dry Air Test Protocol:

Fill: We used air filtered through drierite (100 - 300 ppm), flowing at a rate of 2 L/min to flush each flask for 5 minutes. At this rate, the air in each 650 ml flask turned over 15 times. At the time of filling the flasks, we noted the molar fraction of water vapor in both the ambient atmosphere and the dry-air.

Hold period: We recommend at least 7 days, however, shorter timescales could be used

Measure: Use a *dead end pull measurement* style to measure flasks for 5 minutes. Do not use a carrier gas, because it will dilute the signal.

Data Processing: To determine the water concentration in each flask, we marked the time the flask opened using the 'outlet valve' value from the Picarro. For each new flask we saw the pressure wave as a peak in the Outlet Valve value. The advantage of using this method is that it is also easy to identify flasks that are

likely leaking based on an outlet valve value that is lower and more similar to an ambient pressure value. After marking the start of each flask, we then removed the first 90 seconds of that measurement to discard any memory effects in either the tubing from the swiss to the picarro or the picarro itself. We then averaged the concentration across the subsequent 180 seconds. The code for this process is available via github.

How to 'pass' this protocol: Maintain a water vapor mixing ratio of less than 500 ppm.

Water Vapor Test Protocol:

Fill: Flush flasks with water vapor of known composition produced using the vapor permeable probes at a rate of 150 ml / min for 30 minutes. For a 650 ml flask, this is approximately 6 full turnovers of the water vapor in the flask. We found that 5 full turnovers was the minimum number required to get water vapor molar fraction values that were stable within ± 100 ppm for the final three minutes of the measurement period.

Hold period: We recommend at least 14 days. If the desired storage time is longer than one month, we recommend testing your system with a longer storage period.

Measure: Prior to the start of measuring each flask, we ran dry air via the flask bypass loop for 5 minutes to sufficiently dry and remove memory effects in the impermeable tubing that runs between the SWISS. During that five minute period,

lightly warm the flasks and tubing. The goal is to make sure that everything is uniformly warmed to just at or above room temperature so that there is no condensation. This is especially important for the valco valve and stainless steel tubing. Using the *carrier gas measurement* method, measure each flask for 10 minutes. Closely monitor each flask for signs of condensation (i.e. increasing water vapor mole fraction through the measurement, associated with increasing isotope values). Also closely monitor the water concentration right after switching back to the bypass loop, if the water concentration stays the same or increases with a marked increase in isotope values, mark that flask as problematic.

Data Processing: To mark the start of each flask, we used the rapid increase in water vapor mole fraction as the start time. We then discarded the first three minutes of measurement, and averaged the next 3 minutes (see supplemental figure).

How to 'pass' this protocol: After applying an offset correction, flasks should be evenly distributed about 0, and ideally within the uncertainty of the vapor permeable probes ± 0.5 ‰ and ± 2.4‰ for $\delta^{18}O$ and $\delta^{2}H$, respectively (Oerter et al., 2017).

Chapter IV: Pedogenic carbonate formation in fine-grained soils

Abstract

Clumped isotope thermometry of soil carbonates ($T(\Delta_{47})$) provides an estimate of soil temperature at the time of mineral formation, and historically, that temperature has been interpreted to represent a warm-season biased soil temperature. This interpretation has been primarily based on the results of modern calibration studies conducted over roughly the last decade that suggest pedogenic carbonate forms in response to soil dry-down during the summer season. However, most of these studies have been done in medium to very coarse-grained soils that are not entirely representative of paleosols that preserve pedogenic carbonate in the deeper time rock record. Here, I present a modern calibration study of pedogenic carbonate clumped isotope thermometry in three soils in Colorado and Nebraska, USA, that have a fine-medium grain size, contain clay, and are representative of many paleosols preserved in the rock record. I compare clumped isotope thermometry data with climatic data (air temperature, precipitation), soil conditions (soil moisture and temperature), soil water isotope data, and integrated monthly precipitation isotope data.

The soils at the Briggsdale, CO and Seibert, CO sites have sandy-loam to loamy-silt textures. At each of these two sites, $T(\Delta_{47})$ overlaps with mean annual air temperature, consistent with other observations of fine-medium grained soils recording near mean annual air temperatures. Additionally, the calculated $\delta^{18}O$ of soil water overlaps within uncertainty with measurements of the isotope value of

soil water at carbonate bearing depths in September-October 2022. The soil water isotope data also suggest that there is very little variation in the composition of soil water isotopes at carbonate bearing depths and fall close to the Global Meteoric Water Line, which challenges the assumption that the calculated $\delta^{18}O$ of soil water represents an evaporatively ^{18}O enriched value. The soil from the third site, Oglala National Grassland, NE, has a silt-loam texture, but contains 2:1 swelling clays that facilitate shrink-swell behaviors. At that site, $T(\Delta_{47})$ is 9-10°C warmer than mean annual air temperatures, and the calculated $\delta^{18}O$ of soil water has a significantly higher isotope value than any observations of soil water isotopes at carbonate bearing depths. The temperature of pedogenic carbonate from Oglala National Grassland could indicate either a warm season bias, or be the result of carbonate forming out of isotopic equilibrium. These data suggest that future work on pedogenic carbonate formation should be particularly focused on vertic aridisols and vertisols, which are clay-rich and a key component of the geologic record.

4.1 Introduction

Pedogenic carbonate is formed and distributed in soils in a variety of morphologies (e.g., rhizoliths, clast coatings, nodules, etc.). Pedogenic carbonate nodules, in particular, are commonly used as a proxy material for paleoclimate information, because multiple stable isotope measurements can be made from them (e.g., $\delta^{13}C$, $\delta^{18}O$, Δ_{47}, etc.) to learn about a range of environmental characteristics. For example, $\delta^{13}C$, $\delta^{18}O$, and $T(\Delta_{47})$ values have been used to constrain vegetation changes (e.g. Cerling, 1984; Cerling and Quade, 1993; Passey, 2012), reconstruct

ancient pCO_2(e.g. Breecker et al., 2010)changes in the hydrologic system (e.g. Levin et al., 2011; Passey, 2012), and temperature change associated with both climatic changes and tectonic evolution (e.g. Ghosh et al., 2006; Garzione et al., 2006; Decelles et al., 2007; Snell et al., 2013; Carrapa et al., 2014; Huntington and Lechler, 2015; Ingalls et al., 2018; Rugenstein and Chamberlain, 2018).

To appropriately interpret the relationship between environmental conditions and the stable isotope composition of pedogenic carbonate, the geoscience community has studied the formation of pedogenic carbonate in Holocene soils as a way to approximate 'modern' carbonate formation (e.g. Cerling, 1984; Cerling and Quade, 1993; Breecker et al., 2009; Peters et al., 2013; Hough et al., 2014; Burgener et al., 2016; Huth et al., 2019; Kelson et al., 2020). Modern calibration studies are useful for understanding the strengths and limitations of paleoenvironmental proxies. In the last 10-15 years, since the development of clumped isotope thermometry, most pedogenic carbonate modern calibration studies have been focused on better constraining the relationship between T(Δ_{47}) and air temperature (Peters et al., 2013; Hough et al., 2014; Burgener et al., 2016; Huth et al., 2019; Kelson et al., 2020). These studies have broadly been conducted in immature, medium to coarse grained soils (Peters et al., 2013; Hough et al,. 2014; Oerter and Amundson 2016; Burgener et al., 2016; Burgener et al., 2018; Huth et al., 2019). In general, these soils have been selected because of an abundance of pedogenic carbonate and as part of climatic or elevation gradients. However, many paleoclimate studies source pedogenic carbonate nodules from fine-grained, clay-

rich paleosols, and recent work suggests that soil grain size is an important control on the temperature (e.g. mean annual temperature vs. warm-season biased temperatures) recorded by pedogenic carbonate (Kelson et al., 2020). There is therefore a need to study pedogenic carbonate formation in fine-grained, geologically-relevant soils.

Here, I present a modern calibration study of pedogenic carbonate clumped isotope thermometry in three soils in Colorado and Nebraska, USA, that have a fine-medium grain size and are more representative of many paleosols preserved in the rock record. To better understand the timing of drivers of carbonate formation, I present both climatological data and the stable isotope geochemistry of precipitation and soil water to compare to the $T(\Delta_{47})$ and calculated $\delta^{18}O$ of soil water preserved in pedogenic carbonate at the sites.

4.2 Background

4.2.1 What levers control pedogenic carbonate formation?

While the geologic community understands the sets of processes that influence carbonate mineral formation, it is unclear which (if any) dominate pedogenic carbonate mineral formation, and how these are affected by (or vary with) soil texture. Pedogenic carbonate formation is controlled by two key chemical concepts, acid-base chemistry and solubility. To explore how acid-base chemistry affects pedogenic carbonate formation, it is helpful to examine how the dominant

dissolved inorganic carbon species (DIC, DIC = $CO_{2\,(aq)} + HCO_3^- + CO_3^{2-}$) in a system varies with pH. DIC chemical equilibrium can be described by the equation:

$$CO_{2(gas)} \rightleftharpoons CO_{2(aq)} + H_2O \rightleftharpoons H_2CO_3 \rightleftharpoons HCO_3^- + H^+ \rightleftharpoons CO_3^{2-} + 2H^+ \quad \text{EQ. 4-}$$

The addition of CO_2 pushes the above equation to the right and increases carbonic acid. Carbonate ion formation is favored at higher pH, and so the addition of CO_2 inhibits carbonate ion and carbonate mineral formation (Zeebe and Wolf, 2001). In a soil, pCO_2 is primarily controlled by primary productivity, and secondarily controlled by soil permeability (e.g., Cerling and Quade, 1993; Hillel, 1998; Breecker et al., 2013). At times of high primary productivity, which generates relatively high soil pCO_2, the formation of carbonic acid is favored over carbonate ions.

The solubility of pedogenic carbonate is a function of the concentration of Ca^{2+} and CO_3^{2-} in the solute and a temperature dependent equilibrium constant. The concentration of the Ca^{2+} cation can be controlled in two ways. First, calcium concentration depends on the delivery of calcium either from the soil substrate and/or from detrital material, both of which are influenced by local geology and water movement through the soil column (e.g. Hillel, 1998; Zamanian et al., 2016). Second, the amount of water in the soil column can affect Ca^{2+} cation concentrations; under drying soil conditions, Ca^{2+} can become increasingly concentrated, driving supersaturation (e.g., Hillel, 1998; Breecker et al., 2009; Hough et al., 2014). Calcium carbonate has inverse solubility, meaning that carbonate solids precipitate more readily at higher temperatures and dissolve at colder temperatures. This is primarily a function of temperature-controlled CO_2

solubility in water – at colder temperatures, less CO_2 is dissolved in the water, increasing pH and favoring carbonate ion formation. Soil temperature is controlled by the surface temperature and thermal properties of the soil (e.g., Hillel, 1998; Weil and Brady, 2017).

4.2.2 Stable Isotope Geochemistry of pedogenic carbonate

4.2.2.1 Carbon Isotope geochemistry, $\delta^{13}C$

Pedogenic carbonate inherits its $\delta^{13}C$ value from soil CO_2, and therefore primarily reflects information about biologic activity (e.g., Cerling, 1984; Huth et al., 2019), but can also reflect information about ancient pCO_2 (e.g. Quade et al., 1989; Cerling, 1991; Breecker et al., 2013). In the geologic record, the $\delta^{13}C$ value of pedogenic carbonate ($\delta^{13}C_c$) has been used to identify the transition of environments dominated by C3 photosynthetic pathway species to those dominated by C4 photosynthetic pathway species (e.g. Levin et al., 2004; Uno et al., 2011). The $\delta^{13}C$ value of pedogenic carbonate can also inherit seasonal bias; carbonate clast rinds from Torrey, UT had $\delta^{13}C$ values that were strongly biased towards summer respiration values (Huth et al., 2019).

4.2.2.2 Oxygen Isotope geochemistry, $\delta^{18}O$

The $\delta^{18}O$ value of pedogenic carbonate can be described by the following heterogeneous equilibrium equation:

$$CaC^{16}O_3 + H_2^{18}O \Leftrightarrow CaC^{18}O^{16}O_2 + H_2^{16}O \qquad \text{EQ. 4-2}$$

This reaction is temperature dependent, and from this equation it is possible to see that the $\delta^{18}O$ value of pedogenic carbonate is a function of both the temperature at which the mineral formed and the $\delta^{18}O$ value of the soil water from which the mineral precipitated (e.g., Cerling, 1984; Kim and O'Neil, 1997). The $\delta^{18}O$ value of the soil water is primarily controlled by the $\delta^{18}O$ value of meteoric water, but can be modified by evaporation.

The $\delta^{18}O$ value of meteoric water can be, to first approximation, described as a Rayleigh distillation process:

$$\frac{R}{R_i} = f^{\alpha-1} \qquad \text{EQ. 4-3}$$

where R is the isotopic ratio of a vapor package, R_i is the initial isotope ratio, f is the fraction of original water vapor remaining, and α is the fractionation factor (Craig, 1961; Dansgaard, 1964). While the fractionation factor is temperature dependent, and therefore exerts control on the system, the fraction of water vapor remaining exerts a much stronger control on the observed isotopic signal. As the water vapor fraction decreases (as a moisture source progressively rains out), the water isotope ratios become progressively depleted in the heavier mass isotopes. Observations of global and local distributions of $\delta^{18}O$ and $\delta^{2}H$ values in meteoric waters over the last 60 years have led to the identification of a number of controlling factors (e.g. temperature, continentality, latitude, altitude, and seasonality) (Rozanski et al., 1993; Gat, 1996). On a global scale, under our modern climate, the relationship between ^{18}O value of precipitation and temperature can be described by the equation:

$$\delta^{18}O_{precip} = -15.57 + 0.6 * T \quad \text{EQ. 4-4}$$

where T is the mean annual air temperature in Celsius (Fischer-Femal and Bowen, 2021).

In paleoclimate and paleoenvironmental studies, the $\delta^{18}O$ value of carbonate has been used to infer information about either a change in mineral precipitation temperature or about changes in the isotope composition of soil water (precipitation), which requires making an assumption about the other parameter (e.g. Decelles et al., 2007; Levin et al., 2011; Passey, 2012; Rugenstein and Chamberlain, 2018).

4.2.2.3 Clumped Isotope Thermometry, Δ_{47}

In contrast to the $\delta^{18}O$ value of pedogenic carbonate, which relies on both the isotopic composition of the precipitating fluid and the reaction temperature, carbonate clumped isotope thermometry provides an independent estimate of mineral formation temperature that is independent of the bulk isotopic composition of the water the carbonate formed from. Carbonate clumped isotope thermometry (Δ_{47}) relies on the relationship between temperature and the degree of bond ordering of the heavy, rare isotopes ^{13}C and ^{18}O (Eiler, 2007). The distribution of doubly substituted, 'clumped' isotopologues in carbonate can be described by the homogeneous equilibrium equation:

$$Ca^{12}C^{18}O^{16}O_2 + Ca^{13}C^{16}O_3 \Leftrightarrow Ca^{13}C^{18}O^{16}O_2 + Ca^{12}C^{16}O_3 \quad \text{EQ. 4-5}$$

The extent of bond ordering is expressed as the equation:

$$\Delta_{47}\ (‰) = \left(\frac{R^{47}_{sample}}{R^{47}_{stochastic}} - 1\right) * 1000 \qquad \text{EQ. 4-6}$$

where $R^{47}_{sample} = M^{47}_{sample}/M^{44}_{sample}$ and similarly, $R^{47}_{stochastic} = M^{47}_{stochastic}/M^{44}_{stochastic}$ (Schauble et al., 2006). At low temperatures there is a greater degree of ^{13}C - ^{18}O ordering, or clumping, in the carbonate ion (CO_3^{2-}) compared to a purely random, stochastic distribution of the rare heavy isotopes, leading to an inverse relationship between Δ_{47} and temperature (Eiler, 2007).

In addition, an independent estimate of temperature from Δ_{47} can be used with the simultaneously measured $\delta^{18}O$ of carbonate ($\delta^{18}O_C$) to estimate the $\delta^{18}O$ composition of the water ($\delta^{18}O_w$) from which the carbonate formed, using an equation for the temperature-dependent fractionation of oxygen isotopes between carbonate minerals and water (e.g. Kim and O'Neil, 1997).

4.2.2.4 Seasonal bias of pedogenic carbonate formation revealed by clumped isotope thermometry

Over the last 40 years, there has been considerable effort to constrain the timing and style of pedogenic carbonate formation to improve paleoenvironmental interpretations (e.g., Cerling, 1984; Cerling and Quade, 1993; Breecker et al., 2009; Peters et al., 2013; Hough et al., 2014; Oerter and Amundson, 2016; Burgener et al., 2018; Huth et al., 2019: Kelson et al., 2020). In general, there are three approaches that fall along a continuum that have been used to study pedogenic carbonate formation. The first approach was to compare environmental parameters, the $\delta^{13}C$ value of soil CO_2, and $\delta^{13}C_C$ and $\delta^{18}O_C$ (Breecker et al., 2009; Oerter and Amundson,

2016). These studies either measure $\delta^{18}O$ of soil water ($\delta^{18}O_{sw}$) once to establish equilibrium, or assume equilibrium between $\delta^{18}O_{CO2}$ and the $\delta^{18}O$ value of soil water to interpret the timing of carbonate formation. The second approach was to compare environmental parameters, such as soil temperature, soil moisture, air temperature, precipitation amounts, and $\delta^{18}O$ value of precipitation to $\delta^{13}C_C$, $\delta^{18}O_C$, and Δ_{47} temperatures (Peters et al., 2013; Hough et al., 2014; Burgener et al., 2016, 2018). The final approach, taken by Huth and others (2019), was to add soil water isotopes taken from discrete samples a few times throughout the study to the second approach, thereby circumventing assumptions of isotopic equilibrium.

While all of these studies offer nuance related to their particular field sites, the consensus is that at low to moderate elevations (< 4000 m), across a broad range of environmental conditions, pedogenic carbonate clumped isotope temperatures are typically biased towards warm season temperatures (Kelson et al., 2020). In a meta-analysis of the studies that incorporate clumped isotope thermometry data, the calculated mean $\delta^{18}O_{sw}$ was not biased towards summer precipitation values, and instead reflected an integrated mean annual $\delta^{18}O$ value (Kelson et al., 2020). However, that dataset showed considerable scatter about the mean, and individual datasets within the compilation show clear departures from mean annual precipitation values.

Broadly, the studies highlighted above were conducted in poorly developed (e.g. inceptisol, entisol, aridisol), medium to coarse-grained soils. These soils were targeted because of abundant pedogenic carbonate and were often selected as part

of climatic or elevation gradients. Past researchers have observed variability in the range of formation dynamics across elevation gradients (Hough et al., 2014; Burgener et al., 2016; Oerter and Amundson, 2016). For example, in a study that compared carbonate formation across high altitude and high latitude sites, Burgener and others (2018) found that grain size was a dominant control on maintaining equilibrium carbonate formation; carbonate in cobbly soils at high altitudes and latitudes were interpreted to have formed by carbonate dehydroxylation resulting in Δ_{47} values that reflected disequilibrium in the system. In contrast, carbonate formed in finer grained soils at similar elevations and latitudes maintained equilibrium isotopic values. This suggests that soil texture plays an important role in controlling soil dewatering rates, and therefore the stable isotope composition of pedogenic carbonate.

4.3 Methods

The general approach of this study was to compare pedogenic carbonate formation across three different soil textures within the same soil moisture regime (Ustic), with a particular focus on silt- and clay-rich soils. From north to south, the three field sites are located in Oglala National Grassland, NE (ONG); Briggsdale, CO; and, Seibert, CO (fig. 4-1). These sites were chosen to satisfy soil texture requirements and to span a spectrum of soil development. Additionally, the two finer grained soils chosen (ONG and Seibert) for this study have textures that overlap with paleosols from the Bighorn Basin, WY (chapter V, this dissertation).

To learn more about how pedogenic carbonate encodes information about climate, I aimed to monitor both climate and key soil parameters at all three sites, as well as determine stable isotope values from the soil carbonates and soil water.

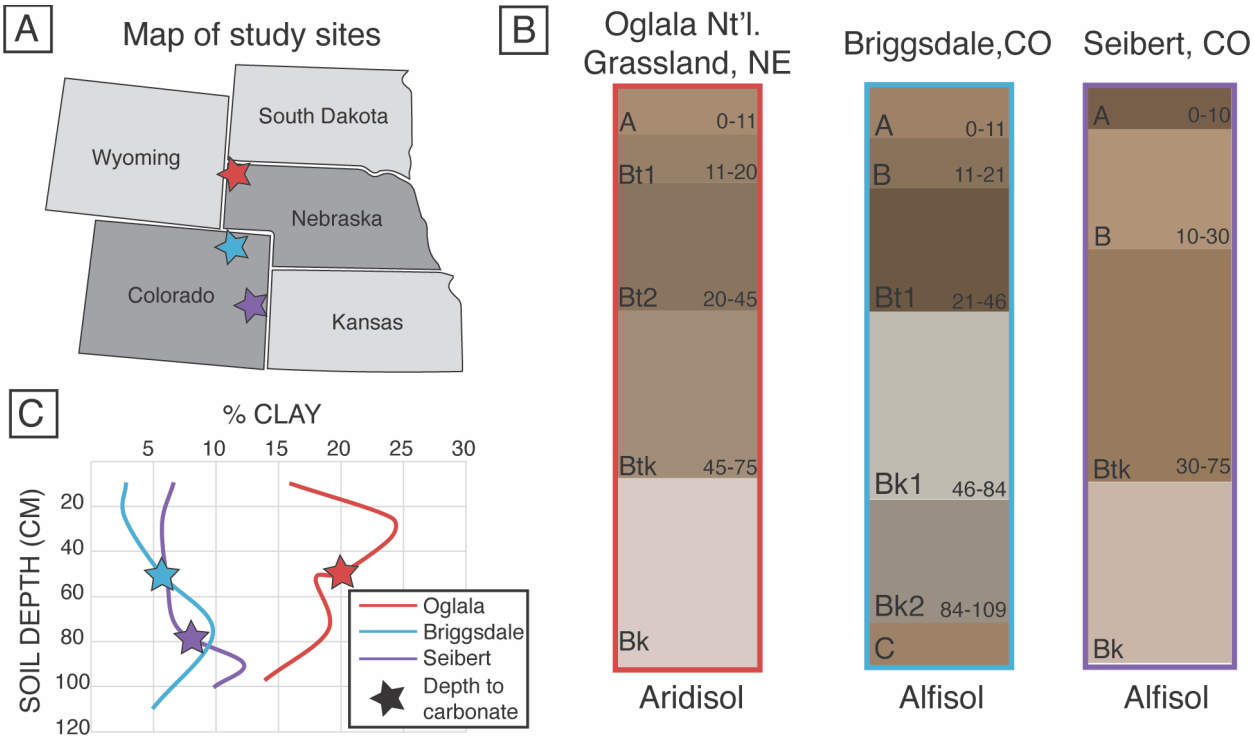

Figure 4-1. A) Map of field site locations. From north to south, the field sites are Oglala National Grassland, Briggsdale, and Seibert. B) Soil profiles of each site. C) The amount of clay (size fraction) as a function of depth.

4.3.1 Field Methods

4.3.1.1 Meteorological data from Briggsdale, CO and Seibert, CO

Both field sites in Colorado are co-located with CoAgMET sites (Colorado's Mesonet), which are operated by the Colorado Climate Center (Colorado State University, Fort Collins, CO). At both sites, the Colorado Climate Center measures air temperature, relative humidity, wind speed and direction, precipitation quantity, and soil temperature at 5 and 15 cm depths (Fig. 4-2A). The Briggsdale

site (Lat: 40.5947/Long: -104.3190/elev: 1480 m) is located in northeastern Colorado, USA, and has been instrumented as a CoAgMET site since July 31, 2002. The Seibert site (Lat: 39.1187/Long: -102.9250/Elev: 1479 m) is located in eastern Colorado, USA, and has been instrumented since April 2, 2015.

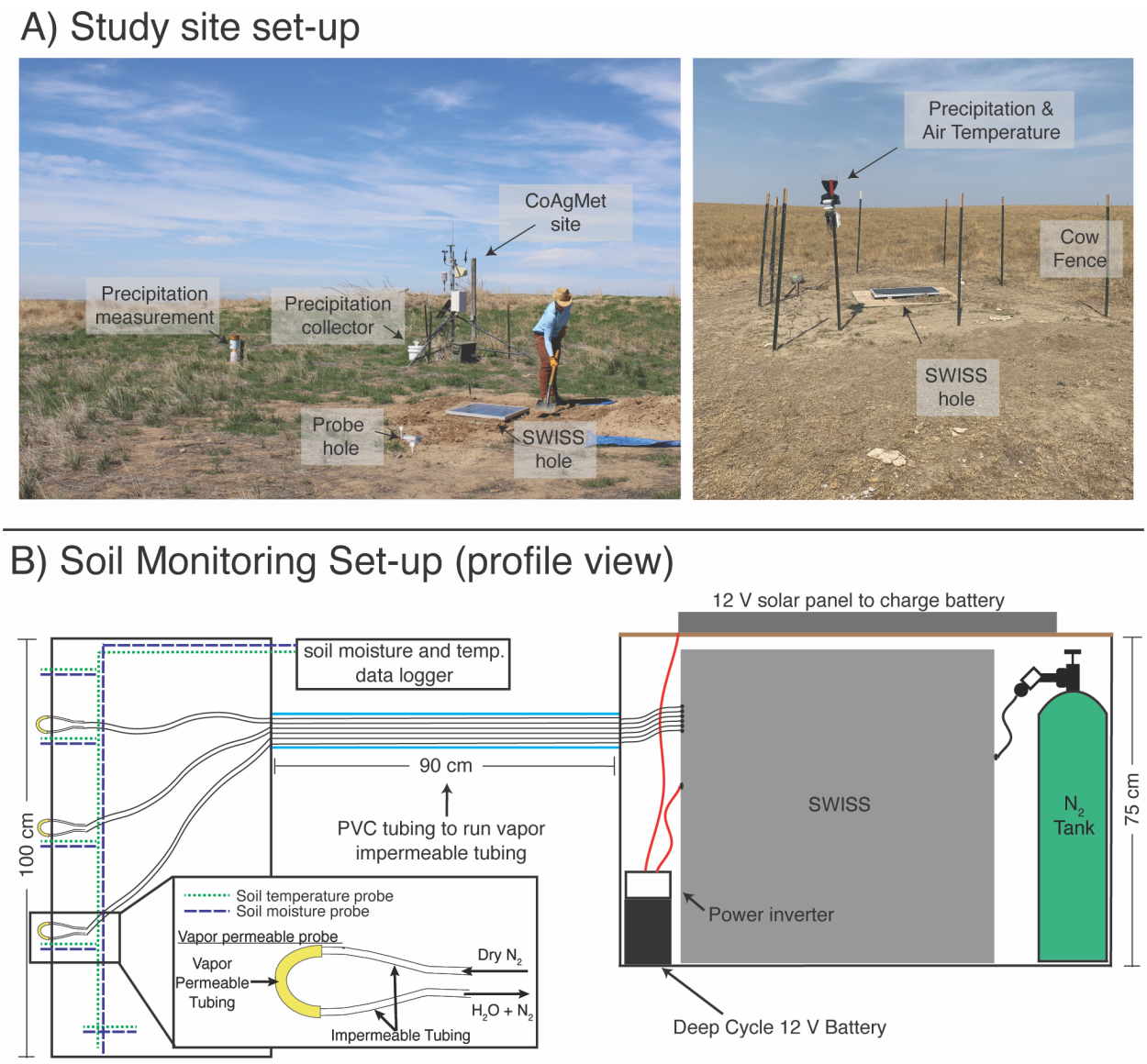

Figure 4-2. A) On the left is the field set-up at the Briggsdale site. The Seibert site is set up nearly identically to Briggsdale. The photo on the right shows the field set up from the ONG site. Key features of each site are labeled. B) A profile view of the setup at each site. On the left is the instrumented hole where the soil temperature and moisture loggers with the vapor permeable probes were installed. On the right is the hole where the SWISS and power components were housed. Vapor impermeable tubing that runs between the two holes was buried at a depth of approx. 15 cm in a PVC pipe.

4.3.1.2 Meteorological data from Oglala National Grassland, NE

The ONG site was instrumented with air temperature, relative humidity and precipitation quantity sensors in June 2021 (Onset, S-THC-M002 and Davis Instruments Rain gauge sensor, S-RGE-M002) (Fig. 4-2A). However, due to significant livestock interference, this data is incomplete. Therefore, I also incorporate data from the Alliance (103 km SE) Nebraska MesoNet site where air temperature, relative humidity, and precipitation quantity are recorded on an hourly basis, as well as soil moisture and temperature at 10, 25, 50, and 100 cm that are recorded at one-minute intervals. Lastly, I also used temperature and precipitation data from the Chadron Municipal Airport (42 km ESE) to provide a more local constraint on climate conditions.

4.3.1.3 Soil conditions

At each site I dug two holes: the first hole, in which all data probes were deployed, was dug once at the start of the study to install the probes, and the second hole housed the Soil Water Isotope Storage System (SWISS) (Fig. 4-2B).

The first hole (instrumentation hole) was instrumented with soil moisture and temperature data loggers as well as water vapor probes. At Briggsdale, soil temperature was measured at soil depths of 10, 25, 50, 75, and 100 cm. At Seibert and Oglala, soil temperature was measured at soil depths of 25, 50, 75, and 100 cm. At all three sites, soil moisture was measured at soil depths of 10, 25, 50, 75, and 100 cm. At all three sites, I installed water vapor probes at 25, 50 and 75 cm depths

into the intact sidewall of the pit. After deploying the three kinds of probes, the hole was carefully backfilled with soil from approximately the same depths, taking care to compact the soil appropriately and maintain horizon depths as much as possible.

The second hole is where the SWISS, dry nitrogen tank, and associated components to power the SWISS were stored. The water vapor probes, which connect to the SWISS via Bev-A-Line impermeable tubing, are run through a PVC pipe buried at approximately 15 cm depth. I chose to run the impermeable tubing to the SWISS underground to reduce the effect of diurnal temperature variability, and to limit condensation as water travels from the relatively warm soil to the SWISS in cooler ground.

4.3.2 Soil Characterization

4.3.2.1 Soil description and sample collection

At all three sites, I dug a pit to a depth of 1 m, and I delineated horizons based on soil color, texture, and ped structure. At this time, I also collected bulk soil samples from at least five depths (10, 25, 50, 75, and 100 cm) for soil texture and mineralogical analyses. Additionally, I collected individual pedogenic carbonate nodules for radiocarbon dating analysis that were wrapped in aluminum foil, before being bagged and labelled. Lastly, at each site I collected pedogenic carbonate nodules for stable isotope analysis from at least two levels in each pit.

4.3.2.2 Soil texture and soil mineralogy

Soil texture and mineralogical analyses were performed in the Sediment/Plant Analysis and Processing Lab and XRD/Soil Processing Lab at the University of Colorado Boulder, Institute of Arctic and Alpine Research (INSTAAR), respectively. Soil particle size was measured using a Malvern Mastersizer 3000, and soil mineralogy was measured using Siemens D5000 XRD with ROCKJOCK6 processing software.

4.3.2.3 Microscopy

I used optical and cathodoluminescence (CL) microscopy to identify carbonate grain size and inclusion grain size within the nodules and to identify typical fabrics and textures of the nodules that may be useful for interpreting primary fabrics of carbonate nodules from paleosols in the future. To create images of the thin sections, I used a Zeiss Axio Imager M2 with a motorized XY scanning stage, circularly polarized transmitted light path, and 6MP 33fps Axiocam 506 color camera. This microscope is capable of automated image collection and construction of high-resolution mosaic images of entire thin sections in polarized and cross polarized transmitted light. I created CL microscopy images using a Technosyn Cathode Luminescence Model 8200 Mk II microscope with an Optronics Magnafire digital camera with a Peltier-cooled image sensor housed in the CU Boulder Earth Systems Stable Isotope Lab (CUBES-SIL; RRID SCR-019300). CL colors from carbonate minerals can vary from non-luminescent/dull to bright yellow, orange and

red according to the spatial distribution of trace elements (i.e. iron and manganese) in carbonate fabrics and the mineralogy (Pagel et al., 2000).

4.3.3 Carbonate Isotope Geochemistry

4.3.3.1 Radiocarbon

To determine the approximate age of carbonate nodule formation, I dated nodules from 2-3 soil levels from each site using ^{14}C radiocarbon dating. Samples were prepared in the INSTAAR Laboratory for AMS Radiocarbon Preparation and Research. For each sample, the fraction dated was from a 0.001M HCl leach, and the resultant CO_2 purified and transferred into flame-sealed tubes prior to graphitization and packing at INSTAAR. This was done along with associated primary measurement standards, measurement blanks, and control materials of appropriate sample type. Packed targets were sent to UC-Irvine for high-precision measurement, typically equating to a 1-sigma error of 20-30 ^{14}C yrs. Raw measurement results were returned to NSRL for correction and reporting according to conventions of Stuiver and Polach, (1977).

4.3.3.2 Single stable isotope data

$\delta^{18}O_c$ and $\delta^{13}C_c$ values of the pedogenic carbonate nodules were measured using a continuous flow Thermo Delta V coupled to a GasBench II headspace analyzer in the CUBES-SIL. Samples were prepared in one of two ways: (1) powder from the nodules that were mounted for thin section microscopy were drilled directly from the paired thin sections billets; or, (2) whole nodules were crushed and

homogenized using a mortar and pestle. Then, approximately 110–500 μg of sample powder (equivalent to ~100–110 μg of pure carbonate mineral) were weighed into Labco Exetainers vials (12 ml) and purged with ultra-high purity helium for 5 minutes. Samples were digested in 105-110% orthophosphoric acid at 70ºC for >30 minutes to release CO_2 for analysis. All stable isotope ratios are reported in delta (δ) notation as the per mil (‰) deviation relative to the Vienna Pee Dee Belemnite (VPDB) standard.

Repeated measurements of internal and internationally accepted carbonate standards (i.e. NBS18, IAEA-C2, USGS44, and CU YULE) yielded precision of ± 0.1 ‰ or better for both $\delta^{13}C$ and $\delta^{18}O_{carb}$. To correct raw values, the Isoreader R package was used to read all raw data files directly into R (Kopf et al., 2021). Raw delta values were evaluated for and, when necessary, corrected for the effects of linearity and drift. These corrected values, rather than the raw values, were then scale corrected. Linearity, drift, and scale corrections to data were done using in-house CUBES-SIL R scripts that utilized the tidyverse (v. 1.3.1) and isoprocessor (v. 0.6.5) R packages (isoverse.org, S. Kopf).

4.3.3.3 Clumped Isotope Thermometry

I prepared samples in one of two ways: (1) powder from the nodules that were mounted for thin section microscopy were drilled from the paired billets; or, (2) nodules were crushed and homogenized using a mortar and pestle. I weighed approximately 15 - 50 mg of sample powder into silver capsules for each analysis

(equivalent to ~ 9 mg of pure carbonate). I analyzed calcium carbonate standards (i.e. ETH 1, 2, 3) to correct the data to the community accepted Intercarb-Carbon Dioxide Equilibrium Scale (ICDES) (Bernasconi et al., 2021), and used the carbonate standard IAEA-C2 as a monitoring standard. The sample powders were digested in 90°C phosphoric acid for 45 minutes. After digestion, all gas produced from samples and carbonate standards were cleaned via an on-line, custom-made vacuum extraction line for the automated processing of carbonate samples for Δ_{47} thermometry.

I collected T(Δ_{47}) data during two sessions in 2022 on a Thermo Scientific 253 Plus dual-inlet isotope ratio mass spectrometer in the CUBES-SIL. The gas was analyzed for the abundance of masses 44-49 of CO_2, and used to determine Δ_{47}, D_{48}, δ^{47}, $\delta^{13}C_{carb}$, and $\delta^{18}O_{carb}$ values for each sample. Precision of individual analyses is reported as two standard errors of the mean (2 s.e.) and includes analytical error of each measurement as well as uncertainty associated with the correction lines used (Bernasconi et al., 2021; Dennis et al., 2011; Huntington et al., 2009).

I analyzed three to six replicates of each sample, and each replicate analysis was composed of 10 repeated analyses of the sample gas (a single "acquisition"). Further, each acquisition comprised 10 sample/reference gas analysis cycles, at 20 second integration times for analysis of both gases measured in a cycle, for a total of 4000 seconds for each sample replicate analyzed. Final sample Δ_{47} values were calculated as weighted means of all the replicate analyses of that sample, and associated errors were calculated using standard errors of the replicates as the

weighting factors, following Huntington et al. (2009). Temperatures were estimated from the mean Δ_{47} values using the Anderson et al. (2021) calibration line, and temperature uncertainties were estimated by propogating the Δ_{47} standard error for every sample; all plots show two standard errors (2 s.e.) for $T(\Delta_{47})$.

From the measured $T(\Delta_{47})$ and $\delta^{18}O_{carb}$ values, I calculated the $\delta^{18}O_w$ value of the water that the carbonate mineral precipitated from using the equilibrium fractionation between calcite and water established by Kim and O'Neil (1997). The $\delta^{18}O_w$ value is reported relative to the VSMOW reference frame (Coplen, 2011).

4.3.4 Precipitation and surface water stable isotope geochemistry

I collected precipitation samples for stable isotope analysis ($\delta^{18}O_p$ and $\delta^{2}H_p$) at each of the three sites monthly. Additionally, I collected samples of surface water within 10 km of the Oglala site once each summer. I did not collect surface water samples near the other two sites, because, to the best of my knowledge, there was no surface water available within 20 km of either site. I collected integrated monthly precipitation samples using a half-gallon Nalgene bucket with a funnel that I attached to the lid and which was covered by a fine mesh to prevent particulates from entering the bucket. At the start of each month I covered the bottom of the bucket with a thin film of mineral oil to prevent evaporation (Scholl et al., 1996). During each site visit, I used a syringe to collect approximately 40 ml of water from below the mineral oil. I filled two 20 ml vials, sealed them, and then wrapped the vials with parafilm to return them to CU Boulder. I then discarded the

rest of the water and mineral oil in the bucket, wiped it out, and set it out to dry for ~ one hour before I would prepare the bucket for a new month of sample collection.

I measured the $\delta^{18}O$ and $\delta^{2}H$ values for precipitation samples in the INSTAAR Stable Isotope Laboratory at CU Boulder. I filtered and pipetted samples into 2 ml vials, and then samples were measured using a Picarro L2130-i Isotope and Gas Concentration Analyzer paired with an autosampler and high precision vaporizer unit. I ran all samples in either duplicate or triplicate. I used three secondary standards that have been calibrated against VSMOW: Florida Water, Keg Antarctic Water, and Keg Boulder Water. Using these standards, I corrected samples for instrument drift during the run period and memory effects between samples. I report the $\delta^{18}O_p$ and $\delta^{2}H_p$ values as the per mil (‰) deviation relative to VSMOW.

4.3.5 Soil water isotope geochemistry

I collected two soil water isotope time series from all three field sites. I collected soil water from all three field sites using the Soil Water Isotope Storage System (SWISS, Havranek et al., 2020; in review; chapter 3, this thesis). In each SWISS there were 15 flasks. The SWISS units collected samples from three depths (25, 50, and 75 cm) on each sampling day, and therefore it was able to collect samples on five days total, at an interval of 5 - 7 days. I stored soil water vapor samples in the SWISS for up to 41 days prior to measurement.

I measured the soil water vapor samples in the INSTAAR Stable Isotope Laboratory using a continuous flow Picarro L2130-i Isotope and Gas Concentration Analyzer. I used the dry-air carrier gas sample introduction method to measure the soil water vapor samples; soil water vapor was 'pushed' out of the flask and into the Picarro using dry-air (<100 ppm H_2O) at a rate of approx. 30 ml/min (Havranek et al., *in review*; Chapter 3, this thesis). For each flask measurement, I discarded the first three minutes of measurement from each flask to mitigate memory effects, and then I averaged the subsequent three minutes of measurement (at 1 Hz, yielding ca. 180 measurements). I measured the flasks for a total of 10 minutes each, which gave me the option to choose a secondary three-minute long measurement window if the initial measurement window did not yield a stable measurement, or if there was a suspected memory effect. Using a secondary measurement was very rare, and typically associated with other challenges, like condensation.

To monitor instrument stability and to apply an isotopic scale compression correction, I immersed water vapor probes that are identical in tubing length to those deployed in the field, in three in-house standard waters. The in-house standards isotopically encompassed the samples (i.e. one had higher values than all the samples, one had lower isotope values than the samples measured, and there was one intermediate value water). I measured the temperature of the water at the time of measurement, as well as used mass flow controller settings that were identical to those used in the field (i.e. 60 ml/min of dry air input into the tubing).

I converted the average water-vapor value to liquid water values using a correction specific to the brand of vapor permeable membrane tubing I used (Rothfuss et al., 2013). This correction takes into account the temperature of either the water or soil at the time of vapor collection and the fractionation that occurs between liquid and vapor as mediated by the vapor permeable tubing. It does not take into account the texture of the soil, which Oerter and Bowen (2017) have argued plays an important role on the measured isotope value. After correcting to liquid values, I applied a scale correction using the liquid water standards described above. I did not apply a drift correction to the soil water vapor data, because the scale of instrument drift over a measurement period was far below the uncertainty of the water vapor probes alone (0.5‰ and 2.4‰ for $\delta^{18}O$ and $\delta^{2}H$, respectively; Oerter et al., 2016). Finally, an offset correction of 1.0‰ and 2.6‰ for $\delta^{18}O$ and $\delta^{2}H$, respectively, associated with the storage and measurement of water vapor via the SWISS, was applied (Havranek et al., in review; chapter 3, this thesis). For all soil water samples, I apply an uncertainty of 0.9‰ and 3.5‰ for $\delta^{18}O$ and $\delta^{2}H$, respectively (Havranek et al., *in review*; chapter 3 of this dissertation).

Due to the novel nature of the soil water isotope measurements being made, I developed a confidence-based metric to describe the reliability of the soil water isotope data. I did this in part, because some of the phenomena I have observed in my data cannot be explicitly ties to a mechanistic cause. This metric also points to future work that will improve the SWISS. Soil water isotope samples that yielded high water vapor concentrations (>17,000 ppm), had precise measurement, and fall

within expected paradigms (i.e., along the global meteoric water line or evaporated water lines) are rated as having high confidence. Soil water isotope samples that yielded low water vapor concentrations (<13,000 ppm) either due to cold temperatures or low volumetric soil water content (VWC) but had precise measurements were rated as having moderate confidence. Soil water isotope samples that had high water vapor concentrations but either imprecise measurements or fall outside expected paradigms were rated as having (low-moderate confidence). Samples that yielded imprecise measurements and were low water concentration were rated as having low confidence.

4.4 Results

4.4.1 Soil Characterization

The soil at the ONG site is consistent with the Olney series (Fig. 4-1B), which is classified as an aridisol (NRCS), and has a silt loam texture (mostly silt with some clay) (Supp. Fig. 4-1). Clay percentage is at a maximum in the Bt2 horizon, at 24% (Fig. 4-1C). The soil is composed of quartz, feldspar, carbonate, kaolinite, smectite and illite (Brookins, 2021). Depth to carbonate formation at this site is 52 cm, with the presence of nodules starting at 75 cm, and the carbonate bearing horizon continues to the bottom of the described pit.

The soil at the Briggsdale site is most consistent, based on horizon depth and texture, with the Ascalon series (Fig. 4-1B), which is classified as a Mollisol (NRCS). However, our observations do not indicate the presence of a mollic epipedon based on the lack of horizons with a chroma ≥ 3. The upper portion of the soil profile (>45

cm) has a loamy sand texture and the lower portion of the soil profile has a sandy loam texture (Supp. Fig. 4-1). Clay percentage is at a maximum at ~75 cm depth at 9.8% (Fig. 4-1C). The soil is composed of quartz and feldspar with minor contributions of smectite and illite (Brookins, 2021). Depth to carbonate formation is 50 cm, with the presence of nodules starting at that level.

The soil at the Seibert site is most consistent with the Olnest series, based on horizon depth and soil texture (Fig. 4-1B, Supp. Fig. 4-1); the Olnest soil series is classified as an alfisol (NRCS). Above 30 cm depth, the soil has a sandy loam texture, and below 30 cm has a silty loam texture (Supp. Fig. 4-1). The depth to carbonate formation is 30 cm, but between 30 - 75 cm carbonate is extremely diffuse and is not present as discrete masses. Carbonate nodule formation starts at a depth of approx. 75 cm. Clay percentage increases with depth to a maximum of 12% at a depth of 90 cm (Fig. 4-1C). This soil is composed of quartz, feldspars, carbonate, smectite and illite (Brookins, 2021).

4.4.2 Climate Station Data

Because of significant livestock interference and technical difficulties, there is a limited amount of meteorological, soil moisture, and soil temperature data from the ONG field site. To bolster this dataset, I also include data from the Alliance, NE Mesonet site (Fig. 4-3). The soil at that site is characterized as the Keith series which is classified as an aridic mollisol (NRCS; Supp. Fig. 4-2). The soil has a clay content between 10 - 20%, and is a carbonate bearing soil, and therefore serves as

an appropriate analogue. At 50 cm soil depth, mean soil temperature was 10.6°C, with a maximum temperature of 23°C and a minimum temperature of -0.9°C between September 26, 2019 and November 5, 2022 (Fig. 4-3A). During summer 2021, soil temperatures at the ONG site at a depth of 50 cm were ~2°C warmer than the Alliance site. Figure 4-3B shows soil moisture between 2017 and 2022 at the Alliance site. There is a drop in soil moisture at all depths in 2020, 2021, and 2022 associated with La Niña conditions, and the effect is especially pronounced at the depth of 50 cm. Mean annual air temperature at the site is 8.5°C between 1988 - 2015, with a mean annual range of temperature (MART) of ~20°C (Fig 4-3C). Peak temperatures are in July. Precipitation dominantly falls between April and October, peaking in June (Fig 4-3D).

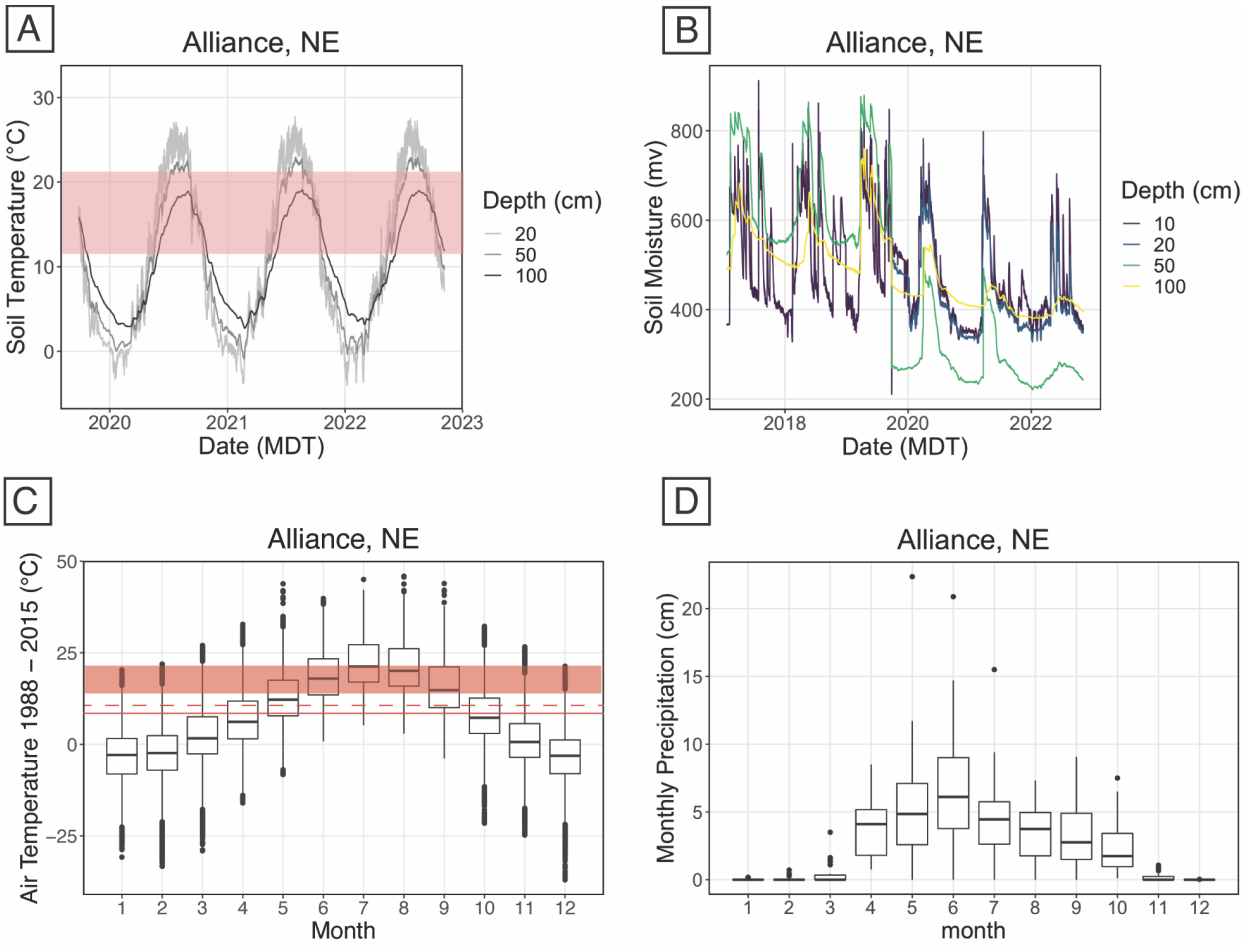

Figure 4-3. A) Soil temperature data from the Alliance, NE mesonet site from 2019-2022. The red highlight bar is the clumped isotope temperature estimate, uncertainty inclusive. B) Soil moisture data from 2017-2022. C) Box plot of monthly air temperature from 1988 - 2015 . The solid red line is the mean annual air temperature, the dashed red line is the mean annual soil temperature of 50 cm depth, and the red highlight bar is the clumped isotope temperature estimate, uncertainty inclusive. D) Box plot of monthly precipitation total from 1988-2015.

At the Briggsdale site, I utilized a combination of logger data from the probes we installed, that extends from December 2020 to October 2022, along with data from the co-located CoAgMet site that was first instrumented on July 31, 2002 (Fig. 4-4). Using the CoAgMet soil temperatures from 2011 -2018, mean soil temperature is 11.9 - 12.1°C. From December 2020 - December 2021, at 50 cm depth, the mean soil temperature using my loggers was ~12.4°C (Fig. 4-4A). Data from soil temperature loggers installed in December 2020, show that at the carbonate bearing depth of about 50 cm, maximum soil temperature was ~26°C and minimum soil temperature was -3.5°C. Maximum soil temperature occurred during late July - Early August. Volumetric soil moisture at a depth of 50 cm varied widely from December 2020 to October 2022 between 0.05 - 0.22 m^3/m^3 (Fig. 4-4b). My logger did register lower soil moisture (~0.03 m^3/m^3), but this value was registered near a time when the soil froze to about that depth, and so those data are unreliable. Maximum soil moisture content occurred in June 2021, and the rapid increase in soil moisture content at that time seems to be largely driven by one large precipitation event on March 15, 2021 where 0.6 inches of precipitation fell on the site (CoAgMet). Mean annual air temperature at the site is 8.9°C from 2002 - 2022 (Fig.4-4C). This is ~3.5°C colder than the mean soil temperature. Precipitation from 2002 - 2022 dominantly fell in late spring (May) and summer (Fig. 4-4D).

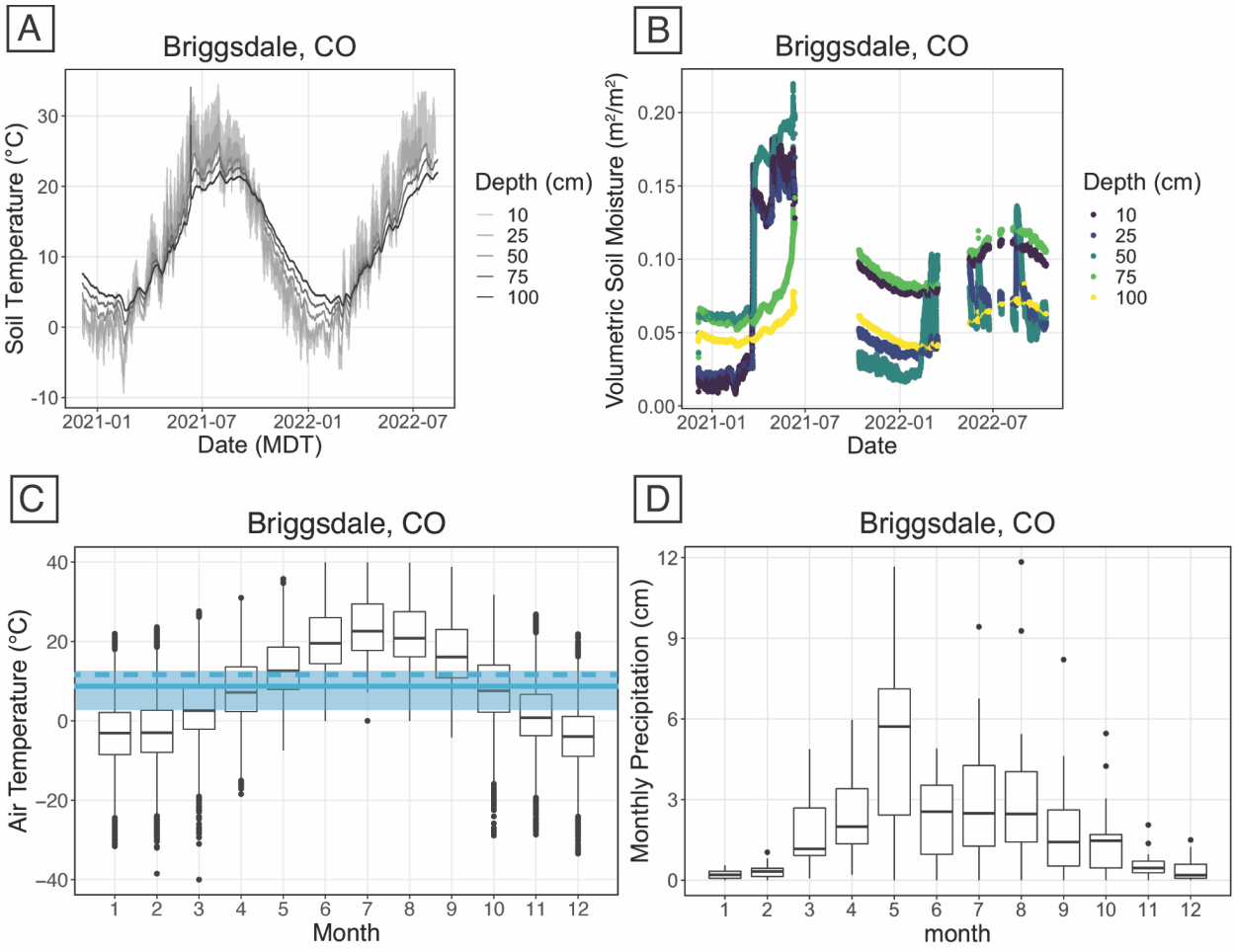

Figure 4-4 A) Soil temperature data measured from December 2021 – August 2022. B) Soil moisture data from December 2020 – August 2022. C) Box plot of monthly air temperature from 2002-2022. The blue line is the mean annual air temperature, the dashed blue line is the mean soil temperature, and the blue highlight bar is the clumped isotope temperature estimate, uncertainty inclusive. D) Box plot of monthly precipitation total from 2002-2022.

At the Seibert site, I rely on a combination of logger data from the probes we installed that extends from April 2021 to October 2022, and data from the co-located CoAgMet site that was first instrumented on April 2, 2015 (Fig. 4-5). Using the CoAgMet data from the Seibert site, mean soil temperature at 15 cm depth from 2016 - 2022 was 11.8°C. From my data loggers, mean soil temperature at 50 cm depth from April 2021 - April 2022 was 12.6°C (Fig 5A). From the CoAgMet data, there seems to be a slight positive trend in peak soil temperatures over the 2016 - 2022 time period. At the carbonate nodule forming level of 75 cm, temperature peaks in August, likely between 22-24°C. Between July 2021 and July 2022, soil moisture is surprisingly invariant at all levels. At the carbonate bearing level of 75 cm, soil moisture varied between 0.045 - 0.08 m^3/m^3 (Fig. 4-5B). Mean annual air temperature at the Seibert site is 10.6°C, with peak air temperatures of 22.2°C (median value) over the last six years in July (Fig. 4-5C). Precipitation dominantly falls in the summer months, with the most precipitation in May and July (Fig. 4-5D).

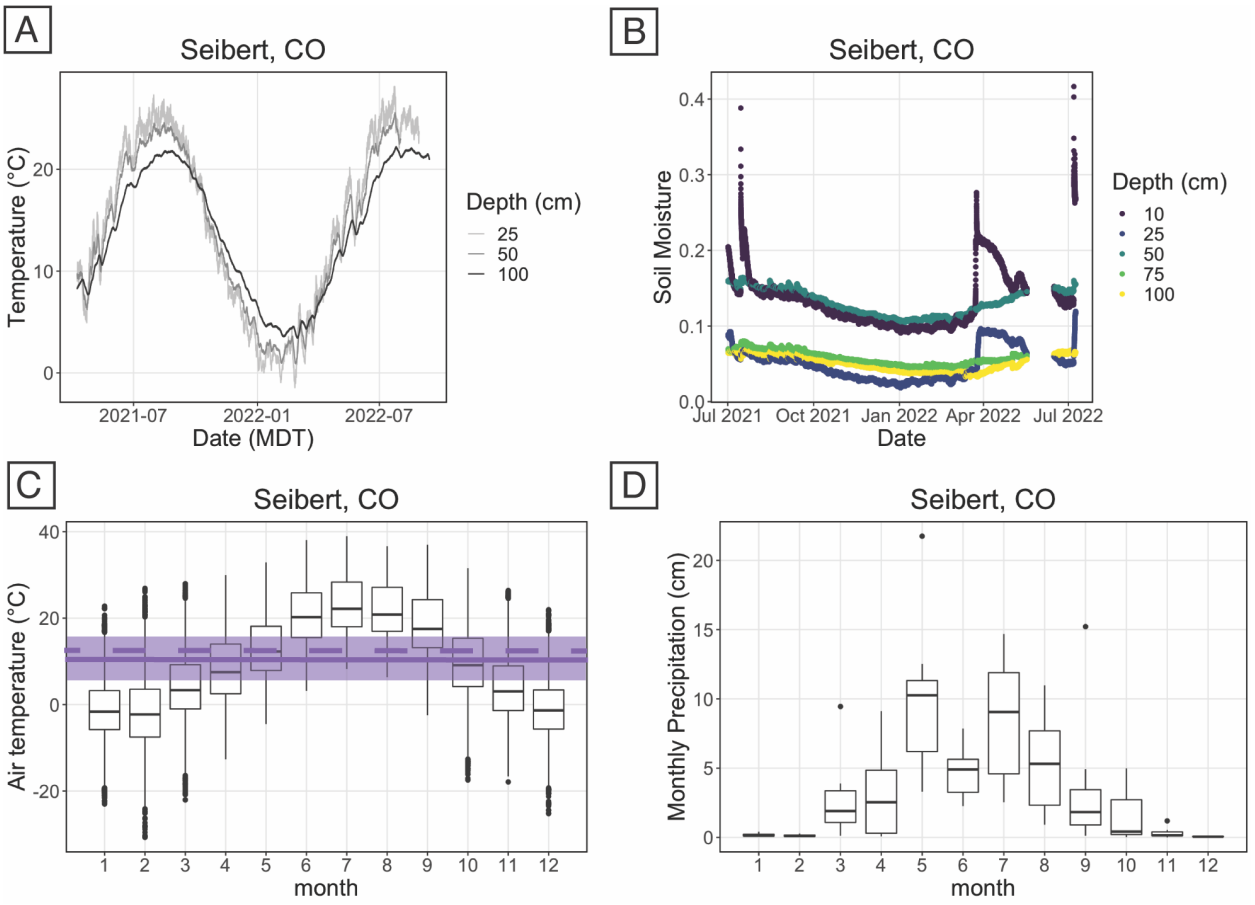

Figure 4-5 A) Soil temperature data measured from April 2021 – August 2022. B) Soil moisture data from July 2021 – July 2022. C) Box plot of monthly air temperature from 2016-2022. The purple line is the mean annual air temperature, and the purple highlight bar is the clumped isotope temperature estimate, uncertainty inclusive. D) Box plot of monthly precipitation total from 2016-2022.

4.4.3 Carbonate Nodule Characterization

The carbonate nodules at the ONG site are dominantly composed of micrite but include many other minerals including quartz and feldspars (Brookins, 2021). Microscopy revealed that the nodules are dominantly micrite with little microspar or spar. The micrite is non-luminescent to dully luminescent under CL, with small microspars that luminesce bright orange (SI Fig. 3, Brookins 2021). Two nodules from this site yield ^{14}C dates of 7220 ± 20 and 8765 ± 25 radiocarbon years BP, from depths of 75 and 100 cm, respectively. Two nodules, from depths of 75 cm and 95 cm yield $\delta^{13}C_C$ values of -3.27 ± 0.28‰ and -3.63± 0.12‰ (VPDB); $\delta^{18}O_C$ values of -8.77 ± 0.11‰ and -8.59 ± 0.06‰ (VPDB); T(Δ_{47}) values of 17.3 ±3.4°C and 18.7 ± 2.8°C (ICDES); and $\delta^{18}O_w$ values of -8.0 ± 0.8‰ and -7.5 ± 0.6‰ (VSMOW) (Fig 4-6, SI Table 1).

The carbonate nodules from Briggsdale have two primary textures: there is dense micrite with homogenous CL and a second, coarser texture that includes many other minerals (Supp. fig. 4-3, Brookins, 2021). In the dense micritic zones, the carbonate is dominantly non-luminescent under CL, with very few (1-2%) coarse crystalline spars that show bright orange luminescence. In the coarse, multi-mineral zones, the carbonate is non- to dully-luminescent under CL, with very few (1-2%) coarse crystalline spars. Carbonate nodules from 64 cm and 84 cm depth yield ^{14}C dates of 6980 ± 20 and 8200 ± 25 radiocarbon years BP, respectively. Two nodules from 50 cm and 105 cm yield $\delta^{13}C_C$ values of -2.55 ± 0.02‰ and -4.85± 0.01‰ (VPDB); $\delta^{18}O_C$ values of -7.77 ± 0.26‰ and -7.44 ± 0.06‰ (VPDB); T(Δ_{47})

values of 11.1 ±3.0°C and 4.1 ± 2.8°C (ICDES); $\delta^{18}O_w$ values of -8.3 ± 0.8‰ and -9.6 ± 0.6‰ (VSMOW) (Fig 4-6, SI Table 1).

The carbonate nodules from Seibert have micritic carbonate, often surrounding large potassium feldspar and quartz grains (SI Fig. 3). There is a notable range of other minerals included within nodules including amphiboles and zircon (Brookins, 2021). The carbonate is dominantly non-luminescent under CL, with the sparse inclusion of brightly orange luminescing spars (<1%). Two nodules from 75 cm and 100 cm depth yield ^{14}C dates of 9680 ± 30 and 7655 ± 25 radiocarbon years BP. Nodules from four levels (75, 80, 90, 100 cm) yielded $\delta^{13}C_C$ values between -0.85 ± 0.06‰ and -0.47± 0.03‰ (VPDB); $\delta^{18}O_C$ values between -7.1 ± 0.14‰ and -6.6 ± 0.12‰ (VPDB); $T(\Delta_{47})$ values between 8.4 ± 4.8°C and 14.6 ± 3.0°C (ICDES); $\delta^{18}O_w$ values between -6.9 ± 0.6‰ and -7.8 ± 1.0‰ (VSMOW) (Fig 4-6, SI Table 1).

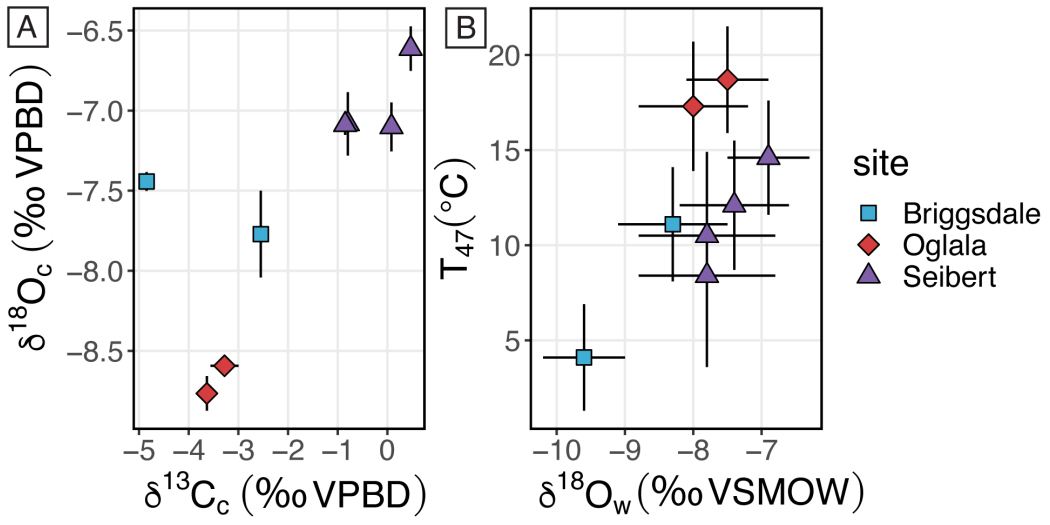

Figure 4-6. Clumped isotope results. A) $\delta^{13}C$ vs $\delta^{18}O$ of carbonate. B) $T(\Delta_{47})$ vs. calculated $\delta^{18}O$ of soil water

4.4.4 Water Isotope Geochemistry

I present results from samples of integrated monthly precipitation samples in figure 4-7, and I present the results from two months (June/July 2022 and September/October 2022) of ~weekly soil water samples in figure 4-8.

I collected integrated monthly precipitation samples in May 2022, September 2022 and October 2022 at the ONG site; $\delta^{18}O$ values ranged between -5.55‰ and -13.78‰, $\delta^{2}H$ values ranged between -34.6‰ and -98.4‰. The highest oxygen isotope values correspond to September 2022 (Table 4-1). I collected weekly soil water isotope samples in June-July 2022 and September 2022. During those two time periods, oxygen isotope values fell between -11.8 ± 1.0‰ and -16.83 ±1.0‰, with the exception of two data points from a soil depth of 25 cm in September that have oxygen isotope values of -1.6 ±1.0‰ and -2.8 ±1.0‰ (Fig. 4-8A). Similarly, the $\delta^{2}H$ values typically fall between -99.0 ± 3.5 ‰ and -120.6 ± 3.5‰, with the exception of 2 samples from 25 cm depth in September that have values of -7.6‰ and -32.9 ± 3.5‰ (Fig. 4-8A). Except for the two data points from a sampling depth of 25 cm, soil water isotope values at this site fall along the global meteoric water line (GMWL) (Fig. 4-8A).

At the Briggsdale site, I collected a monthly integrated sample of precipitation in May 2021, that had an average value of $\delta^{18}O$ = -13.43 ± 0.04‰ and $\delta^{2}H$ = 98.03 ± 0.1‰. I also collected integrated monthly precipitation samples from July 2022 – October 2022 with $\delta^{18}O$ values that ranged between -6.45 ± 0.05‰ and -4.57 ± 0.05‰, and $\delta^{2}H$ values ranged between -98.4‰ and -28.3‰ (Fig. 4-7). The oxygen isotope value of soil water from this site falls between -5.9 ± 1.0‰ and -12.1

± 1.0‰. The δ^2H values fall between -80.4 ± 3.5‰ and -61.1 ± 3.5‰ (Fig. 4-8B). The soil water data from 50 cm and 75 cm depths in July 2022 fall above the global meteoric water line, while soil water isotope values from September 2022 fall below the global meteoric water line.

At the Seibert site, the $\delta^{18}O$ of precipitation had values between -1.78 ± 0.04‰ and -13.52 ± 0.05‰ and δ^2H of precipitation had values between -100.0‰ and -12.1‰ during summer 2022 (Fig. 4-7). Oxygen isotope values for soil water fall between -4.7 ± 1.0‰ and -11.1 ± 1.0‰ (Fig. 4-8C). The δ^2H values fall between -76.4 ± 3.5 ‰ and -41.8 ± 3.5‰ (Fig. 4-8B). Samples from all depths in June 2022 and from 50 and 75 cm depths in September 2022 cluster around the GMWL. The shallow depth (25 cm) samples from September 2022 are offset to high $\delta^{18}O$ values and two of the samples fall below the GMWL.

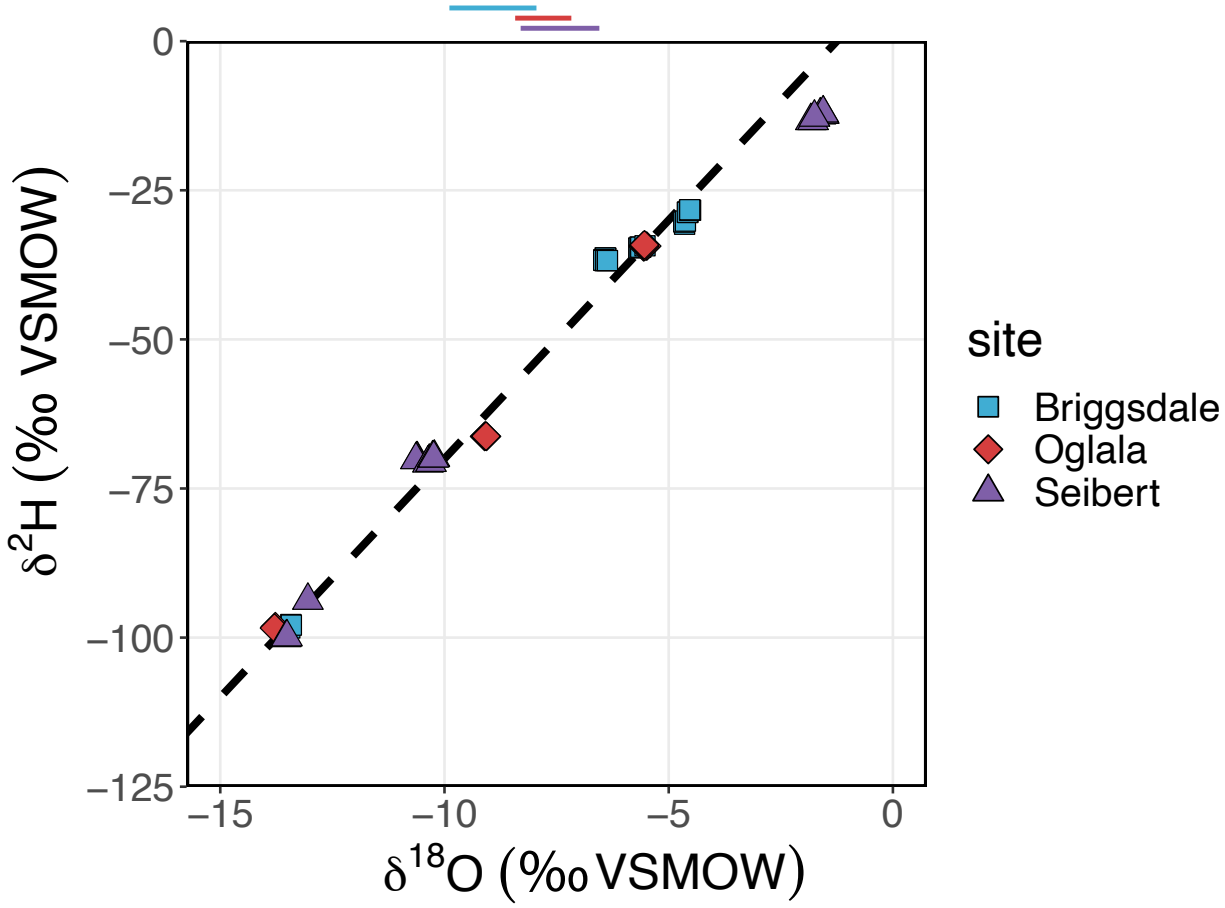

Figure 4-7. Plot of δ^2H vs $\delta^{18}O$ of integrated monthly samples of precipitation from the three field sites. The global meteoric water line is shown as a dashed line. The colored bars above the plot are the calculated $\delta^{18}O$ of soil water from the carbonate clumped isotope thermometry, uncertainty inclusive. The colors of the bars follows the legend; the blue bar is Briggsdale, the red bar is Oglala, and the purple bar is Seibert.

Table 4-1. Integrated monthly precipitation sample stable isotope results.

Sample Identifier	site	type	date	$\delta^{18}O$ (‰ VSMOW)	$\delta^{2}H$(‰ VSMOW)	d-excess (‰ VSMOW)
Briggsdale210507	Briggsdale	Precip	5/7/21	-13.45	-98.38	9.21
Briggsdale210507	Briggsdale	Precip	5/7/21	-13.43	-97.80	9.61
Briggsdale210507	Briggsdale	Precip	5/7/21	-13.41	-97.91	9.40
b080822	Briggsdale	Precip	8/8/22	-4.65	-30.69	6.48
b080822	Briggsdale	Precip	8/8/22	-4.65	-30.29	6.91
b080822_2	Briggsdale	Precip	8/8/22	-4.66	-30.31	7.01
b080822_2	Briggsdale	Precip	8/8/22	-4.63	-30.17	6.85
B71422	Briggsdale	Precip	7/14/22	-5.67	-34.67	10.68
B71422	Briggsdale	Precip	7/14/22	-5.64	-34.51	10.60
B71422_2	Briggsdale	Precip	7/14/22	-5.62	-34.54	10.44
B71422_2	Briggsdale	Precip	7/14/22	-5.53	-34.30	9.92
B_101422_1	Briggsdale	Precip	10/14/22	-6.42	-36.81	14.55
B_101422_1	Briggsdale	Precip	10/14/22	-6.40	-36.39	14.83
B_101422_1	Briggsdale	Precip	10/14/22	-6.42	-36.34	15.00
B_101422_1	Briggsdale	Precip	10/14/22	-6.41	-36.36	14.91
B_101422_2	Briggsdale	Precip	10/14/22	-6.45	-36.63	14.93
B_101422_2	Briggsdale	Precip	10/14/22	-6.45	-36.74	14.86
B_101422_2	Briggsdale	Precip	10/14/22	-6.40	-36.77	14.46
B_101422_2	Briggsdale	Precip	10/14/22	-6.37	-36.78	14.14
B_091522_1	Briggsdale	Precip	9/15/22	-4.57	-28.64	7.96
B_091522_1	Briggsdale	Precip	9/15/22	-4.57	-28.73	7.85
B_091522_1	Briggsdale	Precip	9/15/22	-4.58	-28.69	7.98
B_091522_2	Briggsdale	Precip	9/15/22	-4.51	-28.34	7.75
B_091522_2	Briggsdale	Precip	9/15/22	-4.54	-28.34	7.95
B_091522_2	Briggsdale	Precip	9/15/22	-4.53	-28.26	7.99
OglalaSurface210518	Oglala	Surface	5/18/21	-3.48	-52.50	-24.69
OglalaSurface210518	Oglala	Surface	5/18/21	-3.49	-52.43	-24.54
OglalaSurface210518	Oglala	Surface	5/18/21	-3.45	-52.10	-24.49
Meng210518	Oglala	Surface	5/18/21	-7.80	-71.93	-9.56
Meng210518	Oglala	Surface	5/18/21	-7.76	-71.74	-9.70
Meng210518	Oglala	Surface	5/18/21	-7.83	-71.85	-9.24
Sandcreek	Oglala	Surface	6/25/22	-9.30	-84.85	-10.49
Sandcreek	Oglala	Surface	6/25/22	-9.32	-84.81	-10.23
Sandcreek	Oglala	Surface	6/25/22	-9.30	-85.08	-10.70
OMay22	Oglala	Precip	5/19/22	-13.77	-98.16	12.01
OMay22	Oglala	Precip	5/19/22	-13.79	-98.39	11.94
O_102122_1	Oglala	Precip	10/21/22	-9.11	-66.28	6.57
O_102122_1	Oglala	Precip	10/21/22	-9.06	-66.27	6.23
O_102122_1	Oglala	Precip	10/21/22	-9.09	-66.23	6.50
O_102122_1	Oglala	Precip	10/21/22	-9.09	-66.23	6.51
O_102122_1	Oglala	Precip	10/21/22	-9.07	-66.23	6.35
O_091622_2	Oglala	Precip	9/16/22	-5.54	-34.18	10.12
O_091622_2	Oglala	Precip	9/16/22	-5.57	-34.31	10.22
O_091622_2	Oglala	Precip	9/16/22	-5.49	-34.36	9.56
O_091622_1	Oglala	Precip	9/16/22	-5.56	-34.49	9.99
O_091622_1	Oglala	Precip	9/16/22	-5.54	-34.42	9.87
O_091622_1	Oglala	Precip	9/16/22	-5.54	-34.16	10.17
Siebert2110	Seibert	Precip	10/15/21	-10.61	-70.06	14.80
Siebert2110	Seibert	Precip	10/15/21	-10.62	-70.07	14.88
Siebert2110	Seibert	Precip	10/15/21	-10.64	-70.20	14.89
S0522	Seibert	Precip	5/15/22	-13.05	-93.77	10.59
S071722	Seibert	Precip	7/17/22	-1.26	-15.90	-5.80
S071722	Seibert	Precip	7/17/22	-1.28	-16.36	-6.10
S071722	Seibert	Precip	7/17/22	-1.30	-15.85	-5.42
S61522	Seibert	Precip	6/15/22	-13.54	-100.03	8.27
S61522	Seibert	Precip	6/15/22	-13.51	-99.90	8.20

S_091222_1	Seibert	Precip	9/12/22	-1.56	-12.27	0.20
S_091222_1	Seibert	Precip	9/12/22	-1.62	-12.39	0.56
S_091222_1	Seibert	Precip	9/12/22	-1.54	-12.28	0.06
S_091222_1	Seibert	Precip	9/12/22	-1.56	-12.06	0.38
S_091222_2	Seibert	Precip	9/12/22	-1.83	-13.35	1.29
S_091222_2	Seibert	Precip	9/12/22	-1.78	-13.34	0.90
S_091222_2	Seibert	Precip	9/12/22	-1.39	-12.19	-1.10
S_091222_2	Seibert	Precip	9/12/22	-1.75	-12.77	1.22
S_101522_1	Seibert	Precip	10/15/22	-10.34	-70.47	12.24
S_101522_1	Seibert	Precip	10/15/22	-10.37	-70.76	12.18
S_101522_1	Seibert	Precip	10/15/22	-10.30	-70.65	11.76
S_101522_2	Seibert	Precip	10/15/22	-10.23	-69.79	12.02
S_101522_2	Seibert	Precip	10/15/22	-10.26	-69.91	12.20
S_101522_2	Seibert	Precip	10/15/22	-10.24	-69.91	12.01

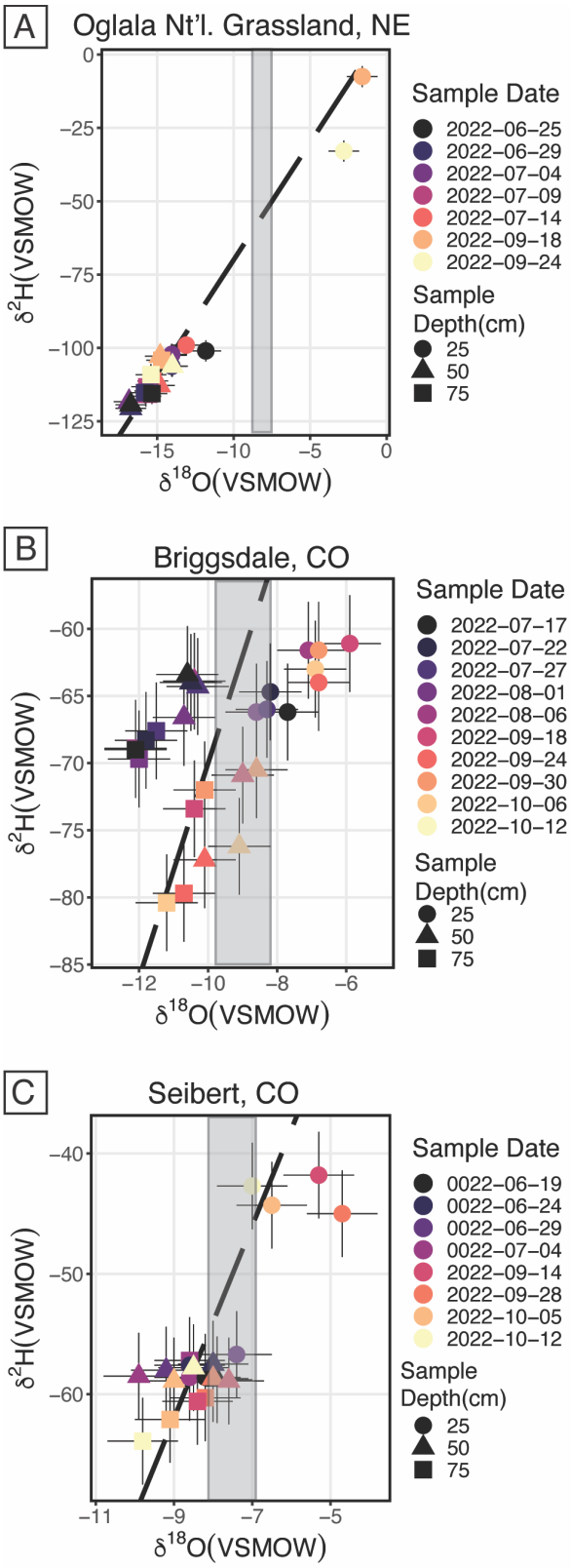

Figure 4-8. Swiss results for A) ONG, B) Briggsdale and C) Seibert. The vertical grey bar in each plot is the calculated $\delta^{18}O$ of soil water from the carbonate clumped isotope thermometry, uncertainty inclusive. The dashed line is the global meteoric water line.

4.5 Discussion

First, I discuss the assumptions associated with measuring modern environmental parameters and comparing those to pedogenic carbonate nodules that likely formed during the Holocene Climatic Optimum. Second, I integrate the climatological and stable isotope geochemistry data for each site individually. I then discuss the implications these data have for pedogenic carbonate formation mechanisms, and how that can and should inform future paleoclimate work. Lastly, I reflect on the limitations of this modern calibration study and how this work may be improved in the future.

4.5.1 Holocene Climate

The ^{14}C dates from the carbonate nodules from all three sites yielded dates between 6980 ± 20 and 9680 ± 30 years before present. These dates are consistent with carbonate nodule formation during the Holocene Climatic Optimum, which persisted from ~9 Ka – ~5Ka (Steig, 1999; Shuman and Marsisek, 2016). In North America, temperatures during the climatic optimum were 0-1°C warmer than pre-industrial conditions, similar to today (IPCC, 2021; Shuman and Marsisek, 2016). In North America, the mid-latitudes experienced a decrease in net precipitation during the Holocene Climatic Optimum, likely as a consequence of a northward shift of westerly storm tracks (e.g Shuman and Serravezza, 2017; Rouston et al., 2019). In southwestern Nebraska, stable carbon isotope values of soil organic matter are similar to present day values (Miao et al., 2007). The modern soil

temperature structure is likely an appropriate approximation of soil temperature conditions at the time of carbonate formation. Mid-latitude drying during the Holocene Climatic Optimum likely altered the annual temporal evolution of soil moisture in the studied soils. Modern observations of soil moisture patterns, especially the magnitude of soil water isotope change at carbonate bearing soil depths, is likely still an appropriate analogue.

4.5.2 Oglala National Grassland, NE

The soil at the ONG site is unique as compared to the other soils, in that it is the most clay rich, and that carbonate formation begins just below the Bt1 horizon with the greatest illuviation of clays (Fig 4-1C). This site is also unique in that it displays some vertic properties associated with the higher percentage of smectite clays; in the fall, (September-October) cracks from the Bt1 horizon extended upwards to the surface of the soil. Additionally, I observed long (5 - 10 cm) horizontal cracks in the soil that could potentially connect with cracks in the Bt1 horizon, providing conduits for soil degassing (Breecker et al., 2013) when I dug a soil pit in May 2021. Lastly, soil peds displayed small slickensides, consistent with shrink-swell behaviors associated with the presence of smectite clays.

At the ONG site, I observed small CAM plants, like the Plains Prickly Pear (*Opuntia polyacantha*), and many C4 grassland plants. The $\delta^{13}C_C$ values of ~ -3.5‰ of pedogenic carbonate at this site are consistent with the observed C4/CAM grassland landscape (Cerling, 1984; Levin et al., 2011; Montañez, 2013).

For the purpose of this study, I do not exclude any soil water isotope data from the ONG site. However, the water vapor concentration for samples from a sampling depth of 25 cm in September 2022 were considerably lower than other samples (i.e. <15,000 ppm), because the volumetric water content (VWC) of the soil at that time fell below 0.1 m^3/m^3; these samples are therefore rated as having moderate confidence. At this site, soil water values largely cluster together, except for two samples from a sampling depth of 25 cm in September 2022; those data are offset to significantly higher values (Fig. 8A). The soil water at carbonate bearing depths (50 and 75 cm) falls within error of the GMWL and does not show significant variability between June and September 2022. This is consistent with other observations of soil water isotope variability at depths greater than 50 cm (e.g. Quade et al., 2018; Oerter and Bowen, 2019). This observation is significant, because it challenges the conventional wisdom that the oxygen isotope value of water calculated from a paleosol carbonate T(Δ_{47}) values are most often evaporatively ^{18}O-enriched relative to the precipitation that sourced the water.

The nodules from the ONG site yield temperatures of 17.3 ± 3.4°C and 18.7 ± 2.8°C, the warmest of the three study sites (Fig. 4-6, Supp. Table 1). The clumped isotope temperature of pedogenic carbonate nodules overlaps within uncertainty of peak soil temperatures at carbonate-bearing depths (Fig. 3A). This corresponds with air temperatures from late spring and fall measured at the Alliance Mesonet Site (Fig. 4-3C). The T(Δ_{47}) at this site is 9-10°C warmer than mean annual air temperature (MAAT) at the Alliance Mesonet site. It is important to note that when

I compared summer 2021 soil temperatures from the ONG site to the Alliance mesonet site, I found that shallow soil depths (0 - 25 cm) are on average 2 - 5°C colder at the Alliance site, and are 1-2°C colder at depths of 75 - 100 cm. So, while the general pattern of a warm season bias holds, the exact timing and magnitude of peak soil temperatures at the ONG site may be slightly different.

At the ONG site, the $\delta^{18}O_w$ values calculated from the clumped isotope measurement do not overlap with measurements of $\delta^{18}O$ of precipitation in 2022, but are more similar to late summer and fall precipitation as opposed to late spring precipitation (Fig. 4-7). Similarly, the calculated $\delta^{18}O_w$ from the carbonate nodules does not overlap with measurements of soil water $\delta^{18}O$ from summer 2022. (Fig. 4-8A). There are three potential experimental or environmental explanations for the discrepancy between the calculated $\delta^{18}O_w$ and my measurements of soil water isotope composition. First, it is possible that there is unidentified isobaric contamination on mass-46 during the clumped isotope measurement; if the measurement yields an erroneously high value on mass-46, that would yield a higher than expected $\delta^{18}O_C$ value, and a warmer than expected $T(\Delta_{47})$ value. This explanation is unlikely given that the samples replicated well and that there was no indication of contamination on mass-48. However, I can test if contamination in these samples exists in two ways. First, the clumped isotope measurements on the ONG site nodules were from powder drilled from epoxy-mounted nodules, and so I could run a nodule that has not been previously mounted in epoxy to see if that was the potential source of contamination (all other nodules in this study were simply

crushed and homogenized with mortar and pestle). Second, I could "double-clean" a sample, meaning that the sample gas is collected after its first run through the vacuum-line, reintroduced prior to the first cleaning step, and is purified a second time prior to entering the mass spectrometer for measurement. The second explanation for the discrepancy between the $\delta^{18}O_w$ calculated from clumped isotope thermometry and soil water isotope values is that the calibration used with the SWISS data are inappropriate for this site. I used a simple temperature-based liquid-vapor calibration created for the vapor permeable probes (Rothfuss et al., 2013). There is no current community agreement on the standardization process for the water vapor probes; some work has shown that there is a significant soil-texture bias associated with the extraction method (e.g. Oerter et al., 2017), while others have not observed a significant soil texture bias (e.g. Quade et al., 2019). To test this hypothesis, I could complete a relatively simple calibration where soil samples are equilibrated with water of known isotope composition at a range of gravimetric water contents and temperatures to create a custom site and depth specific calibration (Oerter et al., 2017; Oerter and Bowen, 2019). The final potential explanation for the discrepancy between the calculated $\delta^{18}O_w$ from pedogenic carbonate and observed soil water isotope geochemistry is that the soil water isotope data I captured this summer do not represent typical conditions. From 2020-2022, La Niña conditions in the east equatorial Pacific Ocean have altered the timing and quantity of precipitation in the region. Figure 4-3b shows that soil

moisture at all depths has been relatively low from 2020-2022 as compared to the previous three years.

Finally, there is one carbonate formation mechanism that could explain both the warm temperatures and an apparent increase in the calculated $\delta^{18}O_w$. Rapid CO_2 degassing can produce kinetic isotope effects that result in lower (warmer) Δ_{47} and higher $\delta^{18}O$ values in carbonate minerals than the solution they form from (Affek and Zaruur, 2014; Tripati et al., 2015; Burgener et al., 2018; Guo, 2020). Given that the soil at the ONG site contains smectite group clays, and I have observed cracking of the soil surface in late summer and fall, it is possible that the soil rapidly degasses through vertical fractures that penetrate 10's of cm into the soil profile as has been observed in other vertisols (Breecker et al., 2013). One potential avenue for exploring if CO_2 degassing is an important carbonate formation mechanism at this site is dual Δ_{47}- Δ_{48} thermometry (Fiebig et al., 2021). This method exploits the measurement of Δ_{48} alongside the measurement of Δ_{47} evolved from the same sample gas, and because these two measurements *should* reflect the same formation temperature if the mineral formed in isotopic equilibrium, kinetic isotope effects can be identified as samples that do not yield equivalent temperatures. Our laboratory has the capability to produce this data, and so future work should incorporate dual-clumped isotope thermometry.

4.5.3 Briggsdale, CO

The land use history of the Briggsdale site over the last 150 years is not well known, but the dustbowl of the 1930's strongly affected the region; in the late 1930's the US government acquired the Pawnee National Grassland, which is less than 25 km away, because the land had become essentially non-arable. Generally, in the region, the topsoil was over-tilled, and the mollic epipedon was largely stripped away. So, it is possible that the upper horizons at this site have been altered within the last 100 years, and do not reflect the soil structure at the time of carbonate formation.

At the Briggsdale site, carbonate nodules form at the shallowest depths of all three sites, at a depth of ~50 cm. Clay particle size fraction in the soil profile slowly increases throughout the profile. There is no evidence of soil cracking associated with the presence of 2:1 silicate clay at this site.

Just like the Oglala site, the $\delta^{13}C_C$ values of pedogenic carbonate at this site are consistent with a C4 grassland landscape (Fig. 4-6A; Cerling, 1984; Levin et al., 2011; Montañez, 2013).

During initial Δ_{47} measurements of a nodule from a depth of 50 cm, I observed indications of isobaric contamination including unrealistically cold temperature (-46°C). After 'double-cleaning' the sample (process described above), I measured a temperature of ~11°C. This indicates that the contamination was on mass-47, resulting in a higher intensity signal on mass-47 than from the sample CO_2 alone. Using the double-cleaned sample from 50 cm depth and the sample at

105 cm depth, the clumped isotope temperatures overlap with the mean annual air temperature at this site; the difference between MAAT and T(Δ_{47}) is -4 - +3°C. At this site, mean soil temperature was ~3.5°C warmer than mean annual air temperature, indicating that radiative warming of the soil may be an important process at this site, and the interpreted timing of carbonate formation should account for this offset.

There are two months of soil water isotope data from this site: July-August 2022 and September-October 2022 (Fig. 4-8B). The soil water isotope data from July-August 2022 are regarded as low-moderate confidence samples; the samples from 25 cm in July-August had water vapor mixing concentrations below 15,000 ppm due to low soil moisture (<0.1 m^3/m^3 VWC), and the samples from both 50 and 75 cm depth fall unexpectedly above the GMWL (Fig. 4-8B). Similarly, due to low water vapor concentration (<15,000 ppm) I interpret the September-October 2022 samples from 25 cm depth as moderate confidence, but I interpret the samples from 50-75 cm as high-confidence soil water isotope samples. Despite having similar oxygen isotope values, the samples collected in July 2022 from depths of 50 cm and 75 cm have δ^2H values that are 10 - 15‰ higher than for soil water samples collected in September-October. It is challenging to hypothesize a mechanism that would alter the observed hydrogen isotope values, and not the oxygen isotope values of soil water. However, during previous mock-field tests of the SWISS (chapter 3, this dissertation), I observed that there is sometimes a positive offset in δ^2H values which is not reflected in the $\delta^{18}O$ values. The source of this error (i.e., during sample

collection vs. sample measurement) is still not known. Further testing of the SWISS should aim to determine this mechanism. These data highlight how important it is to have multiple months of data, so that spurious data can be identified.

The calculated $\delta^{18}O_w$ from the clumped isotope measurement (grey bar, Fig. 4-8B) overlaps within uncertainty of soil water from 50 cm depth measured in September and October of 2022. These data support the formation of pedogenic carbonate at this site in the late fall. The soil water data indicate that the preserved $\delta^{18}O_w$ calculated from a clumped isotope measurement may preserve the isotope signature of soil water that is only modestly evaporatively ^{18}O-enriched. Additional seasons of soil water from this site would help to elucidate the seasonal evolution of soil water isotopes in a fine-medium grained soil. Future work should also include creating a regional precipitation weighted mean isotope value using data from a nearby NEON site in Pawnee National Grassland, to understand how soil water isotopes at 50 and 75 cm relate to mean annual precipitation.

4.5.4 Seibert, CO

The depth of carbonate formation at the Seibert site is the deepest of the three sites at 75 cm. The nodules at this site also have a slightly different morphology than the other sites - they incorporate large fragments (>250 μm length) of other minerals like feldspar and quartz. Like the Oglala site, there is evidence of deep vertical cracks in the Btk horizon consistent with the presence of

2:1 shrink-swell clays, but unlike the Oglala site, I have not observed any evidence that cracks extend to the surface.

The $\delta^{13}C_C$ values of pedogenic carbonate is the highest of the three sites, but like the other two sites, is consistent with a C4 grassland environment (e.g. Cerling, 1984; Levin et al,. 2011; Montañez, 2013). The T(Δ_{47}) temperatures from this site overlap within uncertainty of mean annual air temperature; the residual between MAAT and T(Δ_{47}) is -2.2 - +4°C (Fig 5). At this site, radiative warming of the soil is small (~1.2°C), and so comparison of T(Δ_{47}) with air temperatures is appropriate at this site.

All of the soil water isotope data from this site, with the exception of the September-October 2022 soil water samples from 25 cm depth are viewed with high confidence. The 25 cm samples from September-October 2022 are viewed as moderate-confidence samples because of the lower water vapor concentration. Broadly the soil water isotope values from this site cluster together, except for the samples from a sampling depth of 25 cm in September-October 2022. The samples from 25 cm have higher oxygen and hydrogen isotope values, and data from 9/14/22 and 9/28/22 fall off the global meteoric water line. The return to the GMWL on 10/5/22 and 10/12/22 may be a product of the infiltration of precipitation from 9/30/22 and 10/4/22 at this site. However, data from 50 cm and 75 cm depth are relatively invariant across the nearly 4-month timespan. The calculated $\delta^{18}O_w$ values broadly have a higher value than the cluster of soil water isotope values from 2022, but they do overlap within uncertainty of samples of soil water from 50 and

75 cm depth from September 2022. These data suggest that the calculated $\delta^{18}O_w$ values from clumped isotope thermometry data reflect very little evaporative enrichment. Future work should use precipitation data from a nearby NEON site to create a precipitation weighted mean isotope value for the region, to understand how soil water isotopes at 50 and 75 cm relate to mean annual precipitation.

Together, the measurements of temperature and soil water isotope values suggest that carbonate formation is occurring in the fall or early spring at this site.

4.5.4 Site comparison and carbonate formation mechanism

4.5.4.1 Carbon Stable Isotopes

From all three sites, the carbon isotope values of the soil carbonates range between $\delta^{13}C$ = -4.85‰ – 0.47‰ (Figure 4-6). Broadly, all of these values are consistent with mixed C3-C4 landscapes that are dominated by C4 plants (Cerling, 1984; Montañez, 2013). At the ONG site, small CAM plants, like Plains Prickly Pear (*Opuntia polyacantha*), are also present and contribute to the preserved carbon isotope value of pedogenic carbonate. To first order, the carbon isotope values are consistent with pedogenic carbonate formation in equilibrium with soil organic matter (Montañez, 2013), however, future work could include directly measuring the $\delta^{13}C$ of soil organic matter at each of the sites to verify. The pre-industrial value of $\delta^{13}C$ of atmospheric CO_2 is approx. -6.5‰ (VPDB, NOAA), and the inclusion of atmospheric CO_2 typically results in higher $\delta^{13}C$ values of carbonate (Cerling, 1984).

4.5.4.2 Clumped Isotopes and the calculated $\delta^{18}O_w$

Pedogenic carbonate nodules from two of the three sites (Briggsdale and Seibert) in this study yield carbonate clumped isotope temperatures that overlap with MAAT. This result is consistent with other studies of fine to medium grained soils (Kelson et al., 2020). A temperature approximately equivalent to MAAT points to carbonate formation in either the fall or spring season. Huth et al. (2019) demonstrated that carbonate supersaturation, and therefore mineral formation, tends to occur episodically using a model of Ca^{2+} mass, rather than as a continuous process. Carbonate formation in the spring would be consistent with carbonate mineral formation being driven primarily by Ca^{2+} ion delivery with snowmelt infiltration pulses. Carbonate formation in the fall would be more consistent with soil-dry down as the driving mechanism of carbonate formation. The combination of the calculated $\delta^{18}O_w$ and the soil water isotope data from the Briggsdale and Seibert sites indicates that carbonate is forming in equilibrium with fall-season soil water. Though soil water data from the spring season is lacking, it seems unlikely that carbonate forms at that time, because otherwise I would expect a lower calculated $\delta^{18}O_w$ consistent with soil water sourced from snow-melt, as is seen in the soil water $\delta^{18}O_w$ data from May in the ONG site.

In contrast to the other two sites, at the ONG site, clumped isotope temperatures are ~10°C higher than MAAT. A 10°C residual between MAAT and $T(\Delta_{47})$ is comparable with what has been observed in coarse and very coarse-grained soils (Kelson et al., 2020), and has not previously been observed in other fine-

grained soils. The calculated $\delta^{18}O_w$ has significantly higher values than summer soil water at the depths of carbonate formation. Holocene climate variability is not able to sufficiently explain the difference between the calculated $\delta^{18}O_w$ values and the measured values (Shuman and Marsicek, 2016). There are a few ways to explain these data. The first explanation is that the pedogenic carbonate formed in isotopic equilibrium, at peak summer temperatures. Given that the calculated $\delta^{18}O$ of soil water is ~7‰ higher than isotope values of soil water I observed, this suggests some level of deeply penetrating soil cracks that allow for significant soil water evaporation at depth. The level of shrink behaviors of vertisols is typically commensurate with the level of swelling that occurred previously (Breecker et al., 2013B), and so it is possible that during generally wetter years (i.e. not La Niña), I would have observed evaporation of soil water at depth. The second option to explain these data is that carbonate formation occurs when the soil is warm and water-logged; in a warm, wet soil, carbonate formation could be driven by an increase in Ca^{2+} as a result of either hydrolysis or dissolution of $CaCO_3$, and by the reverse solubility of carbonate (Montañez, 2013). One way to test this hypothesis is to compare the $\delta^{13}C$ of carbonate to that of soil organic matter as a way to target the amount of atmospheric CO_2 in the soil; if the proportion of atmospheric CO_2 preserved by pedogenic carbonate is low, then this would be consistent with carbonate forming under water-logged conditions. Lastly, it is possible that the carbonate formed out of isotopic equilibrium with the soil DIC pool. Rapid CO_2 degassing would result in warmer than expected $T(\Delta_{47})$, and higher than expected

$\delta^{18}O_w$ values based on isotopic equilibrium (Tripati et al., 2015; Burgener et al., 2018). Rapid CO_2 degassing is possible in this soil during the late summer and fall when the soil dries, and cracks propagate to the surface. The soil at ONG is unique compared to the other two sites because clay content peaks above the level of carbonate formation, and it is the only site where soil cracks fully propagate to the surface.

My data do not mechanistically point to a single driver of carbonate formation (i.e. concentration of solute due to drying vs. CO_2 drawdown), but my data are consistent with carbonate formation as the soil dries in late fall at two of the sites. This timing would be consistent with many other studies of carbonate formation that suggest that soil dry-down is the primary driver of carbonate formation (Breecker et al., 2009; Hough et al., 2014; Huth et al., 2019; Kelson et al., 2020).

4.5.5 Implications for paleoclimate studies:

This study demonstrates that using the soil matrix grain size alone may not be sufficient to differentiate a pedogenic carbonate nodule that records a mean annual temperature versus one that records a significant apparent warm-season bias. However, in the rock record, the community may be able to use key features of fine-grained paleosols to diagnose horizons that may record an apparent warm season bias resulting from rapid CO_2 degassing. First the presence or absence of 2:1 shrink-swell clays and other diagnostic features like slickensides should provide a

first-order check. Without evidence of clay minerals that could contribute to shrink-swell behaviors in a fine-grained paleosol, then it is likely that pedogenic carbonate from fine grained soils, even those that include non-swelling clays, formed in equilibrium with the DIC pool, and are more likely to represent a mean annual temperature. In paleosols that do display evidence of shrink-swell behaviors, another key diagnostic feature may be how clay accumulation relates to the depth of carbonate formation. At the ONG site, the highest amount of clay accumulation occurs directly above the depth of carbonate formation, and then drops off. This suggests that carbonate begins to form at the level down to which cracks in the soil are able to propagate. However, this diagnostic feature may be challenging to evaluate in settings where the upper portions of a soil column are not preserved in the rock record. It may also be possible to exploit different facies within a stack of paleosols to examine if there is a temperature effect associated with clay content; an abrupt offset or change in the relationship between $T(\Delta_{47})$ and $\delta^{18}O_w$ could indicate a shift in carbonate formation dynamics. Lastly, dual Δ_{47}-Δ_{48} thermometry provides a way to evaluate if the Δ_{47} of a sample reflects kinetic isotope fractionation, rather than equilibrium temperature dependence (Fiebig et al., 2021).

4.5.6 Study limitations and future research

The largest limitation of this study is the timeframe and data resolution. I completed this research between December 2020 - October 2022, during which La Niña conditions affected the climate of the Western U.S. For example, in Alliance,

NE, observations at the Nebraska Mesonet site indicate a decrease in soil moisture at all depths in 2021 and 2022 as compared to 2017-2019. This suggests that both the precipitation samples and soil water samples I collected for stable isotope geochemistry may not be indicative of mean conditions at my sites. Furthermore, I was only able to collect soil water during two months, and integrated monthly precipitation samples over one summer season. The conclusions of this study about the timing of carbonate formation could be strengthened by the creation of longer soil water isotope records. In particular, records of spring soil water (early April - May) would help provide control on the magnitude of seasonal variability present in the isotope composition of soil water at the carbonate bearing depths. For the purposes of this study, a longer soil temperature record at the ONG site would also strengthen the comparison with the Alliance, NE Mesonet site data.

To strengthen the clumped isotope data from both the Briggsdale and Seibert sites, additional clumped isotope analyses that use a 'double-cleaning' method, where sample gas passes through the vacuum extraction line ("autoline") twice, would help to confirm observed cold temperatures (e.g. $T(\Delta_{47}) = 4°C$ at Briggsdale) and to improve the replication of other samples (i.e. S75-80, S100).

The data from the ONG site are very exciting in that they suggest multiple pathways for future work. First, improved observations of soil moisture and temperature at the field site will help to strengthen the link between a warm-season biased soil temperature and the measured clumped isotope temperatures. Further, longer soil water isotope datasets and precipitation isotope data sets may

help to elucidate the cause of the discrepancy between observed water isotopes and the calculated $\delta^{18}O$ of soil water from clumped isotope thermometry. To make these data as robust as possible, a soil-depth specific calibration for the soil water isotope data should be created for this field site (Oerter and Bowen, 2017). Second, to test the hypothesis that carbonate is forming when the soil is warm and water logged, soil organic matter from the carbonate bearing horizon from multiple near-by locations (within 25 m) should be measured. Third, to test the hypothesis that carbonate is forming outside of homogenous isotopic equilibrium as a result of CO_2 degassing, samples should be run at high enough precisions that allow for the simultaneous measurement of Δ_{48} (Fiebig et al., 2021). This final hypothesis also predicts that carbonate formation should be occurring at the edges of and bottom of cracks in the soil, and so re-analysis of a soil-pit with special care given to the relationship between the location of carbonate nodules and geomorphic features (i.e. slickensides). Lastly, the field sites in Briggsdale, CO and Seibert, CO were especially successful because of my partnership with CoAgMet sites, and my ability to use long-term climatological data. Finding ways to partner with the Nebraska and South Dakota MesoNet networks to find additional clay-rich soils that are carbonate bearing and have long climatological records may prove a fruitful way forward to test which of my observations are universal across clay-rich soils vs. which are site-specific.

4.6 Conclusions

In this study, I present data on carbonate formation in three modern soils from Colorado and Nebraska, USA. These three soils span soil textures from loamy sand (medium grained) to silty loam (fine grained), and offer a perspective on how clay content influences carbonate formation. This fills a critical gap in literature on pedogenic carbonate formation and clumped isotopes, which have previously primarily focused on medium - coarse grained soils. To understand the timing of pedogenic carbonate precipitation I monitored soil moisture, soil temperature, and the stable isotope geochemistry of both precipitation and soil water at the three field sites. Additionally, I use longer-term climate data from 3 mesonet sites; the mesonet sites are co-located with the two field sites in Colorado, and in Nebraska the mesonet site is approximately 100 km from the field site. I compared all of the data on modern climate and soil conditions to the clumped isotope thermometry from pedogenic carbonate nodules at all three sites.

All three field sites are characterized by dominant summer-season precipitation, with soil dry down likely occurring in the fall. Mean annual air temperature at the sites ranges from 8.5 - 10.6°C. Clumped isotope temperatures from pedogenic carbonate overlap with MAAT at both sites in Colorado, but clumped isotope temperatures are 9-10°C warmer than MAAT at the most clay-rich field site in Nebraska. Similarly, the $\delta^{18}O$ of soil water calculated from the clumped isotope temperatures overlap within uncertainty of the isotope composition of soil water from September and October at carbonate bearing depths at both sites in

Colorado. In contrast, at the Nebraska site, the calculated $\delta^{18}O$ of soil water is about 7‰ heavier than observations of modern soil water at carbonate bearing depths. I hypothesize that pedogenic carbonate is forming in isotopic equilibrium with the DIC pool during fall soil dry down at both sites in Colorado, while at the Nebraska site pedogenic carbonate forms from rapid CO_2 degassing as the soil shrinks in response to soil dry-down. Future work on this subject should include dual Δ_{47}-Δ_{48} thermometry, which may be able to shed light on the role of CO_2 degassing on pedogenic carbonate formation in clay-rich soils.

Works Cited

Affek, H. P., & Zaarur, S. (2014). Kinetic isotope effect in CO2 degassing: Insight from clumped and oxygen isotopes in laboratory precipitation experiments. *Geochimica et Cosmochimica Acta*, *143*, 319–330. https://doi.org/10.1016/j.gca.2014.08.005

Anderson, N. T., Kelson, J. R., Kele, S., Daëron, M., Bonifacie, M., Horita, J., Mackey, T. J., John, C. M., Kluge, T., Petschnig, P., Jost, A. B., Huntington, K. W., Bernasconi, S. M., & Bergmann, K. D. (2021). A unified clumped isotope thermometer calibration (0.5–1100°C) using carbonate-based standardization. *Geophysical Research Letters*, 1–11. https://doi.org/10.1029/2020gl092069

Bernasconi, S. M., Daëron, M., Bergmann, K. D., Bonifacie, M., Meckler, A. N., Affek, H. P., Anderson, N., Bajnai, D., Barkan, E., Beverly, E., Blamart, D., Burgener, L., Calmels, D., Chaduteau, C., Clog, M., Davidheiser-Kroll, B., Davies, A., Dux, F., Eiler, J., … Ziegler, M. (2021). InterCarb: A Community Effort to Improve Interlaboratory Standardization of the Carbonate Clumped Isotope Thermometer Using Carbonate Standards. *Geochemistry, Geophysics, Geosystems*, *22*(5). https://doi.org/10.1029/2020GC009588

Breecker, D. O., Sharp, Z. D., & McFadden, L. D. (2009). Seasonal bias in the formation and stable isotopic composition of pedogenic carbonate in modern soils from central New Mexico, USA. *Bulletin of the Geological Society of America*, *121*(3–4), 630–640. https://doi.org/10.1130/B26413.1

Breecker, D. O., Sharp, Z. D., & McFadden, L. D. (2010). Atmospheric CO2 concentrations during ancient greenhouse climates were similar to those predicted for A.D. 2100. *Proceedings of the National Academy of Sciences of the United States of America*, *107*(2), 576–580. https://doi.org/10.1073/pnas.0902323106

Breecker, D. O. (2013). Quantifying and understanding the uncertainty of atmospheric CO2 concentrations determined from calcic paleosols. *Geochemistry, Geophysics, Geosystems*, *14*(8), 3210–3220. https://doi.org/10.1002/ggge.20189

Breecker, D. O., Yoon, J., Michel, L. A., Dinka, T. M., Driese, S. G., Mintz, J. S., Nordt, L. C., Romanak, K. D., & Morgan, C. L. S. (2013). CO2 Concentrations in Vertisols: Seasonal Variability and Shrink–Swell. *SEPM Special Publication No. 104: New Frontiers in Paleopedology and Terrestrial Paleoclimatology: Paleosols and Soil Surface Analog Systems*, *104*, 35–45. https://doi.org/10.2110/sepmsp.104.08

Brookins, S., 2021. Texture and mineralogy: how soil characteristics help to understand soil formation (Honors thesis, University of Colorado at Boulder).

Burgener, L. K., Huntington, K. W., Hoke, G. D., Schauer, A., Ringham, M. C., Latorre, C., & Díaz, F. P. (2016). Variations in soil carbonate formation and seasonal bias over >4 km of relief in the western Andes (30°S) revealed by clumped isotope thermometry. *Earth and Planetary Science Letters*, *441*, 188–199. https://doi.org/10.1016/j.epsl.2016.02.033

Burgener, L. K., Huntington, K. W., Sletten, R., Watkins, J. M., Quade, J., & Hallet, B. (2018). Clumped isotope constraints on equilibrium carbonate formation and kinetic isotope effects in freezing soils. *Geochimica et Cosmochimica Acta*, *235*, 402–430. https://doi.org/10.1016/j.gca.2018.06.006

Carrapa, B., Huntington, K. W., Clementz, M., Quade, J., Bywater-Reyes, S., Schoenbohm, L. M., & Canavan, R. R. (2014). Uplift of the Central Andes of NW Argentina associated with upper crustal shortening, revealed by multiproxy isotopic analyses. *Tectonics*, *33*(6), 1039–1054. https://doi.org/10.1002/2013TC003461

Cerling, T. E. (1984). The stable isotopic composition of modern soil carbonate and its relationship to climate. *Earth and Planetary Science Letters*, *71*, 229–240.

Cerling, T. E., & Quade, J. (1993). Stable Carbon and Oxygen Isotopes in Soil Carbonates. *Geophysical Monograph Series*, *78*, 217–231.

Cerling, T. E., Solomon, D. K., Quade, J., & Bowman, J. R. (1991). On the isotopic composition of carbon in soil carbon dioxide. *Geochimica et Cosmochimica Acta*, *55*(11), 3403–3405. https://doi.org/10.1016/0016-7037(91)90498-T

CoAgMet. Colorado State University, Fort Collins, Colorado. http://www.coagmet.colostate.edu/. Accessed 11/9/2022.

Coplen, T. B. (2011). Guidelines and recommended terms for expression of stable-isotope-ratio and gas-ratio measurement results. *Rapid Communications in Mass Spectrometry*, *25*(17), 2538–2560. https://doi.org/10.1002/rcm.5129

Craig, H., (1961), Isotopic variations in meteoric waters. *Science*, *133*(3465), pp.1702-1703.

Dansgaard, W. (1964). Stable isotopes in precipitation. *Tellus*, 436–468. https://doi.org/10.3402/tellusa.v16i4.8993

DeCelles, P. G., Quade, J., Kapp, P., Fan, M., Dettman, D. L., & Ding, L. (2007). High and dry in central Tibet during the Late Oligocene. *Earth and Planetary Science Letters*, *253*(3–4), 389–401. https://doi.org/10.1016/j.epsl.2006.11.001

Dennis, K. J., Affek, H. P., Passey, B. H., Schrag, D. P., & Eiler, J. M. (2011). Defining an absolute reference frame for "clumped" isotope studies of CO 2. *Geochimica et Cosmochimica Acta*, *75*(22), 7117–7131. https://doi.org/10.1016/j.gca.2011.09.025

Eiler, J. M. (2007). "Clumped-isotope" geochemistry-The study of naturally-occurring, multiply-substituted isotopologues. *Earth and Planetary Science Letters*, *262*(3–4), 309–327. https://doi.org/10.1016/j.epsl.2007.08.020

Fiebig, J., Daëron, M., Bernecker, M., Guo, W., Schneider, G., Boch, R., Bernasconi, S. M., Jautzy, J., & Dietzel, M. (2021). Calibration of the dual clumped isotope thermometer for carbonates. *Geochimica et Cosmochimica Acta*, *312*, 235–256. https://doi.org/10.1016/J.GCA.2021.07.012

Fischer-Femal, B. J., & Bowen, G. J. (2021). Coupled carbon and oxygen isotope model for pedogenic carbonates. *Geochimica et Cosmochimica Acta*, *294*, 126–144. https://doi.org/10.1016/j.gca.2020.10.022

Garzione, C. N., Molnar, P., Libarkin, J. C., & MacFadden, B. J. (2006). Rapid late Miocene rise of the Bolivian Altiplano: Evidence for removal of mantle lithosphere. *Earth and Planetary Science Letters*, *241*(3–4), 543–556. https://doi.org/10.1016/j.epsl.2005.11.026

Gat, J. R. (1996). Oxygen and Hydrogen Isotopes in the Hydrologic Cycle. *Annual Reviews in Earth and Planetary Science*, 1–38. https://doi.org/10.1146/annurev.earth.24.1.225

Ghosh, P., Garzione, C. N., & Eiler, J. M. (2006). Rapid Uplift of the Altiplano Revealed Through 13C-18O Bonds in Paleosol Carbonates. *Science*, *311*(January), 511–515.

Guo, W. (2020). Kinetic clumped isotope fractionation in the DIC-H2O-CO2 system: Patterns, controls, and implications. *Geochimica et Cosmochimica Acta*, *268*, 230–257. https://doi.org/10.1016/j.gca.2019.07.055

Havranek, R.E., Snell, K.E., Kopf, S.H., Davidheiser-Kroll, B., Morris, V. and Vaughn, B., *In Review*. Lessons from and best practices for the deployment of the Soil Water Isotope Storage System. *EGUsphere*, pp.1-29.

Hillel, D. (1998). *Environmental Soil Physics*. Academic Press.

Hough, B. G., Fan, M., & Passey, B. H. (2014). Calibration of the clumped isotope geothermometer in soil carbonate in Wyoming and Nebraska , USA : Implications for paleoelevation and paleoclimate reconstruction. *Earth and Planetary Science Letters*, *391*, 110–120. https://doi.org/10.1016/j.epsl.2014.01.008

Huntington, K. W., & Lechler, A. R. (2015). Carbonate clumped isotope thermometry in continental tectonics. *Tectonophysics*, *647*, 1–20. https://doi.org/10.1016/j.tecto.2015.02.019

Huntington, K. W., Eiler, J. M., Affek, H. P., Guo, W., Bonifacie, M., Yeung, L. Y., Thiagarajan, N., Passey, B., Tripati, A., Daëron, M., & Came, R. (2009). Methods and limitations of "clumped" CO2 isotope (Δ47) analysis by gas-source isotope ratiomass spectrometry. *Journal of Mass Spectrometry*, *44*(9), 1318–1329. https://doi.org/10.1002/jms.1614

Huth, T. E., Cerling, T. E., Marchetti, D. W., Bowling, D. R., Ellwein, A. L., & Passey, B. H. (2019). Seasonal bias in soil carbonate formation and its implications for interpreting high-resolution paleoarchives: evidence from southern Utah. *Journal of Geophysical Research: Biogeosciences*. https://doi.org/10.1029/2018JG004496

IPCC (2021). Masson-Delmotte, V.; Zhai, P.; Pirani, A.; Connors, S. L.; et al. (eds.). *Climate Change 2021: The Physical Science Basis* (PDF). Contribution of Working Group I to the Sixth Assessment Report of the Intergovernmental Panel on Climate Change. Cambridge University Press (In Press). p. SPM-9

Ingalls, M., Rowley, D., Olack, G. A., Currie, B., Li, S., Schmidt, J., Tremblay, M., Polissar, P., Shuster, D. L., Lin, D., & Colman, A. (2018). Paleocene to Pliocene low-latitude, high-elevation basins of southern Tibet: Implications for tectonic models of India-Asia collision, Cenozoic climate, and geochemical weathering.

Bulletin of the Geological Society of America, *130*(1–2), 307–330. https://doi.org/10.1130/B31723.1

Kelson, J. R., Watford, D., Bataille, C., Huntington, K. W., Hyland, E., & Bowen, G. J. (2018). Warm Terrestrial Subtropics During the Paleocene and Eocene: Carbonate Clumped Isotope (Δ47) Evidence From the Tornillo Basin, Texas (USA). *Paleoceanography and Paleoclimatology*, *33*(11), 1230–1249. https://doi.org/10.1029/2018PA003391

Kelson, J. R., Huntington, K. W., Breecker, D. O., Burgener, L. K., Gallagher, T. M., Hoke, G. D., & Petersen, S. v. (2020). A proxy for all seasons ? A synthesis of clumped isotope data from Holocene soil carbonates. *Quaternary Science Reviews*, *234*, 106259. https://doi.org/10.1016/j.quascirev.2020.106259

Kim, S.-T., & O'Neil, J. R. (1997). Equilibrium and nonequilibrium oxygen isotope effects in synthetic carbonates. *Geochimica et Cosmochimica Acta*, *61*(16), 3461–3475. https://doi.org/10.1016/S0016-7037(97)00169-5

Kopf, S., Davidheiser-Kroll, B. and Kocken, I., (2021). Isoreader: An R package to read stable isotope data files for reproducible research. *Journal of Open Source Software*, *6*(61), p.2878.

Levin, N. E., Brown, F. H., Behrensmeyer, A. K., Bobe, R., & Cerling, T. E. (2011). Paleosol carbonates from the Omo Group : Isotopic records of local and regional environmental change in East Africa. *Palaeogeography, Palaeoclimatology, Palaeoecology*, *307*, 75–89. https://doi.org/10.1016/j.palaeo.2011.04.026

Levin, N. E., Quade, J., Simpson, S. W., Semaw, S., & Rogers, M. (2004). Isotopic evidence for Plio-Pleistocene environmental change at Gona, Ethiopia. *Earth and Planetary Science Letters*, *219*(1–2), 93–110. https://doi.org/10.1016/S0012-821X(03)00707-6

Miao, X., Mason, J. A., Johnson, W. C., & Wang, H. (2007). High-resolution proxy record of Holocene climate from a loess section in Southwestern Nebraska, USA. *Palaeogeography, Palaeoclimatology, Palaeoecology*, *245*(3–4), 368–381. https://doi.org/10.1016/j.palaeo.2006.09.004

Montanez, I. P. (2013). Modern soil system constraints on reconstructing deep-time atmospheric CO 2. *Geochemica et Cosmochimica Acta*, *101*(January 2013), 57–75.

Oerter, E. J., Perelet, A., Pardyjak, E., & Bowen, G. J. (2016). Membrane inlet laser spectroscopy to measure H and O stable isotope compositions of soil and sediment pore water with high sample throughput. *Rapid Communications in Mass Spectrometry*, *31*(1), 75–84. https://doi.org/10.1002/rcm.7768

Oerter, E. J., & Bowen, G. J. (2017). In situ monitoring of H and O stable isotopes in soil water reveals ecohydrologic dynamics in managed soil systems. *Ecohydrology*, *10*(4), 1–13. https://doi.org/10.1002/eco.1841

Oerter, E. J., & Amundson, R. (2016). Climate controls on spatial temporal variations in the formation of pedogenic carbonate in the western Great Basin of North Americ. *Bulletin of the Geological Society of America*, *128*(7), 1095–1104. https://doi.org/10.1130/B31367.1

Pagel, M., Barbin, V., Blanc, P. and Ohnenstetter, D., (2000). Cathodoluminescence in geosciences: an introduction (pp. 1-21). Springer Berlin Heidelberg.

Passey, B. H. (2012). Reconstructing terrestrial environments using stable isotopes in fossil teeth and paleosol carbonates. *Reconstructing Earth's Deep-Time Climate*, *18*, 167–193. https://doi.org/10.1017/S1089332600002606

Peters, N. A., Huntington, K. W., & Hoke, G. D. (2013). Hot or not? Impact of seasonally variable soil carbonate formation on paleotemperature and O-isotope records from clumped isotope thermometry. *Earth and Planetary Science Letters*, *361*, 208–218. https://doi.org/10.1016/j.epsl.2012.10.024

Quade, J., Cerling, T. E., & Bowman, J. R. (1989). Systematic variations in the carbon and oxygen isotopic composition of pedogenic carbonate along elevation transects in the southern Great Basin, United States. *Geological Society of America Bulletin*, *101*(4), 464–475. https://doi.org/10.1130/0016-7606(1989)101<0464:SVITCA>2.3.CO;2

Quade, M., Klosterhalfen, A., Graf, A., Brüggemann, N., Hermes, N., Vereecken, H., & Rothfuss, Y. (2019). In-situ monitoring of soil water isotopic composition for partitioning of evapotranspiration during one growing season of sugar beet (Beta vulgaris). *Agricultural and Forest Meteorology*, *266–267*(December 2018), 53–64. https://doi.org/10.1016/j.agrformet.2018.12.002

Rothfuss, Y., Vereecken, H., & Brüggemann, N. (2013). Monitoring water stable isotopic composition in soils using gas-permeable tubing and infrared laser

absorption spectroscopy. *Water Resources Research*. https://doi.org/10.1002/wrcr.20311

Routson, C.C., McKay, N.P., Kaufman, D.S., Erb, M.P., Goosse, H., Shuman, B.N., Rodysill, J.R. and Ault, T., (2019). Mid-latitude net precipitation decreased with Arctic warming during the Holocene. *Nature*, *568*(7750), pp.83-87.

Rozanski, K., Araguas-Araguas, L., & Gonfiantini, R. (1993). Isotopic Patterns in Modern Global Precipitation. *Geophysical Monograph Series*, *78*, 1–36.

Rugenstein, J. K. C., & Chamberlain, C. P. (2018). The evolution of hydroclimate in Asia over the Cenozoic: A stable-isotope perspective. *Earth-Science Reviews*, *185*(May), 1129–1156. https://doi.org/10.1016/j.earscirev.2018.09.003

Schauble, E. A., Ghosh, P., & Eiler, J. M. (2006). Preferential formation of 13C-18O bonds in carbonate minerals, estimated using first-principles lattice dynamics. *Geochimica et Cosmochimica Acta*, *70*(10), 2510–2529. https://doi.org/10.1016/j.gca.2006.02.011

Scholl, M. A., Ingebritsen, S. E., Janik, C. J., & Kauahikaua, J. P. (1996). Use of precipitation and groundwater isotopes to interpret regional hydrology on a tropical volcanic island: Kilauea volcano area, Hawaii. *Water Resources Research*, *32*(12), 3525–3537. https://doi.org/10.1029/95WR02837

Shuman, B. N., & Marsicek, J. (2016). The structure of Holocene climate change in mid-latitude North America. *Quaternary Science Reviews*, *141*, 38–51. https://doi.org/10.1016/j.quascirev.2016.03.009

Shuman, B. N., & Serravezza, M. (2017). Patterns of hydroclimatic change in the Rocky Mountains and surrounding regions since the last glacial maximum. *Quaternary Science Reviews*, *173*, 58–77. https://doi.org/10.1016/j.quascirev.2017.08.012

Snell, K. E., Thrasher, B. L., Eiler, J. M., Koch, P. L., Sloan, L. C., & Tabor, N. J. (2013). Hot summers in the Bighorn Basin during the early Paleogene. *Geology*, *41*(1), 55–58. https://doi.org/10.1130/G33567.1

Steig, E.J., (1999). Mid-Holocene climate change. *Science*, *286*(5444), pp.1485-1487.

Stuiver, M. and Polach, H.A., (1977). Discussion reporting of 14C data. *Radiocarbon*, *19*(3), pp.355-363.

Tripati, A. K., Hill, P. S., Eagle, R. A., Mosenfelder, J. L., Tang, J., Schauble, E. A., Eiler, J. M., Zeebe, R. E., Uchikawa, J., Coplen, T. B., Ries, J. B., & Henry, D. (2015). Beyond temperature: Clumped isotope signatures in dissolved inorganic carbon species and the influence of solution chemistry on carbonate mineral composition. *Geochimica et Cosmochimica Acta*, *166*, 344–371. https://doi.org/10.1016/j.gca.2015.06.021

Uno, K. T., Cerling, T. E., Harris, J. M., Kunimatsu, Y., Leakey, M. G., Nakatsukasa, M., & Nakaya, H. (2011). Late Miocene to Pliocene carbon isotope record of differential diet change among East African herbivores. *Proceedings of the National Academy of Sciences*, *108*(16), 6509–6514. https://doi.org/10.1073/pnas.1018435108

Weil, R. R., & Brady, N. C. (2017). *The Nature and Properties of Soils* (15th editi). Pearson Education.

Zamanian, K., Pustovoytov, K., & Kuzyakov, Y. (2016). Pedogenic carbonates : Forms and formation processes. *Earth Science Reviews*, *157*, 1–17. https://doi.org/10.1016/j.earscirev.2016.03.003

Zeebe, R. E., & Wolf-Gladrow, D. A. (2001). CO2 in seawater: equilibium, kinetics and isotopes. In *Elselvier Oceanography Series* (Vol. 65). Elsevier Science.

Supplemental Information

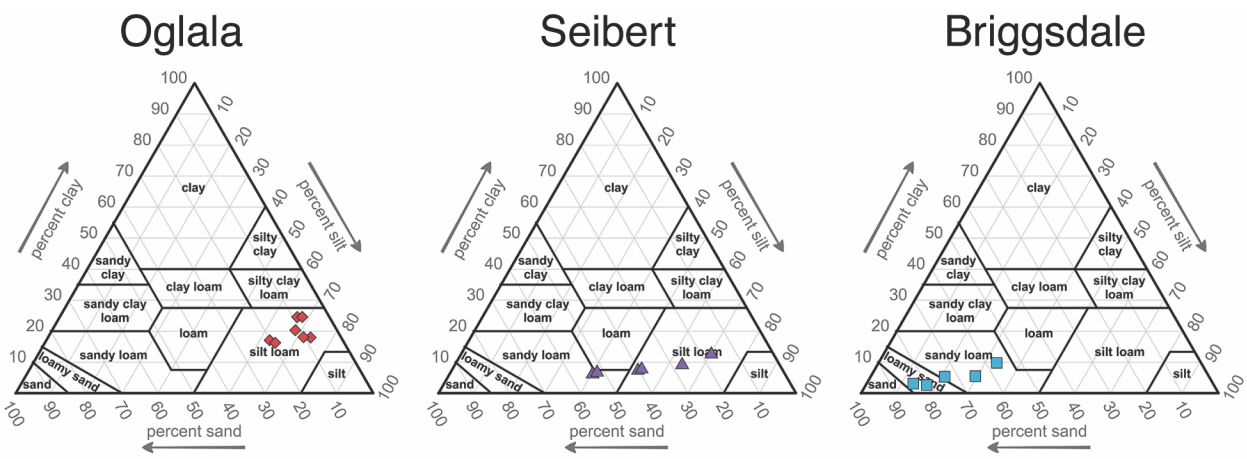

Supplemental Figure 4-1. Soil texture triangles for Oglala National Grassland, NE; Seibert, CO; and, Briggsdale, CO.

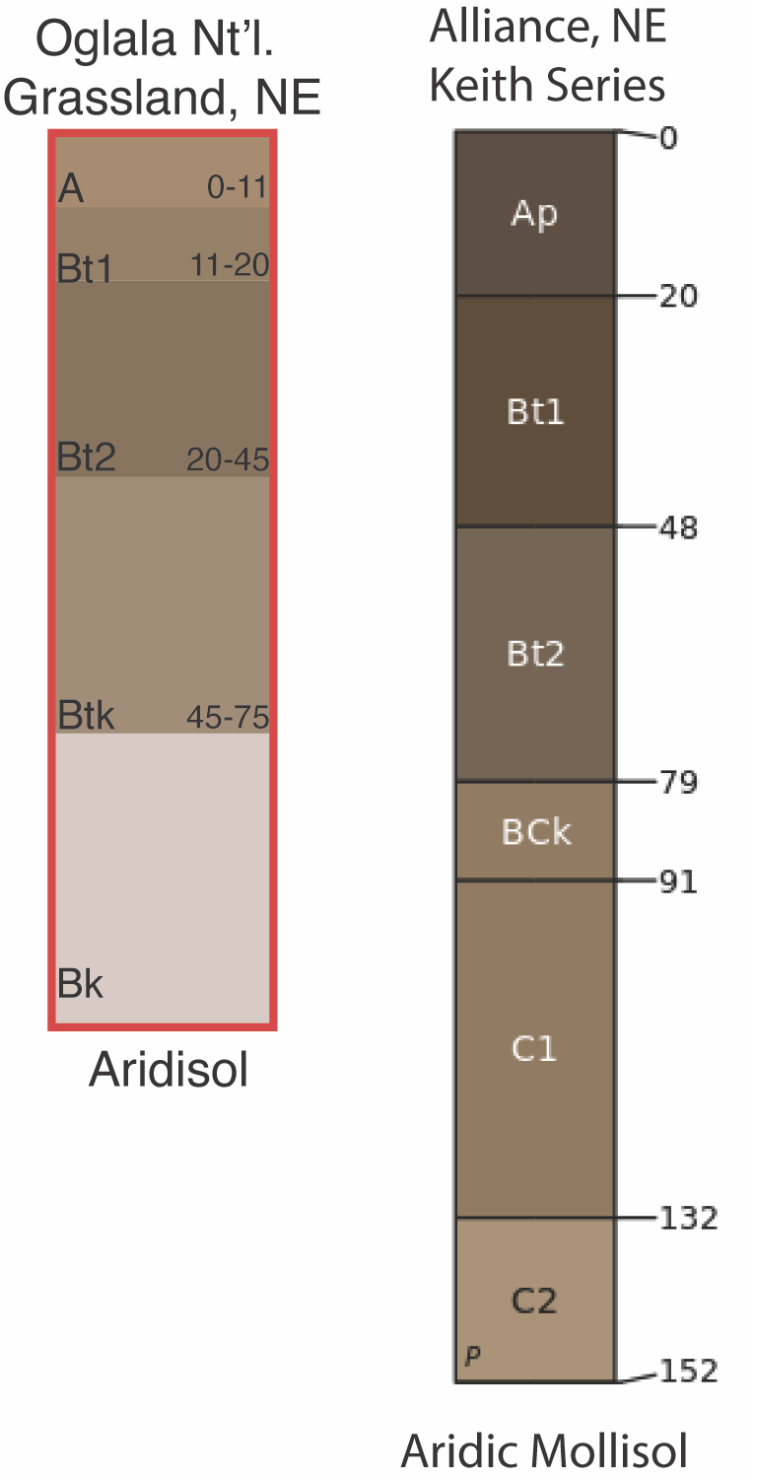

Supplemental Figure 4-2. Comparison of the Keith soil series at the Alliance Nebraska Mesonet site and Oglala National Grassland.

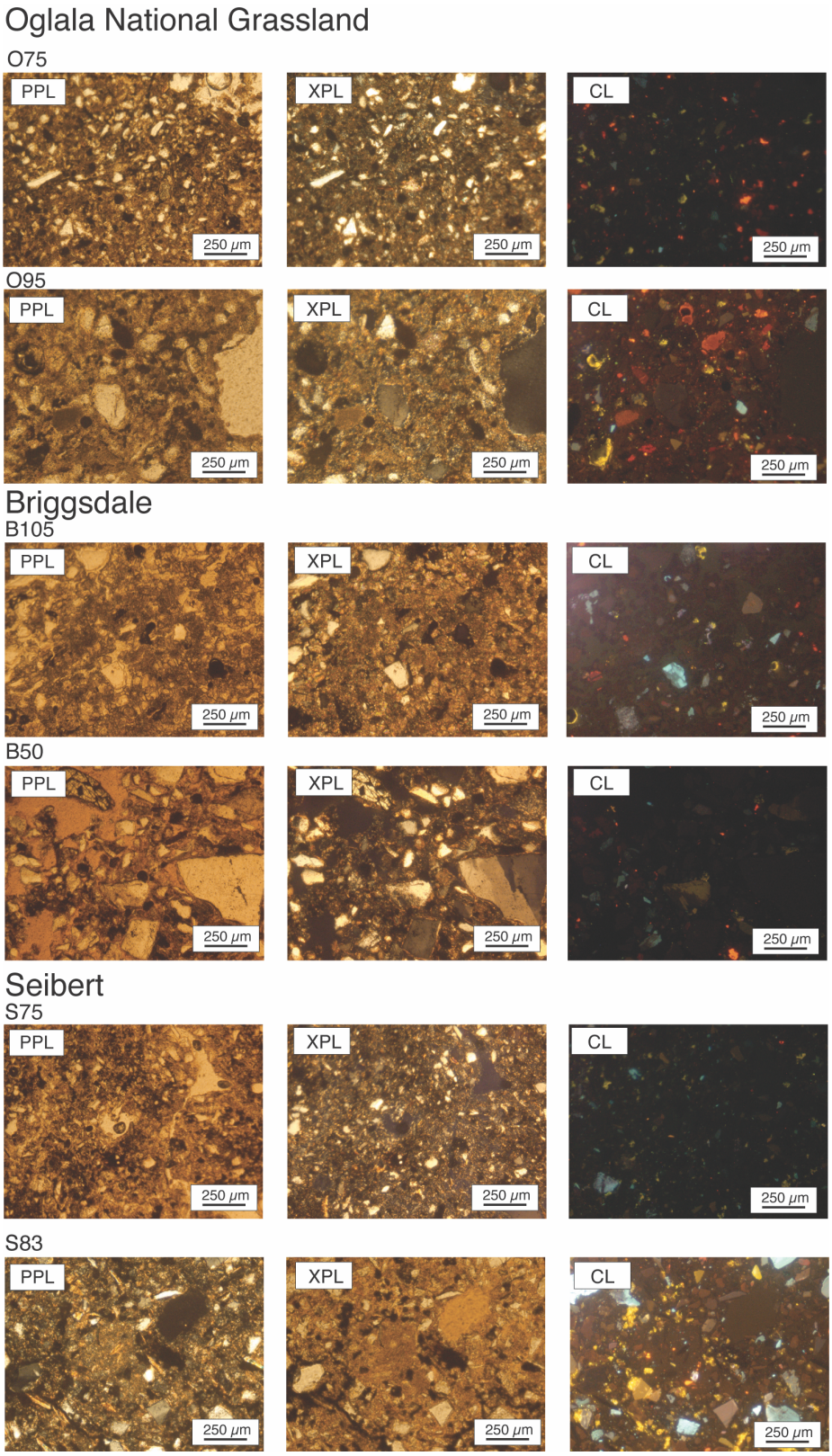

Supplemental Figure 4-3. PPL, XPL, and CL images of 2 nodules from each of the three field sites.

Supplemental Table 4-1. Clumped Isotope results.

Site	Sample ID	$\delta^{13}C$ (‰ VPBD)	$\delta^{13}C$ 2se (‰ VPBD)	$\delta^{18}O$ (‰ VPBD)	$\delta^{18}O$ 2se (‰ VPBD)	Δ_{47} (‰ ICDES)	Δ_{47} se (‰ ICDES)	T47(°C)	T47 2se (°C)	$\delta^{18}O_w$ (‰ VSMOW)	$\delta^{18}O_w$ 2se (‰ VSMOW)
Briggsdale	B105	-4.85	0.01	-7.44	0.06	0.66281	0.00246	4.1	2.8	-9.6	0.6
Briggsdale	B19.5	-2.55	0.03	-7.77	0.27	0.6379	0.00435	11.1	3	-8.3	0.8
Oglala	O75_spot2	-3.63	0.13	-8.77	0.11	0.61759	0.00582	17.3	3.4	-8	0.8
Oglala	O95_spot2	-3.28	0.28	-8.59	0.06	0.61294	0.00309	18.7	2.8	-7.5	0.6
Seibert	S100	-0.8	0.07	-7.08	0.2	0.64005	0.0089	10.5	4.4	-7.8	1
Seibert	S75-80	0.47	0.03	-6.61	0.14	0.64736	0.0106	8.4	4.8	-7.8	1
Seibert	S80-85	0.08	0.02	-7.1	0.15	0.62617	0.00408	14.6	3	-6.9	0.6
Seibert	S90-95	-0.85	0.06	-7.09	0.06	0.63437	0.00607	12.1	3.4	-7.4	0.8

Chapter V: It's getting hot in here: A temperature record of terrestrial climate change through the Paleocene-Eocene Thermal Maximum from the Bighorn Basin, WY

Abstract

The Paleocene-Eocene Thermal Maximum (PETM) is often invoked as an analogue for modern rapid warming of the climate. Terrestrial records of the PETM are particularly useful for understanding how the hydrosphere and biosphere respond to rapid global warming, but are relatively sparse compared to marine records. The Bighorn Basin, Wyoming, USA, contains stacked paleosols that span the PETM, and preserve fossils that show significant floral and faunal changes associated with the PETM. The paleosols also host abundant pedogenic carbonate nodules, to which I applied clumped isotope thermometry ($T(\Delta_{47})$) to generate a record of temperature change during the PETM. My record shows ~20°C of warming in paleosols from pre-PETM conditions to the body of the PETM, with $T(\Delta_{47})$ values up to 36.2 ± 3.8°C during the body of the PETM. I interpret this temperature increase as a ~20°C shift in mean annual temperature, which is larger than has been previously interpreted in the basin, and shows much greater terrestrial amplification of warming than has previously been recorded. Combining the $T(\Delta_{47})$ and $\delta^{18}O$ of carbonate to estimate soil water $\delta^{18}O$, I document a positive 4‰ shift in soil water $\delta^{18}O$ values that is primarily driven by temperature change

rather than aridification in the basin. These data support a shift of floral growing season towards the cool season, and have implications for the equilibrium climate sensitivity value during the PETM.

5.1 Introduction

The latest Paleocene into the early Eocene was marked by ~10 million years of warming, that culminated in the Early Eocene Climatic Optimum (e.g., Zachos et al., 2001; Westerhold et al., 2020). Superimposed on this long-term warming trend are rapid global warming events, termed hyperthermals, that are characterized by negative carbon isotope excursions (CIE) of varying magnitudes and global temperature increases (Kirtland Turner et al., 2014). The co-occurrence of the negative CIE and paleoenvironmental indicators of warming indicates that the warming is, at least partly, driven by an increase in greenhouse gases in the atmosphere. Therefore, over the last 30 years, the geoscience community has intensely studied the hyperthermal events as analogues for future climate warming.

Comparison of records of the first three hyperthermal events (the Paleocene-Eocene Thermal Maximum (PETM), ETM2 and H2) in the Bighorn Basin, WY reveals some commonalities in how terrestrial environments responded to a rapidly warming climate. For example, the fluvial-alluvial sedimentary system is responsive to environmental changes, indicated by the presence of distinctive purple B horizons and channel sandstone complexes (Kraus and Riggins, 2007; Abels et al., 2012; Foreman, 2014). There is documented mammalian turnover and dwarfing in response to warming (Gingerich, 2001; Widlandsky et al., 2022), and distinctive

shifts in basin flora to dry tropical taxa during at least the PETM and ETM2 hyperthermal events (Wing and Currano, 2017; Korasidis et al., 2022).

However, the PETM, which is associated with the largest magnitude negative CIE, remains distinctive as compared to subsequent hyperthermal events. For example, while most of the subsequent hyperthermal events have a symmetrical negative carbon isotope excursion shape, the PETM has a prolonged negative carbon isotope excursion (Bowen et al., 2001; Zeebe et al., 2009), suggesting ongoing release of isotopically light carbon after the initial onset (Penman and Zachos, 2018). Additionally, the trigger mechanism of the PETM is heavily debated within the geoscience community, while the subsequent hyperthermal events seem to be orbitally paced (e.g., Cramer et al., 2003; Kurtz et al., 2003; Dickens, 2011; DeConto et al., 2012; Lourens et al., 2005; Frieling et al., 2016; Gutjhar et al., 2017; Zeebe and Lourens, 2019; Kender et al., 2021). To be able to better understand both biotic and abiotic (i.e., chemical weathering feedbacks) responses, it is important to understand the magnitude of terrestrial warming more precisely. Moreover, to understand how equilibrium climate sensitivity varies with Earth's temperature, which is a critical constraint on models of future warming, we must understand how marine and terrestrial environments respond to the same input of greenhouse gases. To provide data that can add constraints on and context for these issues, I present a record of terrestrial, mid-latitude warming from carbonate clumped isotope thermometry ($T(\Delta_{47})$) of paleosol carbonate nodules through the PETM from the Bighorn Basin.

5.2 Paleocene-Eocene Thermal Maximum

The negative CIE that marks the PETM was first recognized in the carbon isotope values ($\delta^{13}C$) of benthic foraminifera from Cenozoic marine sediments (e.g. Rea et al., 1990; Kennett and Stott, 1991). Shortly thereafter, the PETM was established as a global event that affected both terrestrial and marine environments through the recognition of a contemporaneous negative CIE in a terrestrial stack of paleosols found in the Bighorn Basin (Koch et al., 1992). Since then, the PETM has been identified in numerous marine and terrestrial records worldwide (e.g., Sluijs et al., 2006; Bowen and Bowen, 2008; Tipple et al., 2011; Foreman et al., 2012; Handley et al., 2012; Krishnan et al., 2012; Pujalte et al., 2012; Aze et al., 2014; Chen et al., 2014; Reinhardt et al., 2022).

Based on the $\delta^{18}O$ of foraminifera, it has been interpreted that the deep ocean warmed by ~5 - 8°C (e.g. Kennett and Stott, 1991; Zachos et al., 2006; Westerhold et al., 2020). Similarly, estimates of sea surface temperatures from Mg/Ca ratios of planktic foraminifera and TEX_{86}, as well as coastal terrestrial temperatures MBT'_5 have a range of temperature increase of 3-10°C (Dunkley Jones et al., 2013; Hollis et al., 2019, and references therein; Sluijs et al., 2020; Inglis et al., 2021). Warming appears to have preceded the onset of the main negative CIE in both terrestrial (e.g. Secord et al., 2010) and shallow marine records (e.g. Babila et al., 2022), and is possibly associated with the pre-onset CIE found in terrestrial records (Bowen et al., 2015). Climate models with assimilated proxy data indicate an increase in

global mean temperatures by 5.4-5.9°C (95% CI), with global mean surface temperatures of 33.1-35.5°C (95% CI) during the PETM (Tierney et al., 2022).

Globally, the hydrologic cycle is expected to have intensified during the PETM, meaning that there is greater water vapor transport from low latitudes to high latitudes, and that precipitation falls in fewer, more intense events (Carmichael et al., 2017; Carmichael et al., 2018; Tierney et al., 2022). Global climate models of the hydrologic cycle show considerable spatial heterogeneity in precipitation - evaporation (P-E) over continental interiors, which is a key indicator of whether or not the region experiences dry conditions (Carmichael et al., 2017; Carmichael et al., 2018; Tierney et al., 2022). Additionally, models focused on key aspects of the hydrologic cycle (i.e atmospheric rivers and tropical cyclones) indicate that Earth's eccentricity during the PETM may provide critical control on the strength of hydrologic cycle responses to warming (Shields et al., 2021; Rush et al 2021; Kiehl et al., 2021).

5.2.1 The Bighorn Basin, WY is the most studied terrestrial section of the PETM

The Bighorn Basin (BHB) is a Laramide contractional basin that preserves a thick sequence of Cretaceous – Eocene sedimentary rocks in Wyoming, USA. The BHB is bound by two Laramide uplifts: the Bighorn mountains to the east and the Owl Creek Mountains to the south. On its western edge, the basin is bound by the Eocene Absaroka Volcanic Province. Sedimentary rocks in the basin are dominated

by the Paleocene Fort Union Formation, and the conformable Eocene Willwood Formation (Fig. 5-1A).

The PETM is preserved in a thick succession of stacked paleosols that contain abundant floral and faunal fossils, carbonate nodules, and organic matter that have yielded information about the biotic and climatic response of the region to the PETM (e.g. Gingerich and Clyde, 2001; Fricke and Wing, 2004; Wing et al., 2005; Kraus et al., 2013; Baczyski et al., 2013; Foreman, 2014; Bowen et al., 2015; Widlansky et al., 2022; Korasidis et al., 2022). Sedimentology has been used to interpret the BHB as an alluvial succession where the sediment flux to the basin varied, likely as a result of precipitation fluctuations, throughout the PETM (Kraus et al., 2013; Foreman, 2014; Kraus et al., 2015). The majority of the paleosols below and above the PETM have a sandy siltstone texture (Kraus et al., 2015). In contrast, the paleosols during the PETM are much finer grained, falling into the mudstone and silty mudstone Variegated Mudrock facies (Kraus et al., 2015).

Biostratigraphy in the basin reveals an extensive faunal turnover associated with the PETM, and that some groups experienced dwarfing during the warming event (e.g. Gingerich, 2006; Clyde and Gingerich, 1998). The $\delta^{18}O$ of tooth enamel from an obligate drinking species shows a positive 4‰ shift, which was interpreted to be driven by landscape temperature change (Secord et al., 2012; Baczynski et al., 2016). Generally, palynological and plant macrofossil assemblages reveal extirpation of temperate taxa accompanied with colonization by drought-tolerant and thermophilic taxa (Wing et al., 2005; Wing and Currano, 2013; Korasidis et al.,

2022). Mean annual precipitation (MAP) from floral macrofossil assemblages has been estimated at 800 mm +1140/-560 mm for the lower PETM, 1470 + 1210/-660 mm for intermediate PETM and 1440 mm +2060/-1000 mm for the upper PETM (Wing et al., 2005; Peppe et al., 2011; Wing and Currano, 2013). These estimates are slightly lower than those made using the CALMAG index (Nordt and Driese, 2010) in the paleosols, but they are broadly consistent. Altogether, this large body of research paints a picture of a dramatic environmental shift associated with warming in Wyoming approximately 56 Ma.

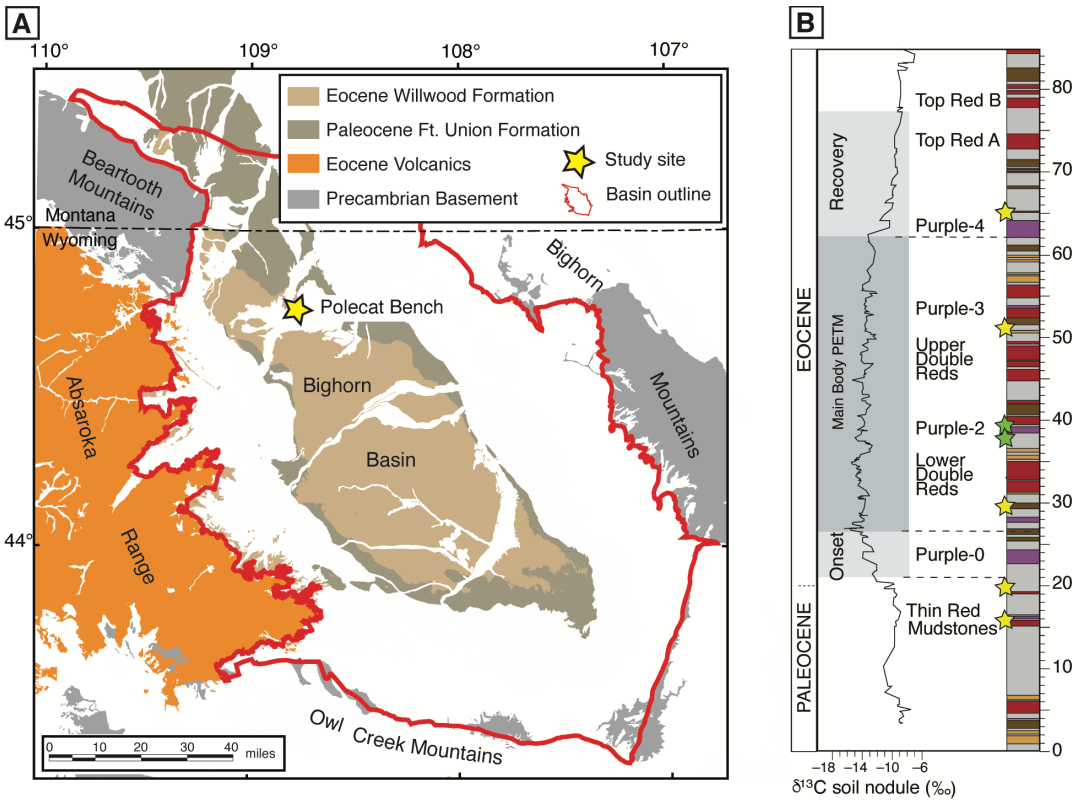

Figure 5-1. A) Geologic map of the Bighorn Basin, WY. Modified from Finn et al., 2010. B) Stratigraphic column of Polecat Bench. The colors of the stratigraphic column correspond to paleosol color. Sample levels are marked with stars; the yellow stars indicate the position of analyses reported in this study and green stars indicate the position of samples with T(Δ_{47}) previously reported by Snell et al., 2013. Note, two samples measured in this study fall above the stratigraphic column at levels ~94 and ~114 meters and are not shown here. Modified from Kraus et al., 2015.

5.3 Methods

5.3.1 Optical Petrography

I used optical and cathodoluminescence (CL) microscopy to identify diagenetic fabrics that may have resulted from dissolution/reprecipitation and/or recrystallization in samples used for Δ_{47} analyses. Plain polarized (PPL) and cross polarized (XPL) microscopy was conducted on a Zeiss Axio Imager, and CL microscopy was conducted on a Technosyn Cathode Luminescence Model 8200 Mk II microscope, both at CU Boulder. Based on the spatial distribution of Fe and Mn, CL colors from carbonate minerals can vary from non-luminescent to yellow, orange, or red, and the patterns of CL variation can be used as a visual aid in determining generations of crystallization through crosscutting relationships and to yield useful information about primary and diagenetic components of carbonate (Budd et al., 2002; Mintz et al., 2011).

5.3.2 Carbonate Clumped Isotope Thermometry

Carbonate clumped isotope thermometry ($T(\Delta_{47})$) relies on the temperature dependence of the degree of bond ordering of heavy, rare isotopes of ^{13}C and ^{18}O in the carbonate ion (CO_3^{2-}), as reflected in the abundance of mass-47 of CO_2 (Δ_{47}) evolved from phosphoric acid digestion of carbonate minerals (Ghosh et al., 2006; Huntington et al., 2009). At low temperatures, there is a greater extent of ^{13}C - ^{18}O bond ordering, or clumping, in CO_3^{2-} compared to a stochastic distribution of the heavy isotopes, leading to an inverse relationship between Δ_{47} and temperature

(Wang et al., 2004; Eiler, 2007). In addition, an independent estimate of temperature from Δ_{47} can be combined with the simultaneously measured $\delta^{18}O$ of carbonate ($\delta^{18}O_c$) to estimate the $\delta^{18}O$ value of the water ($\delta^{18}O_w$) from which the carbonate formed, using the temperature-dependent fractionation of oxygen isotopes between carbonate minerals and water (e.g. Kim and O'Neil, 1997).

I analyzed 7 pedogenic carbonate nodules from a set of nodules that provided the first high resolution $\delta^{13}C_c$ and $\delta^{18}O_c$ record of the PETM on Polecat Bench in the BHB (see Bowen et al., 2001 for details on sampling location and style). Three to six replicates of each sample were analyzed during two sessions in 2022 on a Thermo Scientific 253 Plus dual-inlet isotope ratio mass spectrometer in the CU Boulder Earth Systems Stable Isotope Laboratory (CUBES-SIL; RRID SCR-019300). Calcium carbonate standards (i.e. ETH 1, 2, 3) were analyzed alongside samples and used to correct the data to the community accepted Intercarb-Carbon Dioxide Equilibrium Scale (ICDES) (Bernasconi et al., 2021). The carbonate standard IAEA-C2 was also analyzed and used as a monitoring standard. Carbonate samples and standards were run in 1:1 proportion and were digested in a 90°C common acid bath, and the resulting CO_2 was then subsequently purified with a custom-built sample introduction line (see supplemental information for additional details). The gas was then analyzed for the abundance of masses 44-49 of CO_2, to determine Δ_{47}, δ^{47}, $\delta^{13}C_c$, and $\delta^{18}O_c$ values for each sample. Sample average Δ_{47} values were calculated as weighted means of all the replicate analyses of each sample, and associated errors were calculated using standard errors of the replicates as the

weighting factors, following Huntington et al. (2009). Temperatures were estimated from the mean Δ_{47} values using the Anderson et al. (2021) calibration line and uncertainties were reported as two standard errors of the mean (2 s.e.). Precision of individual Δ_{47} analyses as well as final mean Δ_{47} values are also reported as 2 s.e. and includes analytical error of each measurement as well as errors associated with the correction lines used (Huntington et al., 2009; Bernasconi et al., 2021; Anderson et al., 2021). From the measured Δ_{47} temperature and $\delta^{18}O_c$ values, the $\delta^{18}O$ of the soil water ($\delta^{18}O_{sw}$) from which the carbonate sample precipitated was calculated using the equilibrium fractionation relationship between calcite and water established by Kim and O'Neil (1997). $\delta^{18}O_{sw}$ is reported relative to the VSMOW reference frame (Coplen, 2011).

5.4 Results

5.4.1 Optical petrography

PPL, XPL, and CL images revealed nodules primarily composed of dense micrite with zones of fracture filling, coarse crystalline spar. The micritic zones have a dull-orange luminescence, whereas the fracture filling spars show multiple luminescent bands that range from non-luminescent to brightly luminescent. Previous work on similar nodules from the BHB showed that coarse crystalline zones had relatively negative $\delta^{18}O_c$ values and higher temperature (~55-60°C) as compared to the rest of the dataset, consistent with precipitation from secondary fluids at burial depths of ~1.5-2 km (Snell et al., 2013). I therefore make the inference that micritic zones preserve original pedogenic carbonate textures and

unaltered earth surface conditions. The small zones of recrystallized material can be easily identified, and avoided while drilling samples for stable isotope geochemistry.

5.4.2 Stable Isotope Geochemistry Results

The $\delta^{13}C$ of carbonate ($\delta^{13}C_c$) values for all nodules ranged between -14.21‰ (± 0.12‰, 2s.e.) and -8.19‰ (± 0.1‰, 2s.e.) (Table 5-1, Fig. 5-2A). Before the onset of the PETM, $\delta^{13}C_c$ values average -9.02‰, and decrease to ~-14‰ during the body of the PETM. There is a gradual increase in $\delta^{13}C_c$ values near the end of the excursion, until $\delta^{13}C_c$ values return to background values of around -9‰. These $\delta^{13}C_{carb}$ values are similar to previous analyses of the samples, which were completed in different laboratories (Supplemental Table 1, Bowen et al., 2001; Snell et al., 2013). Our data yield a CIE of ~ -5‰, consistent with a CIE of ~ -6‰ that was determined from the broader sample set (Bowen et al., 2001).

T(Δ_{47}) for all samples ranges between 13.6 ± 2.3°C and 36.2 ± 1.9°C (Table 5-1, Fig. 5-2B). Broadly, the temperature record mirrors the carbon isotope record: it starts with lower temperatures, then shifts to higher temperatures that are maintained throughout the body of the PETM CIE, and decreases near the end of the CIE-body, returning to near background temperatures that range between 18.7 ± 3.4°C and 23.7 ± 3.2°C. (Fig. 5-2B). Unlike the carbon isotope curve, however, the nodule just below the onset of the negative CIE yields a near-peak PETM soil temperature of 34.3 ± 3.6°C (2s.e.).

The $\delta^{18}O_w$ values for these samples range from -8.2 ± 1.0‰ to -3.7 ± 0.8‰ (2s.e.). The structure of the $\delta^{18}O_w$ values is the same as the temperature record (Fig. 5-2C): before the onset of warming, the $\delta^{18}O_w$ has a value of -8.2‰, then increase to between -2.9‰ and -5.3‰ during the PETM, with an overall shift to higher values of ~ 4‰. As the $\delta^{13}C_c$ values decrease towards pre-PETM values, the $\delta^{18}O_w$ values decrease to background values of ~ -8‰.

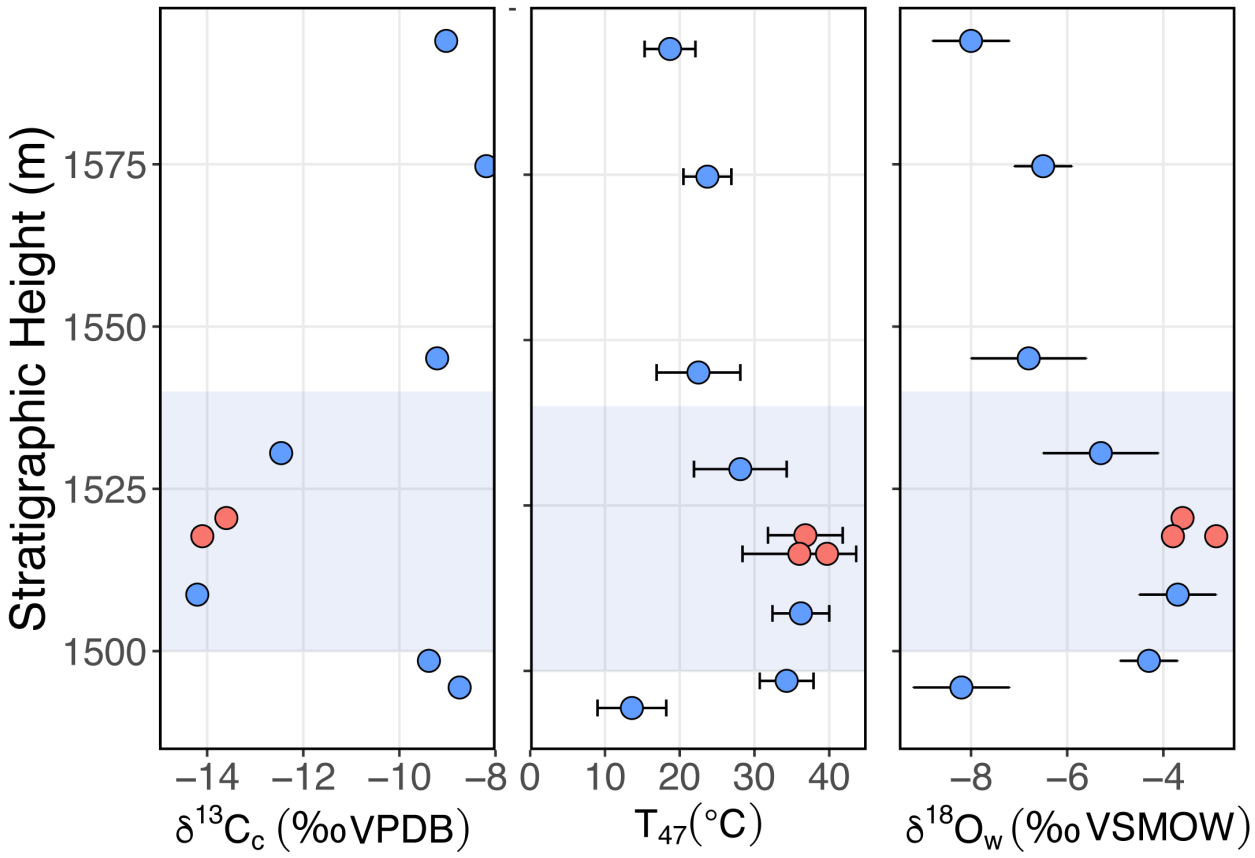

Figure 5-2. A) $\delta^{13}C_{carb}$ (‰), B) T(Δ_{47}) °C, and C) the calculated $\delta^{18}O_w$ (‰) vs. stratigraphic height. Clumped isotope measurements reported in this study are blue in color, and previous estimates from Snell et al. (2013) are red in color. The shaded blue bar is the previously interpreted PETM interval on Polecat Bench (Bowen et al., 2001).

Table 5-1. Clumped Isotope results.

Sample	Strat. height (m)	$\delta^{13}C$ (‰ VPBD)	$\delta^{13}C$ 2se (‰ VPBD)	$\delta^{18}O$ (‰ VPBD)	$\delta^{18}O$ 2se (‰ VPBD)	Δ_{47} (‰ ICDES)	Δ_{47} se (‰ ICDES)	T47(°C)	T47 2se (°C)	$\delta^{18}O_w$ (‰ VSMOW)	$\delta^{18}O_w$ 2se (‰ VSMOW)
PB-00-04-16	1594	-9.03	0.13	-9.06	0.14	0.61297	0.00571	18.7	3.4	-8	0.8
PB-00-04-14	1574.7	-8.19	0.11	-8.60	0.17	0.59769	0.00435	23.7	3.2	-6.5	0.6
PB-00-02-19	1545.1	-9.21	0.02	-8.70	0.10	0.60120	0.01122	22.5	5.6	-6.8	1.2
PB-00-02-09	1530.5	-12.46	0.03	-8.29	0.18	0.58493	0.01176	28.1	6.2	-5.3	1.2
PB-00-01-07	1508.7	-14.20	0.12	-8.27	0.12	0.56271	0.00338	36.2	3.8	-3.7	0.8
PB-00-03-11	1498.5	-9.39	0.12	-8.45	0.08	0.56762	0.00300	34.3	3.6	-4.3	0.6
PB-00-03-08	1494.4	-8.75	0.04	-8.15	0.13	0.62943	0.00963	13.6	4.6	-8.2	1

5.5 Discussion

5.5.1 T(Δ_{47}) values represent primary depositional temperatures

Before I can interpret T(Δ_{47}) temperatures as reflective of primary environmental conditions, I first need to assess the likelihood that temperatures reflect other geologic processes. There are three potential avenues for producing erroneously hot clumped isotope temperatures from pedogenic carbonate nodules. The first is diagenesis via either carbonate solid state reordering or fluid-mediated recrystallization under either high or low water-to-rock ratios. Solid state reordering results from burial of sediments to >100°C for 10^6 - 10^8 years, allowing the C and O atoms to diffusively reorder (Passey and Henkes, 2012; Henkes et al., 2014). However, solid state reordering is unlikely in this situation, given that burial temperatures likely did not exceed 85°C (Roberts et al., 2008), and prior analyses of spar for Bighorn Basin nodules yielded temperatures of 55 - 60°C (Snell et al., 2013), consistent with ~2 km of burial. These spars provide insight into the isotope and temperature values of secondary fluids that could have altered the original micrite. To mitigate this, I used thin section images and a stereoscope to carefully ensure that I only drilled primary micrite. I am confident that I integrated very little altered material because the temperatures and bulk isotopes have not been shifted towards the secondary spar compositions as seen for an altered sample in Snell et al. (2013). The second pathway for producing an erroneously hot clumped isotope temperature is isobaric interference on masses 44-47 of CO_2 during analysis, which can be assessed from the mass-48 isotopologue of CO_2; a few analyses exhibited Δ_{48}-excess, and yielded unreasonably high T(Δ_{47}), and were therefore

discarded. Lastly, carbonate formation processes that encode isotopic disequilibrium (e.g. rapid CO_2 degassing from DIC) can also lead to erroneously high clumped isotope temperatures, which can be identified using dual Δ_{47} - Δ_{48} thermometry (Fiebig et al., 2021). My Δ_{48} data are not of sufficient precision to resolve if this signal is present, and future work should include higher precision measurements of these nodules.

5.5.2 T(Δ_{47}) temperatures

My record of soil temperature during the PETM suggests warming on the order of ~20°C, with maximum soil temperatures of 36.2 ± 3.8°C. Previous estimates of PETM soil temperatures from pedogenic carbonate clumped isotope thermometry are between 36.0 ± 3.8°C and 39.7 ± 3.2 (Snell et al., 2013). The consistency of the soil temperatures between our data and previous data is striking given improvements made over the last decade to measurement methods and Δ_{47} temperature calibrations (i.e. Bernasconi et al., 2021; Anderson et al., 2021). This magnitude of warming at the PETM in the Bighorn Basin is significantly larger than global, marine, and other terrestrial estimates of temperature change (e.g. Hollis et al., 2019, and references therein; Westerhold et al., 2020; Inglis et al., 2021; Tierney et al., 2022). There are several mechanisms that can account for marine vs. terrestrial variability, including terrestrial amplification of warming (Tierney et al., 2022), as well as inter-proxy differences that can be driven, at least in part, by differences in the season each proxy forms. To make sense of this, it is first necessary to address the seasonality of pedogenic carbonate formation.

Clumped isotope thermometry records the temperature of mineral formation (Eiler, 2007). Previously, a pedogenic carbonate clumped isotope record from the BHB in the early Eocene was interpreted to reflect at least warm month temperatures (Snell et al., 2013). At the time of that study, most modern calibration work, including the earliest clumped isotope geochemistry on modern soil carbonates, suggested that pedogenic carbonate clumped isotope temperatures reflected some combination of a warm season bias and radiative heating of the soil (Breecker 2009; Passey et al., 2010; Quade et al., 2013). However, as more studies have been done, temperatures ranging from mean annual to a warm season bias have been found (Hough et al., 2014; Burgener et al., 2016; Gallagher and Sheldon, 2016; Huth et al., 2019). From these data, it has been suggested that the timing of carbonate formation is driven largely by the timing of soil dry down which can vary with the timing and style of meteoric precipitation (Breecker et al., 2009; Hough et al., 2014; Kelson et al., 2020). Additionally, the timing of carbonate formation seems to be in part controlled by soil texture; coarse grained soils seem to have the greatest warm season bias, while fine-grained, clay-rich soils record temperatures closer to a mean-annual air temperature (Kelson et al., 2020; chapter 4, this dissertation).

Within the paleosols of the BHB, there are three different paleosol facies: variegated I, variegated II, and the heterolithic facies (Kraus et al., 2015). The clay weight percent of the paleosols varies between ~10% and 60%. The Pre-PETM and PETM onset paleosols are dominated by the heterolithic facies and have a median

clay weight percent of 22%; these paleosols dominantly have loam – silty clay loam textures. While the Pre-PETM paleosols are slightly coarser grained than the subsequent paleosols, they are fine-grained enough that they likely also record a near mean-annual air temperature. The PETM body paleosols are dominated by the variegated II facies that has a median clay weight percent of 33%, and these paleosols have a silty clay-loam to silty texture, and have vertisol properties like slickensides (Kraus et al., 2015). Paleosols that contain 2:1 shrink-swell clays are susceptible to rapid CO_2 degassing when the soil cracks and opens fast pathways for gas exchange with the atmosphere (Breecker et al., 2013). If rapid CO_2 degassing drives pedogenic carbonate formation in the more clay rich paleosols, then the carbonate would record an apparent warm-biased temperature (Tripati et al., 2015; Fiebig et al., 2021). To test if this effect occurs in my dataset, I compared the clumped isotope temperatures of nodules from the heterolithic facies to those from the variegated facies within the body of the PETM, with the hypothesis that if there are horizons where nodules form out of isotopic equilibrium, temperature variability within the PETM would not track with the carbon isotope excursion or other records of change. However, I do not observe that variability during the PETM. For example, sample PB-00-03-11 is sourced from the heterolithic facies, and sample PB-00-01-07 is sourced from the variegated II facies, but yield very similar temperatures. To further test this hypothesis, it is possible to compare nodules from heterolithic and variegated facies using dual-clumped isotope thermometry (Δ_{48} -

Δ_{47}) to identify samples where rapid CO_2 degassing yields temperatures that are out of equilibrium with the surrounding soil (Fiebig et al., 2021).

Given that there does not appear to be facies-dependent temperature variability, carbonate formation is likely driven by other mechanisms in these soils. These mechanisms can include the timing of calcium infiltration, and any process that will decrease the level of CO_2 in the soil (Breeker et al., 2009; Hough et al., 2014; Huth et al., 2019; Kelson, 2020). All of the nodules from this study are sourced from paleosols that are fine-grained and clay-rich, so it is possible that the clumped isotope temperatures reflect mean annual temperatures.

My estimate of soil temperature prior to the PETM (13.6 ± 2.3°C) overlaps within uncertainty of a mean annual air temperature (MAAT) estimate of 15.7 ± 2.4°C made from leaf margin analysis (LMA) (Wing et al., 2005). Similarly, my estimate of temperature after the PETM of about 21.6°C overlaps within uncertainty of an LMA estimate of MAAT of 18.2 ± 2.3°C (Wing et al., 2005). Given the overlap with LMA estimates, at face value, my soil temperatures are most consistent with mean annual temperatures for the time periods outside the body of the PETM.

For the PETM, however, our estimate of soil temperature (~36°C) is significantly hotter than the MAAT estimates made from LMA (19.8 ± 3.1°C, Wing et al., 2005) and biogenic apatite (26°C, Fricke and Wing, 2004). One possibility to explain the discrepancy between LMA and the clumped isotope temperature is that the timing (season) of pedogenic carbonate formation changed from spring/fall

outside of the PETM to the summer season during PETM. One way to achieve that seasonal shift is by changing the timing of meteoric precipitation in the basin during the PETM. Currently, models do not produce a shift in total mean annual precipitation during the PETM for the region of the Bighorn Basin (Carmichael et al 2017; Tierney et al., 2022), but recent modeling efforts focused on global hydrologic cycle changes during the PETM open the possibility for strengthened winter-time precipitation in the Western U.S (Shields et al., 2021; Tierney et al., 2022). However, models of regional climate near the BHB from the early Eocene favor summer season precipitation (Sewell and Sloane, 2006; Snell et al., 2013). Moreover, global models of terrestrial hydrologic change contain major uncertainties related to terrestrial hydrologic cycle feedbacks (see supplemental information for greater detail) and so caution must be used to not over interpret model results. So, while I cannot rule out that the season of carbonate formation changed during the PETM, I do not currently have enough data to support or refute that hypothesis.

Alternatively, if $T(\Delta_{47})$ values do in fact reflect MAAT during the PETM, then that suggests there is a bias in the estimates made from LMA. One potential explanation for the discrepancy between the leaf margin analysis MAAT estimate and the pedogenic carbonate clumped isotope MAAT estimate during the body of the PETM is that the growing season of plants changed from a warm growing season to a cool growing season. The hydrogen isotope values from leaf waxes (n-c29 δ^2H) are nearly invariant through the PETM, which is consistent with a change in the

season of lipid production (Baczynski et al., 2016). If ~35°C does indeed reflect MAAT in the BHB during the PETM, that suggests extremely warm summers with temperatures on the order of 50-55°C (using a reasonable modern mid-latitude 30°C mean annual range of temperature (MART), Snell et al., 2013), which may be above the habitability limits of many plant species. It would, therefore, make sense that the growing season for most plants would shift to a cooler season.

Beyond estimates of absolute temperature in the BHB during the PETM, I can also turn to the magnitude of temperature change to give us more context for what $T(\Delta_{47})$ values represent. If there is a full seasonal shift of carbonate formation encoded into the clumped isotope temperatures, then potentially 15°C of warming could be explained by the seasonal shift using a 30°C MART, implying a total of 5°C of warming. Alternatively, without the seasonal shift, that implies 20°C warming. Previously, the $\delta^{18}O$ of tooth enamel carbonate was used to estimate that the magnitude of mean annual temperature change from pre-PETM to the PETM body, suggesting ~8-13°C of warming (Secord et al., 2010). This estimate alone suggests that an increase in temperature of 5°C is likely too conservative. Moreover, that calculation relied on a 0.39‰/°C and 0.36‰/°C relationship between $\delta^{18}O_{surface\ water}$ and temperature (Secord et al., 2010). If instead, I apply a 0.21‰/°C rate, as suggested by the clumped isotope $\delta^{18}O_{sw}$ data (fig. 5-3), then the mean annual temperature increase calculated from the $\delta^{18}O_{enamel}$ is ~13-24°C. This temperature range is more compatible with an estimate of 20°C warming.

Recent estimates of global mean surface temperature using a proxy-assimilated model suggest global mean surface temperatures were between 33.1-35.5°C (95% CI) during the PETM (Tierney et al., 2022). My temperature estimate of ~36°C is more compatible with that model as a mean annual temperature rather than a summertime temperature. Moreover, this model also suggests that there is terrestrial amplification of warming, and it is therefore challenging to reconcile records of ocean temperature that suggest 5 – 10°C of warming (Dunkley Jones et al., 2013) with the same magnitude of warming on land.

5.5.3 $\delta^{18}O_w$ records from the Bighorn Basin

Beyond the temperature records from clumped isotope thermometry, I also gain perspective into the climatic changes using the calculated $\delta^{18}O_w$ record. The $\delta^{18}O_w$ encodes information about the climate because it is controlled in part by temperature but is also affected by other hydrologic cycle dynamics like aridification or invigoration of the hydrologic cycle (Dansgaard, 1964; Rozanski et al 1993; Gat, 1996).

Overall, there is a 4‰ increase in the $\delta^{18}O_w$ associated with the onset of warming just prior to the onset of the CIE. This shift is the same magnitude as observed in the $\delta^{18}O_w$ record from obligate drinking species during the PETM (Secord et al., 2012). Previously, this and other records of surface water oxygen isotope composition have been used to interpret shifts in mean annual temperatures (Fricke and Wing, 2004; Secord et al., 2012). In contrast to the record from the obligate drinking species, the hydrogen isotope values from leaf waxes (n-c_{29} δ^2H)

are nearly invariant through the PETM. To explain the contrast between those data, Baczynski et al., (2016) argued that either the surface water must become evaporatively ^{18}O enriched, or plants must change their growing season. Lastly, records of $\delta^{18}O_w$ from hematite crusts on fossil bones suggest that the $\delta^{18}O_w$ is largely controlled by temperatures through the early Eocene in the BHB (Bao et al., 1999)

All of these isotope records give different perspectives of hydrologic changes on the landscape, and historically, the $\delta^{18}O_w$ from pedogenic carbonate is thought to reflect evaporatively ^{18}O enriched meteoric water. This viewpoint largely comes from modern calibration work that has been done in arid environments (e.g. southwestern North America; Cerling, 1984; Cerling and Quade, 1993; Breecker et al., 2009; Hough et al., 2014; Oerter and Amundson, 2016), but given the clay-rich texture of the BHB paleosols, this comparison may be limited. One way I can evaluate the effects of evaporative on the $\delta^{18}O_{sw}$ values is by examining the relationship between the $\delta^{18}O_{sw}$ and temperature. If soil water experienced greater evaporative enrichment during the PETM, it would follow that the relationship between $\delta^{18}O_{sw}$ and temperature would increase (higher slope) during the body of the event (fig. 5-3a; Kukla et al., 2019). Rather than seeing either a non-linear trend or a rotation of the line from before and after the PETM to during the body of the PETM, the $\delta^{18}O_{sw}$ data are best fit by a single relationship between $\delta^{18}O_{sw}$ and temperature, with a slope of 0.21‰/°C ($R^2 = 0.99$) (Fig 5-3b). The slope of this line is reasonable given other observations of temperature and surface water in hothouse

climate states (e.g. Bao et al., 1999; Snell et al., 2013; Secord et al., 2010). Furthermore, given that the paleosols thicken during the body of the PETM and become more clay rich (Kraus et al., 2015), there is likely limited variability in soil water isotope composition at the depth of carbonate formation (e.g. Oerter and Bowen, 2019; chapter IV, this dissertation).

Lastly, I can use the clumped isotope data to examine if I observe a shift in the seasonality of carbonate formation. Recent models of the hydrologic cycle during the PETM suggest the possibility of increased precipitation during winter months in western North America, in fewer but more intense storms (Carmichael et al., 2017; Shields et al., 2021; Tierney et al., 2022). Given this hypothesis, it might be expected that the relationship between temperature and $\delta^{18}O_{sw}$ would decrease, consistent with lower isotope values from the combination of the amount effect and winter precipitation (fig. 5-3A, Rozanski, 1993). But, again, the lack of a rotation of the slope from pre- and post-PETM into the body of the PETM (fig. 5-3B) suggests that the soil water isotope values were not sensitive to changes in the hydrologic cycle, and instead integrate a mean annual precipitation isotope value. I therefore interpret the shift in $\delta^{18}O_{sw}$ as a temperature-driven change in the isotopic composition of mean annual precipitation. This interpretation of the soil water isotope values further supports the hypothesis that the pedogenic carbonate clumped isotope temperatures are recording mean annual temperature throughout the length of this record.

5.5.4 Implications

Overall, my data are consistent with an increase in mean annual temperatures of 20°C during the PETM, up to mean annual temperatures of 36.2 ± 3.8°C. The hot mean annual temperature suggests that summertime temperatures in the Bighorn Basin were likely above the habitability zone for many floral taxa, and sheds light on the magnitude of warming required to force the faunal dwarfing and turnover that has been observed in the Basin. My data support a shift in growing season of floral taxa to cold-weather seasons (Baczynski et al., 2016). These data are consistent with terrestrial amplification of warming, but is of larger magnitude than climate models currently suggest (Tierney et al., 2022). In the future, these data may provide critical context for quantifying the equilibrium climate sensitivity during rapid warming events from a baseline hothouse climate state. The observation of warming to nearly peak PETM temperatures prior to the onset of the main CIE also support multiple injections of isotopically-light carbon into the atmosphere (Bowen et al., 2015; Babila et al., 2022). Lastly, while my data are consistent with a record of mean annual temperature and soil water values, more work is needed to be able to understand how pedogenic carbonate formation in fine grained, clay rich soils encodes information about the climate.

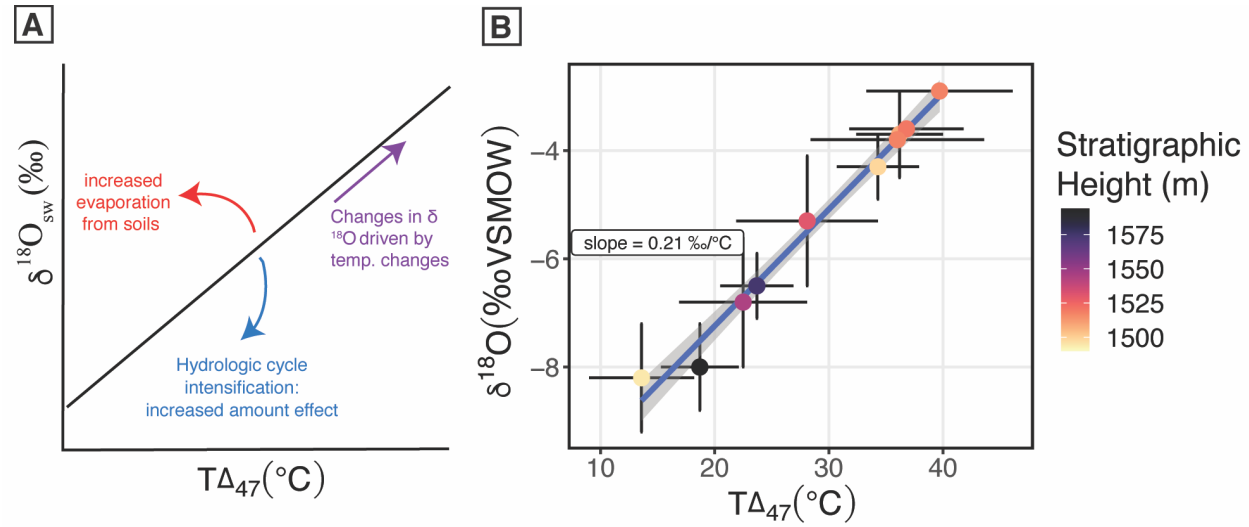

Figure 5-3. A) An interpretive framework for a plots of the calculated $\delta^{18}O$ of soil water vs. the $T(\Delta_{47})$ (°C). B) plots of the calculated $\delta^{18}O$ of soil water vs. the $T(\Delta_{47})$ for all of the clumped isotope data. Standard error on the slope of the line is 0.01‰/°C.

5.6 Conclusions

Here, I present a pedogenic carbonate $T(\Delta_{47})$ from the Bighorn Basin, WY through the Paleocene-Eocene Thermal Maximum. Soil temperatures increase ~20°C just prior to the onset of the negative carbon isotope excursion, and peak at 36.2 ± 3.8°C. These warm temperatures persist for the body of the PETM. Clumped isotope temperatures overlap within uncertainty with estimates of mean annual temperature made from leaf margin analysis both before and after the PETM. However, during the PETM, clumped isotope temperatures are ~15°C warmer than fossil leaf assemblage estimates. Based on similarity of the non-PETM samples to other estimates of MAAT in the Bighorn Basin, and from modern data, I interpret these soil temperatures to represent mean annual temperature in the Bighorn Basin during the PETM. This implies summer temperatures were likely too hot to support plant life, driving changes in the basin from warm season to cold season floral growth during the PETM.

Works Cited

Abdul Aziz, H., Hilgen, F. J., van Luijk, G. M., Sluijs, A., Kraus, M. J., Pares, J. M., & Gingerich, P. D. (2008). Astronomical climate control on paleosol stacking patterns in the upper Paleocene-lower Eocene Willwood Formation, Bighorn Basin, Wyoming. *Geology*, *36*(7), 531–534. https://doi.org/10.1130/G24734A.1

Abels, H. A., Clyde, W. C., Gingerich, P. D., Hilgen, F. J., Fricke, H. C., Bowen, G. J., & Lourens, L. J. (2012). Terrestrial carbon isotope excursions and biotic change during Palaeogene hyperthermals. *Nature Geoscience*, *5*(5), 326–329. https://doi.org/10.1038/ngeo1427

Anderson, N. T., Kelson, J. R., Kele, S., Daëron, M., Bonifacie, M., Horita, J., Mackey, T. J., John, C. M., Kluge, T., Petschnig, P., Jost, A. B., Huntington, K. W., Bernasconi, S. M., & Bergmann, K. D. (2021). A unified clumped isotope thermometer calibration (0.5–1100°C) using carbonate-based standardization. *Geophysical Research Letters*, 1–11. https://doi.org/10.1029/2020gl092069

Aze, T., Pearson, P. N., Dickson, A. J., Badger, M. P. S., Bown, P. R., Pancost, R. D., Gibbs, S. J., & Huber, B. T. (2014). Extreme warming of tropical waters during the Paleocene – Eocene Thermal Maximum. *Geology*, *42*(9), 739–742. https://doi.org/10.1130/G35637.1

Babila, T. L., Penman, D. E., Standish, C. D., Doubrawa, M., Bralower, T. J., Robinson, M. M., Self-Trail, J. M., Speijer, R. P., Stassen, P., Foster, G. L., & Zachos, J. C. (2022). Surface ocean warming and acidification driven by rapid

carbon release precedes Paleocene-Eocene Thermal Maximum. In *Sci. Adv* (Vol. 8). https://www.science.org

Baczynski, A. A., McInerney, F. A., Wing, S. L., Kraus, M. J., Bloch, J. I., & Secord, R. (2016). Constraining paleohydrologic change during the Paleocene-Eocene Thermal Maximum in the continental interior of North America. *Palaeogeography, Palaeoclimatology, Palaeoecology*, *465*, 237–246. https://doi.org/10.1016/j.palaeo.2016.10.030

Baczynski, A. A., McInerney, F. A., Wing, S. L., Kraus, M. J., Bloch, J. I., Boyer, D. M., Secord, R., Morse, P. E., & Fricke, H. C. (2013). Chemostratigraphic implications of spatial variation in the Paleocene-Eocene Thermal Maximum carbon isotope excursion, SE Bighorn Basin, Wyoming. *Geochemistry, Geophysics, Geosystems*, *14*(10), 4133–4152. https://doi.org/10.1002/ggge.20265

Bao, H., Koch, P. L., & Rumble, D. (1999). Paleocene-Eocene climatic variation in western North America: Evidence from the δ18o of pedogenic hematite. *Bulletin of the Geological Society of America*, *111*(9), 1405–1415. https://doi.org/10.1130/0016-7606(1999)111<1405:PECVIW>2.3.CO;2

Bernasconi, S. M., Daëron, M., Bergmann, K. D., Bonifacie, M., Meckler, A. N., Affek, H. P., Anderson, N., Bajnai, D., Barkan, E., Beverly, E., Blamart, D., Burgener, L., Calmels, D., Chaduteau, C., Clog, M., Davidheiser-Kroll, B., Davies, A., Dux, F., Eiler, J., … Ziegler, M. (2021). InterCarb: A Community Effort to Improve Interlaboratory Standardization of the Carbonate Clumped

Isotope Thermometer Using Carbonate Standards. *Geochemistry, Geophysics, Geosystems*, *22*(5). https://doi.org/10.1029/2020GC009588

Bornemann, A., Norris, R. D., Lyman, J. A., D'haenens, S., Groeneveld, J., Röhl, U., Farley, K. A., & Speijer, R. P. (2014). Persistent environmental change after the Paleocene-Eocene Thermal Maximum in the eastern North Atlantic. *Earth and Planetary Science Letters*, *394*, 70–81. https://doi.org/10.1016/j.epsl.2014.03.017

Bowen, G. J., & Bowen, B. B. (2008). Mechanisms of PETM global change constrained by a new record from central Utah. *Geology*, *36*(5), 379–382. https://doi.org/10.1130/G24597A.1

Bowen, G. J., Maibauer, B. J., Kraus, M. J., Röhl, U., Westerhold, T., Steimke, A., Gingerich, P. D., Wing, S. L., & Clyde, W. C. (2015). Two massive, rapid releases of carbon during the onset of the Palaeocene-Eocene thermal maximum. *NATURE GEOSCIENCE |*, *8*. https://doi.org/10.1038/NGEO2316

Bowen, G. J., Koch, P. L., Gingerich, P. D., Norris, D., Bains, S., & Corfield, R. M. (2001). Refined isotope stratigraphy across the continental paleocene-eocene boundary on polecat bench in the northern bighorn basin. In *Paleocene-Eocene Stratigraphy and Biotic Change in the Bighorn and Clarks Fork Basins, Wyoming* (pp. 73–88).

Breecker, D. O., Sharp, Z. D., & McFadden, L. D. (2009). Seasonal bias in the formation and stable isotopic composition of pedogenic carbonate in modern soils from central New Mexico, USA. *Bulletin of the Geological Society of America*, *121*(3–4), 630–640. https://doi.org/10.1130/B26413.1

Budd, D. A., Pack, S. M., & Fogel, M. L. (2002). The destruction of paleoclimatic isotopic signals in Pleistocene carbonate soil nodules of Western Australia. *Palaeogeography, Palaeoclimatology, Palaeoecology*, *188*(3–4), 249–273. https://doi.org/10.1016/S0031-0182(02)00588-6

Burgener, L. K., Huntington, K. W., Hoke, G. D., Schauer, A., Ringham, M. C., Latorre, C., & Díaz, F. P. (2016). Variations in soil carbonate formation and seasonal bias over >4 km of relief in the western Andes (30°S) revealed by clumped isotope thermometry. *Earth and Planetary Science Letters*, *441*, 188–199. https://doi.org/10.1016/j.epsl.2016.02.033

Carmichael, M. J., Inglis, G. N., Badger, M. P. S., Naafs, B. D. A., Behrooz, L., Remmelzwaal, S., Monteiro, F. M., Rohrssen, M., Farnsworth, A., Buss, H. L., Dickson, A. J., Valdes, P. J., Lunt, D. J., & Pancost, R. D. (2017). Hydrological and associated biogeochemical consequences of rapid global warming during the Paleocene-Eocene Thermal Maximum. *Global and Planetary Change*, *157*(July), 114–138. https://doi.org/10.1016/j.gloplacha.2017.07.014

Carmichael, M. J., Pancost, R. D., & Lunt, D. J. (2018). Changes in the occurrence of extreme precipitation events at the Paleocene–Eocene thermal maximum. *Earth and Planetary Science Letters*, *501*, 24–36. https://doi.org/10.1016/j.epsl.2018.08.005

Cerling, T. E. (1984). The stable isotopic composition of modern soil carbonate and its relationship to climate. *Earth and Planetary Science Letters*, *71*, 229–240.

Cerling, T. E., & Quade, J. (1993). Stable Carbon and Oxygen Isotopes in Soil Carbonates. *Geophysical Monograph Series*, *78*, 217–231.

Chen, Z., Wang, X., Hu, J., Yang, S., Zhu, M., Dong, X., Tang, Z., Peng, P., & Ding, Z. (2014). Structure of the carbon isotope excursion in a high-resolution lacustrine Paleocene-Eocene Thermal Maximum record from central China. *Earth and Planetary Science Letters*, *408*, 331–340. https://doi.org/10.1016/j.epsl.2014.10.027

Clyde, W. C., & Gingerich, P. D. (1998). Mammalian community response to the latest Paleocene thermal maximum: An isotaphonomic study in the northernBighorn Basin, Wyoming. *Geology* , *26*(November), 10111014.

Coplen, T. B. (2011). Guidelines and recommended terms for expression of stable-isotope-ratio and gas-ratio measurement results. *Rapid Communications in Mass Spectrometry*, *25*(17), 2538–2560. https://doi.org/10.1002/rcm.5129

Cramer, B. S., Wright, J. D., Kent, D. v., & Aubry, M. P. (2003). Orbital climate forcing of δ13C excursions in the late Paleocene-early Eocene (chrons C24n-C25n). *Paleoceanography*, *18*(4). https://doi.org/10.1029/2003PA000909

Dansgaard, W. (1964). Stable isotopes in precipitation. *Tellus*, 436–468. https://doi.org/10.3402/tellusa.v16i4.8993

Deconto, R. M., Galeotti, S., Pagani, M., Tracy, D., Schaefer, K., Zhang, T., Pollard, D., & Beerling, D. J. (2012). Past extreme warming events linked to massive carbon release from thawing permafrost. *Nature*, *484*, 87–91. https://doi.org/10.1038/nature10929

Dickens, G. R. (2011). Down the Rabbit Hole: Toward appropriate discussion of methane release from gas hydrate systems during the Paleocene-Eocene thermal maximum and other past hyperthermal events. *Climate of the Past*, *7*(3), 831–846. https://doi.org/10.5194/cp-7-831-2011

Diefendorf, A. F., Mueller, K. E., Wing, S. L., Koch, P. L., & Freeman, K. H. (2010). Global patterns in leaf ^{13}C discrimination and implications for studies of past and future climate. *Proceedings of the National Academy of Sciences of the United States of America*, *107*(13), 5738–5743. https://doi.org/10.1073/pnas.0910513107

Dunkley Jones, T., Lunt, D. J., Schmidt, D. N., Ridgwell, A., Sluijs, A., Valdes, P. J., & Maslin, M. (2013). Climate model and proxy data constraints on ocean warming across the Paleocene-Eocene Thermal Maximum. In *Earth-Science Reviews* (Vol. 125, pp. 123–145). https://doi.org/10.1016/j.earscirev.2013.07.004

Eiler, J. M. (2007). "Clumped-isotope" geochemistry-The study of naturally-occurring, multiply-substituted isotopologues. *Earth and Planetary Science Letters*, *262*(3–4), 309–327. https://doi.org/10.1016/j.epsl.2007.08.020

Evans, D., Sagoo, N., Renema, W., Cotton, L. J., Müller, W., Todd, J. A., Saraswati, P. K., Stassen, P., Ziegler, M., Pearson, P. N., Valdes, P. J., & Affek, H. P. (2018). Eocene greenhouse climate revealed by coupled clumped isotope-Mg/Ca thermometry. *Proceedings of the National Academy of Sciences of the United States of America*, *115*(6), 1174–1179. https://doi.org/10.1073/pnas.1714744115

Fetrow, A.C., 2022. *Paleoclimate and paleoelevation changes of the Western US during the Cretaceous* (Doctoral dissertation, University of Colorado).

Fiebig, J., Daëron, M., Bernecker, M., Guo, W., Schneider, G., Boch, R., Bernasconi, S. M., Jautzy, J., & Dietzel, M. (2021). Calibration of the dual clumped isotope thermometer for carbonates. *Geochimica et Cosmochimica Acta*, *312*, 235–256. https://doi.org/10.1016/J.GCA.2021.07.012

Finn, T. M., Kirschbaum, M. A., Roberts, S. B., Condon, S. M., Roberts, L. N. R., & Johnson, R. C. (2010). Cretaceous-Tertiary Composite Total Petroleum System (503402), Bighorn Basin, Wyoming and Montana Chapter 3 of Petroleum Systems and Geologic Assessment of Oil and Gas in the Bighorn Basin Province, Wyoming and Montana. In *Petroleum Systems and Geologic Assessment of Oil and Gas in the Bighorn Basin Province, Wyoming and Montana*. http://www.usgs.gov/pubprod

Foreman, B. Z., Heller, P. L., & Clementz, M. T. (2012). Fluvial response to abrupt global warming at the Palaeocene/Eocene boundary. *Nature*, *491*(7422), 92–95. https://doi.org/10.1038/nature11513

Foreman, B. Z. (2014). Climate-driven generation of a fluvial sheet sand body at the Paleocene-Eocene boundary in north-west Wyoming (USA). *Basin Research*, *26*(2), 225–241. https://doi.org/10.1111/bre.12027

Fricke, H. C., & Wing, S. L. (2004). Oxygen isotope and paleobotanical estimates of temperature and δ18O-latitude gradients over North America during the Early

Eocene. *American Journal of Science*, *304*(7), 612–635. https://doi.org/10.2475/ajs.304.7.612

Frieling, J., Svensen, H. H., Planke, S., Cramwinckel, M. J., Selnes, H., & Sluijs, A. (2016). Thermogenic methane release as a cause for the long duration of the PETM. *Proceedings of the National Academy of Sciences of the United States of America*, *113*(43), 12059–12064. https://doi.org/10.1073/pnas.1603348113

Gallagher, T. M., & Sheldon, N. D. (2016). Combining soil water balance and clumped isotopes to understand the nature and timing of pedogenic carbonate formation. *Chemical Geology*. https://doi.org/10.1016/j.chemgeo.2016.04.023

Gat, J. R. (1996). Oxygen and Hydrogen Isotopes in the Hydrologic Cycle. *Annual Reviews in Earth and Planetary Science*, 1–38. https://doi.org/10.1146/annurev.earth.24.1.225

Ghosh, P., Adkins, J., Affek, H. P., Balta, B., Guo, W., Schauble, E. A., Schrag, D., & Eiler, J. M. (2006). 13C-18O bonds in carbonate minerals: A new kind of paleothermometer. *Geochimica et Cosmochimica Acta*, *70*(6), 1439–1456. https://doi.org/10.1016/j.gca.2005.11.014

Gingerich, P. D. (2001). Paleocene-Eocene Stratigraphy and Biotic Change in the Bighorn and Clarks Fork Basins, Wyoming. *Paleocene-Eocene Stratigraphy and Biotic Change in the Bighorn and Clarks Fork Basins, Wyoming: University of Michigan Papers on Paleontology, v.33*, 89–96.

Gingerich, P. D. (2006). Environment and evolution through the Paleocene–Eocene thermal maximum. *Trends in Ecology & Evolution*, *21*(5), 246–253. https://doi.org/10.1016/J.TREE.2006.03.006

Gingerich, P. D., & Clyde, W. C. (2001). Overview of Mammalian Biostratigraphy in the Paleocene-Eocene Fort Union and Willwood Formations of the Bighorn and Clarks Fork Basin . In *Paleocene-Eocene Stratigraphy and biotic change in the Bighorn and Clarks Fork Basins, Wyoming* (pp. 1–15). University of Michigan .

Gutjahr, M., Ridgwell, A., Sexton, P. F., Anagnostou, E., Pearson, P. N., Pälike, H., Norris, R. D., Thomas, E., & Foster, G. L. (2017). Very large release of mostly volcanic carbon during the Palaeocene-Eocene Thermal Maximum. *Nature*, *548*(7669), 573–577. https://doi.org/10.1038/nature23646

Handley, L., Halloran, A. O., Pearson, P. N., Hawkins, E., Nicholas, C. J., Schouten, S., Mcmillan, I. K., & Richard, D. (2012). Changes in the hydrological cycle in tropical East Africa during the Paleocene-Eocene Thermal Maximum. *Palaeogeography, Palaeoclimatology, Palaeoecology*, *329–330*, 10–21. https://doi.org/10.1016/j.palaeo.2012.02.002

Held, I. M., & Soden, B. J. (2006). Robust Responses of the Hydrological Cycle to Global Warming. *Journal of Climate*, *19*, 5686–5699. https://doi.org/10.5220/0001648603850388

Henkes, G. A., Passey, B. H., Grossman, E. L., Shenton, B. J., Pérez-Huerta, A., & Yancey, T. E. (2014). Temperature limits for preservation of primary calcite

clumped isotope paleotemperatures. *Geochimica et Cosmochimica Acta*, *139*, 362–382. https://doi.org/10.1016/j.gca.2014.04.040

Hollis, C. J., Jones, T. D., Anagnostou, E., Bijl, P. K., Cramwinckel, M. J., Cui, Y., Dickens, G. R., Edgar, K. M., Eley, Y., Evans, D., Foster, G. L., Inglis, G. N., Kennedy, E. M., Kozdon, R., Lauretano, V., Lear, H., Littler, K., Meckler, N., Naafs, B. D. A., … Sluijs, A. (2019). The DeepMIP contribution to PMIP4 : methodologies for selection , compilation and analysis of latest Paleocene and early Eocene climate proxy data , incorporating version 0 . 1 of the DeepMIP database. *Geoscientific Model Development Discussions*, *January*, 1–98.

Hough, B. G., Fan, M., & Passey, B. H. (2014). Calibration of the clumped isotope geothermometer in soil carbonate in Wyoming and Nebraska , USA : Implications for paleoelevation and paleoclimate reconstruction. *Earth and Planetary Science Letters*, *391*, 110–120. https://doi.org/10.1016/j.epsl.2014.01.008

Huntington, K. W., Eiler, J. M., Affek, H. P., Guo, W., Bonifacie, M., Yeung, L. Y., Thiagarajan, N., Passey, B., Tripati, A., Daëron, M., & Came, R. (2009). Methods and limitations of "clumped" CO2 isotope (Δ47) analysis by gas-source isotope ratiomass spectrometry. *Journal of Mass Spectrometry*, *44*(9), 1318–1329. https://doi.org/10.1002/jms.1614

Huth, T. E., Cerling, T. E., Marchetti, D. W., Bowling, D. R., Ellwein, A. L., & Passey, B. H. (2019). Seasonal bias in soil carbonate formation and its implications for interpreting high-resolution paleoarchives: evidence from

southern Utah. *Journal of Geophysical Research: Biogeosciences*. https://doi.org/10.1029/2018JG004496

Inglis, G. N., Rohrssen, M., Kennedy, E. M., Crouch, E. M., Raine, J. I., Strogen, D. P., Naafs, B. D. A., Collinson, M. E., & Pancost, R. D. (2021). Terrestrial methane cycle perturbations during the onset of the Paleocene-Eocene Thermal Maximum. *Geology*, *49*(5), 520–524. https://doi.org/10.1130/G48110.1

Kelson, J. R., Huntington, K. W., Breecker, D. O., Burgener, L. K., Gallagher, T. M., Hoke, G. D., & Petersen, S. v. (2020). A proxy for all seasons ? A synthesis of clumped isotope data from Holocene soil carbonates. *Quaternary Science Reviews*, *234*, 106259. https://doi.org/10.1016/j.quascirev.2020.106259

Kender, S., Bogus, K., Pedersen, G. K., Dybkjaer, K., Mather, T. A., Mariani, E., Ridgwell, A., Riding, J. B., Wagner, T., Hesselbo, S. P., & Leng, M. J. (2021). Paleocene/Eocene carbon feedbacks triggered by volcanic activity. *Nature Communications*, *12*, 5186. https://doi.org/10.1038/s41467-021-25536-0

Kennett, J. P., & Stottt, L. D. (1991). Abrupt deep-sea warming, palaeoceanographic changes and benthic extinctions at the end of the Palaeocene. *Nature* , *353*, 225–229.

Kiehl, J. T., Zarzycki, C. M., Shields, C. A., & Rothstein, M. v. (2021). Simulated changes to tropical cyclones across the Paleocene-Eocene Thermal Maximum (PETM) boundary. *Palaeogeography, Palaeoclimatology, Palaeoecology*, *572*. https://doi.org/10.1016/j.palaeo.2021.110421

Kim, S.-T., & O'Neil, J. R. (1997). Equilibrium and nonequilibrium oxygen isotope effects in synthetic carbonates. *Geochimica et Cosmochimica Acta*, *61*(16), 3461–3475. https://doi.org/10.1016/S0016-7037(97)00169-5

Kirtland Turner, S., Sexton, P. F., Charles, C. D., & Norris, R. D. (2014). Persistence of carbon release events through the peak of early Eocene global warmth. *Nature Geoscience*, *12*(September), 1–17. https://doi.org/10.1038/ngeo2240

Koch, P. L., Zachos, J. C., & Gingerich, P. D. (1992). Correlation between isotope records in marine and continental carbon reservoirs near the Palaeocene/Eocene boundary. *Nature*, *358*. https://doi.org/https://doi.org/10.1038/358319a0

Kohn, M. J. (2010). Carbon isotope compositions of terrestrial C3 plants as indicators of (paleo)ecology and (paleo)climate. *Proceedings of the National Academy of Scienes* , *107*. https://doi.org/10.1073/pnas.1004933107/-/DCSupplemental

Kohn, M. J. (2016). Carbon isotope discrimination in C3 land plants is independent of natural variations in pCO2. *Geochemical Perspectives Letters*, *2*(1), 35–43. https://doi.org/10.7185/geochemlet.1604

Korasidis, V. A., Wing, S. L., Nelson, D. M., & Baczynski, A. A. (2022). Reworked pollen reduces apparent floral change during the Paleocene-Eocene Thermal Maximum. *Geology*. https://doi.org/10.1130/G50441.1

Kraus, M. J., & Riggins, S. (2007). Transient drying during the Paleocene–Eocene Thermal Maximum (PETM): Analysis of paleosols in the bighorn basin, Wyoming. *Palaeogeography, Palaeoclimatology, Palaeoecology*, *245*(3–4), 444–461. https://doi.org/10.1016/J.PALAEO.2006.09.011

Kraus, M. J., McInerney, F. A., Wing, S. L., Secord, R., Baczynski, A. A., & Bloch, J. I. (2013). Paleohydrologic response to continental warming during the Paleocene-Eocene Thermal Maximum, Bighorn Basin, Wyoming. *Palaeogeography, Palaeoclimatology, Palaeoecology*, *370*, 196–208. https://doi.org/10.1016/j.palaeo.2012.12.008

Kraus, M. J., Woody, D. T., Smith, J. J., & Dukic, V. (2015). Alluvial response to the Paleocene-Eocene Thermal Maximum climatic event, Polecat Bench, Wyoming (U.S.A.). *Palaeogeography, Palaeoclimatology, Palaeoecology*, *435*, 177–192. https://doi.org/10.1016/j.palaeo.2015.06.021

Krishnan, S., Pagani, M., Huber, M., & Sluijs, A. (2014). High latitude hydrological changes during the Eocene Thermal Maximum 2. *Earth and Planetary Science Letters*, *404*, 167–177. https://doi.org/10.1016/j.epsl.2014.07.029

Kukla, T., Winnick, M. J., Maher, K., Ibarra, D. E., & Chamberlain, C. P. (2019). The Sensitivity of Terrestrial δ 18 O Gradients to Hydroclimate Evolution. *Journal of Geophysical Research: Atmospheres*, *124*, 563–582. https://doi.org/10.1029/2018JD029571

Kurtz, A. C., Kump, L. R., Arthur, M. A., Zachos, J. C., & Paytan, A. (2003). Early Cenozoic decoupling of the global carbon and sulfur cycles. *Paleoceanography*, *18*(4). https://doi.org/10.1029/2003PA000908

Lourens, L. J., Sluijs, A., Kroon, D., Zachos, J. C., Thomas, E., Röhl, U., Bowles, J., & Raffi, I. (2005). Astronomical pacing of late Palaeocene to early Eocene global warming events. *Nature*, *435*(7045), 1083–1087. https://doi.org/10.1038/nature03814

Lunt, D. J., Huber, M., Anagnostou, E., Baatsen, M. L. J., Caballero, R., DeConto, R., Dijkstra, H. A., Donnadieu, Y., Evans, D., Feng, R., Foster, G. L., Gasson, E., von der Heydt, A. S., Hollis, C. J., Inglis, G. N., Jones, S. M., Kiehl, J., Turner, S. K., Korty, R. L., … Zeebe, R. E. (2017). The DeepMIP contribution to PMIP4: Experimental design for model simulations of the EECO, PETM, and pre-PETM (version 1.0). *Geoscientific Model Development*, *10*(2), 889–901. https://doi.org/10.5194/gmd-10-889-2017

McInerney, F. A., & Wing, S. L. (2011). The Paleocene-Eocene Thermal Maximum: A Perturbation of Carbon Cycle, Climate, and Biosphere with Implications for the Future. *Annual Review of Earth and Planetary Sciences*, *39*(1), 489–516. https://doi.org/10.1146/annurev-earth-040610-133431

Mintz, J. S., Driese, S. G., Breecker, D. O., & Ludvigson, G. A. (2011). Influence of changing hydrology on pedogenic calcite precipitation in vertisols dance bayou, Brazoria County, Texas, U.S.A.: Implications for estimating paleoatmospheric

PCo2. *Journal of Sedimentary Research*, *81*(6), 394–400. https://doi.org/10.2110/jsr.2011.36

Nordt, L. C., & Driese, S. D. (2010). New weathering index improves paleorainfall estimates from Vertisols. *Geology*, *38*(5), 407–410. https://doi.org/10.1130/G30689.1

Oerter, E. J., & Amundson, R. (2016). Climate controls on spatial temporal variations in the formation of pedogenic carbonate in the western Great Basin of North Americ. *Bulletin of the Geological Society of America*, *128*(7), 1095–1104. https://doi.org/10.1130/B31367.1

Passey, B. H., Levin, N. E., Cerling, T. E., Brown, F. H., & Eiler, J. M. (2010). High-temperature environments of human evolution in East Africa based on bond ordering in paleosol carbonates. *Proceedings of the National Academy of Sciences*, *107*(25), 11245–11249. https://doi.org/10.1073/pnas.1001824107

Passey, B. H., & Henkes, G. A. (2012). Carbonate clumped isotope bond reordering and geospeedometry. *Earth and Planetary Science Letters*, *351–352*, 223–236. https://doi.org/10.1016/J.EPSL.2012.07.021

Penman, D. E., & Zachos, J. C. (2018). New constraints on massive carbon release and recovery processes during the Paleocene-Eocene Thermal Maximum. *Environmental Research Letters*, *13*(10). https://doi.org/10.1088/1748-9326/aae285

Peppe, D. J., Royer, D. L., Cariglino, B., Oliver, S. Y., Newman, S., Leight, E., Enikolopov, G., Fernandez-Burgos, M., Herrera, F., Adams, J. M., Correa, E.,

Currano, E. D., Erickson, J. M., Hinojosa, L. F., Hoganson, J. W., Iglesias, A., Jaramillo, C. A., Johnson, K. R., Jordan, G. J., … Wright, I. J. (2011). Sensitivity of leaf size and shape to climate: Global patterns and paleoclimatic applications. *New Phytologist*, *190*(3), 724–739. https://doi.org/10.1111/j.1469-8137.2010.03615.x

Peters, N. A., Huntington, K. W., & Hoke, G. D. (2013). Hot or not? Impact of seasonally variable soil carbonate formation on paleotemperature and O-isotope records from clumped isotope thermometry. *Earth and Planetary Science Letters*, *361*, 208–218. https://doi.org/10.1016/j.epsl.2012.10.024

Pujalte, V., Baceta, J. I., & Schmitz, B. (2015). A massive input of coarse-grained siliciclastics in the Pyrenean Basin during the PETM : the missing ingredient in a coeval abrupt change in hydrological regime A massive input of coarse-grained siliciclastics in the Pyrenean Basin during the PETM. *Climate of the Past* , *11*(January 2017). https://doi.org/https://doi.org/10.5194/cp-11-1653-2015

Quade, J., Eiler, J., Daëron, M., & Achyuthan, H. (2013). The clumped isotope geothermometer in soil and paleosol carbonate. *Geochimica et Cosmochimica Acta*, *105*, 92–107. https://doi.org/10.1016/j.gca.2012.11.031

Rea, D. K., Zachos, J. C., Owen, R. M., & Gingerich, P. D. (1990). Global change at the Paleocene-Eocene boundary: climatic and evolutionary consequences of tectonic events. *Palaeogeography, Palaeoclimatology, Palaeoecology*, *79*(1–2), 117–128. https://doi.org/10.1016/0031-0182(90)90108-J

Reinhardt, L., von Gosen, W., Lückge, A., Blumenberg, M., Galloway, J. M., West, C. K., Sudermann, M., & Dolezych, M. (2022). Geochemical indications for the Paleocene-Eocene Thermal Maximum (PETM) and Eocene Thermal Maximum 2 (ETM-2) hyperthermals in terrestrial sediments of the Canadian Arctic. *Geosphere*, *18*(1), 327–349. https://doi.org/10.1130/GES02398.1

Roberts, L. N. R., Finn, T. M., Lewan, M. D., & Kirschbaum, M. A. (2008). Burial History, Thermal Maturity, and Oil and Gas Generation History of Source Rocks in the Bighorn Basin, Wyoming and Montana. *U.S. Geological Survey Scientific Investigations Report*, 0–28.

Rozanski, K., Araguas-Araguas, L., & Gonfiantini, R. (1993). Isotopic Patterns in Modern Global Precipitation. *Geophysical Monograph Series*, *78*, 1–36.

Rush, W. D., Kiehl, J. T., Shields, C. A., & Zachos, J. C. (2021). Increased frequency of extreme precipitation events in the North Atlantic during the PETM: Observations and theory. *Palaeogeography, Palaeoclimatology, Palaeoecology*, *568*(January), 110289. https://doi.org/10.1016/j.palaeo.2021.110289

Secord, R., Gingerich, P. D., Lohmann, K. C., & MacLeod, K. G. (2010). Continental warming preceding the Palaeocene-Eocene thermal maximum. *Nature*, *467*(7318), 955–958. https://doi.org/10.1038/nature09441

Secord, R., Bloch, J. L., Chester, S. G. B., Boyer, D. M., Wood, A. R., Wing, S. L., Kraus, M. J., McInerney, F. A., & Krigbaum, J. (2012). Evolution of the Earliest HorsesDriven by Climate Change in thePaleocene-Eocene Thermal Maximum. *Science*, *335*(6071), 959–962. https://doi.org/10.1126/science.1213859

Sewall, J.O., and Sloan, L.C., 2006, Come a little bit closer: A high-resolution climate study of the early Paleogene Laramide foreland: Geology, v. 34, p. 81–84, doi:10.1130/G22177.1

Shields, C. A., Kiehl, J. T., Rush, W., Rothstein, M., & Snyder, M. A. (2021). Atmospheric rivers in high-resolution simulations of the Paleocene Eocene Thermal Maximum (PETM). *Palaeogeography, Palaeoclimatology, Palaeoecology*, *567*(November 2020), 110293. https://doi.org/10.1016/j.palaeo.2021.110293

Sluijs, A., Schouten, S., Pagani, M., Woltering, M., Brinkhuis, H., Dickens, G. R., Huber, M., Reichart, G., Stein, R., Matthiessen, J., Lourens, L. J., Pedentchouk, N., Backman, J., & Moran, K. (2006). *Subtropical Arctic Ocean temperatures during the Palaeocene / Eocene thermal maximum*. *441*(June), 3–6. https://doi.org/10.1038/nature04668

Sluijs, A., Frieling, J., Inglis, G. N., Nierop, K. G. J., Peterse, F., Sangiorgi, F., & Schouten, S. (2020). Late Paleocene-early Eocene Arctic Ocean Sea Surface Temperatures; 1 reassessing biomarker paleothermometry at Lomonosov Ridge 2 3 The Integrated Ocean Drilling Program Arctic Coring Expedition on Lomonosov 20. *Climate of the Past*, *16*(6), 2381–2400. https://doi.org/10.5194/cp-2020-13

Smith, F. A., Wing, S. L., & Freeman, K. H. (2007). Magnitude of the carbon isotope excursion at the Paleocene-Eocene thermal maximum: The role of plant community change. *Earth and Planetary Science Letters*, *262*(1–2), 50–65. https://doi.org/10.1016/j.epsl.2007.07.021

Snell, K. E., Thrasher, B. L., Eiler, J. M., Koch, P. L., Sloan, L. C., & Tabor, N. J. (2013). Hot summers in the Bighorn Basin during the early Paleogene. *Geology*, *41*(1), 55–58. https://doi.org/10.1130/G33567.1

Tierney, J. E., Zhu, J., Li, M., Ridgewell, A., Hakim, G. J., Poulsen, C. J., Whiteford, R. D. M., Rae, J. W. B., & Kump, L. R. (2022). Spatial patterns of climate change across the Paleocene-Eocene Thermal Maximum. *Proceedings of the National Academy of Science*, *119*(42). https://doi.org/https://doi.org/10.1073/pnas.2205326119

Tipple, B. J., Pagani, M., Krishnan, S., Dirghangi, S. S., Galeotti, S., Agnini, C., Giusberti, L., & Rio, D. (2011). Coupled high-resolution marine and terrestrial records of carbon and hydrologic cycles variations during the Paleocene-Eocene Thermal Maximum (PETM). *Earth and Planetary Science Letters*, *311*(1–2), 82–92. https://doi.org/10.1016/j.epsl.2011.08.045

Tripati, A. K., Hill, P. S., Eagle, R. A., Mosenfelder, J. L., Tang, J., Schauble, E. A., Eiler, J. M., Zeebe, R. E., Uchikawa, J., Coplen, T. B., Ries, J. B., & Henry, D. (2015). Beyond temperature: Clumped isotope signatures in dissolved inorganic carbon species and the influence of solution chemistry on carbonate mineral composition. *Geochimica et Cosmochimica Acta*, *166*, 344–371. https://doi.org/10.1016/j.gca.2015.06.021

van der Meulen, B., Gingerich, P. D., Lourens, L. J., Meijer, N., van Broekhuizen, S., van Ginneken, S., & Abels, H. A. (2020). Carbon isotope and mammal recovery from extreme greenhouse warming at the Paleocene–Eocene boundary

in astronomically-calibrated fluvial strata, Bighorn Basin, Wyoming, USA. *Earth and Planetary Science Letters*, *534*. https://doi.org/10.1016/j.epsl.2019.116044

Wang, Z., Schauble, E. A., & Eiler, J. M. (2004). Equilibrium thermodynamics of multiply substituted isotopologues of molecular gases. *Geochimica et Cosmochimica Acta*, *68*(23), 4779–4797. https://doi.org/10.1016/j.gca.2004.05.039

Westerhold, T., Marwan, N., Drury, A. J., Liebrand, D., Agnini, C., Anagnostou, E., Barnet, J. S. K., Bohaty, S. M., de Vleeschouwer, D., Florindo, F., Frederichs, T., Hodell, D. A., Holbourn, A. E., Kroon, D., Lauretano, V., Littler, K., Lourens, L. J., Lyle, M., Pälike, H., … Zachos, J. C. (2020). An astronomically dated record of Earth's climate and its predictability over the last 66 million years. *Science*, *369*(6509), 1383–1387. https://doi.org/10.1126/science.aba6853

Westerhold, T., Röhl, U., Wilkens, R. H., Gingerich, P. D., Clyde, W. C., Wing, S. L., Bowen, G. J., & Kraus, M. J. (2018). Synchronizing early Eocene deep-sea and continental records - Cyclostratigraphic age models for the Bighorn Basin Coring Project drill cores. *Climate of the Past*, *14*(3), 303–319. https://doi.org/10.5194/cp-14-303-2018

Widlansky, S. J., Secord, R., Snell, K. E., Chew, A. E., & Clyde, W. C. (2022). Terrestrial carbon isotope stratigraphy and mammal turnover during post-PETM hyperthermals in the Bighorn Basin, Wyoming, USA. *Climate of the Past*, *18*(4), 681–712. https://doi.org/10.5194/cp-18-681-2022

Wing, S. L., Harrington, G. J., Smith, F. a, Bloch, J. I., Boyer, D. M., & Freeman, K. H. (2005). Transient Floral Change and Rapid Global Warming at the Paleocene - Eocene Boundary. *Science*, *310*(November), 993–996. https://doi.org/10.1126/science.1116913

Wing, S. L., & Currano, E. D. (2013). Plant response to a global greenhouse event 56 million years ago. *American Journal of Botany*, *100*(7), 1234–1254. https://doi.org/10.3732/ajb.1200554

Wing, S.L. and Currano, E.D., 2017, December. Terrestrial floral change during the ETM2 hyperthermal. In *AGU Fall Meeting Abstracts* (Vol. 2017, pp. PP31D-08).

Zachos, J., Pagani, M., Sloan, L., Thomas, E., & Billups, K. (2001). Trends, Global Rhythms, Aberrations in Global Climate 65Ma to Present. *Science*, *292*(5517), 686–693. https://doi.org/10.1126/science.1059412

Zachos JC, Schouten S, Bohaty S, Quattlebaum T, Sluijs A, et al. 2006. Extreme warming of mid-latitudecoastal ocean during the Paleocene-Eocene Thermal Maximum: inferences from TEX86 and isotopedata.Geology34:737–40

Zeebe R E, Zachos J C and Dickens G R 2009 Carbon dioxide forcingalone insufficient to explain Palaeocene-Eocene ThermalMaximum warmingNat. Geosci.2576–8014Environ. Res. Lett.13(2018)105008

Zeebe, R. E., & Lourens, L. J. (2019). Solar System chaos and the Paleocene–Eocene boundary age constrained by geology and astronomy. *Science*, *929*(August), 926–929. https://doi.org/10.1126/science.aax0612

Supplemental Information

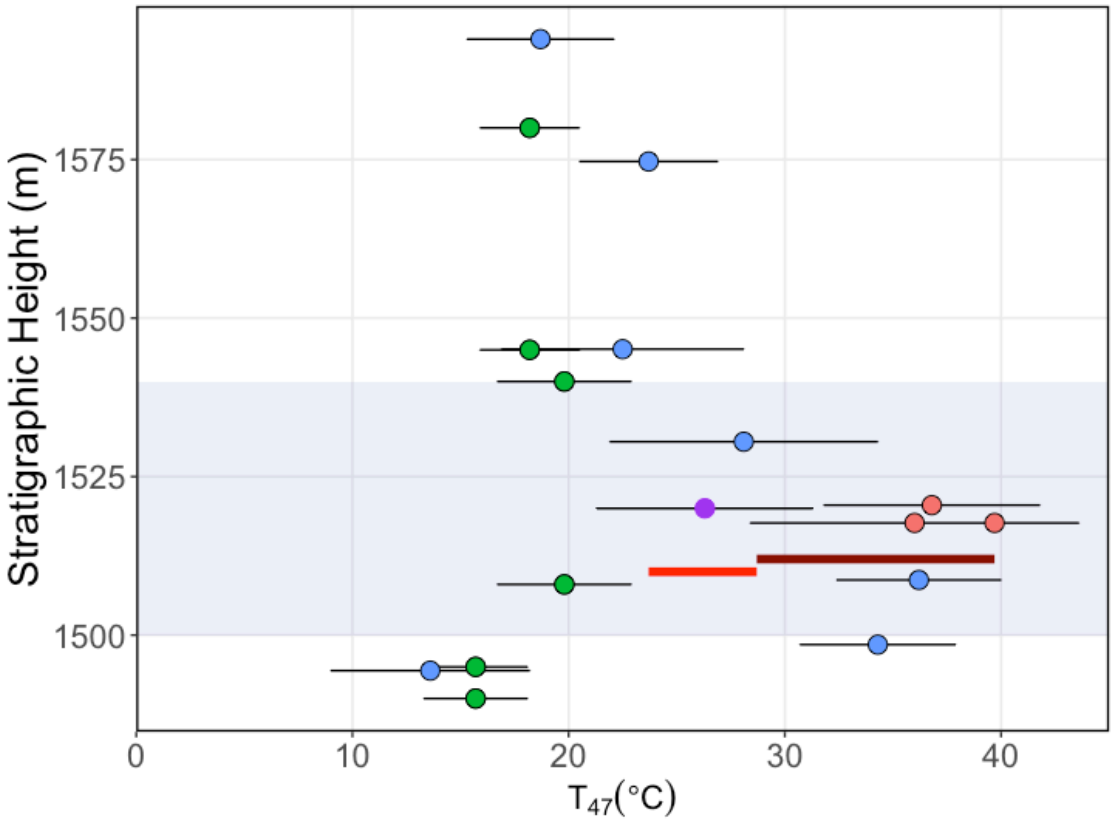

Supplemental Figure 5-1 All temperature estimates from the Bighorn Basin. Clumped isotope data are shown in blue and red circles; recently generated data are in blue and data from Snell et al., 2013 are in red. The purple data point is an estimate of temperature from Fricke and Wing (2004). The green data points are MAT estimates from Leaf margin analysis (Wing et al., 2005); stratigraphic position of these data points are approximate because these samples were collected in the Clarks Fork section. Note, there are two stratigraphic height estimates for each of the 3 temperature estimates because for each estimate, macrofossils were pulled from two levels. Lastly, the estimate of landscape temperature made from the tooth enamel of obligate drinking species at the onset of the PETM is represented by the light red bar. Previously, the $\delta^{18}O$ of tooth enamel carbonate was used to estimate that the magnitude of mean annual temperature change from pre-PETM to the PETM body was ~8-13°C, shown by a bright red bar (Secord et al., 2012). The lower value is defined by added their temperature range (8-13°C) to the Pre-PETM leaf margin analysis temperature. The original calculation relied on a 0.39‰/°C and 0.36‰/°C relationship between $\delta^{18}O$ of surface water and temperature. If instead, I apply a 0.21‰/°C rate, as suggested by the clumped isotope data, then the temperature increase calculated from the $\delta^{18}O_{enamel}$ is ~13-24°C, shown by a dark red bar.

PB-00-02-09, example of homogenous micrite

Whole nodule images

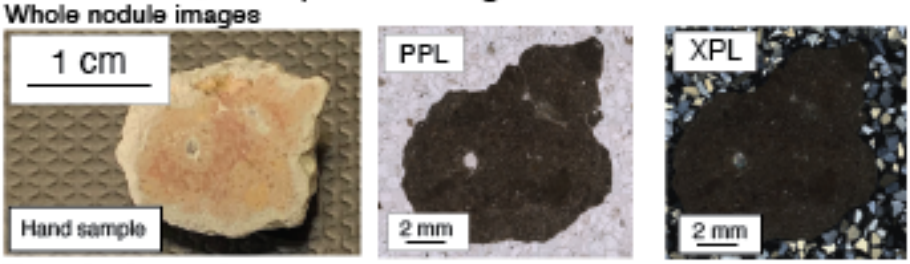

Example close up images

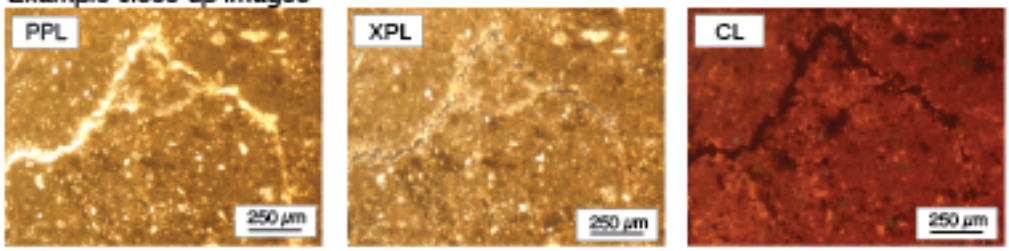

PB-00-03-08, example of avoidable diagentic vein feature

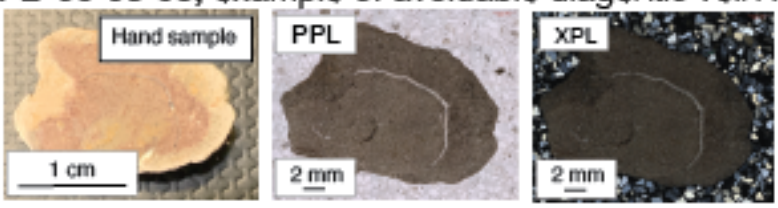

Example close up images

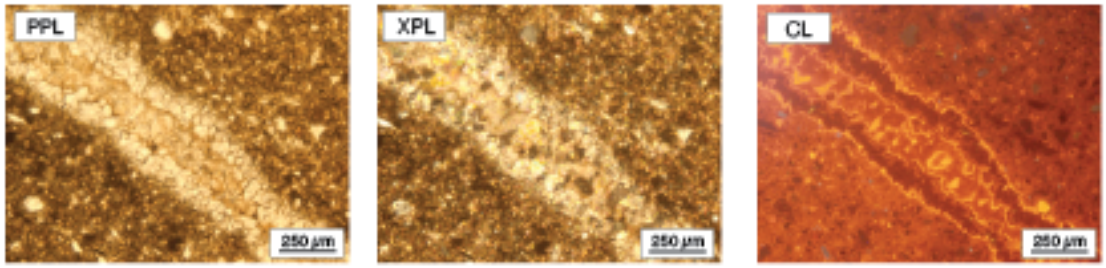

PB-00-04-08, example of many small avoidable diagentic features

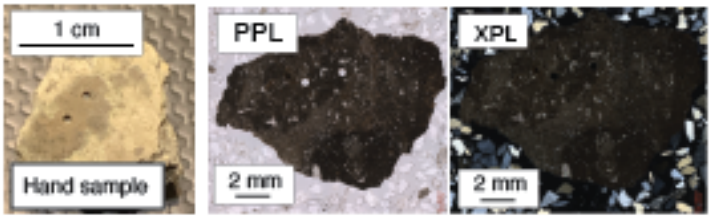

Example close up images

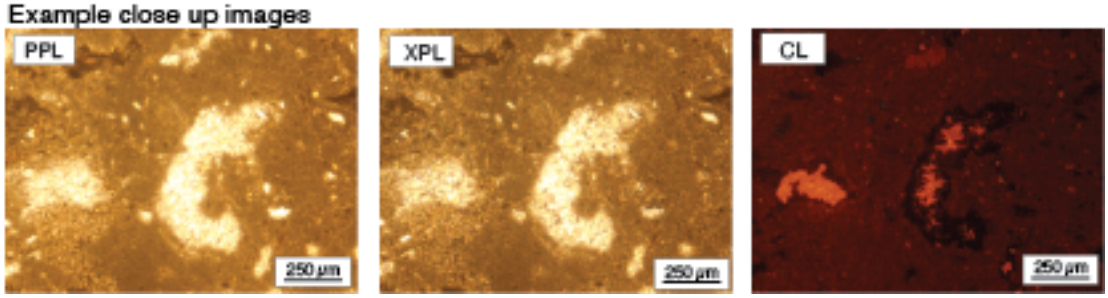

Supplemental Figure 5-2 Hand sample and petrographic images for 3 representative samples: PB-00-02-09 (PETM), PB-00-03-08 (pre-PETM), PB-00-04-08 (post-PETM). In the top row for each sample is a hand sample photo and two mosaics of PPL and XPL images for each nodule. In the bottom row is a close-up image of a key feature of that nodule. PB-00-02-09 is a nodule that is largely dominated by micrite. The close up CL image is of a crack that is non luminescent. PB-00-03-08 is a nodule that is largely dominated by dense micrite (whole nodule PPL and XPL image), but that has a large vein arcing through the nodule. The close up CL images show the large vein has bands of dully – brightly luminescent coarse crystalline spar, surrounded by more uniformly dully luminescent micrite. PB-00-04-08 is an example of a nodule that had many small diagenetic features that required careful drilling. The matrix around the small brightly luminescing features has a dull-orange luminescence.

Supplemental Background

PETM trigger mechanism

The cause of the large negative carbon isotope excursion (CIE) associated with the PETM has been hotly debated within the geoscience community, and a number of sources of ^{13}C-depleted carbon have been proposed, including: a large release of volcanic CO_2 from the North American Igneous Province (e.g. Gutjhar et al., 2017; Kender et al., 2021), destabilized methane hydrates (Dickens, 2011), thermogenic methane release (e.g Frieling et al., 2016), organic matter oxidation (e.g. DeConto et al., 2012), and burning of extensive peat and coal (Kurtz et al., 2003). It has also been proposed that there is a component of orbital forcing (e.g. Zeebe and Lourens, 2019) that precipitated a disturbance to the carbon cycle. It is also possible that more than one of these mechanisms worked in concert with each other, given that observations of a pre-onset negative carbon isotope excursion suggest multiple releases of ^{13}C-depleted carbon (Bowen et al., 2015; Babila et al., 2022).

Carbon Isotope Excursion

The carbon isotope excursion recorded by the pedogenic carbonate nodules is larger than that recorded by organic matter in basin, which estimates a negative carbon isotope excursion of ~4‰ in the tooth enamel of mammal species, pollen, and n-alkanes (Secord et al., 2010; Baczynski et al., 2013; Korasidis et al., 2022b). Generally, $\delta^{13}C$ values from pedogenic carbonate result in a CIE that is larger in magnitude than those observed from the $\delta^{13}C$ of terrestrial bulk organic matter and in the marine record, but the exact CIE magnitude is spatially variable throughout

the Bighorn basin (Bowen et al., 2001; Bowen et al., 2015; Abels et al., 2016; van der Meulen et al., 2022). The CIE variability has largely been attributed to environmental and plant community variability throughout the basin (e.g. Smith et al., 2007; Diefendorf et al., 2010; Kohn, 2010; 2016).

Hydrologic cycle

The hydrologic cycle modeling of Eocene climate contains potentially useful information, but has major uncertainties, particularly for predicting specific local responses in terrestrial regions. There are several reasons for this including major assumptions in how the hydrologic cycle is modified over continental interiors. Changes to the hydrologic cycle in response to warming can be, at first-order, described by the Clausius-Clapeyron equation, which predicts a 7% increase in water vapor saturation per degree celsius of warming (Held and Soden, 2006). The increase in water vapor saturation has the effect of amplifying evaporation and precipitation patterns, which is succinctly described by the adage "wet gets wetter, dry gets drier". The strength of the hydrologic cycle scales below the magnitude of clausius-clapeyron equation, and is on the order of ~2% per degree Celsius (Held and Soden, 2006 and references therein). While the Held and Soden adage is helpful in constructing an interpretive framework to start from, in detail, localized specific changes to the hydrologic cycle are much more complex.

There are three key assumptions built into the Held and Soden framework: first, changes in temperature are spatially uniform across the planet; second, atmospheric circulation patterns, and more specifically wind vectors, remain

unchanged by the warming. Observations of polar amplification of warming during warmhouse and hothouse climates in the geologic past indicate that warming has not been and is unlikely to be uniform across the planet (e.g. Evans et al., 2018; Tierney et al, 2022). Moreover, it is likely that because of this uneven warming across the planet, changes in wind vectors will occur. The third assumption built into the Held and Soden framework is that relative humidity does not change with warming. This final assumption is appropriate over oceans and coastal regions where relative humidity is moderately stable around 100%. However, over continents this assumption rapidly breaks down. Altogether, these assumptions help to explain the uncertainty associated with modeling changes to the hydrologic cycle in a warmer world.

Methods

Sample preparation

Prior to drilling, I polished the samples using 120 µm, 240 µm, 400 µm and 600 µm silica polish. I milled 50 - 100 mg of sample powder from polished surfaces of paleosol carbonate nodules using a dental drill, taking care to avoid areas with coarse crystals, which our combined petrographic and isotopic data, along with the conclusions from similar work in Snell et al., 2013, suggest may result from fluid-based diagenesis and/or later stage filling of voids via precipitation from secondary burial fluids. To avoid drilling 3-dimensionally complex zones of recrystallization and fracture-filling spars, I drilled 1 - 2 mm deep in the nodule, before planing and

repolishing the nodule. When a sufficient quantity of powder had been drilled, I homogenized the sample powder with a mortar and pestle.

For both samples and carbonate standards, I weighed approximately 10-13 mg of carbonate powder into silver capsules for each analysis. The powders were digested in 90°C phosphoric acid for ~20 minutes. After digestion, all gases produced from samples and carbonate standards were cleaned via a custom-built "autoline". The gas was first passed through an ethanol slurry trap held at ~ -85°C to remove CO_2. Then, the gas was passed through a ~10 cm long quartz tube packed with silver wool to remove sulfur compounds. After that, the gas was pushed through a ~ 1.5 m long, 1/8" stainless steel column packed with Poropak, held at –20°C and using helium as the carrier gas, to remove isobaric contaminants. The purified CO_2 was then frozen down again into a final cryogenic trap, then warmed to introduce the sample gas into the IRMS. Reference gas was then introduced to match the sample gas volume.

Analytical setup

Run sessions: May 2022, September 2022

Number of acquisitions per discreet analysis of a sample (ie the gas produce from one acid digestion of sample powder: 10

Reference gas/sample gas cycles per acquisition: 10

Mean Δ47 precision of carbonate standards across all run sessions is:

Diagnosing isobaric contamination via determination of excess mass 48 of CO_2
Clumped isotope temperatures can be influenced by the presence of compounds that have the same masses as the different isotopologues of CO_2 measured for determining $\delta^{13}C$, $\delta^{18}O$ and Δ_{47} (masses 44-47) but are not CO_2; this is known as isobaric interference or contamination. Isobaric contamination can be sourced from hydrocarbon fragments, sulfides, or other organics. Samples that have isobaric contamination of mass 47 will have erroneously cold Δ_{47} temperatures, while samples that have isobaric contamination of masses 45 or 46 will have erroneously hot Δ_{47} temperatures. Samples were closely monitored for potential isobaric contamination using the abundance of simultaneously measured mass-48 of CO_2 (Δ_{48}*),* which is very sensitive to low-levels of contamination. First, Δ_{48} values were calculated analogously to Δ_{47} values, and then corrected for the bulk composition dependence using high temperature carbonate standards ETH1 and ETH2 (similarly to the first step in the Δ_{47} reference frame corrections). Analyses whose corrected Δ_{48} values were greater than 0.345 ‰ (+ the uncertainty of the high temperature carbonate standard correction line) were discarded from the dataset because of suspected contamination. 0.345‰ is the expected difference between 1000°C samples and 25°C samples, and the CUBES-SIL 253+ is currently capable of resolving this temperature-dependent offset. Therefore, analyses that are clean should have Δ_{48} values smaller than 0.345 ‰, while analyses that exceed this value likely contain isobaric contaminants. Analyses that were discarded yielded temperatures of 62 - 124°C.

Supplemental Table 5- 1. Original carbonate stable isotope values for the samples analyzed in this study from Bowen et al., (2001).

Paleosol	Stratigraphic Level (m)	Sample	$\delta^{13}C$ (‰ VPDB)	$\delta^{18}O$ (‰ VPBD)
PB-00-04-16	1594.2	1A	-8.1	-8.3
PB-00-04-16	1594.2	1B	-8.7	-8.6
PB-00-04-16	1594.2	2A	-9.3	-8.4
PB-00-04-16	1594.2	2B	-9.3	-8.3
PB-00-04-14	1574.7	1A	-8.9	-9.2
PB-00-04-14	1574.7	1B	-8.7	-8.6
PB-00-04-14	1574.7	2A	-9.2	-8.8
PB-00-04-14	1574.7	2B	-8.3	-8.5
PB-00-02-19	1545.1	1A	-10.1	-8.7
PB-00-02-19	1545.1	1B	-9.7	-8.8
PB-00-02-19	1545.1	2A	-10.4	-9.4
PB-00-02-19	1545.1	2B	-10.2	-9.3
PB-00-02-09	1530.5	1A	-13.6	-9.2
PB-00-02-09	1530.5	1B	-13.7	-8.7
PB-00-02-09	1530.5	2A	-13.7	-9.5
PB-00-02-09	1530.5	2B	-12.9	-10.7
PB-00-02-09	1530.5	2C	-12.7	-8.4
PB-00-01-07	1508.7	1A	-14.5	-7.9
PB-00-01-07	1508.7	1B	-14.7	-7.9
PB-00-01-07	1508.7	2A	-14.3	-8.1
PB-00-01-07	1508.7	2B	-14.0	-8.1
PB-00-03-11	1498.5	1A	-10.1	-9.7
PB-00-03-11	1498.5	1B	-10.0	-9.7
PB-00-03-11	1498.5	2A	-9.8	-9.6
PB-00-03-11	1498.5	2B	-9.6	-9.6
PB-00-03-08	1494.4	1A	-9.9	-8.9
PB-00-03-08	1494.4	1B	-9.9	-8.9
PB-00-03-08	1494.4	2A	-9.7	-9.2
PB-00-03-08	1494.4	2B	-9.7	-9.4

Chapter VI: Conclusions

In my dissertation, I studied the formation of pedogenic carbonate nodules in modern soils to be able to better interpret a stable isotope record of ancient climate change during the Paleocene-Eocene Thermal Maximum from the Bighorn Basin, WY. Studying pedogenic carbonate formation in modern soils allowed me to probe the strengths and limitations of pedogenic carbonate clumped isotope thermometry in fine-grained soils that are abundant in the geologic record. To understand carbonate formation at a more process-based level, I wanted to be able to create a time-series of soil water stable isotopes to understand how soil water at the carbonate bearing depths evolves on a seasonal scale, because this would give me additional insight into the formation mechanisms and timing of pedogenic carbonate formation. In particular, the addition of soil water isotopes to a modern-calibration study of pedogenic carbonate formation would allow me to test the community's hypothesis that pedogenic carbonate forms as a result of soil dry-down and that the soil water isotope value calculated from clumped isotope measurements represents evaporatively ^{18}O-enriched soil water.

Therefore, in chapters 2 and 3, I focused on developing a method for creating serial records of soil water isotopes. In chapter two, I presented the initial development of the Soil Water Isotope Storage System (SWISS). My tests demonstrated that the SWISSs are capable of reliably storing water vapor for up to 30 days after initial sample collection. This system enables the creation of serial soil water datasets where it is impractical deploy cavity ring down spectrometers or

manually intervene on a regular basis. In chapter three, I presented the fully tested, automated and field deployable version of the SWISS. Through a series of quality assurance and quality control tests, I tested that the SWISS is resistant to both atmospheric intrusion and leaking in both laboratory and field settings over even longer time periods than our results in Chapter 2 suggested (up to 40 days). I assessed the accuracy and precision of the SWISS through a series of experiments where water vapor of known composition was introduced into the flasks, stored for 14 days, and then measured. From these experiments, after applying an offset correction, I assessed the precision of the SWISS at 0.9‰ and 3.7‰ for $\delta^{18}O$ and $\delta^{2}H$, respectively. I also recommended future testing of the SWISS, which should include testing how the region (i.e. the relatively arid Western U.S. vs. more humid regions) changes the offset correction and how soil water collected via membrane tubing compares to other methods of soil water collection (e.g. suction-lysimeter, cryogenic extraction, etc.). The SWISS is a tool that has great potential to address a wide range of ecohydrological questions and can be used to improve geoscientists' understanding of a range of paleoenvironmental proxies. For example, in the geoscience community, the SWISS could be used to better understand the formation of lipid biomarker proxies that are used to reconstruct temperature (GDGTs), and hydrology ($\delta^{2}H$ of n-alkanes), and for the ecohydrologic community, this tool might help shed light on evaporation dynamics across soil textures (i.e. the Craig-Gordon model of evaporation), and root water uptake dynamics (i.e. addressing the two-water-worlds hypothesis).

In chapter 4, I presented a modern study of pedogenic carbonate formation in three fine-medium grained soils in Colorado and Nebraska, USA. For this study, I used a combination of climatological data, soil water and precipitation stable isotope geochemistry and pedogenic carbonate clumped isotope thermometry ($T(\Delta_{47})$) to learn about the timing and drivers of carbonate formation. In the two soils from Colorado, the $T(\Delta_{47})$ values and $\delta^{18}O$ values of soil water are consistent with carbonate formation in the late fall during dry-down, which suggests that interpreting clumped isotope temperatures as similar to mean annual temperature is appropriate. The relative invariance of soil water isotopes at the carbonate bearing depths from summer to fall and the overlap of clumped isotope data with modern measurements of soil water data, suggests that the $\delta^{18}O$ value of soil water calculated from clumped isotope data may not be evaporatively ^{18}O-enriched as often as the community has previously assumed. This would open greater avenues for exploring hydrologic change in the geologic past using clumped isotope thermometry. However, in the third and most clay-rich soil, $T(\Delta_{47})$ was 9-10°C greater than mean annual temperature and the calculated $\delta^{18}O$ of soil water was ~7‰ higher than my observations of soil water isotopes at the carbonate bearing levels. Data from this site may represent a few options: 1) pedogenic carbonate forming in equilibrium, but in contrast to the other soils, carbonate formation occurs during times of peak soil warmth and when the soil water has been evaporatively ^{18}O-enriched; 2) pedogenic carbonate formation is a result of stable isotope disequilibrium caused from rapid CO_2 degassing as the soil cracks in

response to soil dry-down, leading to higher $\delta^{18}O$ and temperatures than expected; or, 3) pedogenic carbonate formation occurs under warm, water-logged conditions when Ca^{2+} is freely available in the soil via hydrolysis and/or carbonate dissolution, and the soil geochemistry hovers just around carbonate saturation. Broadly, the results of this study highlight a continued need to study pedogenic carbonate formation in vertisols and aridisols with vertic properties, because they are an important archive in the geologic record. Future work should include dual Δ_{47}-Δ_{48} thermometry to test the second hypothesis that carbonate formed as a result of rapid CO_2 degassing, long-term monitoring to limit the effects of ephemeral climate phenomena like El Niño/La Niña, and the inclusion of $\delta^{13}C$ data from both soil CO_2 and soil organic matter.

In chapter 5, I presented a pedogenic carbonate clumped isotope record through the Paleocene-Eocene Thermal Maximum. Soil temperatures increased ~20°C just prior to the onset of the negative carbon isotope excursion, and peak at 36.2 ± 3.8°C. Based on what I learned about carbonate formation in fine grained soils in chapter 4, and given the overlap with other records of mean annual temperature both before and after the PETM, I interpret these temperatures to be representative of mean annual temperature. A 20°C increase in mean annual temperature is much larger than has been previously interpreted from the floral record. This implies extremely hot summer temperatures, on the order of 50°C, that are likely too hot to support plant life, so I suggest that conditions changed in the basin from warm season to cold season floral growth during the PETM. This shift

would help to explain the difference between the two estimates of mean annual temperature. These data also have important implications for Earth's equilibrium climate sensitivity in hot-house climates, and provide context for widely observed sedimentary and biotic changes during the PETM. Future work should include dual Δ_{47}-Δ_{48} thermometry to test if pedogenic samples from clay-rich horizons are forming outside of homogenous isotopic equilibrium.

In this dissertation, I developed the SWISS to enable the collection of soil water isotope time series data sets. By capitalizing on new developments in the ecohydrology community, and reaching beyond the geology community, I was able to shed new light on the timing and style of carbonate formation in fine grained soils. My modern calibration study highlighted the utility of using geologically relevant analogues to build more robust interpretations of ancient records. That study will be particularly relevant for many other Cenozoic records of climate that use pedogenic carbonate from fine-grained paleosols. Lastly, my record of climate change through the PETM highlights the sensitivity of terrestrial environments during rapid warming events and highlights a continued need to pursue terrestrial records worldwide.

References

Abdul Aziz, H., Hilgen, F. J., van Luijk, G. M., Sluijs, A., Kraus, M. J., Pares, J. M., & Gingerich, P. D. (2008). Astronomical climate control on paleosol stacking patterns in the upper Paleocene-lower Eocene Willwood Formation, Bighorn Basin, Wyoming. *Geology*, *36*(7), 531–534. https://doi.org/10.1130/G24734A.1

Abels, H. A., Clyde, W. C., Gingerich, P. D., Hilgen, F. J., Fricke, H. C., Bowen, G. J., & Lourens, L. J. (2012). Terrestrial carbon isotope excursions and biotic change during Palaeogene hyperthermals. *Nature Geoscience*, *5*(5), 326–329. https://doi.org/10.1038/ngeo1427

Affek, H. P., & Zaarur, S. (2014). Kinetic isotope effect in CO2 degassing: Insight from clumped and oxygen isotopes in laboratory precipitation experiments. *Geochimica et Cosmochimica Acta*, *143*, 319–330. https://doi.org/10.1016/j.gca.2014.08.005

Anderson, N. T., Kelson, J. R., Kele, S., Daëron, M., Bonifacie, M., Horita, J., Mackey, T. J., John, C. M., Kluge, T., Petschnig, P., Jost, A. B., Huntington, K. W., Bernasconi, S. M., & Bergmann, K. D. (2021). A unified clumped isotope thermometer calibration (0.5–1100°C) using carbonate-based standardization. *Geophysical Research Letters*, 1–11. https://doi.org/10.1029/2020gl092069

Aze, T., Pearson, P. N., Dickson, A. J., Badger, M. P. S., Bown, P. R., Pancost, R. D., Gibbs, S. J., & Huber, B. T. (2014). Extreme warming of tropical waters during the Paleocene – Eocene Thermal Maximum. *Geology*, *42*(9), 739–742. https://doi.org/10.1130/G35637.1

Bao H., Koch, P. L., & Rumble, D. (1999). Paleocene-Eocene climatic variation in western North America: Evidence from the δ18o of pedogenic hematite. *Bulletin of the Geological Society of America*, *111*(9), 1405–1415. https://doi.org/10.1130/0016-7606(1999)111<1405:PECVIW>2.3.CO;2

Babila, T. L., Penman, D. E., Standish, C. D., Doubrawa, M., Bralower, T. J., Robinson, M. M., Self-Trail, J. M., Speijer, R. P., Stassen, P., Foster, G. L., & Zachos, J. C. (2022). Surface ocean warming and acidification driven by rapid carbon release precedes Paleocene-Eocene Thermal Maximum. In *Sci. Adv* (Vol. 8). https://www.science.org

Baczynski, A. A., McInerney, F. A., Wing, S. L., Kraus, M. J., Bloch, J. I., & Secord, R. (2016). Constraining paleohydrologic change during the Paleocene-Eocene Thermal Maximum in the continental interior of North America. *Palaeogeography, Palaeoclimatology, Palaeoecology*, *465*, 237–246. https://doi.org/10.1016/j.palaeo.2016.10.030

Baczynski, A. A., McInerney, F. A., Wing, S. L., Kraus, M. J., Bloch, J. I., Boyer, D. M., Secord, R., Morse, P. E., & Fricke, H. C. (2013). Chemostratigraphic implications of spatial variation in the Paleocene-Eocene Thermal Maximum carbon isotope excursion, SE Bighorn Basin, Wyoming. *Geochemistry, Geophysics, Geosystems*, *14*(10), 4133–4152. https://doi.org/10.1002/ggge.20265

Bernasconi, S. M., Daëron, M., Bergmann, K. D., Bonifacie, M., Meckler, A. N., Affek, H. P., Anderson, N., Bajnai, D., Barkan, E., Beverly, E., Blamart, D., Burgener, L., Calmels, D., Chaduteau, C., Clog, M., Davidheiser-Kroll, B.,

Davies, A., Dux, F., Eiler, J., … Ziegler, M. (2021). InterCarb: A Community Effort to Improve Interlaboratory Standardization of the Carbonate Clumped Isotope Thermometer Using Carbonate Standards. *Geochemistry, Geophysics, Geosystems*, *22*(5). https://doi.org/10.1029/2020GC009588

Beyer, M., Kühnhammer, K., & Dubbert, M. (2020). In situ measurements of soil and plant water isotopes : a review of approaches , practical considerations and a vision for the future. *Hydrology and Earth System Sciences*, *24*, 4413–4440. https://doi.org/https://doi.org/10.5194/hess-24-4413-2020

Bornemann, A., Norris, R. D., Lyman, J. A., D'haenens, S., Groeneveld, J., Röhl, U., Farley, K. A., & Speijer, R. P. (2014). Persistent environmental change after the Paleocene-Eocene Thermal Maximum in the eastern North Atlantic. *Earth and Planetary Science Letters*, *394*, 70–81. https://doi.org/10.1016/j.epsl.2014.03.017

Boutton TW, Archer SR, Midwood AJ. Stable isotopes in ecosystem science: Structure, function and dynamics of a subtropical savanna. *Rapid Commun Mass Spectrom*. 1999;13(13):1263-1277.

Bowen, G. J., & Bowen, B. B. (2008). Mechanisms of PETM global change constrained by a new record from central Utah. *Geology*, *36*(5), 379–382. https://doi.org/10.1130/G24597A.1

Bowen, G. J., Maibauer, B. J., Kraus, M. J., Röhl, U., Westerhold, T., Steimke, A., Gingerich, P. D., Wing, S. L., & Clyde, W. C. (2015). Two massive, rapid releases of carbon during the onset of the Palaeocene-Eocene thermal maximum. *NATURE GEOSCIENCE |*, *8*. https://doi.org/10.1038/NGEO2316

Bowen, G. J., Koch, P. L., Gingerich, P. D., Norris, D., Bains, S., & Corfield, R. M. (2001). Refined isotope stratigraphy across the continental paleocene-eocene boundary on polecat bench in the northern bighorn basin. In *Paleocene-Eocene Stratigraphy and Biotic Change in the Bighorn and Clarks Fork Basins, Wyoming* (pp. 73–88).

Bowen, G. J., Koch, P. L., Gingerich, P. D., Norris, D., Bains, S., & Corfield, R. M. (2001). Refined isotope stratigraphy across the continental Paleocene-Eocene boundary on Polecat Bench in the northern Bighorn Basin. In *Paleocene-Eocene Stratigraphy and Biotic Change in the Bighorn and Clarks Fork Basins, Wyoming,* University of Michigan Papers on Paleontology, p. 73–88.

Bowen GJ, Good SP. Incorporating water isoscapes in hydrological and water resource investigations. *Wiley Interdiscip Rev Water*. 2015;2(2):107-119. doi:10.1002/wat2.1069

Bowen, G. J., Cai, Z., Fiorella, R. P., & Putman, A. L. (2019). Isotopes in the Water Cycle: Regional- to Global-Scale Patterns and Applications. *Annual Review of Earth and Planetary Sciences*, *47*(1), 453–479. https://doi.org/10.1146/annurev-earth-053018-060220

Bowen, G. J., Putman, A., Brooks, J. R., Bowling, D. R., Oerter, E. J., & Good, S. P. (2018). Inferring the source of evaporated waters using stable H and O isotopes. *Oecologia*, *187*(4), 1025–1039. https://doi.org/10.1007/s00442-018-4192-5

Brand WA, Geilmann H, Crosson ER, Rella CW. Cavity ring-down spectroscopy versus high-temperature conversion isotope ratio mass spectrometry; a case

study on d2H and d18O of pure water samples and alcohol/water mixtures. *Rapid Commun Mass Spectrom*. 2009;23(12):119-130. doi:10.1002/rcm

Breecker, D. O., Sharp, Z. D., & McFadden, L. D. (2009). Seasonal bias in the formation and stable isotopic composition of pedogenic carbonate in modern soils from central New Mexico, USA. *Bulletin of the Geological Society of America*, *121*(3–4), 630–640. https://doi.org/10.1130/B26413.1.1

Breecker, D. O., Sharp, Z. D., & McFadden, L. D. (2010). Atmospheric CO2 concentrations during ancient greenhouse climates were similar to those predicted for A.D. 2100. *Proceedings of the National Academy of Sciences of the United States of America*, *107*(2), 576–580. https://doi.org/10.1073/pnas.0902323106

Breecker, D. O. (2013). Quantifying and understanding the uncertainty of atmospheric CO2 concentrations determined from calcic paleosols. *Geochemistry, Geophysics, Geosystems*, *14*(8), 3210–3220. https://doi.org/10.1002/ggge.20189

Breecker, D. O., Yoon, J., Michel, L. A., Dinka, T. M., Driese, S. G., Mintz, J. S., Nordt, L. C., Romanak, K. D., & Morgan, C. L. S. (2013). CO2 Concentrations in Vertisols: Seasonal Variability and Shrink–Swell. *SEPM Special Publication No. 104: New Frontiers in Paleopedology and Terrestrial Paleoclimatology: Paleosols and Soil Surface Analog Systems*, *104*, 35–45. https://doi.org/10.2110/sepmsp.104.08

Brooks, J. R., Barnard, H. R., Coulombe, R., & McDonnell, J. J. (2010). Ecohydrologic separation of water between trees and streams in a

Mediterranean climate. *Nature Geoscience*, *3*(2), 100–104. https://doi.org/10.1038/ngeo722

Brookins, S., 2021. Texture and mineralogy: how soil characteristics help to understand soil formation (Honors thesis, University of Colorado at Boulder).

Budd, D. A., Pack, S. M., & Fogel, M. L. (2002). The destruction of paleoclimatic isotopic signals in Pleistocene carbonate soil nodules of Western Australia. *Palaeogeography, Palaeoclimatology, Palaeoecology*, *188*(3–4), 249–273. https://doi.org/10.1016/S0031-0182(02)00588-6

Burgener, L. K., Huntington, K. W., Hoke, G. D., Schauer, A., Ringham, M. C., Latorre, C., & Díaz, F. P. (2016). Variations in soil carbonate formation and seasonal bias over >4 km of relief in the western Andes (30°S) revealed by clumped isotope thermometry. *Earth and Planetary Science Letters*, *441*, 188–199. https://doi.org/10.1016/j.epsl.2016.02.033

Burgener, L. K., Huntington, K. W., Sletten, R., Watkins, J. M., Quade, J., & Hallet, B. (2018). Clumped isotope constraints on equilibrium carbonate formation and kinetic isotope effects in freezing soils. *Geochimica et Cosmochimica Acta*, *235*, 402–430. https://doi.org/10.1016/j.gca.2018.06.006

Carmichael, M. J., Inglis, G. N., Badger, M. P. S., Naafs, B. D. A., Behrooz, L., Remmelzwaal, S., Monteiro, F. M., Rohrssen, M., Farnsworth, A., Buss, H. L., Dickson, A. J., Valdes, P. J., Lunt, D. J., & Pancost, R. D. (2017). Hydrological and associated biogeochemical consequences of rapid global warming during the

Paleocene-Eocene Thermal Maximum. *Global and Planetary Change*, *157*(July), 114–138. https://doi.org/10.1016/j.gloplacha.2017.07.014

Carmichael, M. J., Pancost, R. D., & Lunt, D. J. (2018). Changes in the occurrence of extreme precipitation events at the Paleocene–Eocene thermal maximum. *Earth and Planetary Science Letters*, *501*, 24–36. https://doi.org/10.1016/j.epsl.2018.08.005

Carrapa, B., Huntington, K. W., Clementz, M., Quade, J., Bywater-Reyes, S., Schoenbohm, L. M., & Canavan, R. R. (2014). Uplift of the Central Andes of NW Argentina associated with upper crustal shortening, revealed by multiproxy isotopic analyses. *Tectonics*, *33*(6), 1039–1054. https://doi.org/10.1002/2013TC003461

Cerling, T. E. (1984). The stable isotopic composition of modern soil carbonate and its relationship to climate. *Earth and Planetary Science Letters*, *71*, 229–240.

Cerling, T. E., & Quade, J. (1993). Stable Carbon and Oxygen Isotopes in Soil Carbonates. *Geophysical Monograph Series*, *78*, 217–231.

Cerling, T. E., Solomon, D. K., Quade, J., & Bowman, J. R. (1991). On the isotopic composition of carbon in soil carbon dioxide. *Geochimica et Cosmochimica Acta*, *55*(11), 3403–3405. https://doi.org/10.1016/0016-7037(91)90498-T

Chen, Z., Wang, X., Hu, J., Yang, S., Zhu, M., Dong, X., Tang, Z., Peng, P., & Ding, Z. (2014). Structure of the carbon isotope excursion in a high-resolution lacustrine Paleocene-Eocene Thermal Maximum record from central China.

Earth and Planetary Science Letters, *408*, 331–340. https://doi.org/10.1016/j.epsl.2014.10.027

Clyde, W. C., & Gingerich, P. D. (1998). Mammalian community response to the latest Paleocene thermal maximum: An isotaphonomic study in the northernBighorn Basin, Wyoming. *Geology* , *26*(November), 10111014.

CoAgMet, Colorado Climate Center, 2023, Colorado State Univerisity, Fort Collins, Colorado. https://climate.colostate.edu/. Accessed 03/31/2023.

Coplen, T. B. (2011). Guidelines and recommended terms for expression of stable-isotope-ratio and gas-ratio measurement results. *Rapid Communications in Mass Spectrometry*, *25*(17), 2538–2560. https://doi.org/10.1002/rcm.5129

Craig, H., (1961), Isotopic variations in meteoric waters. *Science*, *133*(3465), pp.1702-1703.

Cramer, B. S., Wright, J. D., Kent, D. v., & Aubry, M. P. (2003). Orbital climate forcing of δ13C excursions in the late Paleocene-early Eocene (chrons C24n-C25n). *Paleoceanography*, *18*(4). https://doi.org/10.1029/2003PA000909

Dansgaard W. Stable isotopes in precipitation. *Tellus*. 1964:436-468. doi:10.3402/tellusa.v16i4.8993

Dawson, T. E., & Ehleringer, J. R. (1991). Streamside trees that do not use stream-water: evidence from hydrogen isotopes ratios. *Nature*, *350*(March), 335–337.

DeCelles, P. G., Quade, J., Kapp, P., Fan, M., Dettman, D. L., & Ding, L. (2007). High and dry in central Tibet during the Late Oligocene. *Earth and Planetary Science Letters*, *253*(3–4), 389–401. https://doi.org/10.1016/j.epsl.2006.11.001

Deconto, R. M., Galeotti, S., Pagani, M., Tracy, D., Schaefer, K., Zhang, T., Pollard, D., & Beerling, D. J. (2012). Past extreme warming events linked to massive carbon release from thawing permafrost. *Nature*, *484*, 87–91. https://doi.org/10.1038/nature10929

Dennis, K. J., Affek, H. P., Passey, B. H., Schrag, D. P., & Eiler, J. M. (2011). Defining an absolute reference frame for "clumped" isotope studies of CO 2. *Geochimica et Cosmochimica Acta*, *75*(22), 7117–7131. https://doi.org/10.1016/j.gca.2011.09.025

Dickens, G. R. (2011). Down the Rabbit Hole: Toward appropriate discussion of methane release from gas hydrate systems during the Paleocene-Eocene thermal maximum and other past hyperthermal events. *Climate of the Past*, *7*(3), 831–846. https://doi.org/10.5194/cp-7-831-2011

Diefendorf, A. F., Mueller, K. E., Wing, S. L., Koch, P. L., & Freeman, K. H. (2010). Global patterns in leaf ^{13}C discrimination and implications for studies of past and future climate. *Proceedings of the National Academy of Sciences of the United States of America*, *107*(13), 5738–5743. https://doi.org/10.1073/pnas.0910513107

Dunkley Jones, T., Lunt, D. J., Schmidt, D. N., Ridgwell, A., Sluijs, A., Valdes, P. J., & Maslin, M. (2013). Climate model and proxy data constraints on ocean warming across the Paleocene-Eocene Thermal Maximum. In *Earth-Science Reviews* (Vol. 125, pp. 123–145). https://doi.org/10.1016/j.earscirev.2013.07.004

Eiler, J. M. (2007). “Clumped-isotope” geochemistry - The study of naturally-occurring, multiply-substituted isotopologues. *Earth and Planetary Science Letters*, *262*(3–4), 309–327. https://doi.org/10.1016/j.epsl.2007.08.020

Evaristo J, Jasechko S, McDonnell JJ. Global separation of plant transpiration from groundwater and streamflow. *Nature*. 2015;525(7567):91-94. doi:10.1038/nature14983

Evans, D., Sagoo, N., Renema, W., Cotton, L. J., Müller, W., Todd, J. A., Saraswati, P. K., Stassen, P., Ziegler, M., Pearson, P. N., Valdes, P. J., & Affek, H. P. (2018). Eocene greenhouse climate revealed by coupled clumped isotope-Mg/Ca thermometry. *Proceedings of the National Academy of Sciences of the United States of America*, *115*(6), 1174–1179. https://doi.org/10.1073/pnas.1714744115

Fetrow, A.C., 2022. *Paleoclimate and paleoelevation changes of the Western US during the Cretaceous* (Doctoral dissertation, University of Colorado).

Fiebig, J., Daëron, M., Bernecker, M., Guo, W., Schneider, G., Boch, R., Bernasconi, S. M., Jautzy, J., & Dietzel, M. (2021). Calibration of the dual clumped isotope thermometer for carbonates. *Geochimica et Cosmochimica Acta*, *312*, 235–256. https://doi.org/10.1016/J.GCA.2021.07.012

Finn, T. M., Kirschbaum, M. A., Roberts, S. B., Condon, S. M., Roberts, L. N. R., & Johnson, R. C. (2010). Cretaceous-Tertiary Composite Total Petroleum System (503402), Bighorn Basin, Wyoming and Montana Chapter 3 of Petroleum Systems and Geologic Assessment of Oil and Gas in the Bighorn Basin Province, Wyoming and Montana. In *Petroleum Systems and Geologic*

Assessment of Oil and Gas in the Bighorn Basin Province, Wyoming and Montana. http://www.usgs.gov/pubprod

Fischer-Femal, B. J., & Bowen, G. J. (2021). Coupled carbon and oxygen isotope model for pedogenic carbonates. *Geochimica et Cosmochimica Acta*, *294*, 126–144. https://doi.org/10.1016/j.gca.2020.10.022

Foreman, B. Z., Heller, P. L., & Clementz, M. T. (2012). Fluvial response to abrupt global warming at the Palaeocene/Eocene boundary. *Nature*, *491*(7422), 92–95. https://doi.org/10.1038/nature11513

Foreman, B. Z. (2014). Climate-driven generation of a fluvial sheet sand body at the Paleocene-Eocene boundary in north-west Wyoming (USA). *Basin Research*, *26*(2), 225–241. https://doi.org/10.1111/bre.12027

Fricke, H. C., & Wing, S. L. (2004). Oxygen isotope and paleobotanical estimates of temperature and δ18O-latitude gradients over North America during the Early Eocene. *American Journal of Science*, *304*(7), 612–635. https://doi.org/10.2475/ajs.304.7.612

Frieling, J., Svensen, H. H., Planke, S., Cramwinckel, M. J., Selnes, H., & Sluijs, A. (2016). Thermogenic methane release as a cause for the long duration of the PETM. *Proceedings of the National Academy of Sciences of the United States of America*, *113*(43), 12059–12064. https://doi.org/10.1073/pnas.1603348113

Gaj, M., Beyer, M., Koeniger, P., Wanke, H., Hamutoko, J., & Himmelsbach, T. (2015). In-situ unsaturated zone stable water isotope (^{2}H and ^{18}O) measurements in semi-arid environments using tunable off-axis integrated

cavity output spectroscopy. *Hydrology and Earth System Sciences Discussions*, *12*(6), 6115–6149. https://doi.org/10.5194/hessd-12-6115-2015

Gallagher, T. M., & Sheldon, N. D. (2016). Combining soil water balance and clumped isotopes to understand the nature and timing of pedogenic carbonate formation. *Chemical Geology*. https://doi.org/10.1016/j.chemgeo.2016.04.023

Garzione, C. N., Molnar, P., Libarkin, J. C., & MacFadden, B. J. (2006). Rapid late Miocene rise of the Bolivian Altiplano: Evidence for removal of mantle lithosphere. *Earth and Planetary Science Letters*, *241*(3–4), 543–556. https://doi.org/10.1016/j.epsl.2005.11.026

Gat JR. (1996) Oxygen and Hydrogen Isotopes in the Hydrologic Cycle. *Annu Rev Earth Planet Sci*. 1996:1-38. doi:10.1146/annurev.earth.24.1.225

Ghosh, P., Garzione, C. N., & Eiler, J. M. (2006). Rapid Uplift of the Altiplano Revealed Through 13C-18O Bonds in Paleosol Carbonates. *Science*, *311*(January), 511–515.

Gingerich, P. D. (2006). Environment and evolution through the Paleocene–Eocene thermal maximum. *Trends in Ecology & Evolution*, *21*(5), 246–253. https://doi.org/10.1016/J.TREE.2006.03.006

Gingerich, P. D., & Clyde, W. C. (2001). Overview of Mammalian Biostratigraphy in the Paleocene-Eocene Fort Union and Willwood Formations of the Bighorn and Clarks Fork Basin . In *Paleocene-Eocene Stratigraphy and biotic change in the Bighorn and Clarks Fork Basins, Wyoming* (pp. 1–15). University of Michigan .

Gingerich, P. D. (2001). Paleocene-Eocene Stratigraphy and Biotic Change in the Bighorn and Clarks Fork Basins, Wyoming. In *Paleocene-Eocene Stratigraphy and Biotic Change in the Bighorn and Clarks Fork Basins, Wyoming,* University of Michigan Papers on Paleontology, p. 89–96.

Gómez-Navarro, C., Pataki, D. E., Bowen, G. J., & Oerter, E. J. (2019). Spatiotemporal variability in water sources of urban soils and trees in the semiarid, irrigated Salt Lake Valley. *Ecohydrology*, *12*(8). https://doi.org/10.1002/eco.2154

Good, S. P., Noone, D., & Bowen, G. J. (2015). Hydrologic connectivity constrains partitioning of global terrestrial water fluxes. *Science*, *349*(6244), 175–177. https://doi.org/10.1126/science.aaa5931

Green, M. B., Laursen, B. K., Campbell, J. L., Mcguire, K. J., & Kelsey, E. P. (2015). Stable water isotopes suggest sub-canopy water recycling in a northern forested catchment. *Hydrological Processes*, *29*(25), 5193–5202. https://doi.org/10.1002/hyp.10706

Groh, J., Stumpp, C., Lücke, A., Pütz, T., Vanderborght, J. and Vereecken, H., (2018), Inverse estimation of soil hydraulic and transport parameters of layered soils from water stable isotope and lysimeter data. *Vadose Zone Journal*, *17*(1), pp.1-19.

Guo, W. (2020). Kinetic clumped isotope fractionation in the DIC-H2O-CO2 system: Patterns, controls, and implications. *Geochimica et Cosmochimica Acta*, *268*, 230–257. https://doi.org/10.1016/j.gca.2019.07.055 Gutjahr, M., Ridgwell, A.,

Sexton, P. F., Anagnostou, E., Pearson, P. N., Pälike, H., Norris, R. D., Thomas, E., & Foster, G. L. (2017). Very large release of mostly volcanic carbon during the Palaeocene-Eocene Thermal Maximum. *Nature*, *548*(7669), 573–577. https://doi.org/10.1038/nature23646

Handley, L., Halloran, A. O., Pearson, P. N., Hawkins, E., Nicholas, C. J., Schouten, S., Mcmillan, I. K., & Richard, D. (2012). Changes in the hydrological cycle in tropical East Africa during the Paleocene-Eocene Thermal Maximum. *Palaeogeography, Palaeoclimatology, Palaeoecology*, *329–330*, 10–21. https://doi.org/10.1016/j.palaeo.2012.02.002

Harms Sarah M, & Ludwig, T. K. (2016). Retention and removal of nitrogen and phosphorus in saturated soils of arctic hillslopes. *Biogeochemistry*, *127*, 291–304. https://doi.org/10.1007/s10533-016-0181-0

Havranek, R. E., Snell, K. E., Davidheiser-Kroll, B., Bowen, G. J., & Vaughn, B. (2020). The Soil Water Isotope Storage System (SWISS): An integrated soil water vapor sampling and multiport storage system for stable isotope geochemistry. *Rapid Communications in Mass Spectrometry*, *34*(12), 1–11. https://doi.org/10.1002/rcm.8783

Havranek, R.E., Snell, K.E., Kopf, S.H., Davidheiser-Kroll, B., Morris, V. and Vaughn, B., *In Review*. Lessons from and best practices for the deployment of the Soil Water Isotope Storage System. *EGUsphere*, pp.1-29.

Held, I. M., & Soden, B. J. (2006). Robust Responses of the Hydrological Cycle to Global Warming. *Journal of Climate*, *19*, 5686–5699. https://doi.org/10.5220/0001648603850388

Henkes, G. A., Passey, B. H., Grossman, E. L., Shenton, B. J., Pérez-Huerta, A., & Yancey, T. E. (2014). Temperature limits for preservation of primary calcite clumped isotope paleotemperatures. *Geochimica et Cosmochimica Acta*, *139*, 362–382. https://doi.org/10.1016/j.gca.2014.04.040

Herbstritt B, Gralher B, Weiler MF. Continuous in situ measurements of stable isotopes in liquid water. *Water Resour Res*. 2012;48(3):1-6. doi:10.1029/2011WR011369

Hillel, D. (1998). *Environmental Soil Physics*. Academic Press.

Hinckley, E.-L. S., Barnes, R. T., Anderson, S. P., Williams, M. W., & Bernasconi, S. M. (2014). Nitrogen retention and transport differ by hillslope aspect at the rain-snow transition of the Colorado Front Range. *Journal of Geophysical Research: Biogeosciences*, *119*, 12811896. https://doi.org/10.1002/2013JG002588

Hollis, C. J., Jones, T. D., Anagnostou, E., Bijl, P. K., Cramwinckel, M. J., Cui, Y., Dickens, G. R., Edgar, K. M., Eley, Y., Evans, D., Foster, G. L., Inglis, G. N., Kennedy, E. M., Kozdon, R., Lauretano, V., Lear, H., Littler, K., Meckler, N., Naafs, B. D. A., … Sluijs, A. (2019). The DeepMIP contribution to PMIP4 : methodologies for selection , compilation and analysis of latest Paleocene and early Eocene climate proxy data , incorporating version 0 . 1 of the DeepMIP database. *Geoscientific Model Development Discussions*, *January*, 1–98.

Hough, B. G., Fan, M., & Passey, B. H. (2014). Calibration of the clumped isotope geothermometer in soil carbonate in Wyoming and Nebraska, USA : Implications for paleoelevation and paleoclimate reconstruction. *Earth and Planetary Science Letters*, *391*, 110–120. https://doi.org/10.1016/j.epsl.2014.01.008

Huntington, K. W., & Lechler, A. R. (2015). Carbonate clumped isotope thermometry in continental tectonics. *Tectonophysics*, *647*, 1–20. https://doi.org/10.1016/j.tecto.2015.02.019

Huntington, K. W., Eiler, J. M., Affek, H. P., Guo, W., Bonifacie, M., Yeung, L. Y., Thiagarajan, N., Passey, B., Tripati, A., Daëron, M., & Came, R. (2009). Methods and limitations of "clumped" CO2 isotope (Δ47) analysis by gas-source isotope ratiomass spectrometry. *Journal of Mass Spectrometry*, *44*(9), 1318–1329. https://doi.org/10.1002/jms.1614

Huth, T. E., Cerling, T. E., Marchetti, D. W., Bowling, D. R., Ellwein, A. L., & Passey, B. H. (2019). Seasonal bias in soil carbonate formation and its implications for interpreting high-resolution paleoarchives: evidence from southern Utah. *Journal of Geophysical Research: Biogeosciences*. https://doi.org/10.1029/2018JG004496

IAEA/WMO. *Global Network of Isotopes in Precipitation. The GNIP Database. Accessible at: Http://Www.Iaea.Org/Water.*; 2019

IPCC (2021). Masson-Delmotte, V.; Zhai, P.; Pirani, A.; Connors, S. L.; et al. (eds.). *Climate Change 2021: The Physical Science Basis* (PDF). Contribution of

Working Group I to the Sixth Assessment Report of the Intergovernmental Panel on Climate Change. Cambridge University Press (In Press). p. SPM-9

Ingalls, M., Rowley, D., Olack, G. A., Currie, B., Li, S., Schmidt, J., Tremblay, M., Polissar, P., Shuster, D. L., Lin, D., & Colman, A. (2018). Paleocene to Pliocene low-latitude, high-elevation basins of southern Tibet: Implications for tectonic models of India-Asia collision, Cenozoic climate, and geochemical weathering. *Bulletin of the Geological Society of America*, *130*(1–2), 307–330. https://doi.org/10.1130/B31723.1

Inglis, G. N., Bragg, F., Burls, N. J., Cramwinckel, M. J., Evans, D., Foster, G. L., Huber, M., Lunt, D. J., Siler, N., Steinig, S., Tierney, J. E., Wilkinson, R., Anagnostou, E., de Boer, A. M., Dunkley Jones, T., Edgar, K. M., Hollis, C. J., Hutchinson, D. K., and Pancost, R. D.: Global mean surface temperature and climate sensitivity of the early Eocene Climatic Optimum (EECO), Paleocene–Eocene Thermal Maximum (PETM), and latest Paleocene, Clim. Past, 16, 1953–1968, https://doi.org/10.5194/cp-16-1953-2020, 2020.

Inglis, G. N., Rohrssen, M., Kennedy, E. M., Crouch, E. M., Raine, J. I., Strogen, D. P., Naafs, B. D. A., Collinson, M. E., & Pancost, R. D. (2021). Terrestrial methane cycle perturbations during the onset of the Paleocene-Eocene Thermal Maximum. *Geology*, *49*(5), 520–524. https://doi.org/10.1130/G48110.1

Kelson, J. R., Huntington, K. W., Breecker, D. O., Burgener, L. K., Gallagher, T. M., Hoke, G. D., & Petersen, S. v. (2020). A proxy for all seasons? A synthesis of

clumped isotope data from Holocene soil carbonates. *Quaternary Science Reviews*, *234*, 106259. https://doi.org/10.1016/j.quascirev.2020.106259

Kelson, J. R., Watford, D., Bataille, C., Huntington, K. W., Hyland, E., & Bowen, G. J. (2018). Warm Terrestrial Subtropics During the Paleocene and Eocene: Carbonate Clumped Isotope (Δ47) Evidence From the Tornillo Basin, Texas (USA). *Paleoceanography and Paleoclimatology*, *33*(11), 1230–1249. https://doi.org/10.1029/2018PA003391

Kender, S., Bogus, K., Pedersen, G. K., Dybkjaer, K., Mather, T. A., Mariani, E., Ridgwell, A., Riding, J. B., Wagner, T., Hesselbo, S. P., & Leng, M. J. (2021). Paleocene/Eocene carbon feedbacks triggered by volcanic activity. *Nature Communications*, *12*, 5186. https://doi.org/10.1038/s41467-021-25536-0

Kennett, J. P., & Stottt, L. D. (1991). Abrupt deep-sea warming, palaeoceanographic changes and benthic extinctions at the end of the Palaeocene. *Nature*, *353*, 225–229. https://doi.org/10.1038/353225a0

Kiehl, J. T., Zarzycki, C. M., Shields, C. A., & Rothstein, M. v. (2021). Simulated changes to tropical cyclones across the Paleocene-Eocene Thermal Maximum (PETM) boundary. *Palaeogeography, Palaeoclimatology, Palaeoecology*, *572*. https://doi.org/10.1016/j.palaeo.2021.110421

Kim, S.-T., & O'Neil, J. R. (1997). Equilibrium and nonequilibrium oxygen isotope effects in synthetic carbonates. *Geochimica et Cosmochimica Acta*, *61*(16), 3461–3475. https://doi.org/10.1016/S0016-7037(97)00169-5

Kirtland Turner, S., Sexton, P. F., Charles, C. D., & Norris, R. D. (2014). Persistence of carbon release events through the peak of early Eocene global warmth. *Nature Geoscience*, *12*(September), 1–17. https://doi.org/10.1038/ngeo2240

Koch, P. L., Zachos, J. C., & Gingerich, P. D. (1992). Correlation between isotope records in marine and continental carbon reservoirs near the Palaeocene/Eocene boundary. *Nature*, *358*. https://doi.org/https://doi.org/10.1038/358319a0

Kohn, M. J. (2010). Carbon isotope compositions of terrestrial C3 plants as indicators of (paleo)ecology and (paleo)climate. *Proceedings of the National Academy of Scienes* , *107*. https://doi.org/10.1073/pnas.1004933107/-/DCSupplemental

Kohn, M. J. (2016). Carbon isotope discrimination in C3 land plants is independent of natural variations in pCO2. *Geochemical Perspectives Letters*, *2*(1), 35–43. https://doi.org/10.7185/geochemlet.1604

Korasidis, V. A., Wing, S. L., Nelson, D. M., & Baczynski, A. A. (2022). Reworked pollen reduces apparent floral change during the Paleocene-Eocene Thermal Maximum. *Geology*. https://doi.org/10.1130/G50441.1

Kopf, S., Davidheiser-Kroll, B. and Kocken, I., (2021). Isoreader: An R package to read stable isotope data files for reproducible research. *Journal of Open Source Software*, *6*(61), p.2878.

Kraus, M. J., Woody, D. T., Smith, J. J., & Dukic, V. (2015). Alluvial response to the Paleocene-Eocene Thermal Maximum climatic event, Polecat Bench, Wyoming

(U.S.A.). *Palaeogeography, Palaeoclimatology, Palaeoecology*, *435*, 177–192. https://doi.org/10.1016/j.palaeo.2015.06.021

Kraus, M. J., & Riggins, S. (2007). Transient drying during the Paleocene–Eocene Thermal Maximum (PETM): Analysis of paleosols in the bighorn basin, Wyoming. *Palaeogeography, Palaeoclimatology, Palaeoecology*, *245*(3–4), 444–461. https://doi.org/10.1016/J.PALAEO.2006.09.011

Kraus, M. J., McInerney, F. A., Wing, S. L., Secord, R., Baczynski, A. A., & Bloch, J. I. (2013). Paleohydrologic response to continental warming during the Paleocene-Eocene Thermal Maximum, Bighorn Basin, Wyoming. *Palaeogeography, Palaeoclimatology, Palaeoecology*, *370*, 196–208. https://doi.org/10.1016/j.palaeo.2012.12.008

Krishnan, S., Pagani, M., Huber, M., & Sluijs, A. (2014). High latitude hydrological changes during the Eocene Thermal Maximum 2. *Earth and Planetary Science Letters*, *404*, 167–177. https://doi.org/10.1016/j.epsl.2014.07.029

Kübert, A., Paulus, S., Dahlmann, A., Werner, C., Rothfuss, Y., Orlkowski, N., & Dubbertm Maren. (2020). Water Stable Isotopes in Ecohydrological Field Research : Comparison Between In Situ and Destructive Monitoring Methods to Determine Soil Water Isotopic Signatures. *Frontiers in Plant Science*, *11*(April), 1–13. https://doi.org/10.3389/fpls.2020.00387

Kühnhammer, K., Dahlmann, A., Iraheta, A., Gerchow, M., Birkel, C., Marshall, J. D., & Beyer, M. (2022). Continuous in situ measurements of water stable

isotopes in soils, tree trunk and root xylem: Field approval. *Rapid Communications in Mass Spectrometry*, *36*(5). https://doi.org/10.1002/rcm.9232

Kukla, T., Winnick, M. J., Maher, K., Ibarra, D. E., & Chamberlain, C. P. (2019). The Sensitivity of Terrestrial δ 18 O Gradients to Hydroclimate Evolution. *Journal of Geophysical Research: Atmospheres*, *124*, 563–582. https://doi.org/10.1029/2018JD029571

Kurtz, A. C., Kump, L. R., Arthur, M. A., Zachos, J. C., & Paytan, A. (2003). Early Cenozoic decoupling of the global carbon and sulfur cycles. *Paleoceanography*, *18*(4). https://doi.org/10.1029/2003PA000908

Levin, N. E., Brown, F. H., Behrensmeyer, A. K., Bobe, R., & Cerling, T. E. (2011). Paleosol carbonates from the Omo Group : Isotopic records of local and regional environmental change in East Africa. *Palaeogeography, Palaeoclimatology, Palaeoecology*, *307*, 75–89. https://doi.org/10.1016/j.palaeo.2011.04.026

Levin, N. E., Quade, J., Simpson, S. W., Semaw, S., & Rogers, M. (2004). Isotopic evidence for Plio-Pleistocene environmental change at Gona, Ethiopia. *Earth and Planetary Science Letters*, *219*(1–2), 93–110. https://doi.org/10.1016/S0012-821X(03)00707-6

Lourens, L. J., Sluijs, A., Kroon, D., Zachos, J. C., Thomas, E., Röhl, U., Bowles, J., & Raffi, I. (2005). Astronomical pacing of late Palaeocene to early Eocene global warming events. *Nature*, *435*(7045), 1083–1087. https://doi.org/10.1038/nature03814

Lunt, D. J., Huber, M., Anagnostou, E., Baatsen, M. L. J., Caballero, R., DeConto, R., Dijkstra, H. A., Donnadieu, Y., Evans, D., Feng, R., Foster, G. L., Gasson, E., von der Heydt, A. S., Hollis, C. J., Inglis, G. N., Jones, S. M., Kiehl, J., Turner, S. K., Korty, R. L., … Zeebe, R. E. (2017). The DeepMIP contribution to PMIP4: Experimental design for model simulations of the EECO, PETM, and pre-PETM (version 1.0). *Geoscientific Model Development*, *10*(2), 889–901. https://doi.org/10.5194/gmd-10-889-2017

Mahindawansha, A., Orlowski, N., Kraft, P., Rothfuss, Y., Racela, H., & Breuer, L. (2018). Quantification of plant water uptake by water stable isotopes in rice paddy systems. *Plant and Soil*, *429*(1–2), 281–302. https://doi.org/10.1007/s11104-018-3693-7

McInerney, F. A., & Wing, S. L. (2011). The Paleocene-Eocene Thermal Maximum: A Perturbation of Carbon Cycle, Climate, and Biosphere with Implications for the Future. *Annual Review of Earth and Planetary Sciences*, *39*(1), 489–516. https://doi.org/10.1146/annurev-earth-040610-133431

Miao, X., Mason, J. A., Johnson, W. C., & Wang, H. (2007). High-resolution proxy record of Holocene climate from a loess section in Southwestern Nebraska, USA. *Palaeogeography, Palaeoclimatology, Palaeoecology*, *245*(3–4), 368–381. https://doi.org/10.1016/j.palaeo.2006.09.004

Mintz, J. S., Driese, S. G., Breecker, D. O., & Ludvigson, G. A. (2011). Influence of changing hydrology on pedogenic calcite precipitation in vertisols dance bayou, Brazoria County, Texas, U.S.A.: Implications for estimating paleoatmospheric

PCo2. *Journal of Sedimentary Research*, *81*(6), 394–400. https://doi.org/10.2110/jsr.2011.36

Montanez, I. P. (2013). Modern soil system constraints on reconstructing deep-time atmospheric CO 2. *Geochemica et Cosmochimica Acta*, *101*(January 2013), 57–75.

Nordt, L. C., & Driese, S. D. (2010). New weathering index improves paleorainfall estimates from Vertisols. *Geology*, *38*(5), 407–410. https://doi.org/10.1130/G30689.1

Oerter, E. J., Perelet, A., Pardyjak, E., & Bowen, G. J. (2016). Membrane inlet laser spectroscopy to measure H and O stable isotope compositions of soil and sediment pore water with high sample throughput. *Rapid Communications in Mass Spectrometry*, *31*(1), 75–84. https://doi.org/10.1002/rcm.7768

Oerter, E. J., & Amundson, R. (2016). Climate controls on spatial temporal variations in the formation of pedogenic carbonate in the western Great Basin of North Americ. *Bulletin of the Geological Society of America*, *128*(7), 1095–1104. https://doi.org/10.1130/B31367.1

Oerter EJ, Singleton M, Thaw M, Davisson ML. Water vapor exposure chamber for constant humidity and hydrogen and oxygen stable isotope composition. *Rapid Commun Mass Spectrom*. 2019;33(October 2018):89-96. doi:10.1002/rcm.8311

Oerter, E. J., & Bowen, G. J. (2017). In situ monitoring of H and O stable isotopes in soil water reveals ecohydrologic dynamics in managed soil systems. *Ecohydrology*, *10*(4), 1–13. https://doi.org/10.1002/eco.1841

Oerter, E. J., & Bowen, G. J. (2019). Spatio-temporal heterogeneity in soil water stable isotopic composition and its ecohydrologic implications in semiarid ecosystems. *Hydrological Processes*, *March*, 1–15. https://doi.org/10.1002/hyp.13434

Orlowski, N., Pratt, D. L., & McDonnell, J. J. (2016). Intercomparison of soil pore water extraction methods for stable isotope analysis. *Hydrological Processes*, *30*(19), 3434–3449. https://doi.org/10.1002/hyp.10870

Orlowski N, Breuer L, Mcdonnell JJ. Critical issues with cryogenic extraction of soil water for stable isotope analysis. *Ecohydrology*. 2016;9(1):3-10. doi:10.1002/eco.1722

Pagel, M., Barbin, V., Blanc, P. and Ohnenstetter, D., (2000). Cathodoluminescence in geosciences: an introduction (pp. 1-21). Springer Berlin Heidelberg.

Passey, B. H. (2012). Reconstructing terrestrial environments using stable isotopes in fossil teeth and paleosol carbonates. *Reconstructing Earth's Deep-Time Climate*, *18*, 167–193. https://doi.org/10.1017/S1089332600002606

Passey, B. H., Levin, N. E., Cerling, T. E., Brown, F. H., & Eiler, J. M. (2010). High-temperature environments of human evolution in East Africa based on bond ordering in paleosol carbonates. *Proceedings of the National Academy of Sciences*, *107*(25), 11245–11249. https://doi.org/10.1073/pnas.1001824107

Passey, B. H., & Henkes, G. A. (2012). Carbonate clumped isotope bond reordering and geospeedometry. *Earth and Planetary Science Letters*, *351–352*, 223–236. https://doi.org/10.1016/J.EPSL.2012.07.021

Penman, D. E., & Zachos, J. C. (2018). New constraints on massive carbon release and recovery processes during the Paleocene-Eocene Thermal Maximum. *Environmental Research Letters*, *13*(10). https://doi.org/10.1088/1748-9326/aae285

Peppe, D. J., Royer, D. L., Cariglino, B., Oliver, S. Y., Newman, S., Leight, E., Enikolopov, G., Fernandez-Burgos, M., Herrera, F., Adams, J. M., Correa, E., Currano, E. D., Erickson, J. M., Hinojosa, L. F., Hoganson, J. W., Iglesias, A., Jaramillo, C. A., Johnson, K. R., Jordan, G. J., … Wright, I. J. (2011). Sensitivity of leaf size and shape to climate: Global patterns and paleoclimatic applications. *New Phytologist*, *190*(3), 724–739. https://doi.org/10.1111/j.1469-8137.2010.03615.x

Peters, N. A., Huntington, K. W., & Hoke, G. D. (2013). Hot or not? Impact of seasonally variable soil carbonate formation on paleotemperature and O-isotope records from clumped isotope thermometry. *Earth and Planetary Science Letters*, *361*, 208–218. https://doi.org/10.1016/j.epsl.2012.10.024

Peterson, B. J., & Fry, B. (1987). Stable Isotopes in Ecosystem Studies. *Annual Reviews of Ecology and Systematics*, *18*, 293–320. http://www.jstor.org/stable/2097134

Pujalte, V., Baceta, J. I., & Schmitz, B. (2015). A massive input of coarse-grained siliciclastics in the Pyrenean Basin during the PETM : the missing ingredient in a coeval abrupt change in hydrological regime A massive input of coarse-grained

siliciclastics in the Pyrenean Basin during the PETM. *Climate of the Past* , *11*(January 2017). https://doi.org/https://doi.org/10.5194/cp-11-1653-2015

Quade, M., Klosterhalfen, A., Graf, A., Brüggemann, N., Hermes, N., Vereecken, H., & Rothfuss, Y. (2019). In-situ monitoring of soil water isotopic composition for partitioning of evapotranspiration during one growing season of sugar beet (Beta vulgaris). *Agricultural and Forest Meteorology*, *266–267*(December 2018), 53–64. https://doi.org/10.1016/j.agrformet.2018.12.002

Quade, M., Brüggemann, N., Graf, A., Vanderborght, J., Vereecken, H., & Rothfuss, Y. (2018). Investigation of Kinetic Isotopic Fractionation of Water during Bare Soil Evaporation. *Water Resources Research*, *54*(9), 6909–6928. https://doi.org/10.1029/2018WR023159

Quade, J., Cerling, T. E., & Bowman, J. R. (1989). Systematic variations in the carbon and oxygen isotopic composition of pedogenic carbonate along elevation transects in the southern Great Basin, United States. *Geological Society of America Bulletin*, *101*(4), 464–475. https://doi.org/10.1130/0016-7606(1989)101<0464:SVITCA>2.3.CO;2

Quade, J., Eiler, J., Daëron, M., & Achyuthan, H. (2013). The clumped isotope geothermometer in soil and paleosol carbonate. *Geochimica et Cosmochimica Acta*, *105*, 92–107. https://doi.org/10.1016/j.gca.2012.11.031

Rae, J.W., Zhang, Y.G., Liu, X., Foster, G.L., Stoll, H.M. and Whiteford, R.D., 2021. Atmospheric CO2 over the past 66 million years from marine archives. *Annual*

Review of Earth and Planetary Sciences, *49*. *https://doi.org/10.1146/annurev-earth-082420-063026*

Rea, D. K., Zachos, J. C., Owen, R. M., & Gingerich, P. D. (1990). Global change at the Paleocene-Eocene boundary: climatic and evolutionary consequences of tectonic events. *Palaeogeography, Palaeoclimatology, Palaeoecology*, *79*(1–2), 117–128. https://doi.org/10.1016/0031-0182(90)90108-J

Reinhardt, L., von Gosen, W., Lückge, A., Blumenberg, M., Galloway, J. M., West, C. K., Sudermann, M., & Dolezych, M. (2022). Geochemical indications for the Paleocene-Eocene Thermal Maximum (PETM) and Eocene Thermal Maximum 2 (ETM-2) hyperthermals in terrestrial sediments of the Canadian Arctic. *Geosphere*, *18*(1), 327–349. https://doi.org/10.1130/GES02398.1

Roberts, L. N. R., Finn, T. M., Lewan, M. D., & Kirschbaum, M. A. (2008). Burial History, Thermal Maturity, and Oil and Gas Generation History of Source Rocks in the Bighorn Basin, Wyoming and Montana. *U.S. Geological Survey Scientific Investigations Report*, 0–28.

Rothfuss, Y., Vereecken, H., & Brüggemann, N. (2013). Monitoring water stable isotopic composition in soils using gas-permeable tubing and infrared laser absorption spectroscopy. *Water Resources Research*. https://doi.org/10.1002/wrcr.20311

Rothfuss Y, Braud I, Le Moine N, et al. (2012). Factors controlling the isotopic partitioning between soil evaporation and plant transpiration: Assessment using

a multi-objective calibration of SiSPAT-Isotope under controlled conditions. *J Hydrol*. 2012;442-443:75-88. doi:10.1016/j.jhydrol.2012.03.041

Rothfuss, Y., Merz, S., Vanderborght, J., Hermes, N., Weuthen, A., Pohlmeier, A., Vereecken, H., & Brüggemann, N. (2015). Long-term and high-frequency non-destructive monitoring of water stable isotope profiles in an evaporating soil column. *Hydrology and Earth System Sciences*, *19*(10), 4067–4080. https://doi.org/10.5194/hess-19-4067-2015

Rothfuss, Y., Quade, M., Brüggemann, N., Graf, A., Vereecken, H., & Dubbert, M. (2021). Reviews and syntheses: Gaining insights into evapotranspiration partitioning with novel isotopic monitoring methods. In *Biogeosciences* (Vol. 18, Issue 12, pp. 3701–3732). Copernicus GmbH. https://doi.org/10.5194/bg-18-3701-2021 Routson, C.C., McKay, N.P., Kaufman, D.S., Erb, M.P., Goosse, H., Shuman, B.N., Rodysill, J.R. and Ault, T., (2019). Mid-latitude net precipitation decreased with Arctic warming during the Holocene. *Nature*, *568*(7750), pp.83-87.

Rozanski, K., Araguas-Araguas, L., & Gonfiantini, R. (1993). Isotopic Patterns in Modern Global Precipitation. *Geophysical Monograph Series*, *78*, 1–36.

Rozmiarek, K. S., Vaughn, B. H., Jones, T. R., Morris, V., Skorski, W. B., Hughes, A. G., Elston, J., Wahl, S., Faber, A. K., & Steen-Larsen, H. C. (2021). An unmanned aerial vehicle sampling platform for atmospheric water vapor isotopes in polar environments. *Atmospheric Measurement Techniques*, *14*(11), 7045–7067. https://doi.org/10.5194/amt-14-7045-2021

Rugenstein, J. K. C., & Chamberlain, C. P. (2018). The evolution of hydroclimate in Asia over the Cenozoic: A stable-isotope perspective. *Earth-Science Reviews*, *185*(May), 1129–1156. https://doi.org/10.1016/j.earscirev.2018.09.003

Rush, W. D., Kiehl, J. T., Shields, C. A., & Zachos, J. C. (2021). Increased frequency of extreme precipitation events in the North Atlantic during the PETM: Observations and theory. *Palaeogeography, Palaeoclimatology, Palaeoecology*, *568*(January), 110289. https://doi.org/10.1016/j.palaeo.2021.110289

Schauble, E. A., Ghosh, P., & Eiler, J. M. (2006). Preferential formation of 13C-18O bonds in carbonate minerals, estimated using first-principles lattice dynamics. *Geochimica et Cosmochimica Acta*, *70*(10), 2510–2529. https://doi.org/10.1016/j.gca.2006.02.011

Scholl, M. A., Ingebritsen, S. E., Janik, C. J., & Kauahikaua, J. P. (1996). Use of precipitation and groundwater isotopes to interpret regional hydrology on a tropical volcanic island: Kilauea volcano area, Hawaii. *Water Resources Research*, *32*(12), 3525–3537. https://doi.org/10.1029/95WR02837

Secord, R., Gingerich, P. D., Lohmann, K. C., & MacLeod, K. G. (2010). Continental warming preceding the Palaeocene-Eocene thermal maximum. *Nature*, *467*(7318), 955–958. https://doi.org/10.1038/nature09441

Secord, R., Bloch, J. L., Chester, S. G. B., Boyer, D. M., Wood, A. R., Wing, S. L., Kraus, M. J., McInerney, F. A., & Krigbaum, J. (2012). Evolution of the Earliest HorsesDriven by Climate Change in thePaleocene-Eocene Thermal Maximum. *Science*, *335*(6071), 959–962. https://doi.org/10.1126/science.1213859

Sewall, J.O., and Sloan, L.C., 2006, Come a little bit closer: A high-resolution climate study of the early Paleogene Laramide foreland: Geology, v. 34, p. 81–84, doi:10.1130/G22177.1

Shields, C. A., Kiehl, J. T., Rush, W., Rothstein, M., & Snyder, M. A. (2021). Atmospheric rivers in high-resolution simulations of the Paleocene Eocene Thermal Maximum (PETM). *Palaeogeography, Palaeoclimatology, Palaeoecology*, *567*(November 2020), 110293. https://doi.org/10.1016/j.palaeo.2021.110293

Shuman, B. N., & Marsicek, J. (2016). The structure of Holocene climate change in mid-latitude North America. *Quaternary Science Reviews*, *141*, 38–51. https://doi.org/10.1016/j.quascirev.2016.03.009

Shuman, B. N., & Serravezza, M. (2017). Patterns of hydroclimatic change in the Rocky Mountains and surrounding regions since the last glacial maximum. *Quaternary Science Reviews*, *173*, 58–77. https://doi.org/10.1016/j.quascirev.2017.08.012

Sluijs, A., Schouten, S., Pagani, M., Woltering, M., Brinkhuis, H., Dickens, G. R., Huber, M., Reichart, G., Stein, R., Matthiessen, J., Lourens, L. J., Pedentchouk, N., Backman, J., & Moran, K. (2006). *Subtropical Arctic Ocean temperatures during the Palaeocene / Eocene thermal maximum*. *441*(June), 3–6. https://doi.org/10.1038/nature04668

Sluijs, A., Frieling, J., Inglis, G. N., Nierop, K. G. J., Peterse, F., Sangiorgi, F., & Schouten, S. (2020). Late Paleocene-early Eocene Arctic Ocean Sea Surface Temperatures; 1 reassessing biomarker paleothermometry at Lomonosov Ridge

2 3 The Integrated Ocean Drilling Program Arctic Coring Expedition on Lomonosov 20. *Climate of the Past*, *16*(6), 2381–2400. https://doi.org/10.5194/cp-2020-13

Smith, F. A., Wing, S. L., & Freeman, K. H. (2007). Magnitude of the carbon isotope excursion at the Paleocene-Eocene thermal maximum: The role of plant community change. *Earth and Planetary Science Letters*, *262*(1–2), 50–65. https://doi.org/10.1016/j.epsl.2007.07.021

Snell, K.E., Thrasher, B.L., Eiler, J.M., Koch, P.L., Sloan, L.C. and Tabor, N.J., 2013. Hot summers in the Bighorn Basin during the early Paleogene. *Geology*, *41*(1), pp.55-58.

Soderberg, K., Good, S. P., Wang, L., & Caylor, K. (2012). Stable Isotopes of Water Vapor in the Vadose Zone: A Review of Measurement and Modeling Techniques. *Vadose Zone Journal*, *11*(3), 0. https://doi.org/10.2136/vzj2011.0165

Soil Survey Staff, Natural Resources Conservation Service, United States Department of Agriculture. Soil Series Classification Database. Available online. Accessed 09/10/2022.

Sprenger, M., Herbstritt, B. and Weiler, M., (2015). Established methods and new opportunities for pore water stable isotope analysis. *Hydrological Processes*, *29*(25), pp.5174-5192.

Sprenger, M., Leistert, H., Gimbei, G., & Weiler, M. (2016). Illuminating hydrological processes at the soil-vegetation-atmosphere interface with water

stable isotopes. *Reviews in Geophysics*, *54*, 674–704. https://doi.org/10.1002/2015RG000515

Sprenger, M., & Allen, S. T. (2020). What Ecohydrologic Separation Is and Where We Can Go With It (2020). In *Water Resources Research* (Vol. 56, Issue 7). Blackwell Publishing Ltd. https://doi.org/10.1029/2020WR027238

Steig, E.J., (1999). Mid-Holocene climate change. *Science*, *286*(5444), pp.1485-1487.

Steinthorsdottir, M., Coxall, H. K., de Boer, A. M., Huber, M., Barbolini, N., Bradshaw, C. D., Burls, N. J., Feakins, S. J., Gasson, E., Henderiks, J., Holbourn, A., Kiel, S., Kohn, M. J., Knorr, G., Kürschner, W. M., Lear, C. H., Liebrand, D., Lunt, D. J., Mörs, T., Pearson, P. N., Pound, M. J., Stoll, H., and Strömberg, C. A. E., 2020: The Miocene: the Future of the Past: Paleoceanography and Paleoclimatology, 36(4), e2020PA004037. https://doi.org/10.1029/2020PA004037

Stuiver, M. and Polach, H.A., (1977). Discussion reporting of 14C data. *Radiocarbon*, *19*(3), pp.355-363.

Stumpp, C., Stichler, W., Kandolf, M. and Šimůnek, J., (2012). Effects of land cover and fertilization method on water flow and solute transport in five lysimeters: A long-term study using stable water isotopes. *Vadose Zone Journal*, *11*(1).

Theis, D. E., Saurer, M., Blum, H., Frossard, E., & Siegwolf, R. T. W. (2004). A portable automated system for trace gas sampling in the field and stable isotope

analysis in the laboratory. *Rapid Communications in Mass Spectrometry*, *18*(18), 2106–2112. https://doi.org/10.1002/rcm.1596

Tierney, J. E., Zhu, J., Li, M., Ridgewell, A., Hakim, G. J., Poulsen, C. J., Whiteford, R. D. M., Rae, J. W. B., & Kump, L. R. (2022). Spatial patterns of climate change across the Paleocene-Eocene Thermal Maximum. *Proceedings of the National Academy of Science*, *119*(42). https://doi.org/https://doi.org/10.1073/pnas.2205326119

Tipple, B. J., Pagani, M., Krishnan, S., Dirghangi, S. S., Galeotti, S., Agnini, C., Giusberti, L., & Rio, D. (2011). Coupled high-resolution marine and terrestrial records of carbon and hydrologic cycles variations during the Paleocene-Eocene Thermal Maximum (PETM). *Earth and Planetary Science Letters*, *311*(1–2), 82–92. https://doi.org/10.1016/j.epsl.2011.08.045

Tripati, A. K., Hill, P. S., Eagle, R. A., Mosenfelder, J. L., Tang, J., Schauble, E. A., Eiler, J. M., Zeebe, R. E., Uchikawa, J., Coplen, T. B., Ries, J. B., & Henry, D. (2015). Beyond temperature: Clumped isotope signatures in dissolved inorganic carbon species and the influence of solution chemistry on carbonate mineral composition. *Geochimica et Cosmochimica Acta*, *166*, 344–371. https://doi.org/10.1016/j.gca.2015.06.021

Uno, K. T., Cerling, T. E., Harris, J. M., Kunimatsu, Y., Leakey, M. G., Nakatsukasa, M., & Nakaya, H. (2011). Late Miocene to Pliocene carbon isotope record of differential diet change among East African herbivores. *Proceedings of*

the National Academy of Sciences, *108*(16), 6509–6514. https://doi.org/10.1073/pnas.1018435108

van der Meulen, B., Gingerich, P. D., Lourens, L. J., Meijer, N., van Broekhuizen, S., van Ginneken, S., & Abels, H. A. (2020). Carbon isotope and mammal recovery from extreme greenhouse warming at the Paleocene–Eocene boundary in astronomically-calibrated fluvial strata, Bighorn Basin, Wyoming, USA. *Earth and Planetary Science Letters*, *534*. https://doi.org/10.1016/j.epsl.2019.116044

Vereecken, H., Amelung, W., Bauke, S. L., Bogena, H., Brüggemann, N., Montzka, C., Vanderborght, J., Bechtold, M., Blöschl, G., Carminati, A., Javaux, M., Konings, A. G., Kusche, J., Neuweiler, I., Or, D., Steele-Dunne, S., Verhoef, A., Young, M., & Zhang, Y. (2022). Soil hydrology in the Earth system. *Nature Reviews Earth & Environment*. https://doi.org/10.1038/s43017-022-00324-6

Volkmann, T. H. M., & Weiler, M. (2014). Continual in situ monitoring of pore water stable isotopes in the subsurface. *Hydrology and Earth System Sciences*, *18*(5), 1819–1833. https://doi.org/10.5194/hess-18-1819-2014

Wang, Z., Schauble, E. A., & Eiler, J. M. (2004). Equilibrium thermodynamics of multiply substituted isotopologues of molecular gases. *Geochimica et Cosmochimica Acta*, *68*(23), 4779–4797. https://doi.org/10.1016/j.gca.2004.05.039

Wassenaar, L. I., Hendry, M. J., Chostner, V. L., & Lis, G. P. (2008). High resolution pore water δ2H and δ18O measurements by H2O(liquid)-H2O (vapor)

equilibration laser spectroscopy. *Environmental Science and Technology*, *42*(24), 9262–9267. https://doi.org/10.1021/es802065s

Weil, R. R., & Brady, N. C. (2017). *The Nature and Properties of Soils* (15th editi). Pearson Education.

Westerhold, T., Marwan, N., Drury, A. J., Liebrand, D., Agnini, C., Anagnostou, E., Barnet, J. S. K., Bohaty, S. M., de Vleeschouwer, D., Florindo, F., Frederichs, T., Hodell, D. A., Holbourn, A. E., Kroon, D., Lauretano, V., Littler, K., Lourens, L. J., Lyle, M., Pälike, H., … Zachos, J. C. (2020). An astronomically dated record of Earth's climate and its predictability over the last 66 million years. *Science*, *369*(6509), 1383–1387. https://doi.org/10.1126/science.aba6853

Westerhold, T., Röhl, U., Wilkens, R. H., Gingerich, P. D., Clyde, W. C., Wing, S. L., Bowen, G. J., & Kraus, M. J. (2018). Synchronizing early Eocene deep-sea and continental records - Cyclostratigraphic age models for the Bighorn Basin Coring Project drill cores. *Climate of the Past*, *14*(3), 303–319. https://doi.org/10.5194/cp-14-303-2018

Widlansky, S. J., Secord, R., Snell, K. E., Chew, A. E., & Clyde, W. C. (2022). Terrestrial carbon isotope stratigraphy and mammal turnover during post-PETM hyperthermals in the Bighorn Basin, Wyoming, USA. *Climate of the Past*, *18*(4), 681–712. https://doi.org/10.5194/cp-18-681-2022

Wing, S. L., Harrington, G. J., Smith, F. a, Bloch, J. I., Boyer, D. M., & Freeman, K. H. (2005). Transient Floral Change and Rapid Global Warming at the Paleocene

- Eocene Boundary. *Science*, *310*(November), 993–996. https://doi.org/10.1126/science.1116913

Wing, S. L., & Currano, E. D. (2013). Plant response to a global greenhouse event 56 million years ago. *American Journal of Botany*, *100*(7), 1234–1254. https://doi.org/10.3732/ajb.1200554

Wing, S.L. and Currano, E.D., 2017, December. Terrestrial floral change during the ETM2 hyperthermal. In *AGU Fall Meeting Abstracts* (Vol. 2017, pp. PP31D-08).

Zachos, J., Pagani, M., Sloan, L., Thomas, E., & Billups, K. (2001). Trends, Global Rhythms, Aberrations in Global Climate 65Ma to Present. *Science*, *292*(5517), 686–693. https://doi.org/10.1126/science.1059412

Zachos JC, Schouten S, Bohaty S, Quattlebaum T, Sluijs A, et al. 2006. Extreme warming of mid-latitudecoastal ocean during the Paleocene-Eocene Thermal Maximum: inferences from TEX86 and isotopedata.Geology34:737–40

Zamanian, K., Pustovoytov, K., & Kuzyakov, Y. (2016). Pedogenic carbonates : Forms and formation processes. *Earth Science Reviews*, *157*, 1–17. https://doi.org/10.1016/j.earscirev.2016.03.003

Zeebe, R. E., & Wolf-Gladrow, D. A. (2001). CO2 in seawater: equilibium, kinetics and isotopes. In *Elselvier Oceanography Series* (Vol. 65). Elsevier Science

Zeebe R E, Zachos J C and Dickens G R 2009 Carbon dioxide forcingalone insufficient to explain Palaeocene-Eocene ThermalMaximum warmingNat. Geosci.2576–8014Environ. Res. Lett.13(2018)105008

Zeebe, R. E., & Lourens, L. J. (2019). Solar System chaos and the Paleocene–Eocene boundary age constrained by geology and astronomy. *Science*, *929*(August), 926–929. https://doi.org/10.1126/science.aax0612

Zhao, P., Tang, X., Zhao, P., Wang, C. and Tang, J., 2013. Identifying the water source for subsurface flow with deuterium and oxygen-18 isotopes of soil water collected from tension lysimeters and cores. *Journal of Hydrology*, *503*, pp.1-10

Zimmermann, U., Munnich, K. O., & Roether, W. (1966). Tracers Determine Movement of Soil Moisture and Evapotranspiration. *Science*, *152*(3720), 346–347. https://doi.org/10.1126/science.152.3720.346